INVESTIGATION OF MULTIPLE CHARGING PHENOMENON AND GAS-PHASE ION/ION REACTIONS FOR BIOLOGICAL/SYNTHETIC POLYMERS AND GLYCOLIPIDS

by

Hsi-Chun Chao

A Dissertation

Submitted to the Faculty of Purdue University

In Partial Fulfillment of the Requirements for the degree of

Doctor of Philosophy

Department of Chemistry

West Lafayette, Indiana

May 2022

THE PURDUE UNIVERSITY GRADUATE SCHOOL

STATEMENT OF COMMITTEE APPROVAL

Dr. Scott A. McLuckey, Chair

Department of Chemistry

Dr. Hilkka I. Kenttämaa

Department of Chemistry

Dr. Mary J. Wirth

Department of Chemistry

Dr. Julia Laskin

Department of Chemistry

Approved by:

Dr. Christine Hrycyna

Dedicated to my parents

- for their unconditional support and love.

獻給我的父母

and to the ones who never stopped believing

- for your astounding courages

也獻給永不放棄希望的你和妳

ACKNOWLEDGMENTS

Sr. Issac Newton said, “If I have seen farther than others, it is because I was standing on the shoulders of giants.” Metaphorically, I was also standing on the shoulders of many people (although some of them might not be able to hold me on their shoulders, some might!), to see through many incredible sciences (with glasses most of the time) and accomplish my Ph.D. journey.

I am sincerely grateful to the first giant in my Ph.D. study, my advisor, Dr. Scott A. McLuckey (and he sure is a giant). Scott showed me the whole new world of mass spectrometry (not on a carpet), despite my previous related experiences. Scott is not only knowledgeable but more inspiring and couraging. I always remember my first meeting with Scott before I joined the group. He pointed out all the dissertations on the bookshelf and told me that most of the sciences up here mainly were from students’ ideas, and he just supported them to achieve the goals. Therefore, I always like to share my “out of blue” ideas with Scott, and he can always somehow give important insights into them, and sometimes a new research adventure begins like that. It will be such an honor for me that this dissertation may be put up there and be one of the inspired works by Scott.

I would like to thank all my committee members, Dr. Hilkka I. Kenttamaa, Dr. Mary J. Wirth, and Dr. Julia Laskin, for their support during my Ph.D. study. I cherish all the conversations with any committee members because I know I am learning from the best giants of the fields. I would also like to thank Purdue University and the Chemistry department. Studying analytical chemistry at Purdue is a privilege, and now I am ready to take a giant leap. Tracing back to the beginning, I must thank my undergraduate and master research advisor, Dr. Ching-Hua Kuo, at National Taiwan University. Dr. Kuo helped me build the bases for doing research and guiding me with patience while I was too “young” to be on my own. Until now, Dr. Kuo is still willing to listen to my questions if I have any.

Many other giants provided mentorships for my Ph.D. study. I want to thank all the lab members, current and former, from McLuckey’s Lab. To Dr. Mack Shih, Dr. Nan Wang, and Dr. Feifei Zhao, the triad support systen allows me to feel less stressed when I am just “fresh off the boat.” To Dr. Sarju Adhikari, Dr. Elissia Franklin, Dr. Christopher Harrilal, Dr. David Foreman, and Dr. Joshua Johnson, I appreciate all the mentorships from your experiences and our valuable

conversations. To Dr. Caitlin Randolph, thank you for all the proofreading and excellent discussion among our favorites (lipids, not fat). To Dr. Kenneth Lee, thank you for always being patient with me to any of my questions regarding any research topics. To Dr. Anthoy Pitts-McCoy, thank you for the "always-warm" vibe and every greeting in the lab (it feels colder without you in the basement.) To Dr. John Lawer, thank you for the sincere suggestions in real life (outside grad school life). To Dr. Josh Fischer, thank you for all the listening and teaching (even only for a year.) To Dr. Abdirahman Abdillahi, thank you for postponing your graduation from your fourth year to the fifth year and for everything we work together in the lab. To Jay Bhanot, thank you for the journey we have been through since we joined the group. I must also acknowledge the younger students in the lab that they all provide many opportunities for me to learn and grow. To Ian Carrick and DeShovon Shenault, thank you for all our discussions. To Nicole Brundridge, Kimberly Fabijanczuk, Alex (Liangxuan) Fu, and Sarah Nsiah, thank you for tolerating me learning to be a mentor. To Samantha Mehnert, Nick Pizzala, and Gwendylan Turner, I wish you all the best, and we know you are in the best group.

My Ph.D. journey will not have colors without all the companies with my friends. Thank you for all the inside jokes and support from my Taiwanese Purdue Chemistry family, Aaron Chen, Kevin Wee, Judy Kuan-Yu Liu, and Kai-Hung Huang. I am also thankful to my first-year TA office partners, Abdilrahaman (Abdi), Andres (not Andreas), Denilson (Sonson), Sebastian (Sebas), and Victoria (Marie). Abdi, here you are again; thank you for introducing misconduct concepts because we are dramatic anyway. Andres, thank you for always being spontaneous that you will always say no but then yes for hanging out with us. Denilson, thank you for promoting me from 0.1 friends to a true friend, even though I still do not understand how to quantify such an abstract concept as friendship. Moreover, thank you for being the only Brazilian I know. Sebas, thank you for all the intriguing conversations we had, very inspiring and "liberating." Victoria, aka Flucktoria, aka Marie, thank you for trying to survive in a group of five guys (or two guys) and for all the support you gave to me.

It is tough for a graduate student to stay in a foreign country. Therefore, I am grateful to all my former and current roommates, Ching-Yang, Yi-Lin, Li-Chieh, Da-Wei, and Shih-Wen, for your kind hearts, making me feel at home when I come back to the apartment. I would also like to thank all the Taiwanese friends I met at Purdue. Thank you for the Taiwanese vibe every time we meet. Thank you to the Kaluf family for your warm hospitality and gathering whenever. Special

shoutout to my roommates and friends, Yu-Hsin and Cih; thank you for bearing me all the time but still living with me from the beginning till the end and inviting me to all the places we toured together. I must also thank my friends in Taiwan for letting me know I am not alone in the states, but you are always “stand” by me. To Wan-Yu and Chioung-Yi, the fascinating internet allows us still connect despite the fact we are 7700 miles away; thank you for all the support. To Yi-Fu, thank you for trying to stay in the states and the trip to Boston, and I think you will do great wherever you are. To Pei-Ju, thank you for always being there, which is more than enough. There is a phrase in Taiwanese stating: “If there are too many things to thank, then thank the sky,” so I also thank the sky.

Last but not least, I must express my deepest gratitude to my parents. My parents always support me and encourage me to pursue my dream, although the dream is in a faraway kingdom. My father is always proud of me and my dearest mother, who is so brave to overcome her anxiety issue, always believes in me. Without my parents’ unconditional love and support, I would not be able to go this far. Thank you.

TABLE OF CONTENTS

LIST OF TABLES

LIST OF FIGURES

LIST OF ABBREVIATIONS

2D	Two-dimensional
CCS	Collisional Cross-Section
CD	Charge Density
CEM	Chain Ejection Model
Cer	Ceramide
CID	Collisional Induced Dissociation
CNS	Central Nervous System
CRM	Charge Residue Model
CytC	Cytochrome C
DC	Direct Current
DDC	Dipolar DC
EC	Emerald City
EID	Tlectron-Induced Dissociation
ESI	Electrospray Ionization
ETD	Electron Transfer Reaction
FA	Fatty Acids
Fuc	Fucose or Fucosylated
Gal	Galactose
Glc	Glucose
GalNAc	N-Acetylgalactosamine
Gc-	N-Glycolylneuraminic Acid (NeuGc) Conjugated
GSLs	Glycosylsphingolipids
GalSLs	Galactosylsphingolipids
GlcSLs	Glucosylsphingolipids
GM	Gangliosides with a single (mono) sialic acid
GD	Gangliosides with a two (di-) sialic acid
GT	Gangliosides with a three (tri-) sialic acid
HA(s)	Hyaluronic acid(s)

Hex	Hexose
HILIC	Hydrophilic Interaction Liquid Chromatography
HR-IMS	High Resolution Ion Mobility Mass Spectrometry
IEM	Ion Evaporation Model
IMS	Ion Mobility Mass Spectrometry
LC	Liquid Chromatography
M/C	Average Numbers of Residue per Charge
m/z	Mass-to-Charge Ratio
MALDI	Matrix Assisted Laser Desorption/Ionization
MeOH	Methanol
m-NBA	m-Nitrobenzyl Alcohol
MS	Mass spectrometry
MSn	Tandem Mass Spectrometry
MW	Molecular Weight
aMb	Apo-Myoglobin
hMb	Holo-Myoglobin
nano-ESI	nESI
NeuAc	N-Acetylneuraminic Acid
NeuGc	N-Glycolylneuraminic Acid
n-HexCer	Cerebroside (n is the configuration of glycosidic bond)
n-HexSph	Glycosylsphingosine (n is the configuration of glycosidic bond)
NHS	N-Hydroxysuccinimide
NL	Neutral Loss
NMR	Nuclear Magnetic Resonance
OzID	Ozone Induced Dissociation
PA	Proton Affinity
PD	Parkinson’s Disease
PEI	Polyethylenimine
PFO	Perfluoro-1-octanol
PrS	Proton Sponge, N, N, N′, N′-tetramethyl-1,8-naphthalenediamine

RF	Radio Frequency Current
RP	Reversed Phase
RPLC	Reversed Phase Liquid Chromatography
SCA	Supercharging Agent
SFC	Superficial Fluid Chromatography
SLIM	Structures for Lossless Ion Manipulations
Sph	Sphingosine
Terpy	2,2';6',2''-Terpyridine
TLC	Thin Layer Chromatography
Ub	Ubiquitin
UVPD	Ultraviolet Photodissociation

ABSTRACT

Mass spectrometry (MS) is one of the most commonly used analytical techniques in bioanalytical analysis, allowing scientists to characterize molecules with very diverse chemical features. The advance in ionization strategies significantly improves the potential in using MS for that purpose, especially electrospray ionization (ESI) can generate ions directly from solution in ambient conditions, showing high flexibility in coupling with other techniques. Moreover, a hallmark of the ESI of large polymeric molecules is also its tendency to generate a distribution of charge states based on their chemical characteristics, allowing us to exploit the multiple charging phenomenon in various applications.

This dissertation introduces the relationships between ESI and multiple charging phenomena with different proposed ionization models, and how condensed-phase and gas-phase approaches affect the multiple charging phenomenon. Moreover, multiply charged ions permit gas-phase ion/ion reactions to occur without neutralizing the ions. Therefore, various ion/ion reactions can be utilized for distinct analytical purposes. Objectively, this dissertation focuses on the investigation of the multiple charging phenomenon from ESI-MS, and the applications from taking the multiply charged ions to perform gas-phase ion chemistry in order to a) manipulate the charges of the targeted ions; b) invert the polarity of the targeted ions; c) and characterization of the ions from the gas-phase ion/ion reactions.

The first work demonstrates how multiple components (i.e., complicated mixtures) lead to a highly congested spectrum of ions with overlapped m/z values, resulting from the multiple charging phenomenon after the ESI process. Utilizing ionic reactions can de-congest the spectra via manipulating the charges of the ions to separate the overlapped signals. A universal spectral pattern in the ESI mass spectra is observed while analyzing multiply-charged homopolymers. Various parameters, such as the charges of the ions, widths of polymer distributions, monomer mass, and cationizing agent masses, are investigated to show how they can affect the appearance of the unique patterns, which condense the information of the overall distribution of the homopolymers. Combined with gas-phase charge reduction (i.e., proton transfer reaction), we can characterize the size distribution of polydisperse homopolymer samples.

Second, a novel type charge inversion ion/ion reaction summarizing the conversion of multiply charged protein ions to their opposite polarity and still holds multiple charges is reported. The reaction occurs via a single ion/ion collision with highly charged reagent ions, which we usually obtain from biological relevant polymers. Hyaluronic acid (HAs) anions and polyethylenimine (PEI) cations are used as the charge inversion reagents to react with protein ions. Remarkably, inversion of high absolute charge (up to 41) from the reaction is demonstrated. All mechanisms for ion/ion charge inversion involve low-energy ions proceeding via the formation of a long-lived complex. Factors that underlie the charge inversion of protein ions to the opposite polarity with high charge states in reaction with those reagent ions are hypothesized to include: (i) the relatively high charge densities of the HA anions and PEI cations that facilitate the extraction/donation of multiple protons from/to the protein leading to multiply charged protein anions/cations, (ii) the relatively high sum of absolute charges of the reactants that leads to high initial energies in the ion/ion complex, and (iii) the relatively high charge of the ion/ion complex following the multiple proton transfers that tends to destabilize the complex.

Third, shotgun MS strategies coupled with different gas-phase ion chemistry and tandem MS to analyze glycolipids are demonstrated. Glycolipids contain both carbohydrates and lipids structure components that it is incredibly challenging to analyze with MS. Isomeric cerebrosides (n-HexCer) and glycosphingosines (n-HexSph), which hold isomerisms in diastereomeric sugar head groups (glucose and galactose), anomeric glycosidic linkages (alpha- or beta-), and isomeric amide-bonded monounsaturated fatty acyl chain (double bond location) are successfully differentiated by dissociating gas-phase ion/ion reaction products, the charge-inverted complex cations. Both relative and absolute quantification of the isomers is also achieved, and analytical performances are evaluated in terms of accuracy, precision, and inter-day precision, allowing us to perform mixture analysis. Porcine brains were used to demonstrate the ability to profile and quantify those isomers from biological extracts. Moreover, a parallel workflow is also proposed for gangliosides, which have more complicated structures among their glycan moiety. Metal cation transfer, proton transfer, and charge inversion reactions are utilized to manipulate the ion types to provide better structural information. The proposed workflow allows us to clean up the mass spectra by neutralizing interfering isobaric ions, differentiate isomeric gangliosides, and perform relative quantitation when the standards are available. The workflow also is used to obtain gangliosides profiles from biological matrices. Overall, work in this dissertation takes advantage

of the multiple charging phenomenon and couples with gas-phase ion/ion reactions to achieve various analyses among a wide range of biological-related samples.

CHAPTER 1. INTRODUCTION TO MULTIPLE CHARGING PHENOMENON AND GAS-PHASE ION/ION REACTION IN MASS SPECTROMETRY

1.1 Brief History of Mass Spectrometry

Mass spectrometry (MS) has become one of the most widely-used analytical techniques since the early twentieth century, after Sr. J. J. Thomson's first mass spectrometer to measure mass-to-charge ratio (*m/z*) in 1897,[1] and later the first parabola mass spectrum was obtained, in which the first detection of multiply charged mercury cation in 1912.[2] F. W. Aston further modified the mass spectrometer allowing precise and volatile detection of ions[3] and observed the existence of two isotopic neon in "Aston's mass spectrograph,"[4] and the foundation of mass spectrometry had been built ever since.

Modern mass spectrometry instruments have evolved and differed from the mass spectrometer in Thomson's and Aston's time. However, all the mass spectrometers share the basic principle- monitoring ions' trajectories and measuring their mass-to-charge ratio, even in exceedingly divergent ways.[5] Despite the innovation of mass spectrometers tremendously improved the performance of *m/z* measurements, the generation of ions, especially from large molecules, remained a challenge for many decades until the invention of two breakthrough ionization strategies, matrix-assisted laser desorption ionization (MALDI) and electrospray ionization (ESI) in the late twentieth century.[6] Both MALDI and ESI could be considered as "soft ionization" methods, so they could preserve the intact large molecules rather than making fragments from them. This advanced feature drastically changes the role of mass spectrometry in biomolecule characterization that scientists can produce ions with m/z greater than thousands. However, MALDI typically generates singly or doubly charged ions,[7-8] but ESI has the power to generate multiply-charged ions allowing even larger molecules to have a lower mass-to-charge ratio that could be analyzed by some mass analyzers that have a low high-mass limit. Therefore, ESI shows advantages for large biomolecules analysis and allows us to manipulate the numbers of charges on the ions. In this dissertation, ESI is the primary ionization method for the work and will be discussed more in detail in the following sections.

1.2 Electrospray Ionization and Multiple Charging Phenomenon

Electrospray was first introduced by J. Fenn in 1984,[9] and further the application in ionizing large biomolecule was published in 1989.[10] The work was based on the investigation of macro-ions in the gas phase and the charged droplet work by M. Doyle.[11-12] The introduction of ESI immediately caught the attention of all mass spectrometrists, and it became one of the most widely-used ionization strategies since then.

Electrospray ionization has several advantages over other commonly used ionization methods. First, ESI is one of the ionization methods that can be operated under atmospheric pressure allowing ease of operation without the requirement of a vacuum system.[13] Second, the direct ionization from the infused sample solution simplifies the steps for ionization, such as evaporation or desorption.[14] Third, the capability to couple separation techniques, such as liquid chromatography[15-17] or capillary electrophoresis,[18-19] significantly improves the mass spectrometry's ability to analyze complicated biological samples. Last but not least, the generation of multiply-charged ions makes large molecules have a lower m/z value allowing researchers to utilize various mass spectrometers with limited mass range (with their high mass) to analyze them. All the advances mentioned above make ESI the most commonly used ionization method for biological applications.[20]

Despite the applicability of ESI for various usage, the ionization mechanism of ESI has not been fully understood. In the past few decades, researchers have proposed general mechanisms to explain how the charged droplets form via introducing an electric field and the relationships between the charges from the charged droplets to the ions of interest.[21] Besides the general explanation, different models, have been reported to meet the various ionization processes from different types of analytes, including ion evaporation model (IEM), charge residue model (CRM), and chain ejection model (CEM).[22] The following sections will be focused on the general explanation of the ionization process from ESI and the three models individually.

1.2.1 General ESI Mechanism

It is widely accepted by the scientific community that the general mechanic aspect of ESI, which starting with the nebulization of the solution from the capillary tips combined with a high electric field.[23] While applying a high electric field on the capillary tip, the solution moves forward

based on the electrophoresis force,[24] and the combined effects of the surface tension and the electrostatic force from the applied electric field, a cone-like structure of the solution could be obtained at the outlet of the capillary, which is Taylor cone.[25-26] Once the electric force (or the charges) surpasses the surface tension, which is the Rayleigh limit, the cone structure is no longer be able to maintain at the apex, then further "corrupts" into charged droplets, which is so-called electrospray.[25]

After nebulization, the charged droplets are formed, and the solvent is further evaporated, making the sizes of the charged droplets smaller. While the volume of the droplet becomes smaller, the charges on the droplet surface would have stronger Coulomb repulsion to each other. When the Coulomb repulsion equals to the surface tension of the droplet, which again reaches the Rayleigh limit, the charged droplet no longer be able to maintain its structure, then both Coulomb fission, which produces smaller progeny charged droplet, or ejection of the small ions on the surface would occur to reduce the charges on the surface.[5] After multiple events from the fission of charged droplet, de-solvation of the analyte would achieve, and ions would be formed. (**Figure 1.1**)[27-30]

Several analytical relationships could be used to describe the overall ESI process. Starting with electrospray, to generate a Taylor cone, it is needed to apply enough onset electric field (Eon) to overcome the surface tension between solution and capillary tip. Sr. G. Taylor proposed the approximation as the approximation following the relationship:[31]

$$E_{on} \approx \sqrt{\frac{r_c \gamma \cos\theta}{2\varepsilon_0}} \ln\left(\frac{4D}{r_c}\right) \textbf{(eq. 1.1)}$$

where r_c is the radius of capillary, γ is the surface tension, θ is the half-angle from the Taylor cone ($\theta \approx 49°$ while forming regular Taylor cone), ε_0 is the permittivity of vacuum, and D is the distance between the capillary and counter electrode. The experimental electric field at capillary (E_c) can be obtained by **equation 1.2**:

$$E_c = \frac{2V_c}{r_c \ln\left(\frac{4D}{r_c}\right)} \textbf{(eq. 1.2)}$$

where V_c is the applied potential between the capillary and the counter electrode. In the equation, we can understand that the required onset electric field for forming the Taylor cone is in proportion to the radius of the capillary and the surface tension of the solution.

While the numbers of charge (z_R) reach the Rayleigh limit, the charged droplets would form, and further Coulomb fission event to produce progeny droplets from the bigger droplets also follows the Rayleigh limit, and z_R could be described as the following **equation 1.3**:

$$z_R = \frac{8\pi}{e}\sqrt{\varepsilon_0 \gamma R^3} \textbf{ (eq. 1.3)}$$

where e is the elementary charge and R is the droplet radius.

Although the scientific community widely accepts the above explanation of the ESI mechanism and the analytical relationships, researchers proposed three models based on their experimental observations, including IEM, CRM, and CEM.[22] The three different models are applied to explain different ionization events associated with distinct chemical features of analytes and are highly related to the numbers of charges of those ions (**Figure 1.2**). To introduce the multiple charge phenomenon from the ESI process, it is crucial to think of all three different models. The following sections will introduce three models individually and their respective aspects to the multiple charging phenomenon.

1.2.2 Ion Evaporation Model (IEM)

IEM was proposed earlier than general the ESI process, in which Irbarne and Thomson investigated the formation of ions from the evaporation of charged droplets in 1976.[32] They discussed the process of the evaporation of cluster ions from charge droplet using with the estimation of energy barrier and the reaction rates, which they also proposed that driving force of the evaporation of the ions is from the Rayleigh instability. In general, the IEM suggests that while the electric field emanates from a charged nano-droplet (with the radius within 10 nm) is sufficiently high, the ejection of small solvated ions from the droplet surface would occur. The rate constant (k_e) of the ejection can be approximated using transition state (TS) theory:[32-33]

$$k_e = \frac{k_B}{h} e^{\left(\frac{-\Delta G^*}{k_B T}\right)} \textbf{ (eq. 1.4)}$$

where kB is the Boltzmann constant, h is Planck's constant, T is the temperature, and $-\Delta G^*$ is the height of the modified energy barrier. The model can also be considered as the theory for the formation of nanoscale progeny droplet from the droplet surface, in which Ahadi and Konermann used a molecular dynamics model to simulate the ejection of an ion with MeOH/Water-based droplet, that some solvent molecules actually "stick" on the charged ion when it firstly ejected from the bigger droplet surface. Then the solvent molecules evaporate at the later stages (e.g., in

the mass spectrometer).[34] Moreover, Ahadi and Konermann also utilized the TS to mimic how NH_4^+ ion experienced free energy in a water droplet, which demonstrated that a successful ion ejection event occurs under ns time scale and the position of the analytes in the droplet is significantly essential.[34] Therefore, the ionization of the analytes that are analog to NH_4^+ ion, which with low molecular weight (MW) such as small protonated/deprotonated molecules or inorganic ions, and better surface partitioning molecules (i.e., less polar analytes in a polar solvent droplet, high surface affinity) can be explained by IEM (**Figure 1.2a**). Since some inorganic molecules (especially metal cations) may have different oxidation states (different charges) in the condensed phase, the observation of multiple charges on those types of ion is not abnormal. However, IEM is limited to explaining the multiple charging phenomenon when ESI is applied to larger molecules such as proteins, more prominent than the proposed size of the cluster ions (~10 nm), and multiple protonation/deprotonation can be observed.

1.2.3 Charge Residue Model (CRM)

CRM was also based on the charge droplet study back in the days earlier than ESI that Doyle first proposed in 1968.[35] CRM introduced that multiple Coulomb fission events lead to the volume shrinkage of the droplet, and approaching the end of the evaporation process, the Rayleigh-charged droplet only contains one (or few) large molecules. After the last few solvent molecules evaporate, the charges from the droplet surface can transfer to the molecule, resulting in ionization of the analyte.[35-36] The numbers of charges on the ions from the fission events only occur while the charged droplet reaches the Rayleigh limit. Many research has demonstrated the relationship between charge states and the size of protein in terms of mass and the accommodated surface area of the proteins,[37-38] which charge states can be predicted by modifying the Rayleigh limit equation (**eq. 1.3**).[27] Besides, CRM might be affected by the early stage of IEM that when some salts take the charges away at the early evaporation, the remained charges may be lower, then lower the charge states were observed.[39] In sum, the general CRM illustrates that the larger the molecules, the more charges can be observed through the CRM process, demonstrating the multiple charge phenomenon from the ESI process. However, in some cases, such as unfolded proteins, they can be charged up much more than the intact protein (native and globular-like structure), which are

much higher than the theoretical Rayleigh charges. Therefore, CRM is majorly used for explaining the charging for large globular biomolecules (**Figure 1.2b**).

1.2.4 Chain Ejection Model (CEM)

To further understand why different structures of proteins hold such various charge states, Konermann and colleagues proposed chain ejection model (CEM), an analog to the production of highly charged unfolded proteins from activation of the original protein complex ions (**Figure 1.2c and 1.2d**).[40] The original scenario states that a protein unit from the protein complex would unfold under the activation. With further charge redistribution between the unfolded unit and the complex, t the Coulomb repulsion between the unfolded chain and the other intact part of the complex overcomes the activation energy. The chain is then ejected to form the fragment ions, the unfolded protein ions.[41] The site on the unfolded chain to reach the ejection point is called the "scission point." In charged droplets, unfolded proteins usually hold a higher hydrophobicity, making it easier to partition on the droplet's surface, not the center. The excess charges on the ESI droplet tend to find the distance to minimize the electrostatic potential on the surface; therefore, the charge equilibrium occurs between the droplet surface and the unfolded protein chain. Equation 1.5 can be used to approximate the charge equilibrium phenomenon, which the system is trying to find the minimum electrostatic potential ^{V}:[41]

$$V = \frac{1}{4\pi\epsilon_0}\left(\frac{1}{2}\sum_{i=0}^{N}\frac{q_i}{r_i} + \sum_{i=0}^{N-1}\sum_{j=i+1}^{N}\frac{q_i q_j}{r_{ij}}\right) \textbf{(eq. 1.5)}$$

where i is the sequence of the chargeable unit on the chain, which the droplet surface has i = 0, and the first charged site on the chain designates as i = 1 (and further to N, which represents the number of chargeable units on the chain until the scission point). The absolute charge on each i is q_i, and the corresponding distance is r_i. The values r_{ij} refer to any midpoint distances between entities i and j to consider the Coloumb repulsion within the chain, not only between the chain and droplet. The mobile charges (i.e., protons) tend to rapidly redistribute to minimizes the overall electrostatic potential. While the charge configurations from the lowest possible V(N), and the energy (i.e., the Coulomb repulsion) is higher than the "scission point (N)," the chain would further be ejected from the droplet. The charges on the protein can further be denoted as **equation 1.6**:[40]

$$q_{protein} = q_{total} - q_0 \textbf{ (eq. 1.6)}$$

where q_{total} is the total charges on the original droplet and q_0 is the charge on the surface at the "scission point (N)." And the numbers of charges of the unfolded protein can be found from **equation 1.7**:[40]

$$z_{CEM} = \frac{q_{protein}}{e} \textbf{ (eq 1.7)}$$

Under CEM, the Rayleigh charge is no longer the limit for the number of charges on the unfolded proteins. V(N) and the affinity between the chain and the droplet lead to the multiple charging on the unfolded chain. Analogous linear polymer models were also used to demonstrate various scenarios, such as the boundary among the three models (IEM, CRM and CEM), for the ionization process through CEM, including "model polymer"[42], polypropylene glycol,[43] and polylactide.[44] Some evidence from other techniques, including ion mobility mass spectrometry (IMS), supports the CEM that the ejected unfolded proteins with different charge states share similarities in collisional cross-section (CCS) from IMS, which the difference in CCS occurs when the ejection time (activation time) is different, so the structures are different.[45] CEM explains the higher charging phenomenon from the ESI process that CRM and IEM cannot fully address. However, there is no clear boundary among all three models under the whole ESI process, so the triad models occur in every ESI event, only with different percentages among the type of the ions.

1.3 Condensed Phase Effects on Multiple Charging Phenomenon

The three main models described above rely on the analytes' chemical characteristics and their interaction with the charged droplets. Therefore, the solution conditions make the most significant contributions to the multiple charging phenomenon from the direct ESI process. In the following discussion, protein will be used as the system for demonstrating how various factors would affect its charge states.

1.3.1 pH value

pH value of the original solutions already represents if the targeted analyte is charged (i.e., protonated or deprotonated) or not in the condensed phase, depending on the natural pKa value from the different functional groups on the analytes, such as carboxylic acids or amines.[46] In the earlier investigation, researchers found that the pH of the solution is highly related to protein charge states under the ESI process.[47] The first consideration of different pH values of the solution

is supposed to be how the protein structures are withheld under the pH value. It is well-known that low and high pH tend to denature protein, making it have unfolded structure.[48] Ion mobility mass spectrometry has been used to correlate the folded and unfolded structure with the average charge states, suggesting unfolded structures have greater average charge states than folded ones.[49] Therefore, they tend to have more charges based on the CEM pathway than CRM.

However, pH value not only affects the structures of protein, which determine the charging ESI path, but also the charging efficiency under different spray polarities.[50] Two different spraying modes, right-way-round and wrong-way-round, indicating the relationship between the pH value of the solution and the ESI polarities, have been proposed to demonstrate the charging phenomena upon the different spray modes.[51] For example, a wrong-way-round experiment is spraying protein negatively under low pH (natural protonated condition). A wrong-way-round spray usually results in much lower signals (i.e., lower ionization efficiency) and sometimes with slightly lower absolute charge state distribution.[50] Besides, spraying in a wrong-way-round mode tends to have a greater degree of metal ion adduction, indicating the condensing effect of the charges (from the nonvolatile ions) on the surface to the protein, suggesting the evidence of the CRM charging model that the ions are formed at the later stage of ESI but are not charged at the initial stage in the condensed phase.

1.3.2 Organic Solvent

As the pH value, organic solvents can be used as the denaturing condition for proteins, affecting the folding of the proteins.[52] Therefore, the protein structures are affected by the percentages of organic solvent in the condensed phase, which further affect how they can be charged from the ESI process (e.g., CRM or CEM.) Researchers have investigated the degrees of different percentages of additive organic solvent into the solution to find the correlation between the percentages and charge states distribution.[53] Again, IMS results verified that mixtures of protein structures were found, leading to the difference among charge states distributions under different percentages of organic solvent.[54]

1.3.3 Other Solvent Modifier

Different solvent modifiers would have individual contributions to the charging effect from the ESI process. As we previously discussed, the volatile salt that tends to be ionized through IEM would take away the charges on the surface at the early ESI stage.[22] The process is part of the formation of progeny droplets, leading to the Coulomb fission event, but it might also lead to lower charges on the final droplet to charge up the protein.[55] Therefore, volatile salt additives play a part in charging through the ESI process.

Some researchers investigated other solvent modifiers, which dominantly called supercharging agents (SCAs), including sulfolane or m-nitrobenzyl alcohol (m-NBA), to modulate protein charge states, that we are not able to fully address the higher charging phenomenon based on the triad models.[56] SCAs tend to give a greater average charge states distribution compared to both unfolded and folded protein solutions. Several mechanisms have been proposed to explain their effects on the ESI process. For example, Adding SCAs can modulate the surface tension on the charged droplet leading to different Rayleigh charges based on **eq. 1.3**.[36]

Although SCAs addition could preserve the noncovalent component/interaction within the protein complex,[57] SCAs may still change protein structures in the condensed phase, which significantly affects the charge states of protein ions.[58] Therefore, SCAs effect on native supercharging (i.e., preserving the native protein structures) is controversial, but researchers reported additional evidence for the native supercharging events. The charge trapping model, reported by Konermann's group, demonstrates that the prevention of evaporation of small ions (e.g., Na^+) at an early stage is achieved by the SCAs shells.[59] As a result, native proteins with higher charge states are formed from condensing higher degrees of those cations from the CRM process. The same group also reported anti-supercharging with 18C6 crown ether by adding both sulfolane and 18C6. The experimental results suggested that almost no supercharging phenomenon was observed after adding 18C6 crown ether to the solution. They suggested that the complexation between 18C6 and sulfolane makes sulfolane more soluble, preventing them from forming a trapped shell, so no native supercharging was observed.[60] The charge trapping model provides alternative insights on native supercharging phenomenon, but it does not exclude the fact that denaturing of protein still occurs while adding none native components into the solution.

Besides the native supercharging, SCAs also give greater average charge states among denatured proteins.[56] One explanation may be that SCAs might serve as much stronger denaturing

reagents that break some of the disulfide bonds within the protein leading to a more extended chain structure with higher charge states.[61] Another explanation, proposed by Konermann's group, is that SCAs provide the electrostatic stabilization of protein-bound proton via charge–dipole interactions.[62] Therefore, SCAs-mediated favorable charge–dipole interactions on the chain can result in the accumulation of more proton on the unfolded protein after charge equilibrium from CEM, then further cause supercharging.[62] **Figure 1.3** summarizes all the possible charging processes from regular and supercharging scenarios for proteins.

Overall, solution conditions that we discussed above would lead to different scenarios for the analytes (majorly proteins above) to be ionized by the ESI process, causing various multiple charging phenomena. Those conditions also give us a room to manipulate charges on the analytes. However, ambiguity is remained because of the gap between the actual experimental charge states and all the modeling results as well as the theory.

1.4 Gas-Phase Reactions and Multiple Charging Phenomenon

Despite the modification among solution conditions providing scientists ways to generate various cases for different charging results from ESI, the condensed phase approaches usually give bulky changes in the solution that manipulation of charging phenomenon relies on the different charging models. Therefore, gas-phase approaches were introduced to provide another way for manipulating the charges on the analyte ions without considering the ionization theory. Two major types of gas-phase reactions are commonly used for the purposed, including ion/molecule reaction and ion/ion reaction. The following sections will introduce the two types of reactions individually, with a greater focus on ion/ion reactions.

1.4.1 Ion/Molecule Reaction

Ion/molecule reaction has been widely studied in mass spectrometry and was first used for chemical ionization.[63] The general theory of ion/molecule reaction depends on the gas-phase acidity/basicity of the ion and neutral that the difference in proton affinities (PA) between the two reagents results in proton transfer. The general reaction can be found below

$$M + RH^+ \rightarrow MH^+ + R \quad (\textbf{reaction 1.1})$$

when PA(M) > PA(R), the overall reaction would be exothermic, and proton would transfer from RH^+ to M to form proton transfer product, MH^+.[64] PA can be determined by using different mass spectrometry-based approaches, including experimental determination of the ionization energy of the molecular ion or the measurement of equilibrium constants for the proton transfer reactions to relatively determine the PA between the two reagents.[65]

Unlike the ionization process, which focuses on giving a charge (proton) to the targeted analyte (M), the ion/molecule reaction for the existed multiply charged ions is dominantly used for charge reduction reaction that proton transfer reactions allow to extract (or donate) proton from multiply protonated ions (or deprotonated anions). **Reaction 1.2** represents the proton transfer reaction from a multiply protonated ion, $(M+nH)^{n+}$ to the reagent molecule (R).

$$(M + nH)^{n+} + R \rightarrow (M + (n-1)H)^{(n-1)+} + RH^+ \text{ (\textbf{reaction 1.2})}$$

The PA(R) is much greater than $PA(M+(n-1)H)^{(n-1)+}$ because of the Coulomb repulsion between proton (H^+) and $(M+(n-1)H)^{(n-1)+}$, which both of them has the same polarity of positive charge, resulting in a very efficient reaction.[66] However, the reaction rates gradually decrease while we have lower charges on the targeted analytes because of the decrease in PA (or gas-phase basicity) of the ions.[67] Therefore, ion/molecule reaction would meet an issue at the end when PA(R) is less than the targeted ions (see **reaction 1.1**), indicating the limitation for the reaction would be the selection of optimal neutral reagents.

1.4.2 Gas-Phase Ion/Ion Reaction

Theory of Ion/Ion Reaction

Unlike ion/molecule reaction, ion/ion reaction is not limited by the gas-phase basicity of the reagent because of the long-range Coulomb attraction potential between the opposite polarities of ions, not ion-dipole or ion-induced dipole interactions in ion/molecule reaction. In kinetic consideration with the following assumption: a) the rate constant ($k_{i/i}$) for the reaction is same as forming a stable orbiting complex; b) ignoring the internal energies of the reactants; c) point charge model is used, the collisional cross-section for ion/ion capture can be denoted as the following **equation 1.8** with **equation 1.9**, and **1.10** show the different rate constant between ion/ion reaction and ion/molecule reaction:[68]

$$\sigma_{i/i} = \left(\frac{\pi}{2}\right)\left[\frac{Z_1 Z_2 e^2}{\mu v^2}\right]^2 \textbf{(eq. 1.8)}$$

$$k_{i/i} = v\sigma_{i/i} = v\left(\frac{\pi}{2}\right)\left[\frac{Z_1 Z_2 e^2}{\mu v^2}\right]^2 \textbf{(eq. 1.9)}$$

$$k_{i/M} = 2\pi Z\left(\frac{\alpha}{\mu}\right)^{\frac{1}{2}} \textbf{(eq. 1.10)}$$

where Z_1 and Z_2 (or Z) are the unit charges of the reacting ions for ion/ion reaction, e is the electron charge, v is the relative velocity, μ is the reduced mass, and α is the polarizability of neutral reactant. The kinetic models provide insight into the different factors that impact the reaction rates that ion/ion reactions rate has proportion relationships to Z^2. The general ion/ion reaction is represented as the following **reaction 1.3.**

$$(\mathrm{M} + \mathrm{nH})^{\mathrm{n}+} + \mathrm{R}^- \rightarrow (\mathrm{M} + (\mathrm{n}-1)\mathrm{H})^{(\mathrm{n}-1)+} + \mathrm{RH} \textbf{ (reaction 1.3)}$$

However, the model explained the proton transfer phenomenon from ion/ion reaction, which we can use ion/ion reaction to reduce charges on multiply charged analytes, but not really for the formation of the electrostatic complex from the ions with opposite polarities. To further elaborate, three different models were discussed for forming the complex product via gas-phase ion/ion reactions.[69]

The first mechanism directly assumes the reaction for forming complex is from a hard-sphere collision event. The relationship between the collision radius (r_{hs}) and impact parameter (b_{hs}) can be expressed as:[70]

$$b_{hs}{}^2 = r_{hs}{}^2\left[1 + \frac{2Z_1 Z_2 e^2}{4\pi\epsilon_0 r_{hs}\mu v^2}\right] \textbf{(eq. 1.11)}$$

The above model cannot be used for the reaction occurring at a further distance than the hard-sphere collision. Therefore, the maximum distance (r_{ph}) for the successful reaction of "simple proton transfer" reaction, which we refer to as proton hopping, is then included, and the impact parameter can be again expressed as:

$$b_{ph}{}^2 = r_{ph}{}^2\left[1 + \frac{2Z_1 Z_2 e^2}{4\pi\epsilon_0 r_{hs}\mu v^2}\right] \textbf{(eq. 1.12)}$$

The third model is from Thomson's three-body interaction model that ionic reactants form bound orbit within the critical distance (d_{orbit}), and the maximum cross-section for that orbital complex formation can be approximated as:[71]

$$\sigma_{orbit,max} \approx \pi d_{orbit}{}^2 \approx \frac{Z_1{}^2 Z_2{}^2 e^4}{4\pi\varepsilon_0 \mu^2 v^4} \textbf{ (eq. 1.13)}$$

In the early work from our group, experimental results suggested that both protons hopping and orbital bound electrostatic complex formation meet the different reaction schemes. Proton

transfer reaction involving transferring single or double proton can be achieved both from proton hopping or the charge separation channels after the complex formation.[69] In the later chapter 3, we will further discuss the multiple protons (more than two) transfer reaction that only occurs at a single collision event through the formation of the complexes.

Different Ion/Ion Reactions

By taking advantage of the multiple charging phenomenon, we can perform various gas-phase ion/ion reactions in the mass spectrometry without neutralizing the ion (i.e., +1 and −1 lead to a net charge = 0), which we cannot analyze the neutral in a typical mass spectrometer. Ion/ion reactions allow us to manipulate not only charges based on protons, but various reactions can be performed to achieve a wide range of analytical purposes.[72] The following sections will introduce some ion/ion reactions and how they can be used for analytical purposes.

Proton Transfer Reaction

As we heavily discussed above, utilizing proton transfer reactions to reduce charges on the multiply charged biomolecule ions are widely used. There are many applications for us to manipulate charge with proton transfer reaction for mass spectrometry standpoints. First, proton transfer reaction allows us to reduce the charges from the targeted ion populations, which is useful for mixture analysis.[73-74] To elaborate, congested mass spectra formed from different closed m/z signals of mixtures through the ESI process can be deconvoluted by charge reduction so that the signals can be separated to higher m/z windows.[75] Second, combined with ion parking techniques, it is possible to reduce the reaction rate of the proton transfer reaction so that the concentration of ion signals into a single charge state is achievable.[76-77] Therefore, more control among the proton transfer reactions can be done in the mass spectrometry for various purposes. For example, for top-down proteomic study, different charge states many give distinct fragmentation patterns leading for complementary sequencing information among different charge states.[78] Again, coupling with different dissociation techniques that the fragment ions might create overlapped signals (congested spectra from the mixture of fragment ions), so proton transfer reaction can be used to separate them and retrieve better sequencing results.[79-81] An example utilizing proton transfer reactions to

study polydispersed polymer mixtures and deconvolute congested mass spectra will be discussed later in chapter 2.

Electron Transfer Reaction

Ion/election reaction is another type of ion/ion reaction in which ions react with different thermalized electrons (i.e., with different kinetic energy). Most of the time, further fragmentation occurs after the ion/electron reactions.[82] Electron transfer reaction, in contrast, the electron is transferred from one ion to another, which the general reactions are expressed as **reactions 1.4** and **1.5**, shares the similarity in the dissociation part, and is commonly referred as electron transfer dissociation (ETD).[83] ETD usually provides more sequence information among proteins and can preserve post-translation modification information.

$$(\mathrm{M}+\mathrm{nH})^{\mathrm{n}+}+\mathrm{R}^{-\bullet}\rightarrow(\mathrm{M}+\mathrm{nH})^{(\mathrm{n}-1)+\bullet *}+\mathrm{R}\rightarrow \text{fragments}\ (\textbf{reaction 1.4})$$

$$(\mathrm{M}-\mathrm{nH})^{\mathrm{n}-}+\mathrm{R}^{+\bullet}\rightarrow(\mathrm{M}+\mathrm{nH})^{(\mathrm{n}-1)-\bullet *}+\mathrm{R}\rightarrow \text{fragments}\ (\textbf{reaction 1.5})$$

Complex Formation Reaction

The complex formation reactions also play a significant role in ion/ion reactions. The general complex formation reaction is expressed as the following **reaction 1.6**:

$$(\mathrm{M}+\mathrm{nH})^{\mathrm{n}+}+(\mathrm{A}-\mathrm{bH})^{\mathrm{b}-}\rightarrow(\mathrm{AM}+(\mathrm{n}-\mathrm{b})\mathrm{H})^{(\mathrm{n}-\mathrm{b})+}\ (\textbf{reaction 1.6})$$

Protein complexes can be formed through the complex formation in the gas phase.[69] Moreover, many gas-phase reactions go through the intermediate stage of forming complex, then moving forward on the reaction coordinates. In the following parts, we will give three examples that the reactions require the formation complexes.

Metal Transfer Reaction

Metal transfer reaction is achieved in analogous to the proton transfer reaction from forming a long-lived complex initially. In the further reaction processes, instability of the complex (via activation or excess internal energy) leads to the loss of neutral ligand, resulting in overall metal transfer. The general reaction is shown as below:[84]

$$(M + nH)^{n+} + MeL_2^- \rightarrow (M + Me + nH + 2L)^{(n-1)+} \rightarrow (M + Me + (n-2)H)^{(n-1)+} + 2HL$$

(**reaction 1.7**)

There are some benefits for doing metal transfer reactions, including providing different fragmentation patterns after dissociation. In the later chapter 6, we utilized a similar metal transfer reaction for better characterizing glycan moiety on gangliosides.[85]

Charge Inversion Reaction

While awhilepplying the general **reaction 1.6**, under the condition that n > b, the anion, $[A-bH]^{b-}$, can be considered polarity inverted to form the charge inverted complex cations $[AM+(n-b)H)]^{(n-b)+}$. The formation of charge inverted complex cations have been intensively studied in our group for lipidomics analysis, allowing us to generate cationized lipid from their respectively dominantly polarities, negative polarity.[86-88] In brief, lipid anions react with metal-complex cations to produce charge-inverted complex cations. Following by activation techniques, in-depth structural characterization can be achieved. Examples applying charge inversion reactions for lipidomics analysis are shown in later chapters 4 to 6.

Moreover, after forming a complex ion, various charge separation channels allow multiple protons to be transferred. In analog of losing ligand in metal transfer reaction, final product ions show the inversion of polarity can also be achieved.[89] Details of this type of charge inversion is introduced in the later chapter 3.

Covalent Modification Reaction

Ion/ion reaction can also achieve covalent modification in the gas phase, and this type of reaction usually requires the formation of complex product ion followed by external energy input (i.e., ion activation) to overcome the activation energy.[90] Covalent modification usually competes with the above reactions, such as proton transfer reaction and metal transfer reaction, after forming a complex. Our group demonstrated the competing channels between proton transfer reaction and nucleophilic substitution in the reactions between peptide cations with primary amine or guanidine group and sulfo-N-hydroxysuccinimide (sulfo-NHS) ester reagent anions that it is possible to have selectivity in the reactions according to the predicted energy surfaces.[91] Our group is currently investigating a better way to measure the ion temperature in the mass spectrometer, so more

controlled conditions are allowed to produce covalently modified products. Several covalent modifications have been achieved from our group, including the nucleophilic substitution mentioned above, Schiff base formation[92-93], and gas-phase oxidation.[94-95]

1.5 Conclusions

Ionization of the targeted analytes is always the first consideration while using mass spectrometry, despite the advances in novel mass spectrometers. ESI opens the window of mass spectrometry for forming multiply charged ions directly from the solution, allowing us to achieve various analytical purposes. However, the complete theory behind ESI to form multiply charged ions is still missing that three complementary models, IEM, CRM, and CEM, are proposed to explain different charging events. To interrogate the multiple charging phenomena from the ESI process, modification of condense phase condition has been widely used, and evidence supports different models. Moreover, it is also common to adjust solution composition to form different charging product ions.

On the other hand, gas-phase approaches, including ion/molecule reactions and ion/ion reactions, allow scientists to manipulate the charges on the ion in a more analytical sense. Proton affinities of the reagents limit the reaction efficiency in ion/molecule reactions; therefore, ion/ion reactions show their advantages in this case. Last but not least, various ion/ion reactions can be utilized for a wide range of analytical purposes.

In this dissertation, work will focus on investigating multiple charging phenomena and their contribution to the congested mass spectra. Another focus would be taking advantage of the multiply charged ions to perform various ion/ion reactions on biological/synthetic polymers and glycolipids for better characterizing targeted analytes.

1.6 References

1. Thomson, J. J., XL. Cathode Rays. The London, Edinburgh, and Dublin Philosophical Magazine and Journal of Science 1897, 44 (269), 293-316.
2. Thomson, J. J., XIX. Further experiments on positive rays. The London, Edinburgh, and Dublin Philosophical Magazine and Journal of Science 1912, 24 (140), 209-253.
3. Aston, F. W., LXXIV. A positive ray spectrograph. The London, Edinburgh, and Dublin Philosophical Magazine and Journal of Science 1919, 38 (228), 707-714.

4. Aston, F. W., XLIV. The constitution of atmospheric neon. The London, Edinburgh, and Dublin Philosophical Magazine and Journal of Science 1920, 39 (232), 449-455.

5. de Hoffmann, E., and Stroobant, V, Mass Spectrometry: Principles and Applications. 3rd edition ed.; 2007.

6. Griffiths, J., A Brief History of Mass Spectrometry. Anal Chem 2008, 80 (15), 5678-5683.

7. Karas, M.; Bachmann, D.; Bahr, U.; Hillenkamp, F., Matrix-assisted ultraviolet laser desorption of non-volatile compounds. Int J Mass Spectrom Ion Processes 1987, 78, 53-68.

8. Karas, M.; Krüger, R., Ion Formation in MALDI: The Cluster Ionization Mechanism. Chem Rev 2003, 103 (2), 427-440.

9. Yamashita, M.; Fenn, J. B., Electrospray ion source. Another variation on the free-jet theme. J Phys Chem 1984, 88 (20), 4451-4459.

10. Fenn, J. B.; Mann, M.; Meng, C. K.; Wong, S. F.; Whitehouse, C. M., Electrospray Ionization for Mass Spectrometry of Large Biomolecules. Science 1989, 246 (4926), 64-71.

11. Dole, M.; Hines, R.; Mack, L.; Mobley, R.; Ferguson, L.; Alice, M., Gas phase macroions. Macromolecules 1968, 1 (1), 96-97.

12. Doyle, A.; Moffett, D. R.; Vonnegut, B., Behavior of evaporating electrically charged droplets. J Colloid Sci 1964, 19 (2), 136-143.

13. Covey, T. R.; Thomson, B. A.; Schneider, B. B., Atmospheric pressure ion sources. Mass Spectrom Rev 2009, 28 (6), 870-897.

14. Kebarle, P.; Verkerk, U. H., Electrospray: From ions in solution to ions in the gas phase, what we know now. Mass Spectrom Rev 2009, 28 (6), 898-917.

15. Korfmacher, W. A., Foundation review: Principles and applications of LC-MS in new drug discovery. Drug Discov Today 2005, 10 (20), 1357-1367.

16. Zwiener, C.; Frimmel, F. H., LC-MS analysis in the aquatic environment and in water treatment--a critical review. Part I: Instrumentation and general aspects of analysis and detection. Anal Bioanal Chem 2003, 378 (4), 851-861.

17. Xu, R. N.; Fan, L.; Rieser, M. J.; El-Shourbagy, T. A., Recent advances in high-throughput quantitative bioanalysis by LC–MS/MS. J Pharm Biomed Anal 2007, 44 (2), 342-355.

18. Ding, J.; Vouros, P., Peer Reviewed: Advances in CE/MS. Anal Chem 1999, 71 (11), 378A-385A.

19. Klampfl, C. W., CE with MS detection: a rapidly developing hyphenated technique. Electrophoresis 2009, 30 (S1), S83-S91.

20. Ho, C. S.; Lam, C. W. K.; Chan, M. H. M.; Cheung, R. C. K.; Law, L. K.; Lit, L. C. W.; Ng, K. F.; Suen, M. W. M.; Tai, H. L., Electrospray ionisation mass spectrometry: principles and clinical applications. The Clinical biochemist. Reviews 2003, 24 (1), 3-12.

21. Fenn, J. B.; Mann, M.; Meng, C. K.; Wong, S. F.; Whitehouse, C. M., Electrospray ionization–principles and practice. Mass Spectrom Rev 1990, 9 (1), 37-70.

22. Konermann, L.; Ahadi, E.; Rodriguez, A. D.; Vahidi, S., Unraveling the Mechanism of Electrospray Ionization. Anal Chem 2013, 85 (1), 2-9.

23. Bruins, A. P., Mechanistic aspects of electrospray ionization. J Chromatogr A 1998, 794 (1), 345-357.

24. Gañán-Calvo, A. M.; López-Herrera, J. M.; Herrada, M. A.; Ramos, A.; Montanero, J. M., Review on the physics of electrospray: From electrokinetics to the operating conditions of single and coaxial Taylor cone-jets, and AC electrospray. J Aerosol Sci 2018, 125, 32-56.

25. Wilm, M. S.; Mann, M., Electrospray and Taylor-Cone theory, Dole's beam of macromolecules at last? Int J Mass Spectrom Ion Processes 1994, 136 (2), 167-180.

26. Mora, J. F. d. l., The Fluid Dynamics of Taylor Cones. Annu Rev Fluid Mech 2007, 39 (1), 217-243.

27. Kebarle, P.; Peschke, M., On the mechanisms by which the charged droplets produced by electrospray lead to gas phase ions. Anal Chim Acta 2000, 406 (1), 11-35.

28. Peschke, M.; Verkerk, U. H.; Kebarle, P., Features of the ESI mechanism that affect the observation of multiply charged noncovalent protein complexes and the determination of the association constant by the titration method. J Am Soc Mass Spectrom 2004, 15 (10), 1424-1434.

29. Gomez, A.; Tang, K., Charge and fission of droplets in electrostatic sprays. Phys Fluids 1994, 6 (1), 404-414.

30. Banerjee, S.; Mazumdar, S., Electrospray Ionization Mass Spectrometry: A Technique to Access the Information beyond the Molecular Weight of the Analyte. Int J Anal Chem 2012, 282574.

31. Taylor, G. I., Disintegration of water drops in an electric field. Proceedings of the Royal Society of London. Series A. Mathematical and Physical Sciences 1964, 280 (1382), 383-397.

32. Iribarne, J. V.; Thomson, B. A., On the evaporation of small ions from charged droplets. J Chem Phys 1976, 64 (6), 2287-2294.

33. Labowsky, M.; Fenn, J. B.; Fernandez de la Mora, J., A continuum model for ion evaporation from a drop: effect of curvature and charge on ion solvation energy. Anal Chim Acta 2000, 406 (1), 105-118.

34. Ahadi, E.; Konermann, L., Ejection of Solvated Ions from Electrosprayed Methanol/Water Nanodroplets Studied by Molecular Dynamics Simulations. J Am Chem Soc 2011, 133 (24), 9354-9363.

35. Dole, M.; Hines, R. L.; Mack, L. L.; Mobley, R. C.; Ferguson, L. D.; Alice, M. B., Gas Phase Macroions. Macromolecules 1968, 1 (1), 96-97.

36. Iavarone, A. T.; Williams, E. R., Mechanism of Charging and Supercharging Molecules in Electrospray Ionization. J Am Chem Soc 2003, 125 (8), 2319-2327.

37. Kaltashov, I. A.; Mohimen, A., Estimates of Protein Surface Areas in Solution by Electrospray Ionization Mass Spectrometry. Anal Chem 2005, 77 (16), 5370-5379.

38. Heck, A. J. R.; van den Heuvel, R. H. H., Investigation of intact protein complexes by mass spectrometry. Mass Spectrom Rev 2004, 23 (5), 368-389.

39. Hogan, C. J.; Carroll, J. A.; Rohrs, H. W.; Biswas, P.; Gross, M. L., Charge Carrier Field Emission Determines the Number of Charges on Native State Proteins in Electrospray Ionization. J Am Chem Soc 2008, 130 (22), 6926-6927.

40. Konermann, L.; Rodriguez, A. D.; Liu, J., On the Formation of Highly Charged Gaseous Ions from Unfolded Proteins by Electrospray Ionization. Anal Chem 2012, 84 (15), 6798-6804.

41. Sciuto, S. V.; Liu, J.; Konermann, L., An Electrostatic Charge Partitioning Model for the Dissociation of Protein Complexes in the Gas Phase. J Am Soc Mass Spectrom 2011, 22 (10).

42. Ahadi, E.; Konermann, L., Modeling the Behavior of Coarse-Grained Polymer Chains in Charged Water Droplets: Implications for the Mechanism of Electrospray Ionization. J Phys Chem B 2012, 116 (1), 104-112.

43. Duez, Q.; Metwally, H.; Konermann, L., Electrospray Ionization of Polypropylene Glycol: Rayleigh-Charged Droplets, Competing Pathways, and Charge State-Dependent Conformations. Anal Chem 2018, 90 (16), 9912-9920.

44. Duez, Q.; Metwally, H.; Hoyas, S.; Lemaur, V.; Cornil, J.; De Winter, J.; Konermann, L.; Gerbaux, P., Effects of electrospray mechanisms and structural relaxation on polylactide ion conformations in the gas phase: insights from ion mobility spectrometry and molecular dynamics simulations. PCCP 2020, 22 (7), 4193-4204.

45. Metwally, H.; Duez, Q.; Konermann, L., Chain Ejection Model for Electrospray Ionization of Unfolded Proteins: Evidence from Atomistic Simulations and Ion Mobility Spectrometry. Anal Chem 2018, 90 (16), 10069-10077.

46. Gao, S.; Zhang, Z.-P.; Karnes, H. T., Sensitivity enhancement in liquid chromatography/atmospheric pressure ionization mass spectrometry using derivatization and mobile phase additives. J Chromatogr B 2005, 825 (2), 98-110.

47. Kelly, M. A.; Vestling, M. M.; Fenselau, C. C.; Smith, P. B., Electrospray analysis of proteins: A comparison of positive-ion and negative-ion mass spectra at high and low pH. Org Mass Spectrom 1992, 27 (10), 1143-1147.

48. Kishore, D.; Kundu, S.; Kayastha, A. M., Thermal, chemical and pH induced denaturation of a multimeric β-galactosidase reveals multiple unfolding pathways. PLoS One 2012, 7 (11), e50380-e50380.

49. Wyttenbach, T.; Bowers, M. T., Structural Stability from Solution to the Gas Phase: Native Solution Structure of Ubiquitin Survives Analysis in a Solvent-Free Ion Mobility–Mass Spectrometry Environment. J Phys Chem B 2011, 115 (42), 12266-12275.

50. Pan, P.; Gunawardena, H. P.; Xia, Y.; McLuckey, S. A., Nanoelectrospray Ionization of Protein Mixtures: Solution pH and Protein pI. Anal Chem 2004, 76 (4), 1165-1174.

51. Zhou, S.; Cook, K. D., Protonation in electrospray mass spectrometry: wrong-way-round or right-way-round? J Am Soc Mass Spectrom 2000, 11 (11), 961-966.

52. Yu, Y.; Wang, J.; Shao, Q.; Shi, J.; Zhu, W., The effects of organic solvents on the folding pathway and associated thermodynamics of proteins: a microscopic view. Sci Rep 2016, 6 (1), 19500.

53. Girod, M.; Dagany, X.; Boutou, V.; Broyer, M.; Antoine, R.; Dugourd, P.; Mordehai, A.; Love, C.; Werlich, M.; Fjeldsted, J.; Stafford, G., Profiling an electrospray plume by laser-induced fluorescence and Fraunhofer diffraction combined to mass spectrometry: influence of size and composition of droplets on charge-state distributions of electrosprayed proteins. PCCP 2012, 14 (26), 9389-9396.

54. Shi, H.; Clemmer, D. E., Evidence for Two New Solution States of Ubiquitin by IMS–MS Analysis. J Phys Chem B 2014, 118 (13), 3498-3506.

55. Konermann, L.; Metwally, H.; Duez, Q.; Peters, I., Charging and supercharging of proteins for mass spectrometry: recent insights into the mechanisms of electrospray ionization. Analyst 2019, 144 (21), 6157-6171.

56. Teo, C. A.; Donald, W. A., Solution Additives for Supercharging Proteins beyond the Theoretical Maximum Proton-Transfer Limit in Electrospray Ionization Mass Spectrometry. Anal Chem 2014, 86 (9), 4455-4462.

57. Lomeli, S. H.; Yin, S.; Ogorzalek Loo, R. R.; Loo, J. A., Increasing charge while preserving noncovalent protein complexes for ESI-MS. J Am Soc Mass Spectrom 2009, 20 (4), 593-596.

58. Hogan Jr, C. J.; Ogorzalek Loo, R. R.; Loo, J. A.; Mora, J. F. d. l., Ion mobility–mass spectrometry of phosphorylase B ions generated with supercharging reagents but in charge-reducing buffer. PCCP 2010, 12 (41), 13476-13483.

59. Metwally, H.; McAllister, R. G.; Popa, V.; Konermann, L., Mechanism of Protein Supercharging by Sulfolane and m-Nitrobenzyl Alcohol: Molecular Dynamics Simulations of the Electrospray Process. Anal Chem 2016, 88 (10), 5345-5354.

60. Metwally, H.; Konermann, L., Crown Ether Effects on the Location of Charge Carriers in Electrospray Droplets: Implications for the Mechanism of Protein Charging and Supercharging. Anal Chem 2018, 90 (6), 4126-4134.

61. Donor, M. T.; Ewing, S. A.; Zenaidee, M. A.; Donald, W. A.; Prell, J. S., Extended Protein Ions Are Formed by the Chain Ejection Model in Chemical Supercharging Electrospray Ionization. Anal Chem 2017, 89 (9), 5107-5114.

62. Peters, I.; Metwally, H.; Konermann, L., Mechanism of Electrospray Supercharging for Unfolded Proteins: Solvent-Mediated Stabilization of Protonated Sites During Chain Ejection. Anal Chem 2019, 91 (10), 6943-6952.

63. Futrell, J. H.; Tiernan, T. O., Ion-Molecule Reactions. Science 1968, 162 (3852), 415-422.

64. Wilson, M. S.; McCloskey, J. A., Chemical ionization mass spectrometry of nucleosides. Mechanisms of ion formation and estimations of proton affinity. J Am Chem Soc 1975, 97 (12), 3436-44.

65. Hunter, E. P. L.; Lias, S. G., Proton Affinities Determined Using Mass Spectrometry. In Encyclopedia of Spectroscopy and Spectrometry (Third Edition), Lindon, J. C.; Tranter, G. E.; Koppenaal, D. W., Eds. Academic Press: Oxford, 2017; pp 779-784.

66. Williams, E. R., Proton Transfer Reactivity of Large Multiply Charged Ions. J Mass Spectrom 1996, 31 (8), 831-842.

67. McLuckey, S. A.; Van Berkel, G. J.; Glish, G. L., Reactions of dimethylamine with multiply charged ions of cytochrome c. J Am Chem Soc 1990, 112 (14), 5668-5670.

68. Stephenson, J. L.; McLuckey, S. A., Ion/Ion Reactions in the Gas Phase: Proton Transfer Reactions Involving Multiply-Charged Proteins. J Am Chem Soc 1996, 118 (31), 7390-7397.

69. Wells, J. M.; Chrisman, P. A.; McLuckey, S. A., Formation and Characterization of Protein−Protein Complexes in Vacuo. J Am Chem Soc 2003, 125 (24), 7238-7249.

70. Mahan, B. H., Recombination of Gaseous Ions. In Adv Chem Phys, 1973; pp 1-40.

71. Thomson, J. J., XXIX. Recombination of gaseous ions, the chemical combination of gases, and monomolecular reactions. The London, Edinburgh, and Dublin Philosophical Magazine and Journal of Science 1924, 47 (278), 337-378.

72. McLuckey, S. A.; Huang, T.-Y., Ion/Ion Reactions: New Chemistry for Analytical MS. Anal Chem 2009, 81 (21), 8669-8676.

73. Scalf, M.; Westphall, M. S.; Smith, L. M., Charge Reduction Electrospray Mass Spectrometry. Anal Chem 2000, 72 (1), 52-60.

74. McLuckey, S. A.; Wu, J.; Bundy, J. L.; Stephenson, J. L.; Hurst, G. B., Oligonucleotide Mixture Analysis via Electrospray and Ion/Ion Reactions in a Quadrupole Ion Trap. Anal Chem 2002, 74 (5), 976-984.

75. Stephenson, J. L.; McLuckey, S. A., Simplification of Product Ion Spectra Derived from Multiply Charged Parent Ions via Ion/Ion Chemistry. Anal Chem 1998, 70 (17), 3533-3544.

76. McLuckey, S. A.; Reid, G. E.; Wells, J. M., Ion Parking during Ion/Ion Reactions in Electrodynamic Ion Traps. Anal Chem 2002, 74 (2), 336-346.

77. Chrisman, P. A.; Pitteri, S. J.; McLuckey, S. A., Parallel Ion Parking: Improving Conversion of Parents to First-Generation Products in Electron Transfer Dissociation. Anal Chem 2005, 77 (10), 3411-3414.

78. Reid, G. E.; Wu, J.; Chrisman, P. A.; Wells, J. M.; McLuckey, S. A., Charge-State-Dependent Sequence Analysis of Protonated Ubiquitin Ions via Ion Trap Tandem Mass Spectrometry. Anal Chem 2001, 73 (14), 3274-3281.

79. Liu, J.; Huang, T.-Y.; McLuckey, S. A., Top-Down Protein Identification/Characterization of a Priori Unknown Proteins via Ion Trap Collision-Induced Dissociation and Ion/Ion Reactions in a Quadrupole/Time-of-Flight Tandem Mass Spectrometer. Anal Chem 2009, 81 (4), 1433-1441.

80. Holden, D. D.; McGee, W. M.; Brodbelt, J. S., Integration of Ultraviolet Photodissociation with Proton Transfer Reactions and Ion Parking for Analysis of Intact Proteins. Anal Chem 2016, 88 (1), 1008-1016.

81. Anderson, L. C.; English, A. M.; Wang, W.-H.; Bai, D. L.; Shabanowitz, J.; Hunt, D. F., Protein derivatization and sequential ion/ion reactions to enhance sequence coverage produced by electron transfer dissociation mass spectrometry. Int J Mass spectrom 2015, 377, 617-624.

82. McLuckey, S. A.; Mentinova, M., Ion/Neutral, Ion/Electron, Ion/Photon, and Ion/Ion Interactions in Tandem Mass Spectrometry: Do We Need Them All? Are They Enough? J Am Soc Mass Spectrom 2011, 22 (1), 3-12.

83. Syka, J. E. P.; Coon, J. J.; Schroeder, M. J.; Shabanowitz, J.; Hunt, D. F., Peptide and protein sequence analysis by electron transfer dissociation mass spectrometry. Proc Natl Acad Sci U S A 2004, 101 (26), 9528-9533.

84. Newton, K. A.; Amunugama, R.; McLuckey, S. A., Gas-Phase Ion/Ion Reactions of Multiply Protonated Polypeptides with Metal Containing Anions. J Phys Chem A 2005, 109 (16), 3608-3616.

85. Chao, H.-C.; McLuckey, S. A., Manipulation of Ion Types via Gas-Phase Ion/Ion Chemistry for the Structural Characterization of the Glycan Moiety on Gangliosides. Anal Chem 2021, 93 (47), 15752-15760.

86. Randolph, C. E.; Foreman, D. J.; Betancourt, S. K.; Blanksby, S. J.; McLuckey, S. A., Gas-Phase Ion/Ion Reactions Involving Tris-Phenanthroline Alkaline Earth Metal Complexes as Charge Inversion Reagents for the Identification of Fatty Acids. Anal Chem 2018, 90 (21), 12861-12869.

87. Chao, H.-C.; McLuckey, S. A., Differentiation and Quantification of Diastereomeric Pairs of Glycosphingolipids Using Gas-Phase Ion Chemistry. Anal Chem 2020, 92 (19), 13387-13395.

88. Randolph, C. E.; Marshall, D. L.; Blanksby, S. J.; McLuckey, S. A., Charge-switch derivatization of fatty acid esters of hydroxy fatty acids via gas-phase ion/ion reactions. Anal Chim Acta 2020, 1129, 31-39.

89. Chao, H.-C.; Shih, M.; McLuckey, S. A., Generation of Multiply Charged Protein Anions from Multiply Charged Protein Cations via Gas-Phase Ion/Ion Reactions. J Am Soc Mass Spectrom 2020, 31 (7), 1509-1517.

90. Prentice, B. M.; McLuckey, S. A., Gas-phase ion/ion reactions of peptides and proteins: acid/base, redox, and covalent chemistries. Chem Commun 2013, 49 (10), 947-965.

91. Bu, J.; Fisher, C. M.; Gilbert, J. D.; Prentice, B. M.; McLuckey, S. A., Selective Covalent Chemistry via Gas-Phase Ion/ion Reactions: An Exploration of the Energy Surfaces Associated with N-Hydroxysuccinimide Ester Reagents and Primary Amines and Guanidine Groups. J Am Soc Mass Spectrom 2016, 27 (6), 1089-1098.

92. Han, H.; McLuckey, S. A., Selective Covalent Bond Formation in Polypeptide Ions via Gas-Phase Ion/Ion Reaction Chemistry. J Am Chem Soc 2009, 131 (36), 12884-12885.

93. Wang, N.; Pilo, A. L.; Zhao, F.; Bu, J.; McLuckey, S. A., Gas-phase rearrangement reaction of Schiff-base-modified peptide ions. Rapid Commun Mass Spectrom 2018, 32 (24), 2166-2173.

94. Pilo, A. L.; Zhao, F.; McLuckey, S. A., Selective Gas-Phase Oxidation and Localization of Alkylated Cysteine Residues in Polypeptide Ions via Ion/Ion Chemistry. J Proteome Res 2016, 15 (9), 3139-3146.

95. Pilo, A. L.; Zhao, F.; McLuckey, S. A., Gas-Phase Oxidation via Ion/Ion Reactions: Pathways and Applications. J Am Soc Mass Spectrom 2017, 28 (6), 991-1004.

1.7 Figures

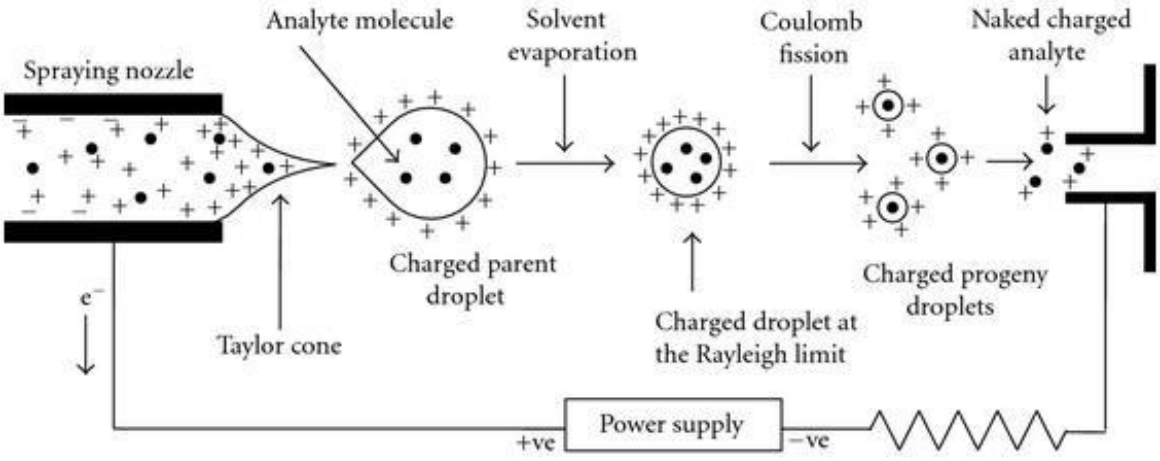

Figure 1.1. The general electrospray ionization process. Reprinted from reference 30. Copyright © 2012 S. Banerjee and S. Mazumdar.

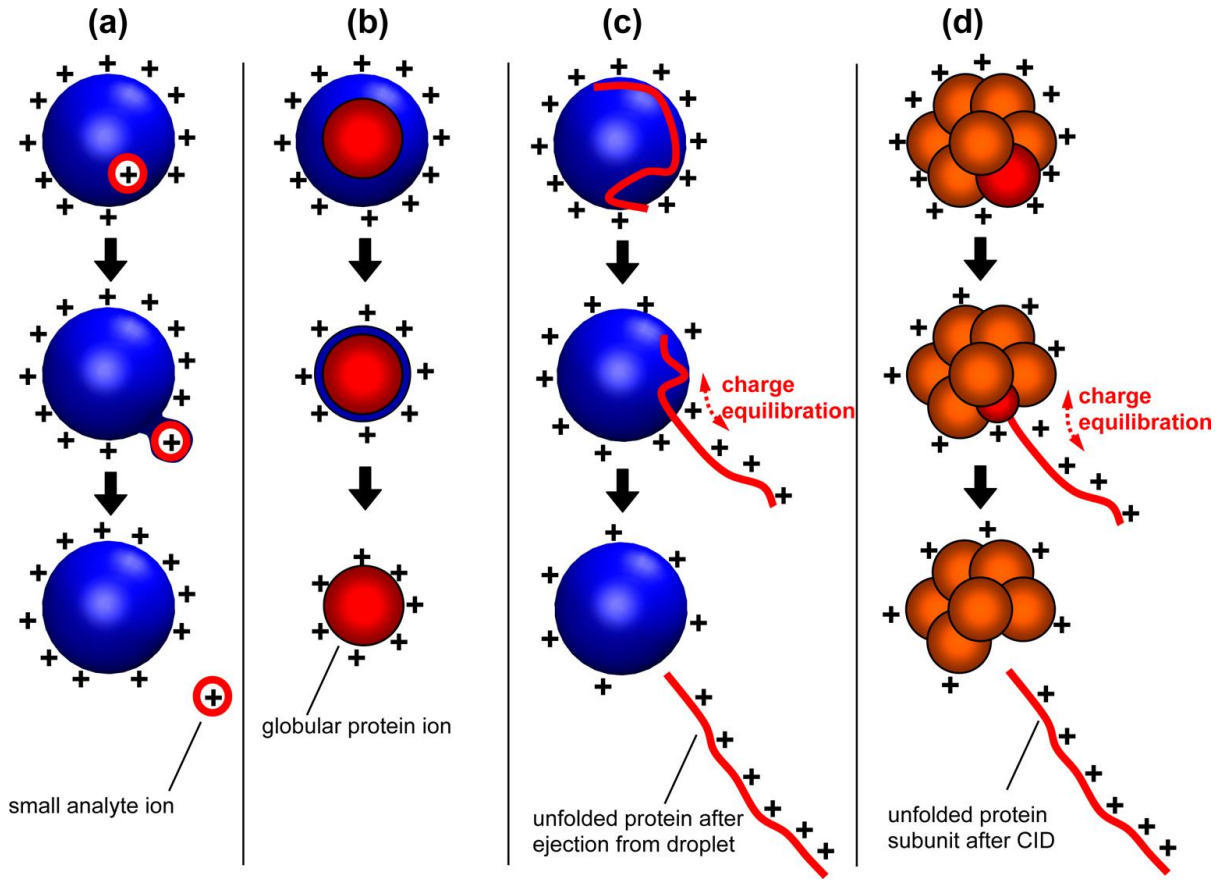

Figure 1.2. Summary of the three ESI models. (a) IEM, (b) CRM. (c) CEM, and (d) collision-induced dissociation of protein complex cations. Reprinted from reference 22. Copyright 2013 American Chemical Society.

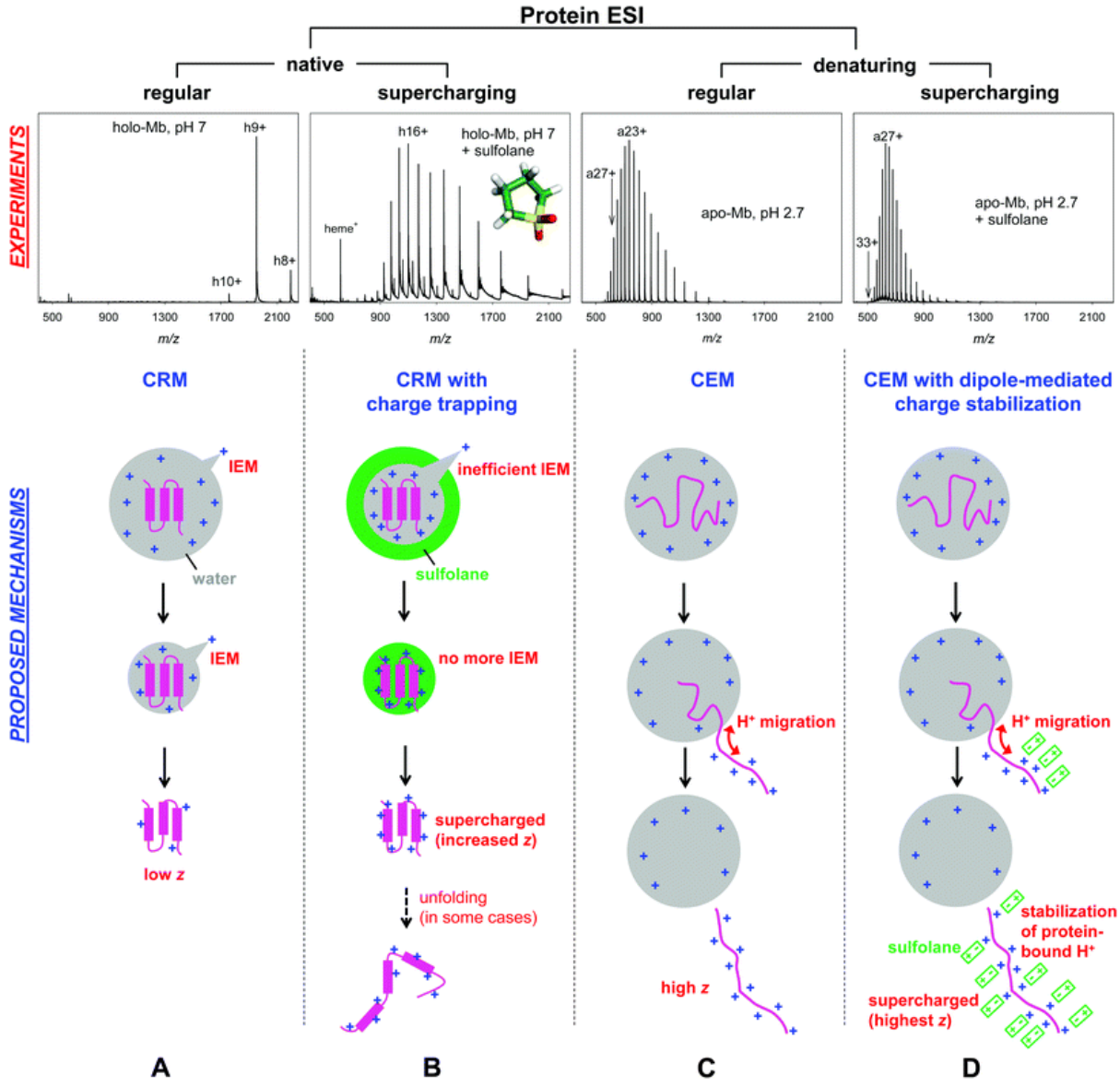

Figure 1.3. Summary of ESI process among different experimental conditions. The corresponding proposed ESI mechanisms are depicted below in cartoon representation. (A) Native ESI, (B) native supercharging ESI, (C) denaturing ESI, (D) Denatured supercharging ESI. The examples were used holo ("h") and apo ("a") myoglobin. Reprinted from reference 55 with permission (CCC Marketplace). Copyright 2019 Royal Society of Chemistry.

CHAPTER 2. CHARACTERIZATION OF HOMOPOLYER DISTRIBUTIONS VIA DIRECT INFUSION ESI-MS/MS USING WIDE MASS-TO-CHARGE WINDOWS AND GAS-PHASE ION/ION REACTIONS

Abstract

A hallmark of the electrospray ionization (ESI) of large polymeric molecules is its tendency to generate a distribution of charge states. When a distribution of polymers is subjected to ESI, the charge state distribution of each component can lead to a mass spectrum comprised of a highly congested mixture of ions with various masses and charges with overlapping mass-to-charge (m/z) ratios. When the distribution of polymers is comprised of a common monomeric unit (i.e., a homopolymer), the overlap of the charge state distributions of the various polymer components can give rise to striking spectral patterns comprised of a dense central cluster of peaks with similar, but not identical, m/z values, usually with wing-like patterns on either side. We refer to the central cluster of peaks as an "Emerald City", with a nod to the Wizard of Oz, with the wings contributing to an "Emerald City pattern". The Emerald City pattern can appear in the mass spectrum of any homopolymer with a distribution of charge states and oligomer sizes. We developed a web-based tool to simulate ESI mass spectra of homopolymers to study the effects of various parameters, such as the charges of the ions, widths of polymer distributions, monomer mass, and cationizing agents, on the appearance of Emerald City patterns. We used two size distributions of Dextran to experimentally demonstrate the results of the model. We also demonstrate a strategy using direct infusion ESI-MS coupled with segmented m/z windows that encompass Emerald Cities followed by gas-phase proton transfer reactions for characterizing size distributions as well as identifying individual polymer species within poly-disperse synthetic polymer samples. PEI 4k and 10k were used as model systems to demonstrate the approach. The selection of a windows of m/z prior to ion/ion reaction is demonstrated to lead to improved sample characterization using the proposed strategy relative to conventional zero charge deconvolution or proton transfer reactions without prior isolation of the targeted ion populations.

2.1 Introduction

Electrospray ionization (ESI) of large polymeric molecules tends to form multiply-charged ions.[1-2] While the multiple-charging phenomenon has several beneficial consequences, such as lowering the mass-to-charge ratio (*m/z*) of analyte ions to facilitate mass analysis, mixture analysis can be difficult due to overlapping charge state distributions. Therefore, different strategies to process and/or simplify spectra have been developed, including ion/ion reactions[3] and spectral deconvolution.[4-5] In this work, we discuss a general phenomenon observed when forming multiply-charged ions from homopolymers with nano-ESI (nESI) and ESI and use spectral modeling to study characteristic features in the spectra. The spectra include three features: a dense cluster of peaks that we refer to as an 'Emerald City' and 'wings' of peaks to the left and right of the central clusters. An Emerald City appears when there is a concentration of peaks within a narrow *m/z* distribution corresponding to those components of the distribution with the same n-mer/charge ratio.

Homopolymers are comprised of a single monomer unit and are usually ionized via matrix-assisted laser desorption/ionization (MALDI), which normally gives mostly singly charged polymer ions.[6] However, homopolymers with one or more polar groups per monomer tend to form multiply-charged ions via ESI or nESI because of a charged group within the monomer unit (e.g., a carboxylic acid group) or through ion adduction. Coulomb repulsion between neighboring charge sites generally inhibits charges residing on every monomer;[7] nevertheless, it remains possible to form ions with high charge density from homopolymers. This high charge density coupled with the range of molecular sizes inherent in a homopolymer distribution leads to the 'Emerald City' phenomenon. In this work, we developed a web-based tool to calculate ESI mass spectra of homo-polymers with defined size distribution and charges of virtual homopolymer ions to simulate the Emerald City phenomenon under well-defined conditions. Additionally, a commercial polysaccharide, dextran, was used to demonstrate the appearance of Emerald Cities in experimental data. We also discuss the effects of various parameters relevant to the observation of the Emerald City phenomenon, such as numbers of charges of the ions, size distributions of the homopolymers, monomer unit mass, and different cationizing agents using the web-tool calculator.

In the past few decades, researchers established strategies for analyzing polymer samples using ESI-MS coupled with separation techniques, including reversed-phase liquid chromatography,[8] gel permeation chromatography,[9] and size-exclusion chromatography.[10]

However, the condensed-phase separation techniques require relatively long separation times and can also require extensive experimentation to optimize elution conditons. Therefore, we take the advantage of the tendency for homopolymers to form Emerald Cities to analze polydisperse homopolymer samples via ESI-MS using direct infusion coupled with gas-phase proton transfer reactions to rapidly charactize the homopolymer components.

2.2 Experimental

2.2.1 Materials

Dextran samples with labeled average molecular weights of 5k and 12k, poly(ethylenimine) (PEI) linear HCl salts with labeled average molecular weights of 4k (dpi=1.3) and 10k (dpi=1.5), and perfluoro-1-octanol (PFO) were all purchased from Sigma-Aldrich (St. Louis, MO, U.S.A.). Optima LC-MS grade water and methanol (MeOH) were purchased from Fisher Scientific (Fair Lawn, NJ, U.S.A.).

2.2.2 Sample Preparation

Dextran stock solutions were initially prepared by dissolving the powders in LC-MS grade water to a concentration around 1 mg mL^{-1}. The working nESI solutions were directly diluted from the stock solutions to 1 - 10 μg mL^{-1} with LC-MS grade water. PEI solutions were freshly prepared in optima water every day before the experiment, the concentrations were at 10 μg mL^{-1} and 50 μg mL^{-1} for 4k and 10k PEI, respectively. PFO stock solution was initially prepared by dissolving the powders in LC-MS grade MeOH to a concentration around 1 mg mL^{-1} then further diluted to 200 μM as the working solution.

2.2.3 Mass Spectrometry

All experiments were performed on a Sciex™ TripleTOF 5600 quadrupole time-of-flight mass spectrometer (Concord, ON, Canada).[11-12] Dextran cations were formed via nESI with pulsed borosilicate glass emitters at approximately +1300 V applied to the wire in contact with the solution. The emitters were placed before the inlet aperture of the atmosphere/vacuum interface. To avoid in-source fragmentation, a low DC gradient was used and tuned manually every day. The

ions were injected and directly transmitted into the q2 cell for trapping. The pressure of q2 was maintained at approximately 6 to 8 mtorr. The ions were released from q2 and mass-analyzed via orthogonal acceleration time-of-flight mass spectrometry.

For characterization of the polymer sample, PEI cations were first generated via +nESI, as mentioned above, followed by low resolution Q1 RF/DC isolation to select the ion populations for the analysis. The selected ion population was transmitted into q2 for storage. Next, deprotonated PFO dimer anions were generated via –nESI using the alternatively pulsed emitter system, mass selected in Q1, and transferred into q2 for mutual storage (10 – 30 ms).

2.2.4 Mass Spectral (Emerald City) Simulations

An R Shiny Application was created to model polymer spectra for comparison with experimental data (Ion/ion Reaction Calculator, https://mcluckey-apps.shinyapps.io/iirxnspeccalc/). The application allows a user to define separate isotopic distributions for the non-repeating and repeating parts of a polymer as well as the distribution of polymer lengths. Mass distributions are defined by inputting the different masses and relative intensities. The distribution of polymer lengths is assumed to follow a gamma distribution parameterized using the mode (most probable value) and a loosely-defined "entropy" parameter. Gamma distributions are typically defined using a "shape" parameter and a "scale" parameter. The app uses "entropy" in place of "scale" to suggest that a higher entropy will lead to a wider distribution of polymer sizes. The shape parameter is calculated by $shape = \frac{mode}{entropy} + 1$. The user then defines the mass and charge of the charging agent on the ions (e.g., proton, sodium ion, etc.) and a distribution that defines the average number of charging agents per monomer unit. For example, if a polymer has on average a proton on every two to four monomer units, the distribution will range from 0.5 to 0.25. For consistency, this distribution also follows a gamma distribution and is defined with a mode and entropy. This approach will calculate fractional numbers of charge carriers for some polymer lengths, which is not physically possible; therefore, each fractional value is rounded in both directions, which results in two *m/z* values corresponding to one polymer length with a particular number of charge carriers per monomer. Using the mass distributions, the polymer size distribution, and distribution of charge carriers per monomer unit, all possible mass and charge pairs can be calculated to generate a mass-to-charge spectrum. We identify different ranges of the

measured spectra of homopolymers using the average number of monomers per charge (M/C) given by:

$$M/C = \frac{n}{iz_c}$$

where n is the number of monomer units, i is the number of charge carriers, and z_c is the charge of the charge carrier. Using the above example, where a polymer has a proton on every two to four monomer units, the spectrum would range from M/C = 2 to 4.

2.2.5 Zero-Charge Deconvolution Procedure

The zero-charge deconvolution is achieved by applying a research version of a THRASH algorithm written in MATLAB (MathWorks, Natick, MA, USA) developed by AB SCIEX.[13] The different criteria for the deconvolution were set as follow: mass-to-charge (*m/z*) range 500 to 2500; maximum output molecular weights of 9,000 Da and 14,000 Da for Dextran 5k and 12k samples, respectively; signal-to-noise ratio (S/N) of three; and the minimum ion counts of 5 ions.

2.3 Results and Discussion

2.3.1 The Emerald City Spectral Pattern

The regularity in mass spacing of homopolymers and the multiple-charging phenomenon associated with ESI gives rise to the possibility for the appearance of regions of high concentrations of ions on the *m/z* scale. We refer herein to these regions as "Emerald Cities." For example, if each monomer of a homopolymer carries a single charge, an M/C =1 as defined above, every oligomer will have a very similar mass-to-charge ratio within a range dependent upon the combined mass of the terminal groups, often 18 Da, divided by the range of charge states. If M/C = 2, half (even number of oligomers) or nearly half (odd number of oligomers) will fall into a narrow range of *m/z* values. If M/C = 3, one-third or nearly one-third of the oligomers will fall into a very narrow range of *m/z* values, and so on. Oligomers that are not wholly divisible by a unit charge will fall on either side of the region of high *m/z* concentration, giving rise to wings on either side of the peaks within the highly concentrated *m/z* range. This situation is illustrated with the simulation associated with **Figure 2.1**. In this simulation, a mass spectrum of ions generated by sodium adduction to a homopolymer distribution consisting of 5-20 monomers of 162 Da with an

18 Da combined mass of the termini was modeled over a range of M/C = 1 to 4. All parameters used for this model, including those associated with the polymer distribution, are given in Supplemental Information.

Figure 2.1a shows the calculated spectrum of the sodiated polymer distribution with the ions associated with M/C = 1, 2, 3, and 4 indicated in the figure. In the case of M/C = 1, all ions are found in a narrow region near *m/z* 162+23. No wings are associated with this Emerald City as all n-mers of the distribution are wholly divisible by 1. We focus our attention on the region surrounding M/C = 2, which represents ions formed by sodium cation adduction to every other monomer. The insert in **Figure 2.1a** shows an expanded region showing the Emerald City associated with M/C = 2. There are 8 oligomers in the simulated distribution and the even-numbered oligomers appear in the Emerald City. **Figure 2.1b** shows a region of the *m/z* scale that includes the M/C = 2 Emerald City along with nearby ions on either side. Adjacent charge states of all the odd-numbered oligomers from the distribution fall on the left (M/C < 2) and right (M/C >2) sides of the Emerald City. Higher and lower charge states of the even-numbered oligomers also appear in this *m/z* window. **Figure 2.1c** shows a slightly narrower *m/z* window that restricts the wings to the peaks with declining abundances in the direction of Emerald City. This pattern can give the eye a sense of perspective that, with some imagination, looks like light posts leading to a city in the distance and hence the reason we refer to this spectral pattern as an Emerald City from the Wizard of Oz.

2.3.2 Demonstration of the Emerald City Phenomenon with Dextrans

We chose to use dextrans, a class of polysaccharides, to demonstrate experimentally the Emerald City spectral pattern. **Figure 2.2a** shows the +nESI experimental spectrum of Dextran 12k (labeled MW = 12,000 Da) along with simulated results, and **Figure 2.2b** shows a zoomed-in region of the experimental and simulated results that include the Emerald Cities for M/C 8-10 from **Figure 2.2a**. The simulation is primarily intended to predict the positions of the modelled components on the mass-to-charge scale and to provide approximate relative abundances, based on the crude assumptions used to model shapes of the distributions. There may also be peaks in the experimental spectrum that do not match the calculated spectrum if they arise from adduction of other metal ions, such as potassium, that are not included in the simulation. Also, for clarity,

the calculated spectra are mono-isotopic, so that the simulated spectra appear less congested than the experimental results. **Figure 2.2c** shows a zoomed-in portion of the experimental and simulated spectra that show the emerald city with M/C = 9. These comparisons clearly demonstrate experimentally the Emerald City phenomenon that arises for a homopolymer distribution subjected to nESI along with an approximate match to simulated data.

2.3.3 Factors that Contribute to Emerald City Formation

Given that ESI mass spectrometry has been used for decades for various homopolymer analyses, including those involving dextrans, it is noteworthy that the spectral pattern described above, referred to here as an Emerald City, does not appear to be widely recognized by the mass spectrometry community despite such patterns in mass spectra are apparent in the literature.[14-15]. Therefore, we also examined via modelling and experiments four factors that could play roles in the appearance, or lack thereof, of the Emerald City pattern, including the extent of multiple charging (charge density), size distributions of the homopolymers, monomer unit mass, and different ionizing agents.

To illustrate how the extent of multiple-charging impacts the formation or significance of the Emerald City phenomenon, we simulated mass spectra of dextran ions generated from a distribution of 10 to 50-mers with various M/C values. An analogous way to classify the ions is on the basis of charge density (CD), which is defined as charge/monomer (or the reciprocal of M/C). **Figure 2.3** shows three different charge densities, 0.2, 0.1, and 0.05, (corresponding to M/C = 5, 10, and 20, respectively) for the 10-50 mer dextran distribution. **Figures 2.3b** to **2.3d** show the spectra with the mass ranges associated with the respective charge densities. An Emerald City is clearly apparent in **Figure 2.3b** (M/C = 5) over the *m/z* range from 700 to 1000, but Emerald Cities are not as clearly obvious for M/C = 10 and M/C = 20, at least at the *m/z* scale expansions in **Figures 2.3c** and **2.3d**. **Figures 2.3e** to **2.3g** show the zoom-in spectra of the Emerald City regions from each M/C value. At these levels of expansion, the Emerald Cities for M/C =5 and M/C = 10 are obvious. These regions have 10 and 5 ions, respectively, comprising the higher concentrations of peaks, which prominently shows Emerald Cities. In contrast, for M/C = 20, only two ions, D_{40}^{2+} and D_{20}^{+}, are present in the region, which hardly comprises a "city". This figure illustrates that higher charging increases the number of ions in an Emerald City and higher charge

density compresses the ions into a narrower (and lower) *m/z* window. In contrast, lower charge states and the resulting lower charge density results in fewer ions within the overlap region and greater separation between the ions. In summary, the higher the number of charges and charge densities of the homopolymer ions, the more visually striking Emerald City pattern will be.

While the number of components within a given Emerald City is limited by the maximum charge that can contribute to it, the homopolymer size distribution determines how nearly the maximum is realized. **Figure 2.4** shows the effect of homopolymer size distribution on Emerald City formation from the calculation with the theoretical M/C = 10 Emerald City window. For example, **Figure 2.4a** shows the calculated spectrum of dextran with size distribution from 10-mers to 30-mers indicating only three ions are observed (D_{30}^{3+}, D_{20}^{2+}, and D_{10}^{+}) within the M/C = 10 Emerald City window. In contrast, more ions are observed within the Emerald City windows in **Figures 2.4b** to **2.4f**, which represent successively wider n-mer distributions. The results show that wider size distributions of homopolymers are more likely to lead to more significant Emerald City spectral patterns. Besides the number of peaks within the Emerald City, the wings appearing on either side of the Emerald City are also clearer by virtue of more peaks as the distribution width increases. The spacing between the Emerald City and its wings is mostly due to the finite upper molecular weight of the polymer distribution. Therefore, as the upper mass of the distribution increases and as the charge increases, the spacing between the Emerald City and its wings could decrease to the point that might make the spectral pattern less apparent. Based on **Figures 2.3** and **2.4** and the related discussion, it is clear that if a charge state distribution applies to each n-mer component of a homopolymer distribution, they will combine to yield an overall mass spectrum that can exhibit the Emerald City effect with the number of potential Emerald City patterns and the number of components within each Emerald City dependent upon the charge state distribution and the number of n-mers within the distribution.

From the above discussion, we summarize that both multiple charging and size distribution of the homopolymer play roles in the appearance of an Emerald City region by determining the number of ions located within the Emerald City *m/z* window. Therefore, we compare, experimental nESI data for Dextran 5k (**Figure 2.5a**) and 12k (**Figure 2.5b**). Based on the differences in polymer size, it can be expected that the 12k sample leads to higher absolute charge states and has a wider distribution. When the spectra of **Figure 2.5** were subjected to zero-charge deconvolution, the Dextran 5k ions showed a distribution ranging from roughly 5-mer to 40-mer whereas the

Dextran 12k ions showed a distribution ranging from roughly 10-mer to 70-mer (see **Figure 2.6**). Based on the components observed in the various Emerald Cities, it was also apparent that the Dextran 12k spectrum reflected the presence of higher maximum charge states than that of the Dextran 5k spectrum (see below). **Figure 2.5a** shows six Emerald Cities whereas **Figure 2.5b** shows roughly nine. The former are less clearly defined than the latter due both to relatively fewer components within each Emerald City and relatively fewer peaks that comprise the wings. The insert in **Figure 2.5a** shows the zoom-in *m/z* range representing the M/C = 7 Emerald City regions for both polymers. **Figure 2.5c** shows an even greater expansion of the *m/z* scale to highlight the compositions of the M/C = 7 regions of the two spectra. The insert shows that the larger polymer distribution has more components in the wings and **Figure 2.5c** shows the greater number of components for the 12k distribution in the Emerald City itself.

We also investigated how the mass of the monomer unit and the adduction of different cations affect the appearance of an Emerald City. These factors play relatively minor roles in the formation of the Emerald City pattern in the mass spectrum. However, both of them can affect the appearance of the Emerald Cities, leading to, for example, difficulty in clearly resolving Emerald Cities in the spectrum. **Figure 2.7** shows simulations for three 10 to 50-mer homopolymer distributions of monomer masses 44 Da, 128 Da, and 162 Da, with protonation, and a CD of 0.2 (M/C = 5). In the zoomed-in spectra (**Figure 2.7b** to **2.7d**), the Emerald City for M/C = 5 is observed in all three spectra. A smaller monomer unit has narrower spacings between ions of adjacent n-mers, which may lead to overlap in signals from the wings and the Emerald City. For example, **Figure 2.7e** shows the zoomed-in spectrum of the *m/z* range 216 to 232 from **Figure 2.7b**, which applies to a 44 Da monomer for a homopolymer such as polyethylene glycol (PEG). The homopolymer ions that fall within this M/C = 5 Emerald City include the 10-mer, 15-mer, 20-mer ions and so on. Ions with the number of monomers not wholly divisible by 5 appear in either the left or right wings. The ions in **Figure 2.7b** are labelled as PEG ions. We note that, in this case, the PEG_{10}^{2+} ion appears within the ions that comprise the higher *m/z* wing of the Emerald City pattern. Overlap of Emerald City ions with one of its wings can make the Emerald City pattern less prominent.

Mixtures of cationizing agents (e.g., protons, sodium ions, potassium ions, ammonium ions, etc.) might be present in ESI mass spectra of homopolymers, depending upon solution conditions, where the presence of such mixtures can impact the appearance of Emerald Cities. For illustration,

we simulated dextran mass spectra in which sodium ions (**Figure 2.8a**) and potassium ions (**Figure 2.8b**) were the exclusive cationizing agents. In each case, various Emerald Cities are clearly apparent. **Figure 2.8c** shows the spectrum that includes both the ions of **Figure 2.8a** and **2.8b**. **Figure 2.8d** shows an expansion of **Figure 2.8c** to highlight the M/C = 7 region for both the sodium- and potassium-adducted ions. Two distinct Emerald Cities are apparent in **Figure 2.8d** that show overlap in the respective wings. This overlap makes appearance of the Emerald Cities less obvious in **Figure 2.8c**. This example applies to ions that are ionized exclusively by either sodium or potassium ion adduction. In practice, mixtures of sodium and potassium adduction can likely occur for a given polymer molecule. Each cationizing agent composition (e.g., 2:1, Na^+:K^+) would have its own *m/z* window for Emerald City with the exclusive versions (see **Figure 2.8d**) constituting the upper and lower limits for the windows of the Emerald Cities. The net effect for the presence of multiple cationizing agents is a potentially significant overlap of the Emerald Cities such that they are not clearly apparent upon casual inspection.

2.3.4 Characterization of Homopolymer Distributions via Direct Infusion ESI-MS/MS by Selection of an Emerald City Followed by Gas-Phase Proton Transfer Reactions

Recognizing the spectral overlap phenomena (i.e., Emerald Cities) that appear in the nESI mass spectra of homopolymer distributions enables the development of a strategy for characterizing a polydisperse polymer distribution by focusing on the regions of fixed whole number M/C and using such ions as a sampling of the distribution. Therefore, we propose a strategy that involves mass selection of a *m/z* window encompassing an Emerald City region followed by charge reducing reactions to disperse the components of the Emerald City. In this way, the size distribution of the homopolymer samples can be sampled. The general strategy of isolating a portion of an ESI mass spectrum of a complex mixture that encompasses a range of precursor ions followed by charge reduction to determine the components in the isolated window has been illustrated using ion/molecule reactions,[16] electron transfer reactions,[17] proton transfer reactions,[18] and multiply-charged ion attachment[19]. An initial broad-band mass selection simplifies the mixture of ions subjected to charge state reduction resulting in a more readily interpretable product ion spectrum. The studies cited above have involved mixtures of biologically relevant polymers. Here we apply the general concept to homopolymer distributions, which lend themselves particularly well to such an experiment due to the Emerald City phenomenon. Here, we illustrate

the approach using mixtures of ions generated from poly(ethylenimine) (PEI) samples. PEI is a synthetic polymer that is used, for example, as a nucleic acid delivery vector for cellular therapy[20] in which the size of PEI significantly affects transfection efficiency.[21] Therefore, an alternative method for rapid characterization of a PEI distribution will be valuable.

A mass spectrum of a PEI 4k sample generated via nESI with ion accumulation in q2 followed by TOF mass analysis is shown in **Figure 2.9a**. The spectrum shows most of the ions to appear within a range of *m/z* 250-650, with much of the signal concentrated in a highly congested region of *m/z* < 400. The application of a zero-charge deconvolution algorithm to this spectrum (**Figure 2.10a**) showed very few of the expected PEI components, presumably due to the high spectral congestion. The same ion population was then subjected to ion/ion proton transfer reactions (see **Figure 2.10b**) to convert most of the ions to the 1+ charge state, which showed the presence of ions extending up to roughly 3200 Da. However, this experiment revealed that the ion population was comprised of a mixture of species, including abundant fragment ions. Some of the fragments were likely to originate from the sampling/transmission process (e.g., in-source fragmentation and injection into q2), despite the use of relatively low potential gradients in regions of relatively high pressure. However, some fragmentation likely arose from space-charge induced ion heating in the accumulation quadrupole.[22] For highly complex mixtures, such as those present with heterogeneous homopolymer distributions, space-charging can arise even when no single component gives rise to a strong signal.

To study the impact of space charge, we investigated both ion fill time, which can be used to vary the number of ions in the ion trap, and ion trapping time in q2, which influences the time that ions are exposed to the electric fields present during ion storage. **Figure 2.11** shows the pre and post-proton transfer reaction spectra with different fill times. The post-ion/ion reaction result indicated that the relative abundance of the major PEI distribution (singly charged PEI with $^{m/z}$ window 1,500 to 3,500) decreased as a function of increasing fill time. Furthermore, a zoom-in of the spectra (**Figure 2.12**) clearly showed that fragments corresponding to neutral loss (NL) of CH_3OH and water increased in relative abundance with increased fill time. We also increased the ion trapping time in q2 (see **Figure 2.13**). In addition to increases in losses of water and methanol, lower *m/z* ions can be observed at the longer trapping times. This is consistent with sequential fragmentation resulting from longer activation times.[23,24]

A strategy for reducing the total number of ions in the trap while simultaneously maximizing the presence of informative ions is to select smaller regions of the mass spectrum that contain a high concentration of informative ions (e.g., an Emerald City). When Q1 was used to transmit only ions within the window of $^{m/z}$ 260-263 (**Figure 2.9b**), which corresponds to the M/C = 6 Emerald City of PEI ($CH_3(C_2H_5N)_bOH$), followed by ion/ion proton transfer, the post-ion/ion reaction spectrum shows a much cleaner spectrum (**Figure 2.9c**). A much higher size distribution than zero charge deconvolution and proton transfer reaction without a segmented window can be observed (compare **Figure 2.9c** with **Figures 2.10 and 2.11**). The mass spacing between the identified PEI ions in **Figure 2.9c** equals six monomer units (6 * 43 Da), which is consistent with the known M/C = 6 Emerald City. We also observed slightly lower size distributions of PEI with CH_3OH loss with one water adduct ($(C_2H_5N)_e$+H2O) from the isolated ion population. When we mass-selected another *m/z* window (*m/z* 258-261, **Figure 2.9d**), we noted that the major PEI species distribution changed from intact PEI ($CH_3(C_2H_5N)_bOH$) to CH_3OH loss (formula = $(C_2H_5N)_d$) and its water adduction ($(C_2H_5N)_e$+H2O) (**Figure 2.9e**), suggesting that these species might be present in the sample solution or arise from in-source fragmentations despite gentle ion transmission conditions.

We further applied the same strategy to a PEI 10k sample (labeled average MW = 10,000, with polymer dispersity index = 1.5). **Figure 2.14a** and **Figure 2.15** provide mass spectra obtained with no mass selection before and after ion/ion reaction, respectively. Like the PEI 4k results described above, highly complex spectra that include abundant products from fragmentation are observed that complicate the identification of the various ions. The post-ion/ion reaction data (see **Figure 2.15**) indicates that almost all of the ions in the spectra are less than 3000 Da in mass. Extensive fragmentation, much of which likely arises from space charge, is indicated, in analogy with the findings with the PEI 4k sample described above. We note that both the PEI 4k (**Figure 2.9a**) and 10k (**Figure 2.14a**) samples both showed distributions with series of particularly narrow peaks (see, for example, the shaded peaks in **Figure 2.14a**). Isolation of ions in these peaks followed by proton transfer revealed them to be Emerald Cities of n-mers formed from methanol loss (i.e. PEI formula = $(C_2H_5N)_n$). (See, for example, **Figure 2.9e** for the 4k sample and the data in **Figure 2.16** for the 10k sample.) Polymer ions that lack the masses of the termini (CH_3 and OH), lead to Emerald Cities with identical *m/z* values for the monoisotopic species of the various n-mers, leading to narrower Emerald Cities relative to those generated from polymer ions that contain the termini. In the case of **Figure 2.16**, ions of *m/z* 302 were selected for ion/ion reactions.

The mass spacing between the singly-charged product ions after the reaction equaled seven monomer units (7 * 43 Da), which is consistent with the M/C = 7 Emerald City for $(C_2H_5N)_n$. We note that the size distribution for $(C_2H_5N)_n$, as determined from its Emerald Cities, extended up to around 2,000 Da, which is much less than what label (average MW = 10k Da). This suggests that they are degradation products, either from gas-phase fragmentation or from condensed-phase processes, derived from the larger PEI species.

In order to selectively sample intact PEI oligomers (PEI formula = $CH_3(C_2H_5N)_nOH$), we selected the *m/z* window from 258 to 263 (see **Figure 2.14b**), which includes the Emerald City M/C=6 (6 * 43 Da), and subjected the ions to proton transfer. A larger *m/z* window than that used with the PEI 4k sample (see **Figure 2.9b**) was selected in this case due to larger labeled PEI size. The wider window also allows for the presence of other species, such as, for example, $(C_2H_5N)_e+H_2O$. **Figure 2.14c** shows the post-ion/ion reaction mass spectrum from the mass-selected *m/z* window. Several distributions are apparent with spacings between the peaks in each distribution consistent with six monomer units of PEI (6 * 43 Da), as expected. (The relatively low abundance ions that do not fall within a 6 * n-mer pattern probably arise from "wing regions" (see above) of distributions that can contribute due to the relatively broad selection window that we sampled.) Intact PEI oligomers are noted in **Figure 2.14c** up to around *m/z* 8,000 (singly charged), which is closer to the labeled molecular weight (MW=10k, with dpi=1.5) than noted in **Figure 2.15**. However, the dominant PEI distributions are $(C_2H_5N)_e+H_2O$ (purple dots and numbers) and $(C_2H_5N)_e+H_2O+HCl$ (blue dots). There is also a series of peaks consistent with $CH_3(C_2H_5N)_nOH-H_2O$. The ion sampling and transmission conditions were made a gentle as possible to minimize fragmentation. It is therefore not surprising that HCl adducts might be observed given that the sample was supplied as an HCl salt or that water adducts might appear. (We note that water adduction in q2 is sometimes observed in the present apparatus.) However, the origin of the species (gas-phase versus condensed-phase) that appear to be methanol and water loss products is less clear.

We also selected other $^{m/z}$ windows from different Emerald City regions, including *m/z* 298-304 (Emerald City with M/C = 7, **Figure 2.17a**) and m/z 346-352 (Emerald City with M/C = 8, **Figure 2.17b**). The post-ion/ion spectrum from the m/z 298-304 window (**Figure 2.17c**) is dominated by the $[(C_2H_5N)_7+H]^+$ ion at *m/z* 302, which was present in the precursor ion distribution. However, singly charged ions extending in mass to at least as high as those in **Figure 2.14c** were

observed. For the selected window with *m/z* 346-352, a relatively abundant series of peaks are observed below m/z 3600 (**Figure 2.17c**) that are consistent with the lower mass distribution in **Figure 2.14c**. Higher mass species of much lower abundance are also seen beyond 8,000 Da that are mixtures of n-mers with water and HCl adducts. The nESI mass spectrum of the 10k PEI sample is clearly a highly complex mixture of ions that is difficult to interpret. However, the selection of Emerald City windows followed by ion/ion reactions allows for the identification of many of the mixture components.

2.4 Conclusions

We describe a general spectral pattern that is possible in the electrospray ionization of multiply-charged homopolymers. Closely spaced signals on the *m/z* scale arise from homopolymer ions with a common M/C value while those ions that do not have an integer M/C value appear as wings on either side of the concentration of ions with the same integer M/C value. We refer to this pattern herein as an Emerald City. This pattern was demonstrated here using nESI mass spectra of dextran samples as examples of homopolymer distributions. A web-based tool to simulate the distribution of the homopolymer ions was developed to allow for the study of various factors that can affect the appearance, or lack thereof, of the Emerald City spectral pattern. We find that particularly important factors for the appearance of distinct Emerald Cities is the magnitude of charging and the width of the polymer distribution. The mass of the monomer, along with its charge, determines the spacings of the ions along the *m/z* scale, which impacts the ability of a given analyzer for resolving the ions in an Emerald City.

We also proposed a strategy to characterize homopolymer samples with a form of direct infusion tandem mass spectrometry involving gas phase ion/ion reactions. The proposed strategy involves mass selection of a window that includes an Emerald City spectral pattern described above to sample the overall distribution. Emerald Cities concentrate information about a polymer distribution into a narrow m/z range. This information is ordinarily difficult to extract via direct mass measurement alone due to extensive *m/z* overlap. Ion/ion reactions serve to separate the charge states allowing for a straightforward identification of the Emerald City components. The locations of Emerald Cities are readily predicted from monomer masses and can be selected even when they may not be obvious in highly congested mass spectra. The concept was illustrated here

with PEI distributions that included multiple related distributions comprised of fragments and adducts.

2.5 Acknowledgement

This work was supported by the National Institutes of Health (NIH) under Grant R37-GM45372.

2.6 References

1. Fenn, J. B.; Mann, M.; Meng, C. K.; Wong, S. F.; Whitehouse, C. M., Electrospray Ionization for Mass Spectrometry of Large Biomolecules. Science 1989, 246 (4926), 64-71.
2. Konermann, L.; Ahadi, E.; Rodriguez, A. D.; Vahidi, S., Unraveling the Mechanism of Electrospray Ionization. Anal Chem 2013, 85 (1), 2-9.
3. Foreman, D. J.; McLuckey, S. A., Recent Developments in Gas-Phase Ion/Ion Reactions for Analytical Mass Spectrometry. Anal Chem 2020, 92 (1), 252-266.
4. Zhang, Z.; Marshall, A. G., A universal algorithm for fast and automated charge state deconvolution of electrospray mass-to-charge ratio spectra. J Am Soc Mass Spectrom 1998, 9 (3), 225-233.
5. Horn, D. M.; Zubarev, R. A.; McLafferty, F. W., Automated reduction and interpretation of high resolution electrospray mass spectra of large molecules. J Am Soc Mass Spectrom 2000, 11 (4), 320-32.
6. Nielen, M. W. F., Maldi time-of-flight mass spectrometry of synthetic polymers. Mass Spectrom Rev 1999, 18 (5), 309-344.
7. Chao, H.-C.; Shih, M.; McLuckey, S. A., Generation of Multiply Charged Protein Anions from Multiply Charged Protein Cations via Gas-Phase Ion/Ion Reactions. J Am Soc Mass Spectrom 2020, 31 (7), 1509-1517.
8. Cuers, J.; Rinken, M.; Adden, R.; Mischnick, P., Critical investigation of the substituent distribution in the polymer chains of hydroxypropyl methylcelluloses by (LC-)ESI-MS. Anal Bioanal Chem 2013, 405 (28), 9021-9032.
9. Aaserud, D. J.; Prokai, L.; Simonsick, W. J., Gel Permeation Chromatography Coupled to Fourier Transform Mass Spectrometry for Polymer Characterization. Anal Chem 1999, 71 (21), 4793-4799.
10. Jovic, K.; Nitsche, T.; Lang, C.; Blinco, J. P.; De Bruycker, K.; Barner-Kowollik, C., Hyphenation of size-exclusion chromatography to mass spectrometry for precision polymer analysis – a tutorial review. Polym Chem 2019, 10 (24), 3241-3256.
11. Xia, Y.; Liang, X.; McLuckey, S. A., Pulsed Dual Electrospray Ionization for Ion/Ion Reactions. J Am Soc Mass Spectrom 2005, 16 (11), 1750-1756.

12. Xia, Y.; Chrisman, P. A.; Erickson, D. E.; Liu, J.; Liang, X.; Londry, F. A.; Yang, M. J.; McLuckey, S. A., Implementation of Ion/Ion Reactions in a Quadrupole/Time-of-Flight Tandem Mass Spectrometer. Anal Chem 2006, 78 (12), 4146-4154.

13. Horn, D. M.; Zubarev, R. A.; McLafferty, F. W., Automated reduction and interpretation of high resolution electrospray mass spectra of large molecules. J Am Soc Mass Spectrom 2000, 11 (4), 320-32

14. O'Connor, P. B.; McLafferty, F. W., Oligomer Characterization of 4-23 kDa Polymers by Electrospray Fourier Transform Mass Spectrometry. J Am Chem Soc 1995, 117 (51), 12826-12831.

15. Marty, M. T.; Baldwin, A. J.; Marklund, E. G.; Hochberg, G. K. A.; Benesch, J. L. P.; Robinson, C. V., Bayesian Deconvolution of Mass and Ion Mobility Spectra: From Binary Interactions to Polydisperse Ensembles. Anal Chem 2015, 87 (8), 4370-4376.

16. McLuckey, S. A.; Goeringer, D. E., Ion/Molecule Reactions for Improved Effective Mass Resolution in Electrospray Mass Spectrometry. Anal Chem 1995, 67 (14), 2493-2497.

17. Abzalimov, R. R.; Kaltashov, I. A., Electrospray Ionization Mass Spectrometry of Highly Heterogeneous Protein Systems: Protein Ion Charge State Assignment via Incomplete Charge Reduction. Anal Chem 2010, 82 (18), 7523-7526.

18. Huguet, R.; Mullen, C.; Srzentić, K.; Greer, J. B.; Fellers, R. T.; Zabrouskov, V.; Syka, J. E. P.; Kelleher, N. L.; Fornelli, L., Proton Transfer Charge Reduction Enables High-Throughput Top-Down Analysis of Large Proteoforms. Anal Chem 2019, 91 (24), 15732-15739.

19. Abdillahi, A. M.; Lee, K. W.; McLuckey, S. A., Mass Analysis of Macro-molecular Analytes via Multiply-Charged Ion Attachment. Anal Chem 2020, 92 (24), 16301-16306.

20. Pandey, A. P.; Sawant, K. K., Polyethylenimine: A versatile, multifunctional non-viral vector for nucleic acid delivery. Mater Sci Eng C 2016, 68, 904-918.

21. Godbey, W. T.; Wu, K. K.; Mikos, A. G., Size matters: Molecular weight affects the efficiency of poly(ethylenimine) as a gene delivery vehicle. J Biomed Mater Res 1999, 45 (3), 268-275.

22. Belov, M. E.; Gorshkov, M. V.; Udseth, H. R.; Smith, R. D., Controlled ion fragmentation in a 2-D quadrupole ion trap for external ion accumulation in ESI FTICR mass spectrometry. J Am Soc Mass Spectrom 2001, 12 (12), 1312-1319.

23. Sleno, L.; Volmer, D. A., Ion activation methods for tandem mass spectrometry. J Mass Spectrom 2004, 39 (10), 1091-1112.

24. Prentice, B. M.; Santini, R. E.; McLuckey, S. A., Adaptation of a 3-D Quadrupole Ion Trap for Dipolar DC Collisional Activation. J Am Soc Mass Spectrom 2011, 22 (9), 1486-1492.

2.7 Scheme and Figures

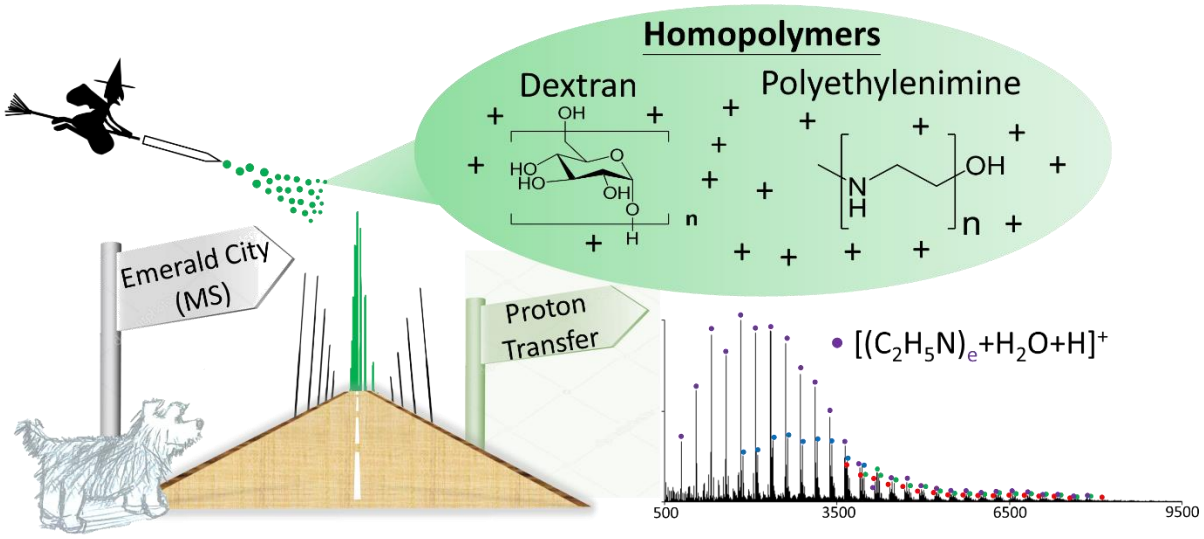

Scheme 2.1. Graphical abstract of chapter 2.

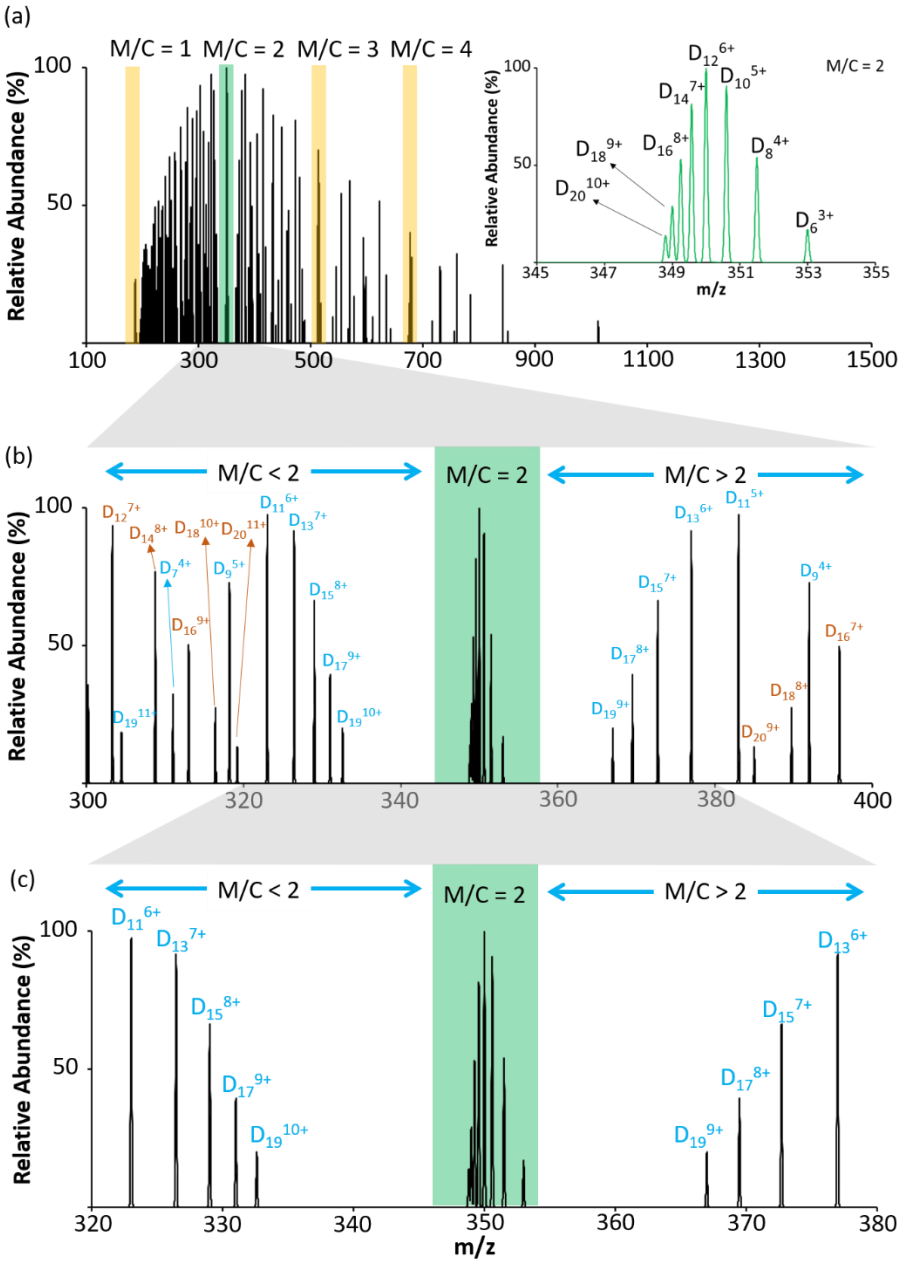

Figure 2.1. The demonstration of the Emerald City phenomenon. (a) The calculated spectrum from a sodiated virtual homopolymer sample (with the size distribution from 5 to 20 monomer units) using the web tool. (b) The zoom-in spectrum (m/z 300 to 400) from (a). (c) The zoom-in spectrum (m/z 320 to 380) from (a). The inserted spectrum at the top-right corner is the zoom-in spectrum (m/z 345 to 355) to show the ions within the same M/C = 2 that form the Emerald City. D_n^{x+} denotes the different dextran ions in the spectrum, where n is the number of monomer units in the polymer, and x is the number of charges on the polymer, all of which arise from sodium adduction.

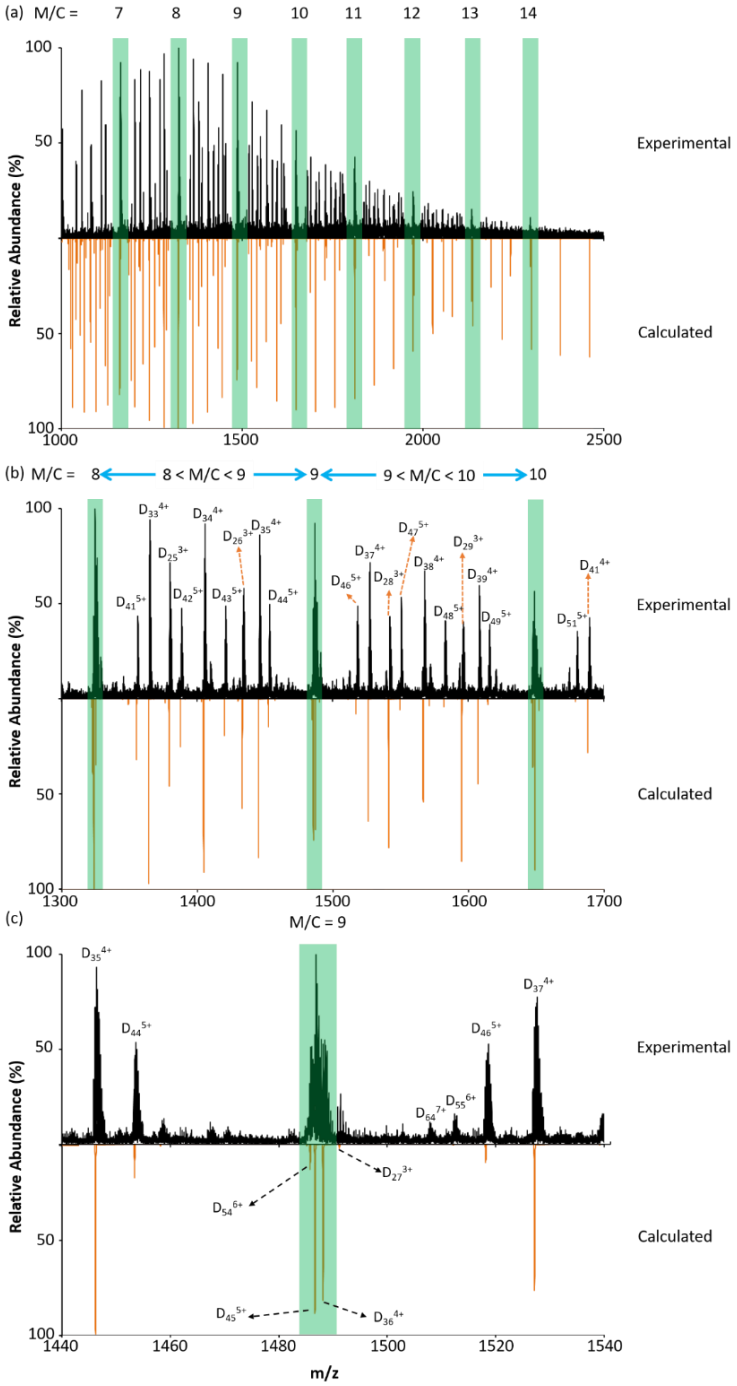

Figure 2.2. Emerald City in +nESI mass spectra of Dextran 12k. (a) The butterfly spectrum for experimental results (top) and simulated results (bottom) (m/z 1000-2500). (b) The butterfly spectrum for experimental results (top) and simulated results (bottom) of the zoom-in EC mass range (m/z 1300-1700). Note that in the experimental spectrum, the labels only represent the mar peak of the m/z value that also has well-defined charge states. There are many more peaks overlapping within some clusters so that the charge states are difficult to identify manually.

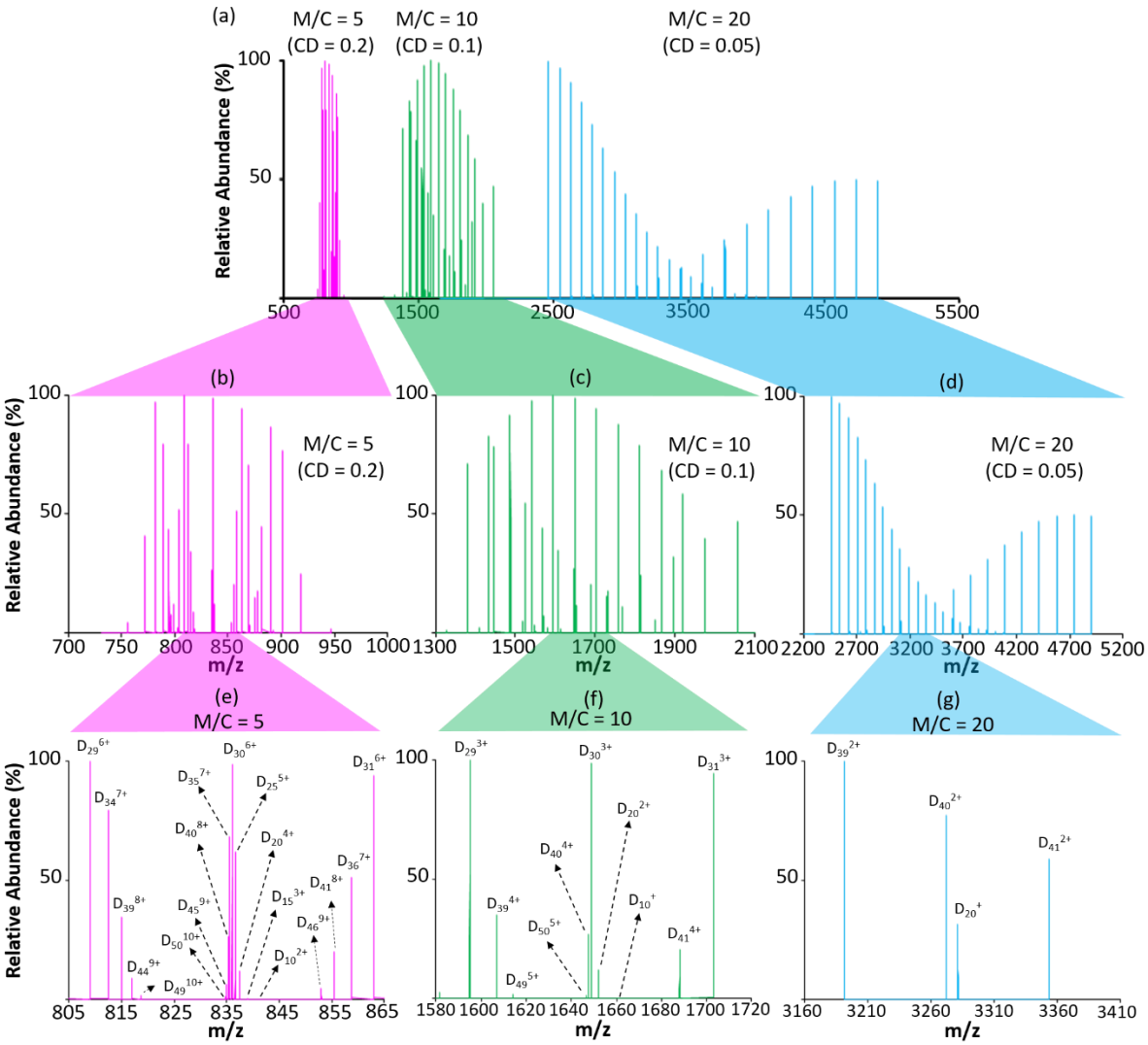

Figure 2.3. The effect of charge density for Emerald City formation. (a) The calculated spectra from three different CDs, 0.2, 0.1, and 0.05 from defined size distribution of the ions (Dextran, from 10 mers to 50 mers). (b) to (d), the zoom-in spectra of the m/z range corresponding to different CDs, 0.2, 0.1, and 0.05, respectively. (e) to (g), the zoom-in spectra of the Emerald Cities of m/z range from the theoretical M/C values, 5, 10, and 20, respectively.

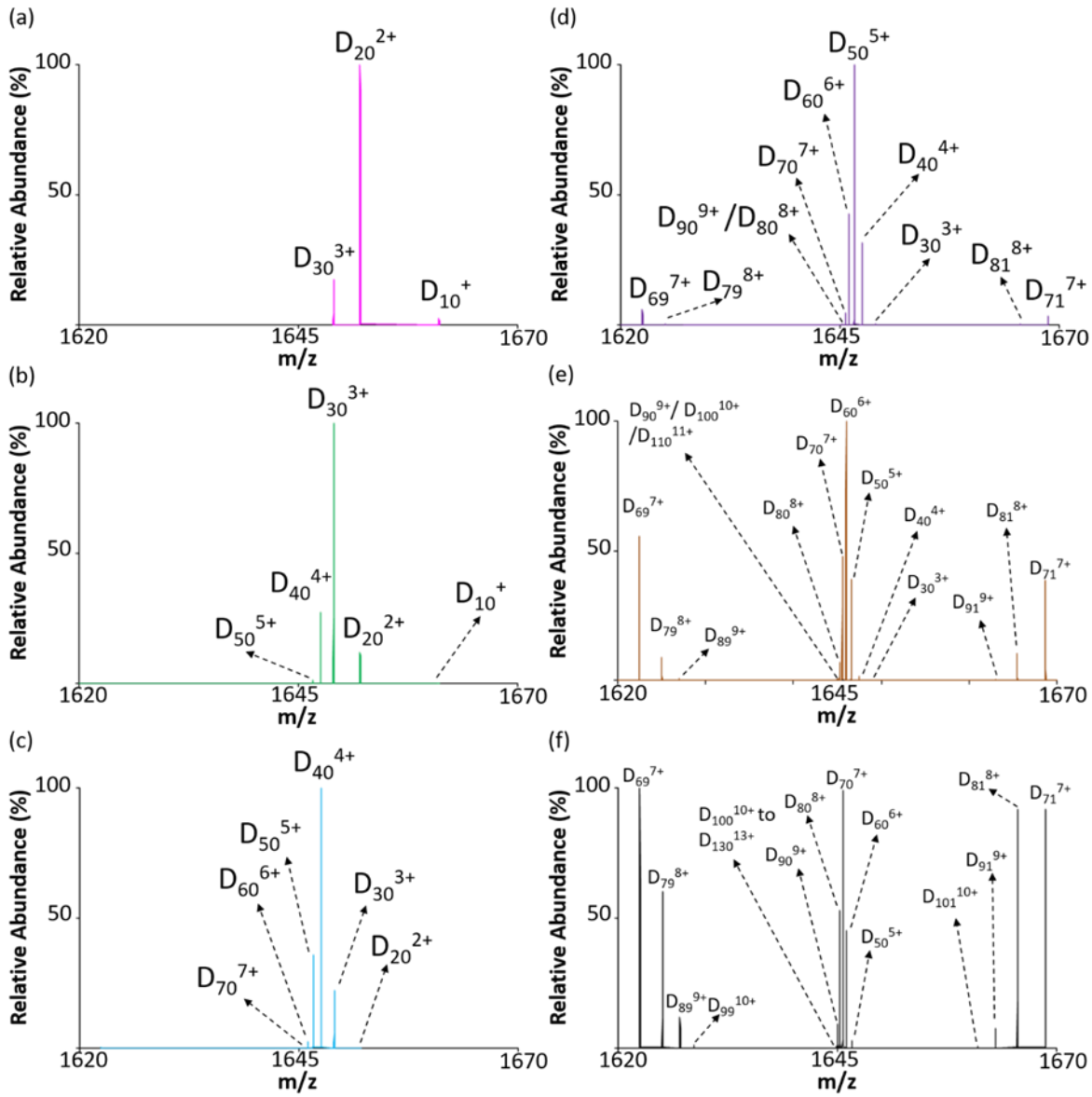

Figure 2.4. The effect of size distributions of homopolymers for Emerald City formation. The calculated spectra from different size distributions with defined charge density (CD = 0.1), (a) 10 to 30, (b) 10 to 50, (c) 10 to 70, (d) 10 to 90, (e) 10 to 110, and (f) 10 to 130. Note that different size distributions are not only with the sizes but also the statistical mean of the sizes contributing to the different abundance of the ions in the spectra. Besides, all the labeled ions are the ions with significant abundance in their respective spectra, and some ions are not labeled but exist in the spectra (especially for the ions in the Emerald City, e.g., D_{10}^{+} in **Figure 2.4c**)

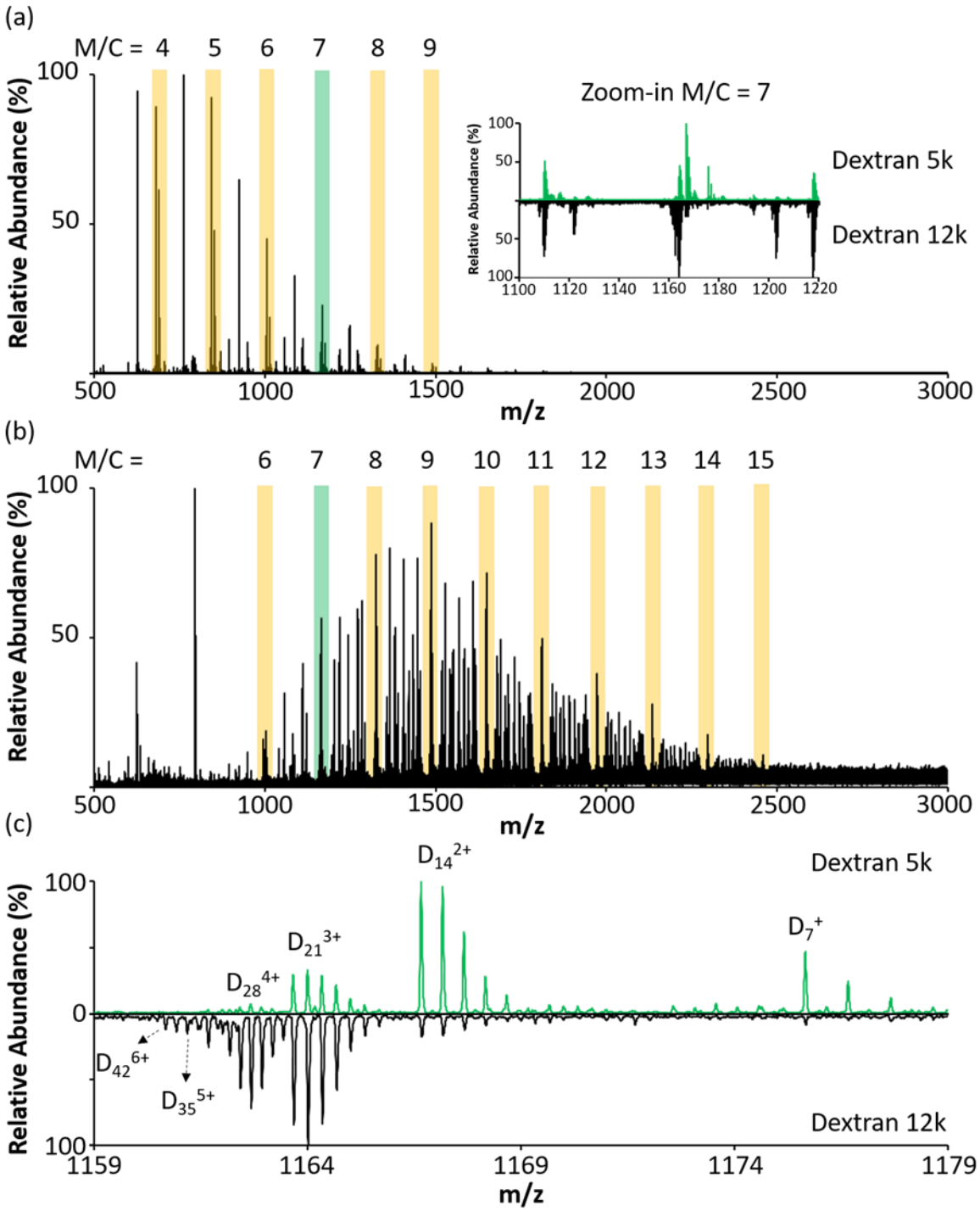

Figure 2.5. The comparison of Dextran 5k and 12k. (a) The +nESI mass spectrum of Dextran 5k. (b) The +nESI mass spectrum of Dextran 12k. (c) Zoom-in of the respective Emerald Cities for M/C = 7 (top: Dextran 5k; bottom: Dextran 12k). The inserted butterfly spectrum shows the zoom-in m/z range of M/C = 7 Emerald City and its wings from (top) Dextran 5k (a) and Dextran 12k (b).

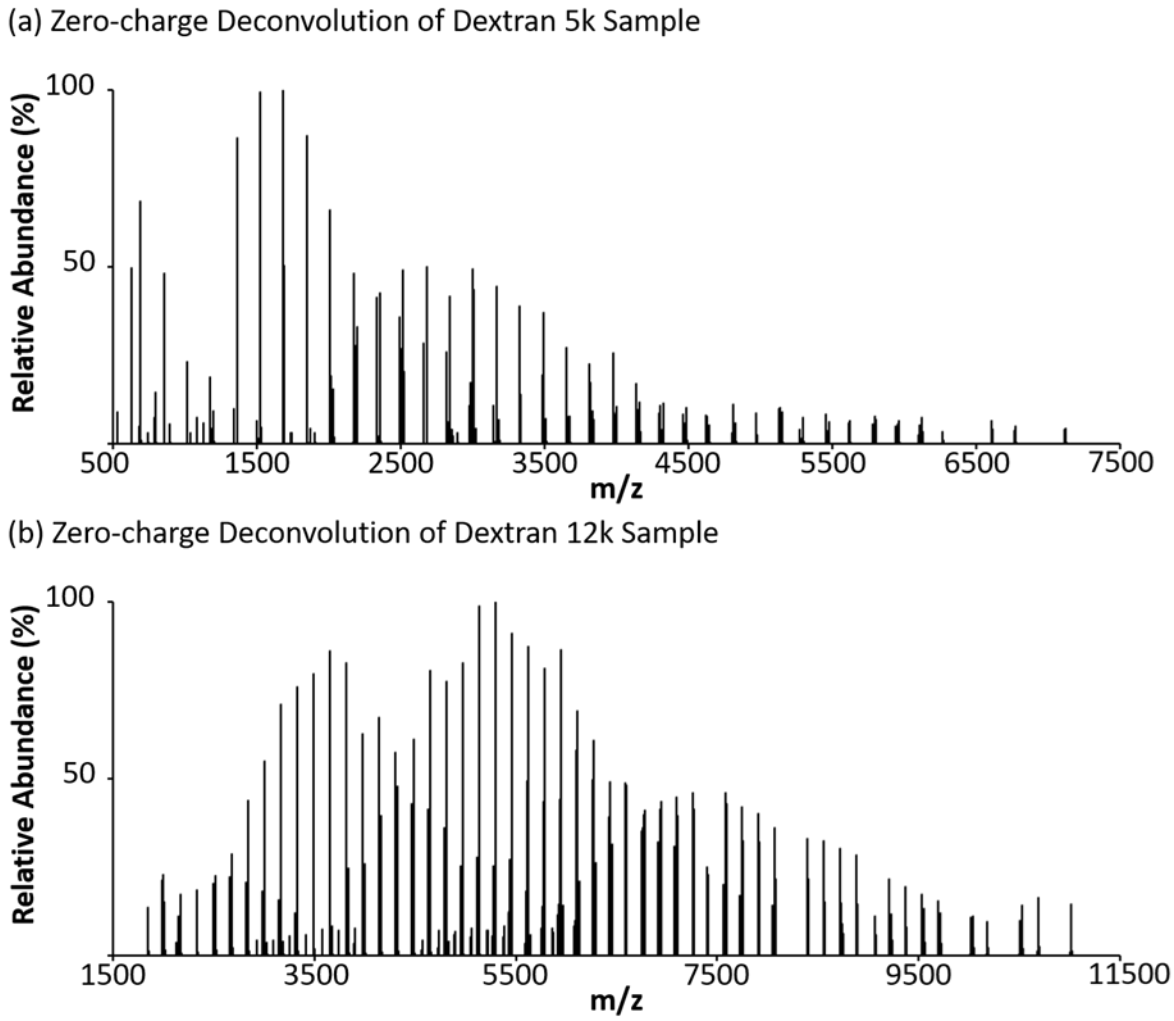

Figure 2.6. Zero-charge deconvolution spectra of the Dextran samples. The spectra give us a rough size distribution from different Dextran samples, (a) Dextran 5k and (c) Dextran 12k. Noted that there might be different combinations of cationizing agents for dextran samples, so peaks in the spectra show not only singlet. Also, the zero-charge deconvolution include the Na+ mass, so the molecular weight here is the mass after the adduction of sodium (i.e., +22 Da).

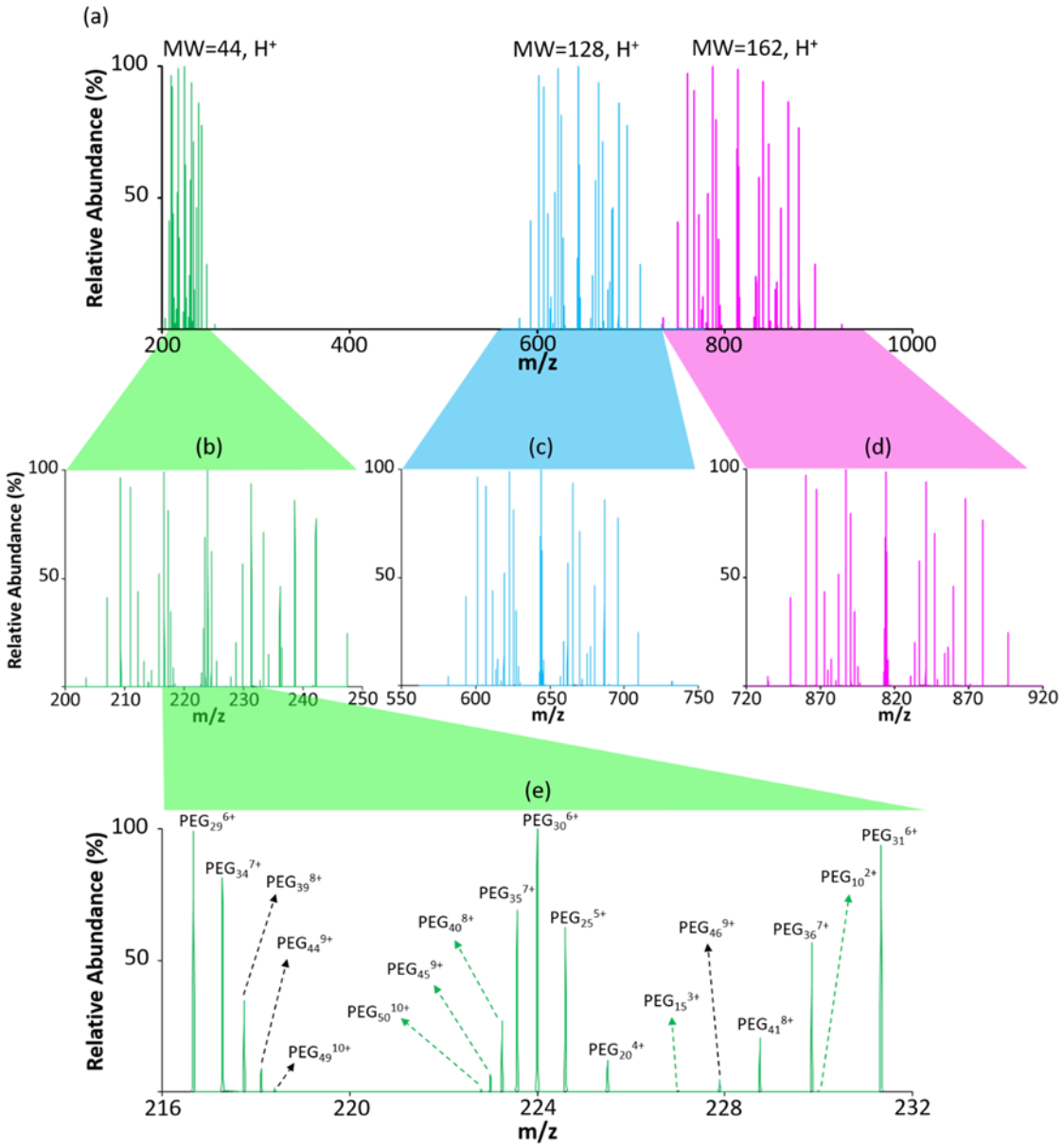

Figure 2.7. The effect of monomer unit size on the Emerald City phenomenon. (a) The calculated results from three homopolymers with different monomer unit size (and ionization) and identical degree of polymerization (10 to 50) and charge density (CD = 0.2). (b) to (d) the zoom-in spectra from the different monomer sizes results, (b) 44 Da, (c) 128 Da, and (d) 162 Da. (e) The zoom-in spectrum of M/C = 5 Emerald City from (b). Poly(ethylene oxide) (PEG) has the monomer unit as 44 Da, we therefore expressed the ions from (e) with PEG. PEG_n^{x+} denoted the different PEG ions in the spectrum, where n is the degrees of polymerization, and x is the number of charges on the polymer, which the charges are all from protonation.

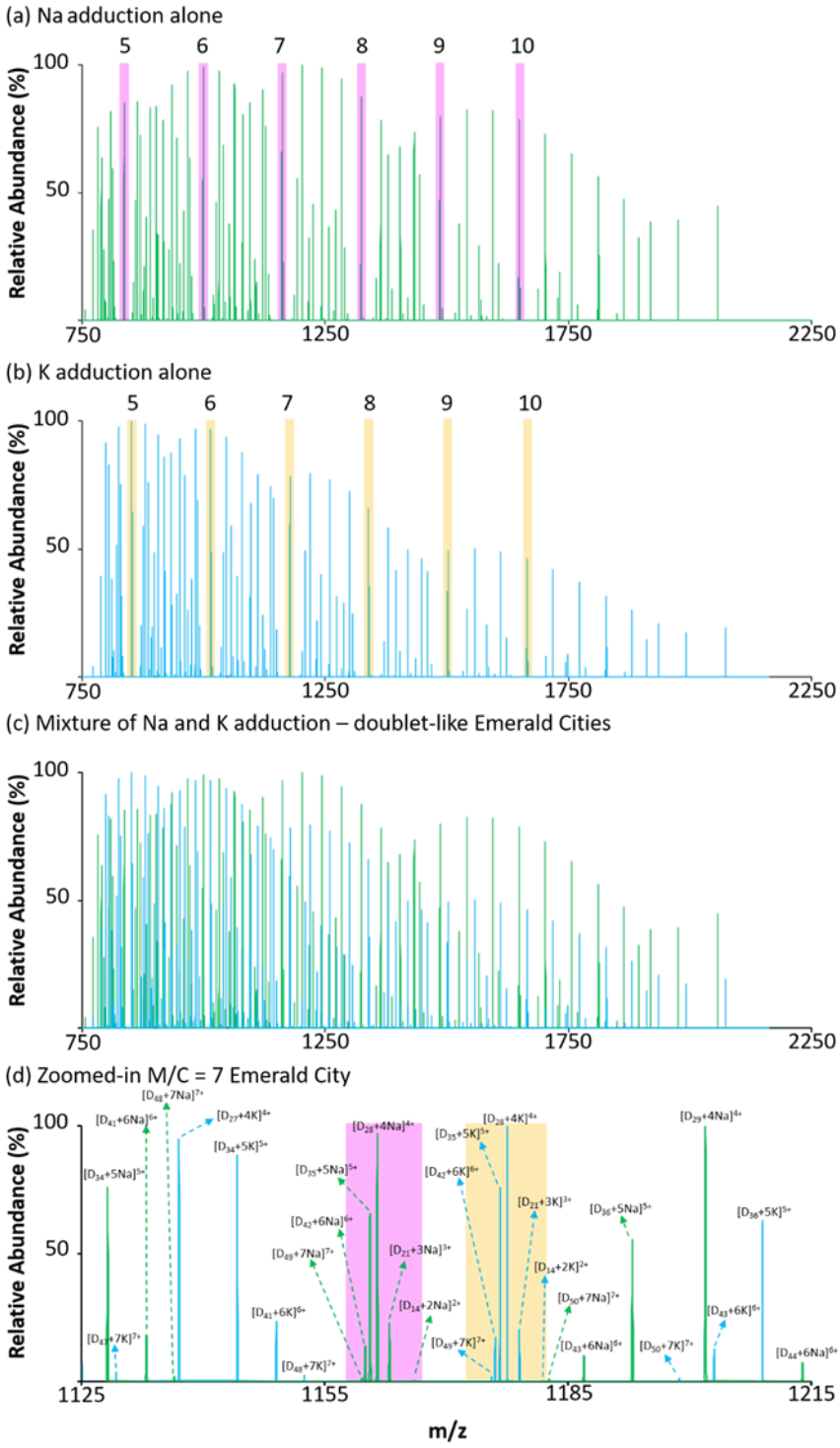

Figure 2.8. The effect of different degree of metal adduction on the Emerald City phenomenon. (a) The calculated +ESI mass spectrum from sodium adducted Dextran. (b) The calculated +ESI mass spectrum from potassium adducted dextran. (c) The overlapped mass spectra from (a) and (b). (d) The zoom-in spectrum of M/C = 7 Emerald City from (c), showing a doublet Emerald City in the m/z region.

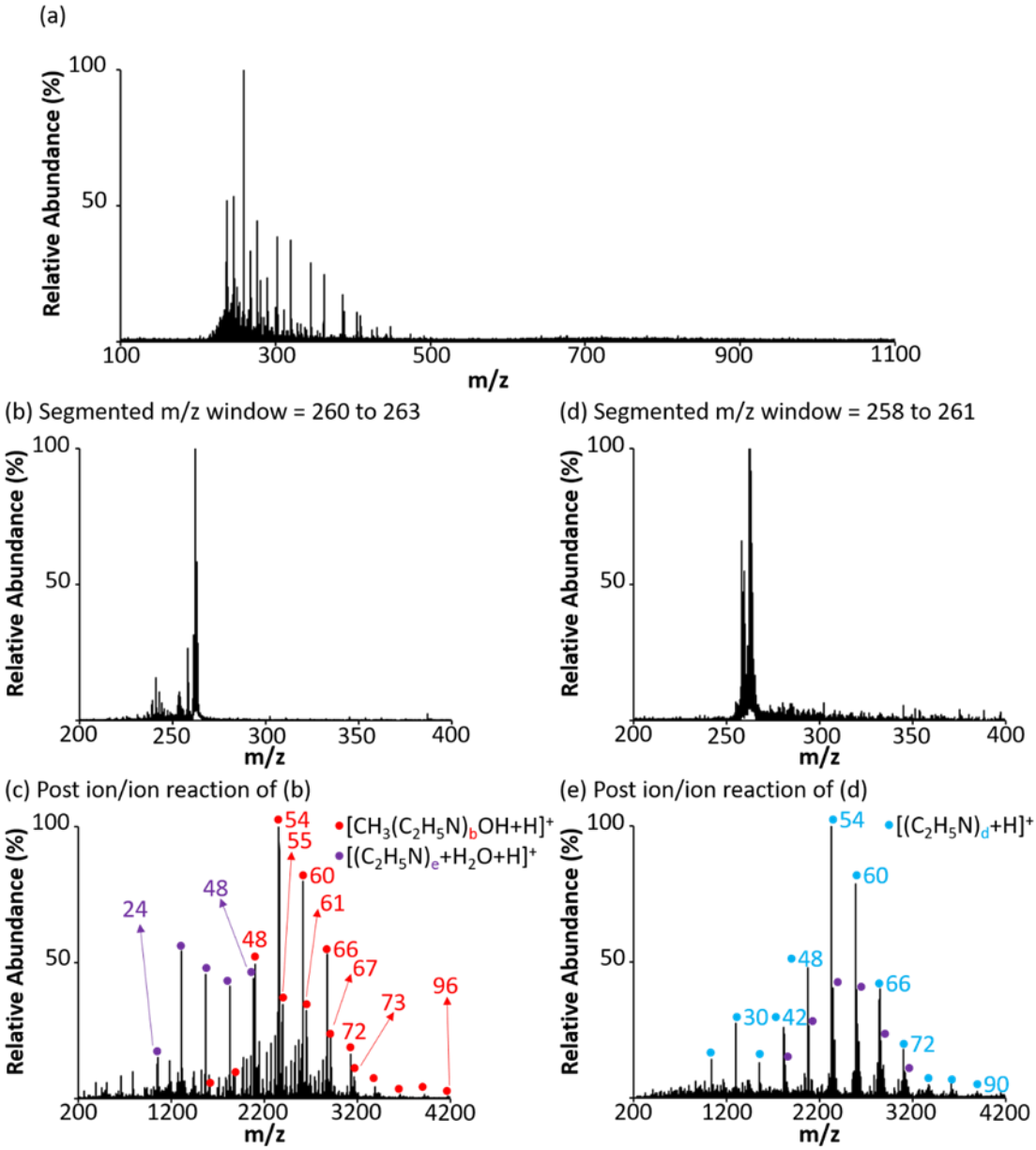

Figure 2.9. The mass spectra of PEI 4k sample. (a) The +nESI mass spectrum of PEI 4k. (b) The mass selected segmented m/z window (m/z = 260-263) mass spectrum of PEI 4k sample. (c) Post-ion/ion reaction mass spectrum from (b). The labeled numbers in (c) are the b or e from the inserted PEI cation formula. (d) The mass selected segmented m/z window (m/z = 258 to 261) mass spectrum of PEI 4k sample. (e) Post-ion/ion reaction mass spectrum from (d) The labeled numbers with different colors are the d from the inserted PEI cation formulas.

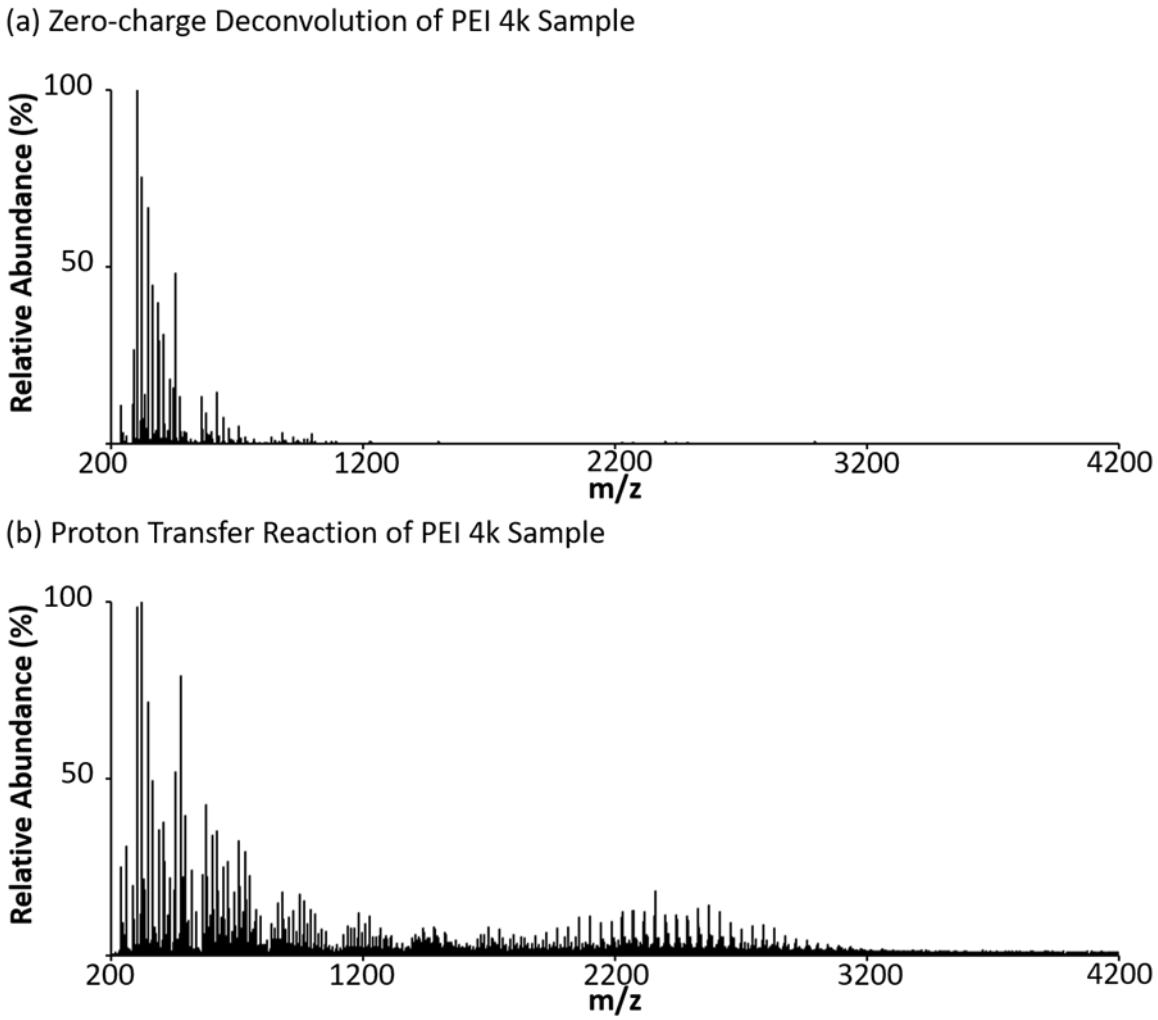

Figure 2.10. (a) Zero-charge deconvolution spectra of the PEI 4k samples. (b) Post-ion/ion reaction mass spectrum of PEI 4k sample. The spectrum roughly shows the size distribution of PEI polymers within the sample.

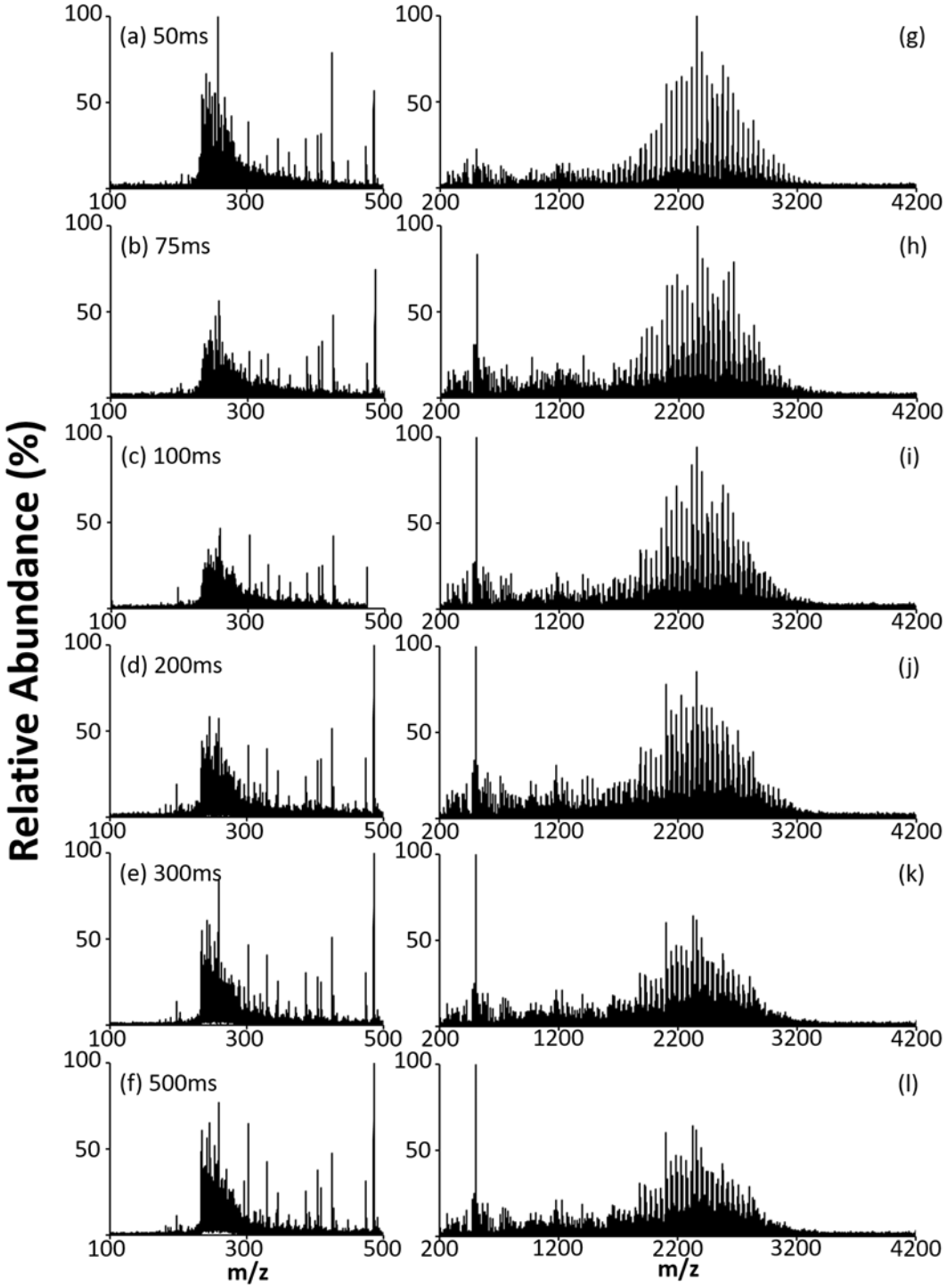

Figure 2.11. The comparison between different fill time for PEI 4k sample. The mass spectra of PEI-4k sample with fill time (a) 50ms, (b) 75ms, (c) 100ms, (d) 200 ms, (e) 300ms, and (f) 500ms, and their respective post-ion/ion reaction mass spectra (g) to (l).

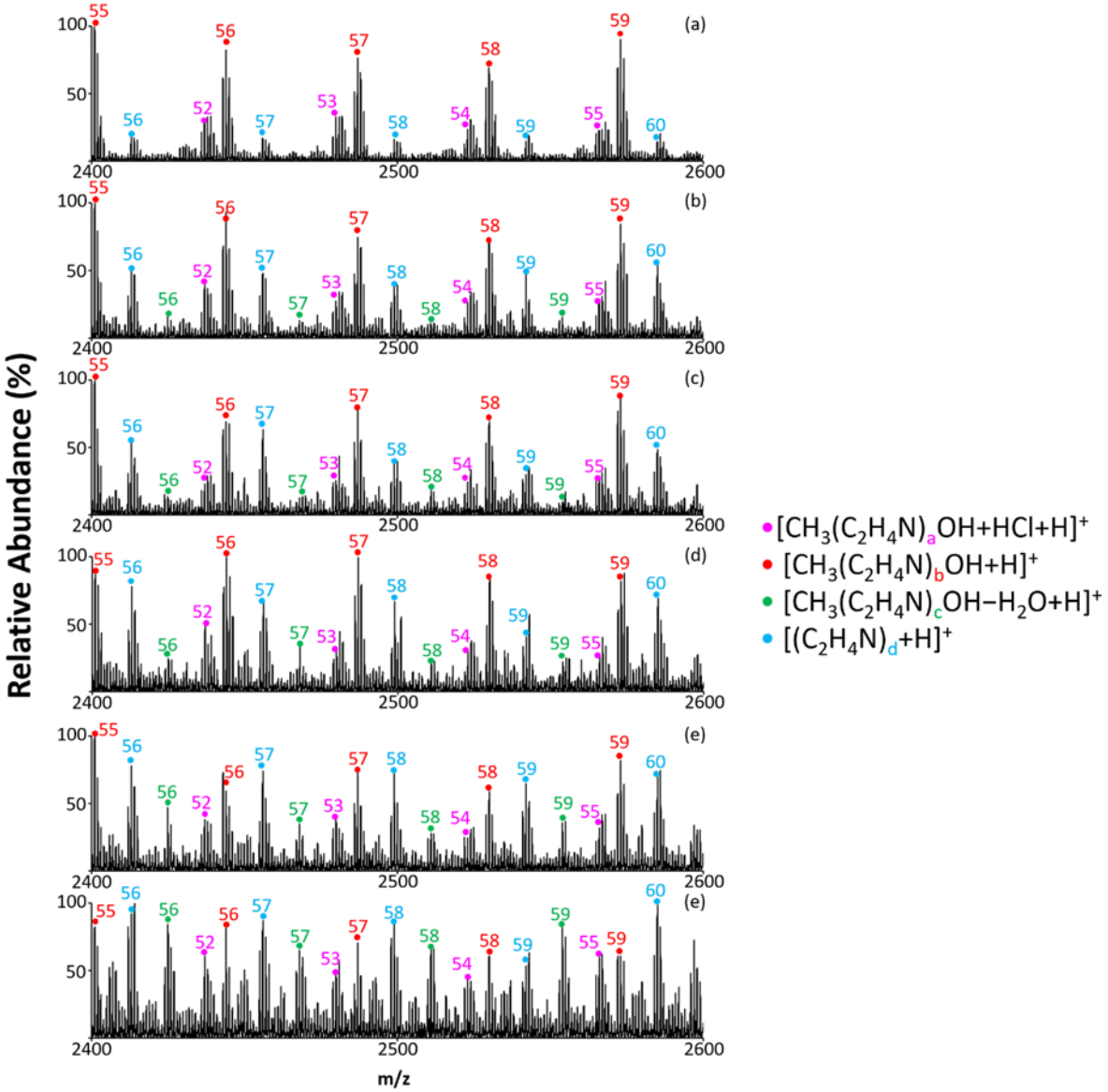

Figure 2.12. The zoom-in mass spectra from the post-ion/ion reaction spectra in **Figure 2.11**. (a) 50ms, (b) 75ms, (c) 100ms, (d) 200 ms, (e) 300ms, and (f) 500ms. The numbers are the degrees of polymerization showing in the different profiled PEI species.

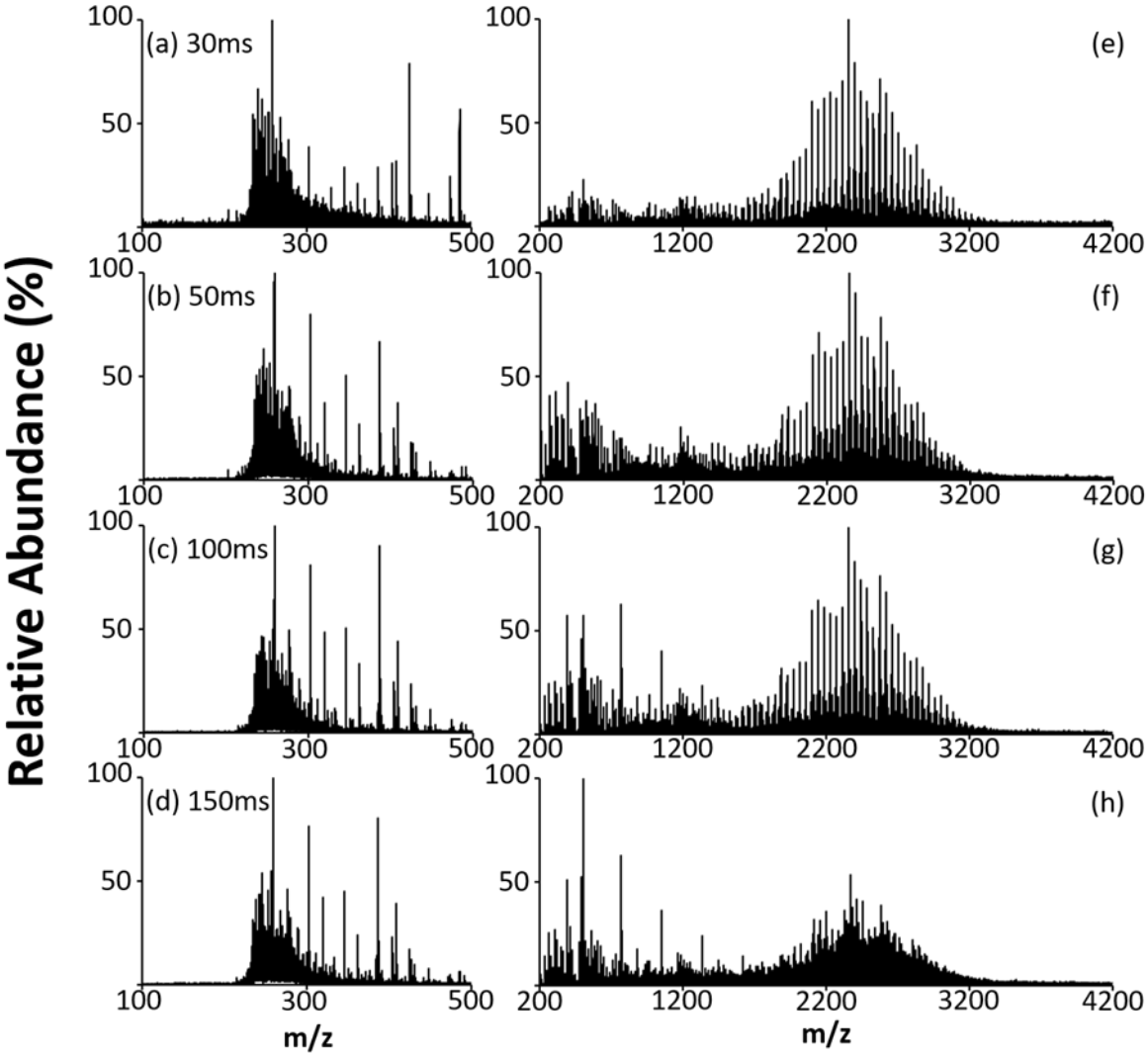

Figure 2.13. The comparison between different q2 trapping time. The mass spectra of PEI-4k sample with q2 trapping time (a) 30ms, (b) 50ms, (c) 100ms, and (d) 150 ms, and their respective post-ion/ion reaction mass spectra (e) to (h).

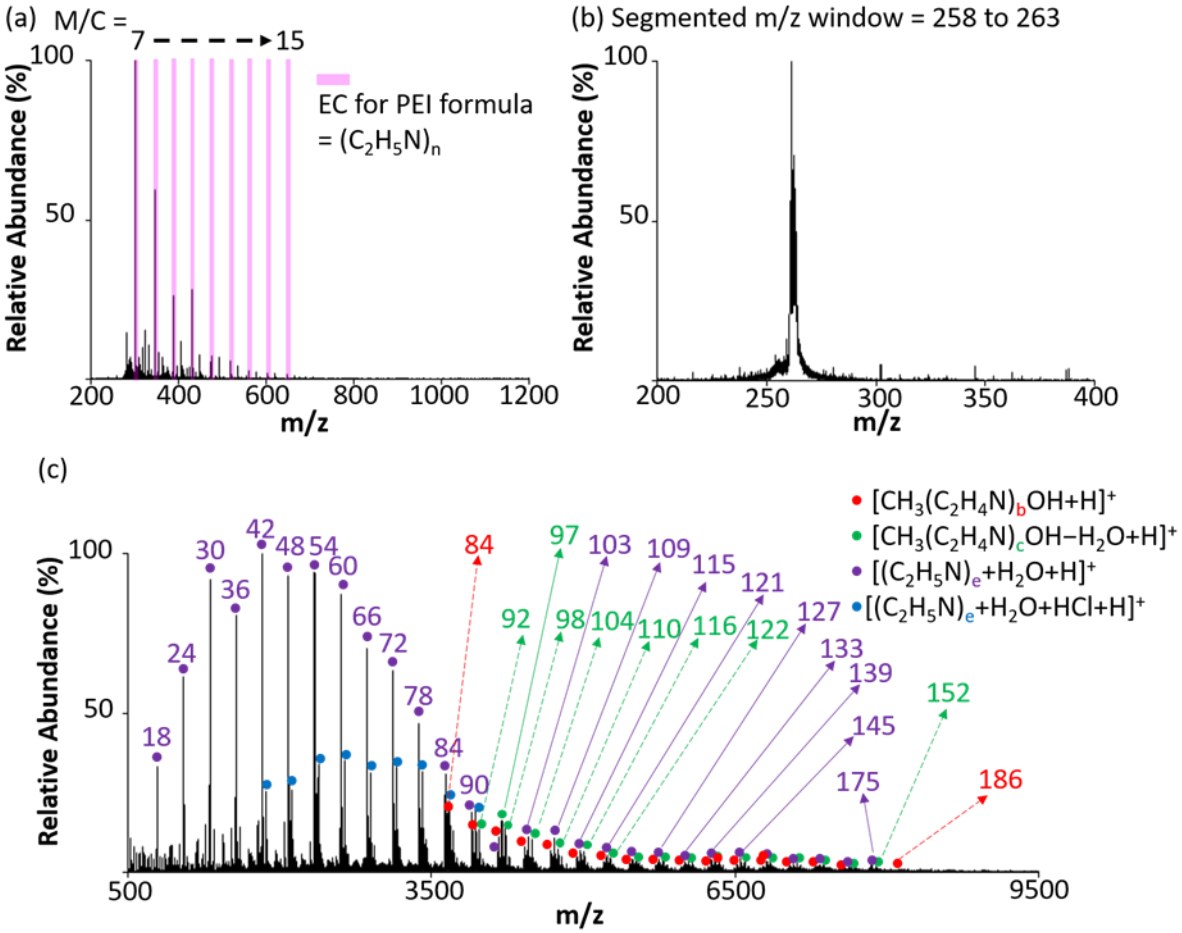

Figure 2.14. The mass spectra of PEI 10k sample. (a) The +nESI mass spectrum of PEI 10k. (b) The mass selected segmented m/z window (m/z = 258-263) mass spectrum of PEI 10k sample. (c) Post ion/ion reaction mass spectrum from (b). The labeled numbers in (c) are the b, c, or e from the inserted PEI cation formula.

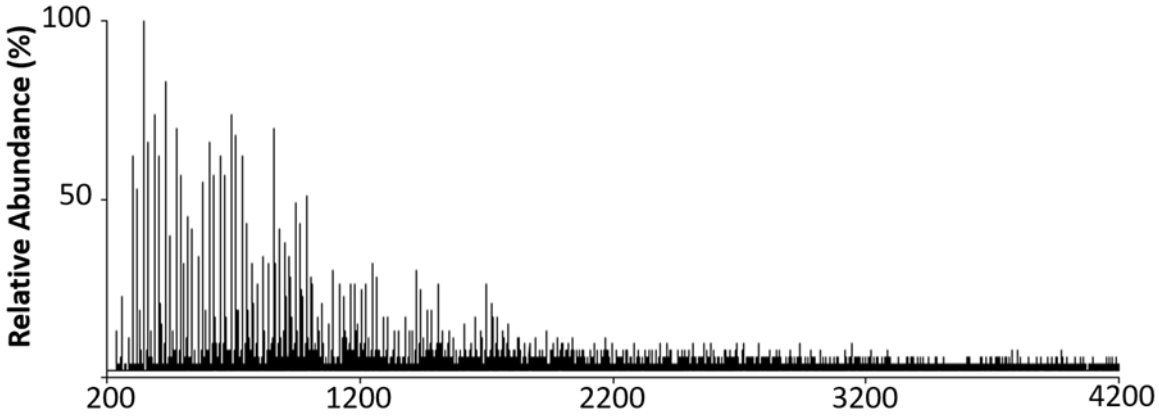

Figure 2.15. Post-ion/ion reaction mass spectrum of PEI 10k sample. The spectrum shows way smaller size distribution of the label on PEI 10k sample indicating simply shotgun MS with segmented m/z window with ion/ion reaction strategy may not suitable for polymer size characterization.

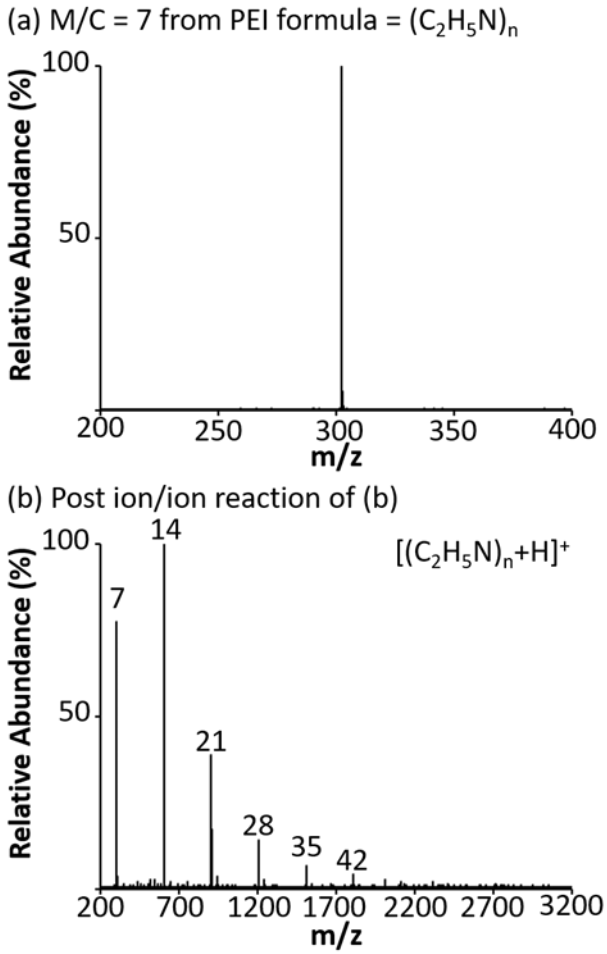

Figure 2.16. (a) The mass selected segmented m/z window (m/z = 302) mass spectrum of PEI 10k sample. (b) Post-ion/ion reaction mass spectrum from (a). The labeled numbers in (b) are the n from the inserted PEI cation formula, $[(C_2H_5N)_n+H]^+$.

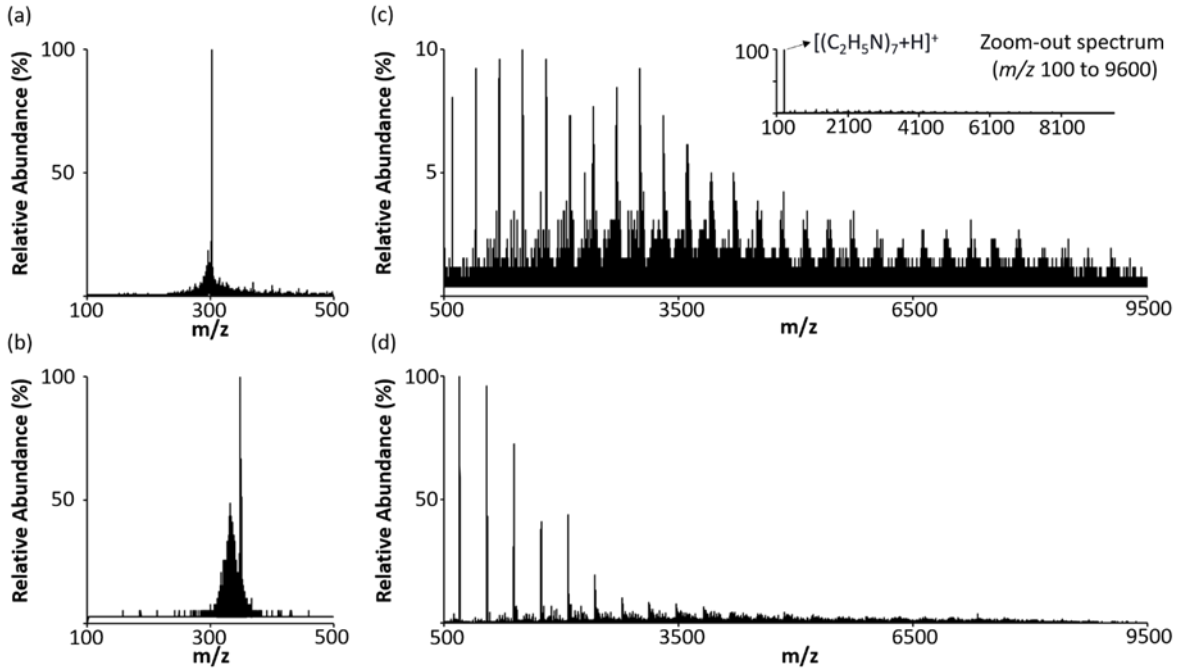

Figure 2.17. The comparison between different selected segmented m/z window from different Emerald Cities. The mass spectra of mass selected segmented m/z window of (a) m/z = 298 to 304 (M/C =7), (b) m/z = 346 to 352 (M/C =8), and their respective post-ion/ion reaction mass spectra (c) and (d). The insert in (c) is the zoom-out mass spectrum of (c) showing the interference of one fragment ion, $[(C_2H_5N)_7+H]^+$ (m/z 302) in the spectrum.

CHAPTER 3. THE GENERATION OF MULTIPLY-CHARGED PROTEIN IONS FROM OPPOSITE POLARITY OF MULTIPLY-CHARGED PROTEIN IONS VIA GAS-PHASE CHARGE INVERSION REACTIONS

Abstract

In this chapter, we investigated the gas-phase ion/ion reactions with those highly charged ions generated by ESI or nESI, and reported a type of ion/ion reaction that converts multiply charged protein ions to their opposite polarities with multiple charges. The reaction event only involves a single ion/ion collision while the charge-inversion reagents hold high enough charges derived from nESI. For multiply charged protein cations to anions, highly charged anions derived from nESI of hyaluronic acids (HAs) were used to achieve the purpose. This type of charge inversion reaction is demonstrated with cations derived from ubiquitin (Ub), cytochrome c (CytC), apo-myoglobin (aMb), and carbonic anhydrase (CA) cations. For example, the reaction has been demonstrated to convert the $[CA+22H]^{22+}$ carbonic anhydrase cation to a distribution of anions as high in absolute charge as $[CA-19H]^{19-}$. For the opposite polarity (protein anions to protein cations), the use of polyethylenimine (PEI) cations were used to charge invert Ub, CytC, and holo-myoglobin (hMb) anions into cations. Ion/ion reactions involving multiply charged ions of opposite polarity have previously been observed to result predominantly in the attachment of the reactant ions. All mechanisms for ion/ion charge inversion involving low energy ions proceed via the formation of a long-lived complex. Factors that underlie the charge inversion of protein ions to the opposite polarity with high charge states in reaction with those reagent ions are hypothesized to include: (i) the relatively high charge densities of the HA anions and PEI cations that facilitate the extraction/donation of multiple protons from/to the protein leading to multiply charged protein anions/cations, (ii) the relatively high sum of absolute charges of the reactants that leads to high initial energies in the ion/ion complex, and (iii) the relatively high charge of the ion/ion complex following the multiple proton transfers that tends to destabilize the complex.

3.1 Introduction

The application of mass spectrometry and tandem mass spectrometry to multiply-charged peptide and protein ions generated by electrospray ionization (ESI)[1] is commonplace in modern analytical mass spectrometry. The multiple-charging phenomenon has many practical effects in the application of mass spectrometry to several categories of analytes, including proteins. For example, the multiple charging phenomenon generally produces ions of relatively low *m/z*, which makes ESI amenable with mass analyzers where high *m/z* performance is limited. Furthermore, it is widely appreciated that favored dissociation pathways of precursor ions can be highly dependent on the charge state[2] such that complementary structural information can be obtained from dissociation of different charge states of the same molecule. For these and other reasons, it is sometimes desirable to manipulate the charge states of analyte ions. There is a variety of strategies for controlling the charges of protein ions. Solution-based approaches[3] involve, for example, altering pH or solvent composition, or adding so-called super-charging reagents.[4-5] Gas-phase approaches include one or sequential single-charge transfer reactions after ionization involving either gas-phase ion/molecule[6-7] or ion/ion chemistry.[8-11] Included among these, for example, are proton transfer applications for mixture analysis,[12-13] ion parking,[14] and product ion charge state determination in tandem mass spectrometry,[15-16] as well as electron transfer applications, which primarily involve structural characterization (i.e., electron transfer dissociation (ETD)).[17-18] Such single-charge transfer reactions take place via the use of neutral reagents with, for example, high proton affinities or gas-phase acidities or singly-charged reagent ions of opposite polarity.

Due to the high exothermicities of gas-phase ion/ion reactions, it is possible to reduce protein ion charge states to arbitrarily low values using sequential one-at-a-time proton transfer reactions with singly-charged reagent ions.[19] However, there are scenarios in which it is desirable that two or more charges transfer in a single collision. For example, sequential single-charge-transfer reactions are not suitable for changing the polarity of a gas phase ion. In order to change the polarity of a gas phase ion, there should be more than one charge change via a single collision to avoid neutralization of the analyte ion. For example, high energy collisions (e.g., keV collisions of relatively low mass ions) involving electronic transitions have been shown to lead to charge reversal of singly-charged ions via the ejection of two electrons.[20-21] However, charge reversal reactions induced by high energy collisions are relatively inefficient and compete with other more efficient processes, such as collision-induced dissociation (CID). An alternative approach is the

use of ion/ion reactions at relatively low translational energies using reagents that lead to two or more charge transfers in a single collision.[22-23] This has been effected using multiply-charged reagent ions leading to efficiencies of tens of percent.[23] Indeed, a number of applications have been developed for the charge inversion of singly-charged analyte ions, including, for example, those derived from oligonucleotides[24], polypeptides[25-27], and lipids,[28-29] using one or more of a variety of multiply-charged reagent anions.

The conversion of a multiply-charged protein to their opposite polarity and also with multiple charges via a single ion/ion encounter is reported here for the first time. The phenomenon was noted serendipitously while studying the ESI of highly charged homopolymers including hyaluronic acid (HA) and polyethlyenimine (PEI) mixtures. It is a surprising observation in that previous studies involving reactions of multiply-charged ions of opposite polarity have shown ion/ion attachment to dominate, sometimes competing with partial proton transfer.[30] The latter phenomenon is most likely to occur when the electrostatic repulsion in the cation is sufficiently high for proton transfer to occur via a curve-crossing mechanism within the electrostatically bound ion/ion capture orbit that does not involve an intimate collision. Large multiply-charged cations with relatively low internal electrostatic repulsion have been observed to react largely via attachment to large multiply-charged reactants of opposite polarity, at least when both reactants are proteins.[31] In fact, ion attachment in ion/ion reactions is a common observation and is maximized for reactants with large physical cross-sections, low relative charge, and functional groups in each reactant that can undergo relatively strong electrostatic interactions.[32] In this report, we demonstrate the conversion of multiply-protonated proteins to multiply-deprotonated proteins, and the other-way-round inversion of polarity via a single-collision event and discuss the mechanism and characteristics of the reactants that are most likely to lead to multiple proton transfer in a single collision with minimal ion attachment. The phenomena reported here point to a novel means for charge state manipulation that may serve as an alternative to single charge transfer or ion attachment events for charge state manipulation applications.

3.2 Experimental

3.2.1 Materials

All the protein standards, hyaluronic acids (HAs with different labeled molecular weight, MW=1155 Da, MW=8-15k, and MW=50k), linear polyethlyleneimine (PEI with different labeled molecular weight, MW=4k Da and MW=10k Da, and reported dpi = 1.3 and 1.5, respectively) and piperidine were purchased from Sigma-Aldrich (St. Louis, MO, U.S.A.). HA-dp18 (MW=3412 Da) was purchased from AMSBIO (Abingdon, UK). Optima LC-MS grade water and methanol (MeOH) was purchased from Fisher Scientific (Fair Lawn, NJ, U.S.A.). Acetic acid was purchased from Mallinckrodt (Phillipsburg, NJ, U.S.A.).

3.2.2 Sample preparation

Protein stock solutions were initially prepared by dissolving the powders in LC-MS grade water to a concentration around 1 mg-mL^{-1}. The working nano electrospray ionization (nESI) protein solutions were directly diluted from the stock solutions to 5 to 20 μM with either LC-MS grade water, to yield ions under near-neutral pH conditions, or in LC-MS grade water with 0.5 to 2%, v/v, acetic acid, or 0% to 2% v/v ammonium hydroxide, to give rise to denaturing conditions under positive or negative ion mode, respectively.

For BSA solution, a final concentration at 5 μM with 0 or 1% acetic acid (v/v) was prepared. Hyaluronic acid stock solutions were prepared by dissolving the lyophilized powders with water to a concentration of 1 mg-mL^{-1}, then further diluted with water to 0.1 to 0.01 mg mL^{-1} as the working nESI solutions. Polyethylenimine stock solution were prepared by dissolving the lyophilized powders with water/MeOH (9:1, v/v) to a concentration of 1 mg-mL^{-1}, then further diluted with the same solvent to 0.05 mg mL^{-1} as the working nESI solutions The negative nESI (-nESI) solution for denatured apo-myoglobin (aMb) was prepared by diluting the stock solution with water then further spiked piperidine to the solution at final 20 μM piperidine concentration.

3.2.3 Ion/Ion Mass Spectrometry

All experiments were performed on a Sciex^{TM} TripleTOF 5600 quadrupole time-of-flight mass spectrometer (Concord, ON, Canada) that has been modified for ion/ion reactions, similar to a previously described instrument,[33] using alternatively pulsed dual nano-electrospray ionization

(nESI) emitters.[34] Both anions and cations were formed via nano-electrospray ionization. The emitters were placed before the inlet aperture of the atmosphere vacuum interface. Targeted protein ions were firstly isolated in Q1 then transferred to q2. The reagent ions, including mixtures, were then injected, isolated in Q1, transferred to q2, and mutually stored in q2 for up to 50 ms for the gas phase ion/ion reaction.

3.3 Results and Discussion

3.3.1 Charge Inversion Phenomena

It is common for top-town proteomics approach to do the MS analysis with protein cations. Therefore, we will discuss the charge mainly with the starting protein polarity in positive ion mode. The main phenomena noted for the reaction of analyte ions with reagent ions of greater absolute charge are illustrated in the comparison of data shown in **Figures 3.1** and **3.2**. **Figure 3.1** summarizes the reaction of a multiply protonated polypeptide, the $[Ub+6H]^{6+}$ ion of ubiquitin (Ub), with a reagent anion of greater absolute charge, as represented by the apo-myoglobin (aMb) $[aMb-17H]^{17-}$ ion. **Figures 3.1A** and **3.1B** show the isolated cationic and anionic reactants, respectively, while **Figure 3.1C** shows the negative mode post-ion/ion reaction spectrum. The three most abundant peaks in **Figure 3.1C** are the residual unreacted $[aMb-17H]^{17-}$ ions, the attachment of a single $[Ub+6H]^{6+}$ ion to $[aMb-17H]^{17-}$ resulting in the $[aMB+Ub-11H]^{11-}$ complex, and the attachment of two $[Ub+6H]^{6+}$ ions to $[aMb-17H]^{17-}$ resulting in the $[aMB+2Ub-5H]^{5-}$ complex. The positive ion post-ion/ion reaction mass spectrum (**Figure 3.3**) showed small contributions of single proton transfers giving rise to lower charge states of ubiquitin that account for the smaller complex signals arising from $[aMb+Ub-12H]^{12-}$ and $[aMb+Ub-13H]^{13-}$, which result from the attachment of $[Ub+5H]^{5+}$ and $[Ub+4H]^{4+}$ to $[aMb-17H]^{17-}$, respectively. Likewise, sequential additions of ubiquitin cations, one or more of which have lower charge than $[Ub+6H]^{6+}$, are also observed. This experiment is fully consistent with previous observations of protein cations in reactions with protein anions in that the results predominantly show partial proton transfer, arising from proton transfers at crossing points along the energy surface, along with complex formation.[30,31] In this case, the charge states of the reactants are relatively low such that the attachment process dominates.

Figure 3.2 summarizes the phenomenon observed when the $[Ub+6H]^{6+}$ cation (isolated cation shown in Figure 3.2A) was allowed to react with a mixture of anions derived from a 50 kDa mixture of hyaluronic acid (HA) polymers primarily within the *m/z* range of 350-500 (isolated anions shown in **Figure 3.2B** for 20 ms. In this case, the post-ion/ion reaction negative ion spectrum shown in **Figure 3.2C** is dominated by a distribution of deprotonated ubiquitin charge states over the range $[Ub-7H]^{7-}$ to $[Ub-H]^{-}$ with little to no evidence for adduct formation. This experiment reflects the transfer of as many as 13 protons from the $[Ub+6H]^{6+}$ cation and suggests that these transfers largely occurred as a result of a single ion/ion encounter. (We note that the relative abundances of the ubiquitin product ions in both polarities was insensitive to reaction time over the range of up to 30 ms, which indicates that sequential ion/ion reactions played little role in the spectrum of **Figure 3.2C**).

3.3.2 Processes Arising from the Interaction of $[M+mH]^{m+}$ with $[R-nH]^{n-}$

The $[aMb-17H]^{17-}$ anions associated with **Figure 3.1** and the HA anions associated with **Figure 3.2** give rise to quite distinct product ion spectra. To clarify the origins of these differences in behavior, it is instructive to consider a generic interaction between two large multiply-charged ions of opposite polarity, $[M+mH]^{m+}$ and $[R-nH]^{n-}$, at low relative velocities. The rate determining step for gas-phase ion/ion reactions at low relative velocities involves the mutual capture of reactant ions into a stable orbit, the cross-section for which can be approximated by the Thomson three-body model[35-36]:

$$\sigma_{orb} \cong \frac{4\pi Z_1^2 Z_2^2 e^4}{(4\pi\epsilon_0 \mu v^2)^2} \quad \textbf{(eq. 3.1)}$$

where σ_{orb} is the cross-section (m^2) for formation of a Coulomb-bound orbit, Z_1 and Z_2 are the unit charges of the ions, e is the electron charge in Coulombs, υ is the relative velocity in m/s, μ is the reduced mass in kg and $1/(4\pi\varepsilon_0)$ is in units of $kg\text{-}m^3\text{-}s^{-2}\text{-}C^{-2}$. Once oppositely-charged ions are captured in their mutually attractive electric field, they can come into close proximity, depending upon the degree of eccentricity of the orbit, and the orbit can collapse due to tidal effects[37-38] and/or collisions to the point at which chemical interactions can take place. Under low energy conditions (e.g., thermal energies), the formation of a Coulomb-bound orbit is the rate-limiting process for an ion-ion reaction.[30]

There are two classes of chemical interactions that can take place when the distances between the ions become sufficiently low. The key category for the process of interest here is the formation of a long-lived complex, which we refer to as an attachment collision. The cross-section for an intimate or 'sticky' collision, σ_{att}, is estimated by:

$$\sigma_{att} \approx \pi r_{att}^2 \left[1 + \frac{2Z_1 Z_2 e^2}{4\pi\epsilon_0 r_{att} \mu v^2}\right] \textbf{(eq. 3.2)}$$

where r_{att} represents the distance for a physical collision between the oppositely charged reactant ions. The second category of interaction involves the transfer of a small charged particle, such as a proton or an electron, at a crossing point on the interaction surface. This type of reaction does not require the formation of a long-lived complex and can occur as a 'fly by' process. We distinguish between proton transfer at a crossing point versus within a long-lived complex by referring to the former as a proton 'hop'. (We are concerned here with proton transfer at a crossing point as no evidence for electron transfer has been noted in this work.) The cross-section for proton hopping can be estimated by:

$$\sigma_{hop} \approx P_{rxn} \pi r_{PT}^2 \left[1 + \frac{2Z_1 Z_2 e^2}{4\pi\epsilon_0 r_{PT} \mu v^2}\right] \textbf{(eq. 3.3)}$$

where r_{PT} is the distance between reactants at which proton transfer can occur, which can be estimated as the point at which the energy surfaces of the reactants and products cross:

$$r_{PT} \approx \frac{Z_1 Z_2 e^2}{4\pi\epsilon_0 \Delta H_{PT}} \textbf{(eq. 3.4)}$$

where ΔH_{PT} is the enthalpy for proton transfer in Joules. The P_{rxn} term in **equation 3.3** is the probability that the proton will transfer at the crossing point. This term is difficult to determine *a priori* and, given that this process is a side-reaction with respect to the process of interest in this work, is not addressed further herein. We note that it is possible for a proton hop to occur at a crossing point with subsequent intimate collision to give rise to a long-lived complex. Such a process cannot be distinguished from the direct formation of a long-lived complex. The likelihood for the observance of 'fly by' proton transfer products, $\sigma_{fly\ by}$ is therefore related to the difference between the cross-sections of **equations 3.2** and **3.3**, i.e.:

$$\sigma_{fly\ by} \approx \sigma_{hop} - \sigma_{att} \textbf{(eq. 3.5)}$$

We finally note that multiple proton hopping reactions can occur within an orbiting complex before the products escape from the orbit due to the reduction of the mutual attraction. This gives rise to a distribution of partial neutralization products, as observed in **Figure 3.3**.

The preceding discussion provides context for considering the differences in behaviors of the two reagent species associated with **Figures 3.1** and **3.2**. It is important to recognize that charge inversion to absolute charge states greater that one via a one-charge-a-time process is highly unlikely. Proton transfer via hopping takes place one-at-a-time with each transfer giving rise to a significant change in the interaction potential. Once one of the reactants is fully neutralized, the interaction potential is that of an ion/molecule interaction and the long range Coulomb attraction of the ion/ion interaction is no longer present. If there is substantial relative velocity in the orbiting complex when one of the reactants is neutralized, it is likely that the ion and neutral will fly apart without undergoing an ion/molecule proton transfer, even if the ΔH_{PT} for the ion/molecule reaction were to be favorable. In the unlikely event that another proton transfer were to occur via an ion/molecule collision, both products would be of like charge thereby precluding further charge transfers. The formation of multiply-deprotonated ubiquitin from multiply-protonated ubiquitin via a single ion/ion encounter, as suggested in **Figure 3.2**, can only occur through a long-lived complex that allows for multiple proton transfers in a single collision. A kinetic scheme that summarizes the processes discussed here is provided in **Scheme 3.1**, which includes the break-up of the collision complex into various partitions of charge between the complex components. The dissociation of the initially formed long-lived ion/ion complex, represented by $[M+R-(n-m)H]^{(n-m)-*}$ in **Scheme 3.1**, is indicated by the dissociation reactions with rate constants indicated as k_{diss}. The processes that lead to charge inversion via ion attachment are indicated with blue arrows whereas the processes that lead to charge inversion via multiple proton transfers are indicated with red arrows.

The charge inversion of the ubiquitin ions reflected in **Figures 3.1** and **3.2**, either via attachment or multiple proton transfer, is expected to take place via long-lived complex formation. The difference in the results from the different charge inversion reagents is therefore determined by the fate of the long-lived complex. Generic energy diagrams are provided in **Figure 3.4** that compare qualitatively the role of the total electric field associated with the reactions of oppositely charged ions in which the charge of the reagent anion exceeds that of the cation. Two cases are illustrated with the total charge of the reagent anion differing by a factor of two. This difference leads to a greater degree of initial potential energy for the more highly charged reagent as well as a greater degree of electrostatic repulsion in the intermediate. For comparison, the entrance channels are normalized to zero energy. The blue lines relate to the reaction of $[M+mH]^{m+}$ with

$[R-nH]^{n-}$ and the red line relates to the reaction of $[M+mH]^{m+}$ with $[R-2nH]^{2n-}$. The total energy in the complex for thermalized reactants is largely determined by the Coulombic attraction of the reactants, as determined by the magnitudes of the reactant charges. This is augmented by the interactions that form between the reactants (e.g., non-covalent ion/dipole, dipole/dipole, etc.) by virtue of the intimate collision. The lifetime of the complex is determined by the initial total internal energy within the complex and the various exit channel barriers associated with the variety of charge partitioning that can arise upon the dissociation of the complex. The likelihood that the complex survives to be observed experimentally is determined by the lifetime of the complex and the cooling rates (collisional and radiative). In the case of **Figure 3.1C**, most, if not all, of the initially formed complexes survived and could be observed. In the case of **Figure 3.2C**, essentially none of the initially formed complexes survived. The former scenario is more likely for the blue line energy surface whereas the latter is more likely with the red line surface. Regardless of the chemical nature of the reagent anion, e.g., protein versus carbohydrate, increasing the charge of the reagent increases the potential energy of the system as reflected in the comparison of **Figure 3.4**.

The characteristics of the reagent anions determine the fate of the initially formed ion/ion complexes with $[Ub+6H]^{6+}$. The HA anions and the aMb anions differ in two important ways: i) the HA anions (*m/z* 350-500) have higher charge densities than the aMb anions (*m/z* 996) and ii) the aMb ions can engage in a wider array of electrostatic interactions due to the greater diversity of functional groups associated with the amino acid side-chains. The former difference alone may underlie the different reagent anion behavior (see **Figure 3.4**). HAs are comprised of 379 Da disaccharide (glucuronic acid and N-acetylglucosamine bound via a β-1,4 linkage, **Figure 3.5A** repeating units with a single carboxylic acid per monomer. We have found that is it possible to generate HA anions in which most, and often all, of the carboxylic acid groups are deprotonated. The largest single n-mer sample of a hyaluronic acid-related molecule that we could purchase was HA-dp18, which lacks one –OH group on the non-reducing end sugar. **Figure 3.5B** shows the negative ion nESI mass spectrum of HA-dp18 (MW=3412 Da), which is dominated by the fully deprotonated $[HA\text{-}dp18-9H]^{9-}$ ion. Unfortunately, larger single n-mer HA oligomers are not commercially available. For this reason, it is difficult to study the charge inversion reactivity of single well-defined HA n-mers of defined charge state, in contrast with, for example, a charge state of a specific protein. The mass spectra of HA mixtures are generally highly complex as they are

comprised of mixtures of n-mers, charge states, and fragments derived therefrom. However, by mass-selecting portions of the HA anion distributions within the range of roughly m/z 350-500, ions with a charge on every or nearly every n-mer are selected from the distribution. The fact that prominent signals in the region of m/z 350-500 are observed for every HA distribution used in this work indicates that it is possible to generate "highly charged" HA anions of various sizes and charges. In contrast, it is difficult to generate such highly charged protein anions as the *m/z* values are generally a factor of 2-4 greater than those of the fully charged HA anions.

3.3.3 Experimental Evidence for the Role of Reagent Anion in Leading to Charge Inversion via Ion Attachment versus Multiple-Proton Transfer

As indicated above, efficient charge inversion must take place via the formation of a relatively long-lived complex, as sequential individual proton transfer reactions lead to neutralization. Fragmentation of the complex can lead to charge states of the analyte of opposite polarity to those of the initial reactant ions and stabilization of the ion/ion complex can lead to the observation of adduction products. Protein reagent anions have been observed to lead to charge inversion largely via adduct formation. This is further illustrated in **Figure 3.6**, which shows the negative ion post-ion/ion reaction spectrum of $[Ub+6H]^{6+}$ with a range of apo-myoglobin anion charge states (viz., $[aMb-18H]^{18-}$ to $[aMb-13H]^{13-}$). The products are dominated by adducts of ubiquitin with apo-myoglobin (i.e. $[aMb+Ub-nH]^{n-}$, where n = 12 to 7).

The highly charged anions derived from the HA 50k sample (**Figure 3.2C**), gave rise to essentially no adduct formation. We therefore reacted $[Ub+6H]^{6+}$ cations with a series of HA-related anions of relatively modest charge to evaluate the competition between adduct formation and stabilization versus adduct formation and breakup. We generated HA anions from a 8k-15k mixture and selected fully charged anions with 7 to 12 charges. It is very difficult to isolate fully charged ions from a homopolymer distribution due to the fact that all ions have similar *m/z* ratios. Therefore, in order to be able to isolate each charge state, we selected from fragment ions observed in the mass spectrum generated from the loss of the reducing-end terminal sugar. In the carbohydrate fragmentation lexicon, these fragment ions are referred to as C-ions.[39] These ions have a whole number of di-sugar monomers plus one additional glucuronic acid sugar. The relevant C-ion from $[HA22-11H]^{11-}$, for example, is denoted here as $[HA21-11H]^{11-}$. The post-ion/ion reaction negative ion spectrum from the reaction of $[Ub+6H]^{6+}$ with $[HA17-9H]^{9-}$ is

shown in **Figure 3.7A**. A prominent peak associated with complex formation, viz. $[HA17+Ub-3H]^{3-}$, is observed, which reflects the attachment of the oppositely charged reactants. A series of charge-reduced HA17 peaks are also observed, at least some of which arise from proton hopping. Prominent signals for $[HA17-3H]^{3-}$, $[HA17-2H]^{2-}$, and $[HA17-H]^{-}$ can also arise, at least in part, from the break-up of $[HA17+Ub-3H]^{3-}$. Relatively small signals corresponding to $[Ub-3H]^{3-}$, $[Ub-2H]^{2-}$, and $[Ub-H]^{-}$, suggest the formation of the complex with rapid cleavage to give the charge-inverted ubiquitin ions. **Figure 3.7B** shows a plot that summarizes the ratio (areas under the peaks) of ubiquitin anions/adduct anions as a function of the HA-related anion charge states. (The spectra used to generate this plot are shown in **Figure 3.7A** and in **Figures 3.8** to **3.11**.) The degree of charge inversion via multiple proton transfer relative to adduct formation increases monotonically with the charge of the HA anions. This general trend is consistent with the hypothesis that use of highly charged reagent anions lead to the formation of highly charged complexes which facilitates dissociation of the complex with charge partitioning between the reagent and analyte (see **Figure 3.4**). Protein reagent anions react predominantly via proton hopping and formation of a stable ion/ion complex whereas highly charged HA anions, while also reacting via hopping, lead to the generation of highly charged ion/ion complexes that dissociate via the pathways denoted as k_{diss} in **Scheme 1**.

3.3.4 Charge Inversion of Larger Protein Cations

The phenomenon illustrated above for $[Ub+6H]^{6+}$ appears to be general, at least for protein cations of moderate size. We reacted the highly charged (*m/z* 350-500) HA anions with a range of protein cations and observed extensive charge inversion via multiple proton transfers from a single collision. **Figure 3.12**, for example, shows data for reactions with cytochrome *c* $[CytC+15H]^{15+}$ (**Figure 3.12A**), apo-myoglobin (aMb) $[aMb+17H]^{17+}$ (**Figure 3.12B**), and carbonic anhydrase (CA) $[CA+22H]^{22+}$ (**Figure 3.12C**). The isolated cationic reactants are shown in **Figures 3.13A** to **3.13C**. These protein cations were converted to anions with the highest negative charge states at 7^{-}, 11^{-}, and 19^{-}, respectively. Remarkably, as many as 41 charges were changed in CA. In each case, a distribution of anionic charge states was generated. Interestingly, there appears to be at least two overlapping charge state distributions in the case of the apo-myoglobin experiment and perhaps in the carbonic anhydrase data as well. It is not surprising that a single cationic charge

state is converted to a distribution of anionic charge states in these experiments. The experiment involves a mixture of reagent anions with various charges, the possible convolution of sequential proton hopping reactions followed by complex formation, and a range of charge partitioning upon breakup of a multiply-charged complex.[40]

We note that larger proteins of greater charge, e.g. the bovine serum albumin (BSA) $[BSA+40H]^{40+}$ did not show charge inversion via multiple proton transfer with the HA 50k anions used to generate the data of **Figure 3.12**. To ensure the charges are enough for the charge inversion, $[BSA+nH]^{n+}$ (n = 13-17) cations are used and complex ions both in the positive and negative ion polarities were observed, which indicates ion attachment as the major mechanism while reacting BSA with HAs (**Figure 3.14**). This is likely due in part to insufficient negative charge in the reagent anion population. However, the size of the protein, which is a factor in determining the lifetime of the initially formed complex, may also play a role.

3.3.5 Charge Inversion of Protein Anions

A similar charge inversion reaction could be utilized for the opposite polarity, from multiple charge protein anions to multiple charge protein cations. To demonstrate, polyethylenimine (PEI) mixtures are used as the charge inversion reagent, which we can also generate highly charge density of the protonated PEI through the nESI process (Chapter 2 and **Figure 3.15B**). One of the major differences between HA and PEI reagent is that the highest degrees of protonation on PEI are about one charge every six monomers, but HA can be deprotonated every monomer. However, the observed charge density of PEI ions is slightly greater than HA (m/z 260 comparing to m/z 350, **Figure 3.15B** v.s. **Figure 3.2B**). **Figure 3.15** shows the charge inversion reaction between $[Ub-5H]^-$ and mass-selected PEI window (m/z 260-262). As we expected, the post-ion/ion reaction spectrum shows only simply charge-inverted ubiquitin cation (protonated ubiquitin, $[Ub+nH]^{n+}$, n= 1 to 5, **Figure 3.15C**). The result suggested a similar reaction is also true for charge-inverting multiply-charged protein anion to protein cations.

To further test the limits of the charge inversion reactions with PEI cations, we performed the reactions using the same PEI ion population (**Figure 3.15B**) with $[CytC-6H]^{6-}$ and $[hMb-7H]^{7-}$, and we were able to invert the charge to either 4+ or 5+ respectively, which a total 12 charges were changed (**Figure 3.16**). However, we are not able to perform the charge inversion reaction with

higher charge states of aMb anions (e.g. $[aMb-10H]^{10-}$), and instead, we mainly observed ion attachment product (data not shown), which agrees with our observation with the reaction using HA and BSA. Therefore, we concluded that the PEI that we used might not have as high charge states as HA, so we could not invert similar degrees of charges using PEI to HA. We are currently investigating other reagents to be the charge inversion reagent for inverting protein anions into cations, and several reagents showed similar effects as PEI, including polyallylamine and polylysine (data not shown). However, PEI still holds the best record for converting multiply charged protein anions into cations. Other future work is also proposed, including eliminating the possible in-source/in-instrument fragmentation of those high charge densities of ions, so that we can perform the reactions with those highly charged reagent ions, but not the fragments that we mentioned in the earlier chapter and sections.

3.4 Conclusions

In this work, we note the first observation of the charge inversion of a multiply protonated protein to a multiply deprotonated protein via gas-phase ion/ion reactions. Evidence for the transfer of as many as 41 protons was provided for the reaction of the carbonic anhydrase $[CA+22H]^{22+}$ ion in yielding the $[CA-19H]^{19-}$ ion. This phenomenon was observed using multiply-charged anions derived from hyaluronic acid in which most, if not all, of the carboxylic acid groups in the polymer were deprotonated. The reaction in the opposite polarity (viz. deprotonated protein to protein cations with protonated polyethylenimine) was also observed. While this observation is novel, it is consistent with the overall picture for ion/ion reactions involving multiply-charged ions of opposite polarity. Previous studies have reported combinations of proton hopping and ion attachment when reactants were oppositely charged proteins. We hypothesize that the current observations also arise from the formation of relatively highly charged complexes upon protein cation/anion attachment to highly charged hyaluronic acid anions/polyethylenimine followed by spontaneous Coulomb-assisted cleavage of the complex to yield the multiply charged proteins with opposite polarities, along with charge-reduced reagent ions. While extensive charge inversion via multiple proton transfer was observed for cations of ubiquitin, cytochrome *c*, and myoglobin, in addition to carbonic anhydrase, mostly ion attachment was seen with cations of bovine serum albumin with the anions used in this study. In the opposite

polarity, anions of ubiquitin, cytochrome *c*, and myoglobin were charge inverted. We are interested in exploring the limits of this variation of charge inversion chemistry in terms of both the characteristics of the protein cations and the reagent anions, and vice versa. The discovery and optimization of such reagents may enable the development of novel charge inversion applications in biological mass spectrometry.

3.5 Acknowledgement

This work was supported by the National Institutes of Health (NIH) under Grant R37-GM45372.

3.6 References

1. Fenn, J. B.; Mann, M.; Meng, C. K.; Wong, S. F.; Whitehouse, C. M., Electrospray Ionization for Mass Spectrometry of Large Biomolecules. Science 1989, 246 (4926), 64-7.
2. Hogan, J. M.; McLuckey, S. A., Charge state dependent collision-induced dissociation of native and reduced porcine elastase. J Mass Spectrom 2003, 38 (3), 245-256.
3. Muddiman, D. C.; Cheng, X.; Udseth, H. R.; Smith, R. D., Charge-state reduction with improved signal intensity of oligonucleotides in electrospray ionization mass spectrometry. J Am Soc Mass Spectrom 1996, 7 (8), 697-706.
4. Iavarone, A. T.; Williams, E. R., Mechanism of Charging and Supercharging Molecules in Electrospray Ionization. J Am Chem Soc 2003, 125 (8), 2319-2327.
5. Yin, S.; Loo, J. A., Top-down mass spectrometry of supercharged native protein–ligand complexes. Int J Mass spectrom 2011, 300 (2), 118-122.
6. McLuckey, S. A.; Van Berkel, G. J.; Glish, G. L., Reactions of dimethylamine with multiply charged ions of cytochrome c. J Am Chem Soc 1990, 112 (14), 5668-5670.
7. Williams, E. R., Proton Transfer Reactivity of Large Multiply Charged Ions. J Mass Spectrom 1996, 31 (8), 831-842.
8. Foreman, D. J.; McLuckey, S. A., Recent Developments in Gas-Phase Ion/Ion Reactions for Analytical Mass Spectrometry. Anal Chem 2020, 92 (1), 252-266.
9. Prentice, B. M.; McLuckey, S. A., Gas-phase ion/ion reactions of peptides and proteins: acid/base, redox, and covalent chemistries. Chem Commun 2013, 49 (10), 947-965.
10. Pitteri, S. J.; McLuckey, S. A., Recent developments in the ion/ion chemistry of high-mass multiply charged ions. Mass Spectrom Rev 2005, 24 (6), 931-958.
11. McLuckey, S. A.; Stephenson, J. L., Ion/ion chemistry of high-mass multiply charged ions. Mass Spectrom Rev 1998, 17 (6), 369-407.

12. Stephenson, J. L.; McLuckey, S. A., Ion/Ion Reactions for Oligopeptide Mixture Analysis: Application to Mixtures Comprised of 0.5–100 kDa Components. J Am Soc Mass Spectrom 1998, 9 (6), 585-596.

13. Ugrin, S. A.; English, A. M.; Syka, J. E. P.; Bai, D. L.; Anderson, L. C.; Shabanowitz, J.; Hunt, D. F., Ion-Ion Proton Transfer and Parallel Ion Parking for the Analysis of Mixtures of Intact Proteins on a Modified Orbitrap Mass Analyzer. J Am Soc Mass Spectrom 2019, 30 (10), 2163-2173.

14. McLuckey, S. A.; Reid, G. E.; Wells, J. M., Ion Parking during Ion/Ion Reactions in Electrodynamic Ion Traps. Anal Chem 2002, 74 (2), 336-346.

15. McLuckey, S. A.; Glish, G. L.; Van Berkel, G. J., Charge determination of product ions formed from collision-induced dissociation of multiply protonated molecules via ion/molecule reactions. Anal Chem 1991, 63 (18), 1971-1978.

16. Stephenson, J. L.; McLuckey, S. A., Simplification of Product Ion Spectra Derived from Multiply Charged Parent Ions via Ion/Ion Chemistry. Anal Chem 1998, 70 (17), 3533-3544.

17. Syka, J. E. P.; Coon, J. J.; Schroeder, M. J.; Shabanowitz, J.; Hunt, D. F., Peptide and protein sequence analysis by electron transfer dissociation mass spectrometry. Proc Natl Acad Sci U S A 2004, 101 (26), 9528-9533.

18. Riley, N. M.; Coon, J. J., The Role of Electron Transfer Dissociation in Modern Proteomics. Anal Chem 2018, 90 (1), 40-64.

19. Stephenson, J. L.; McLuckey, S. A., Ion/Ion Reactions in the Gas Phase: Proton Transfer Reactions Involving Multiply-Charged Proteins. J Am Chem Soc 1996, 118 (31), 7390-7397.

20. Danell, A. S.; Glish, G. L., Charge permutation reactions in beam type mass spectrometers. Int J Mass spectrom 2001, 212 (1), 219-227.

21. Hayakawa, S., Internal energy distribution in charge inversion mass spectrometry using alkali metal targets. Int J Mass spectrom 2001, 212 (1), 229-247.

22. Loo, R. R. O.; Udseth, H. R.; Smith, R. D., Evidence of charge inversion in the reaction of singly charged anions with multiply charged macroions. J Phys Chem 1991, 95 (17), 6412-6415.

23. He, M.; McLuckey, S. A., Two Ion/Ion Charge Inversion Steps To Form a Doubly Protonated Peptide from a Singly Protonated Peptide in the Gas Phase. J Am Chem Soc 2003, 125 (26), 7756-7757.

24. He, M.; McLuckey, S. A., Increasing the Negative Charge of a Macroanion in the Gas Phase via Sequential Charge Inversion Reactions. Anal Chem 2004, 76 (14), 4189-4192.

25. Hassell, K. M.; Stutzman, J. R.; McLuckey, S. A., Gas-Phase Bioconjugation of Peptides via Ion/Ion Charge Inversion: Schiff Base Formation on the Conversion of Cations to Anions. Anal Chem 2010, 82 (5), 1594-1597.

26. He, M.; Emory, J. F.; McLuckey, S. A., Reagent Anions for Charge Inversion of Polypeptide/Protein Cations in the Gas Phase. Anal Chem 2005, 77 (10), 3173-3182.

27. Stutzman, J. R.; Luongo, C. A.; McLuckey, S. A., Covalent and non-covalent binding in the ion/ion charge inversion of peptide cations with benzene-disulfonic acid anions. J Mass Spectrom 2012, 47 (6), 669-675.

28. Rojas-Betancourt, S.; Stutzman, J. R.; Londry, F. A.; Blanksby, S. J.; McLuckey, S. A., Gas-Phase Chemical Separation of Phosphatidylcholine and Phosphatidylethanolamine Cations via Charge Inversion Ion/Ion Chemistry. Anal Chem 2015, 87 (22), 11255-11262.

29. Randolph, C. E.; Foreman, D. J.; Betancourt, S. K.; Blanksby, S. J.; McLuckey, S. A., Gas-Phase Ion/Ion Reactions Involving Tris-Phenanthroline Alkaline Earth Metal Complexes as Charge Inversion Reagents for the Identification of Fatty Acids. Anal Chem 2018, 90 (21), 12861-12869.

30. Wells, J. M.; Chrisman, P. A.; McLuckey, S. A., Formation and Characterization of Protein−Protein Complexes in Vacuo. J Am Chem Soc 2003, 125 (24), 7238-7249.

31. Gunawardena, H. P.; McLuckey, S. A., Synthesis of multi-unit protein hetero-complexes in the gas phase via ion–ion chemistry. J Mass Spectrom 2004, 39 (6), 630-638.

32. Bu, J.; Peng, Z.; Zhao, F.; McLuckey, S. A., Enhanced Reactivity in Nucleophilic Acyl Substitution Ion/Ion Reactions Using Triazole-Ester Reagents. J Am Soc Mass Spectrom 2017, 28 (7), 1254-1261.

33. Xia, Y.; Chrisman, P. A.; Erickson, D. E.; Liu, J.; Liang, X.; Londry, F. A.; Yang, M. J.; McLuckey, S. A., Implementation of Ion/Ion Reactions in a Quadrupole/Time-of-Flight Tandem Mass Spectrometer. Anal Chem 2006, 78 (12), 4146-4154.

34. Xia, Y.; Liang, X.; McLuckey, S. A., Pulsed Dual Electrospray Ionization for Ion/Ion Reactions. J Am Soc Mass Spectrom 2005, 16 (11), 1750-1756.

35. Thomson, J. J., XXIX. Recombination of gaseous ions, the chemical combination of gases, and monomolecular reactions. The London, Edinburgh, and Dublin Philosophical Magazine and Journal of Science 1924, 47 (278), 337-378.

36. Mahan, B. H., Recombination of Gaseous Ions. In Adv Chem Phys, 1973; pp 1-40.

37. Bates, D. R.; Morgan, W. L., New recombination mechanism: Tidal termolecular ionic recombination. Phys Rev Lett 1990, 64 (19), 2258-2260.

38. Morgan, W. L.; Bates, D. R., Tidal termolecular ionic recombination. J Phys B: At Mol Opt Phys 1992, 25 (24), 5421-5430

39. Domon, B.; Costello, C. E., A systematic nomenclature for carbohydrate fragmentations in FAB-MS/MS spectra of glycoconjugates. Glycoconjugate J 1988, 5 (4), 397-409.

40. Jurchen, J. C.; Williams, E. R., Origin of Asymmetric Charge Partitioning in the Dissociation of Gas-Phase Protein Homodimers. J Am Chem Soc 2003, 125 (9), 2817-2826.

3.7 Scheme and Figures

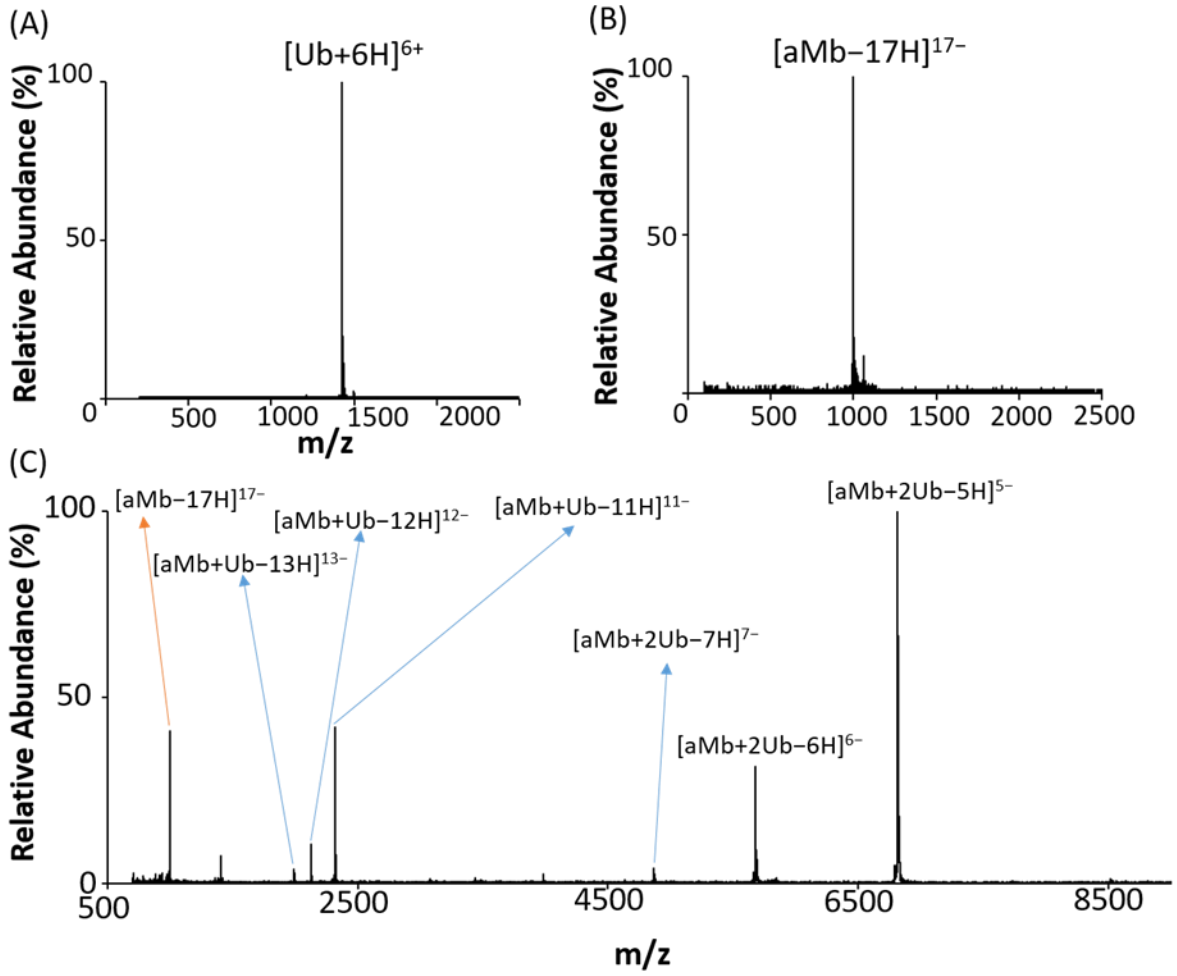

Figure 3.1. (A) The +nESI spectrum of isolation of protonated ubiquitin, $[Ub+6H]^{6+}$. (B) The –nESI spectrum of deprotonated apo-myoglobin, $[aMb-17H]^{17-}$. (C) The mass spectrum after gas phase ion/ion reaction. The different protein-protein complex anions were observed with different charge states. The ubiquitin was prepared as the procedures in experimental section with a final concentration at 20 μM in LC-MS graded water.

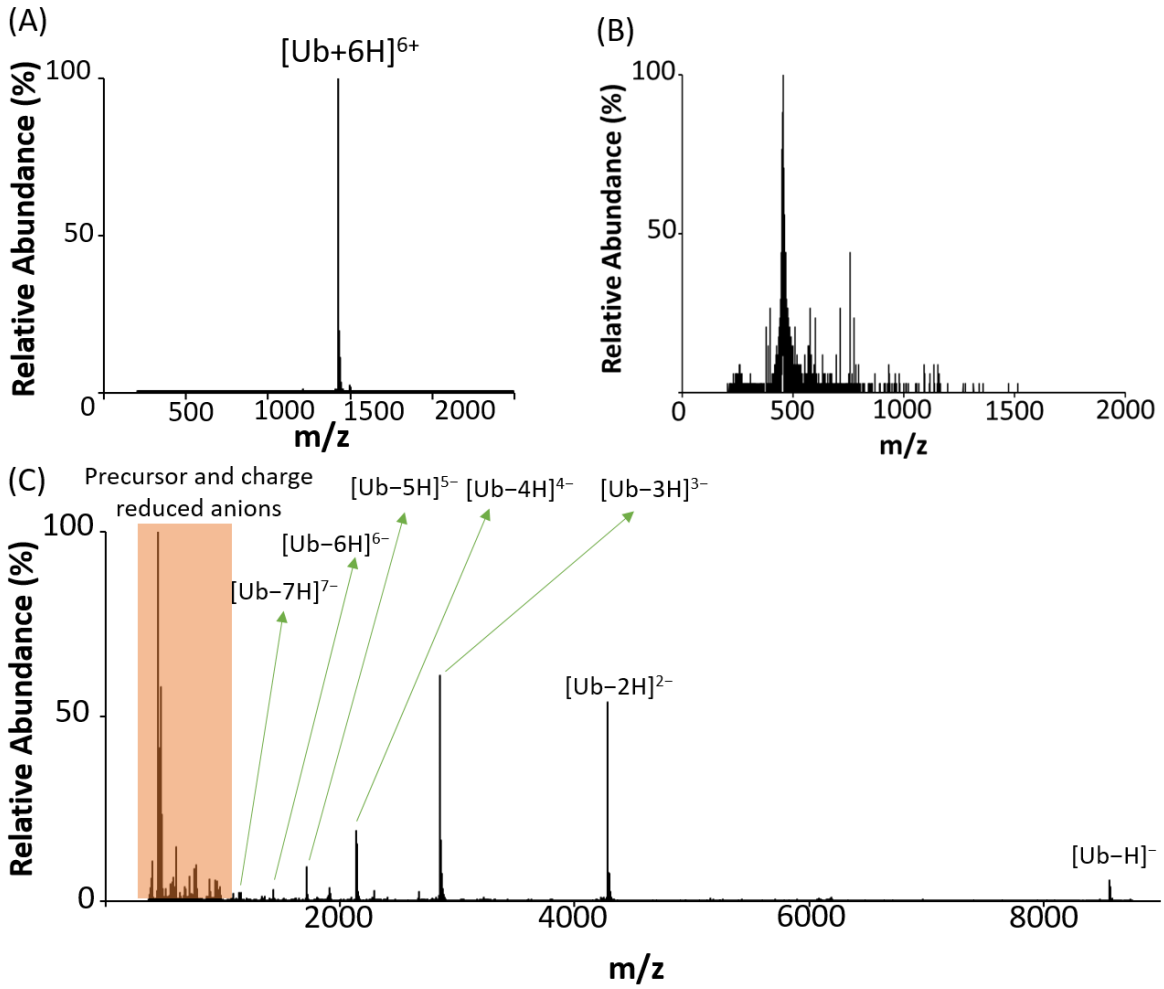

Figure 3.2. (A) The +nESI spectrum of isolation of protonated ubiquitin, $[Ub+6H]^{6+}$. (B) The –nESI spectrum of wide isolation of the HA 50k mixture. (C) The mass spectrum after gas phase ion/ion reaction. The charge-inverted ubiquitin anions were observed with different charge states. The same condition of ubiquitin solution as in **Figure 3.1** was used.

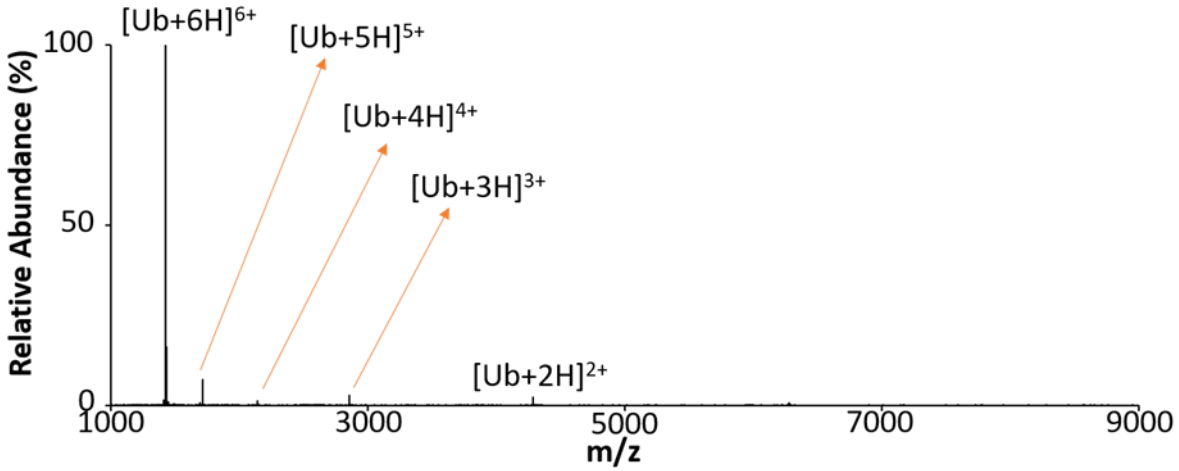

Figure 3.3. The post-ion/ion reaction mass spectrum of $[Ub+6H]^{6+}$ reacted with $[aMb-17H]^{17-}$ in positive mode.

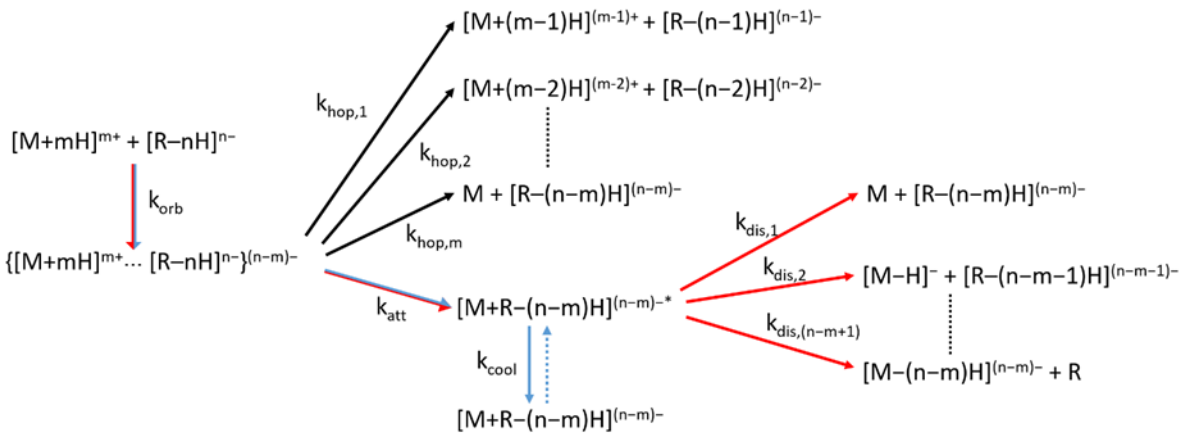

Scheme 3.1. Kinetic scheme that summarizes processes associated with ion/ion reactions between $[M+mH]^{m+}$ and $[R-nH]^{n-}$ where $|n| > |m|$. Blue arrows indicate steps that lead to charge inversion via adduct formation, red arrows indicate steps that lead to charge inversion via multiple proton transfers, and black arrows indicate proton transfers at crossing points on the energy surface. The latter processes constitute side reactions when charge inversion is the objective.

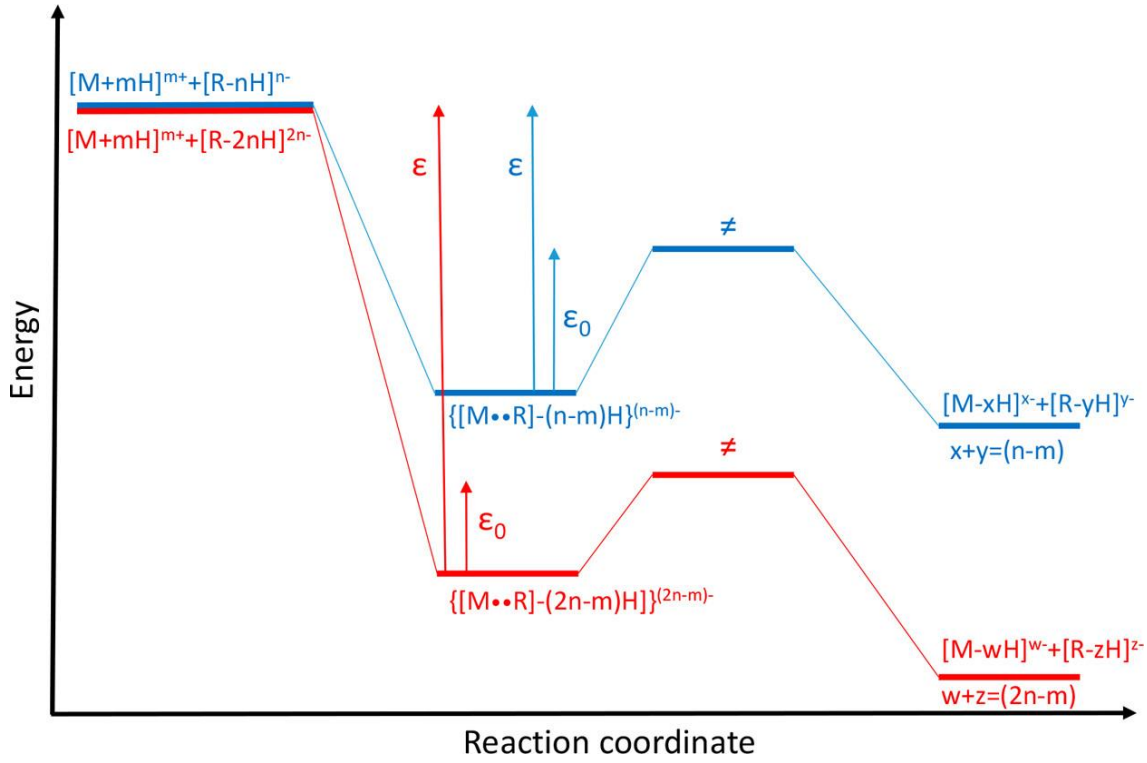

Figure 3.4. Qualitative energy diagrams for the reaction of $[M+nH]^{n+}$ with $[R-nH]^{n-}$ (blue lines) and for the reaction of $[M+nH]^{n+}$ with $[R-2nH]^{2n-}$ (red lines). The ≠ symbols represent the transition states for the charge partitioning channels arising from break-up of the complex.

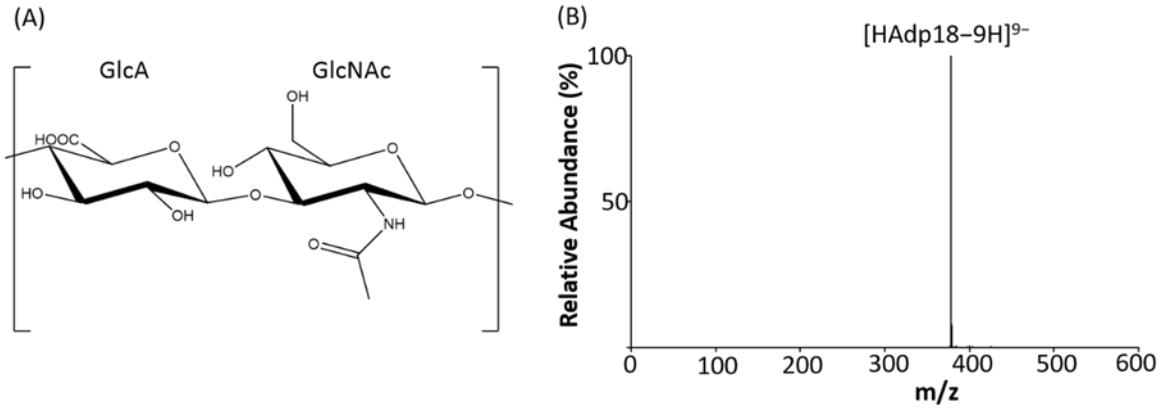

Figure 3.5. (A) The repeating unit of HA and (B) the −nESI spectrum of HA-dp18 (MW=3412 Da).

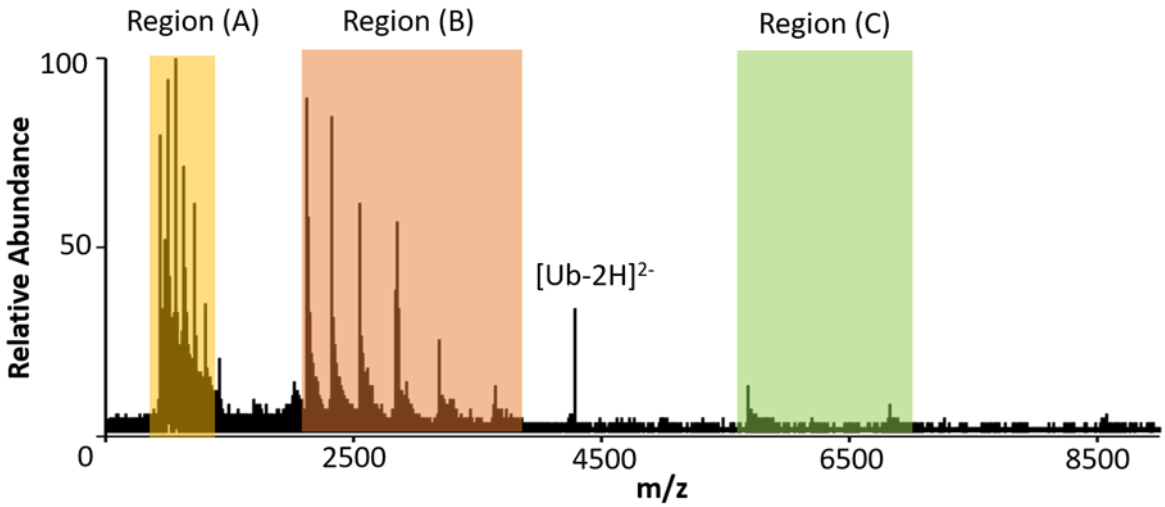

Figure 3.6. The mass spectrum of post-ion/ion reaction of deprotonated apo-myoglobin anions and protonated ubiquitin ($[Ub+6H]^{6+}$). Region (A) is the precursor anions of the deprotonated apo-myoglobin at different charge states from 18− to 13−; Region (B) is the product ions of protein-protein complexes anions ($[aMb+Ub-nH]^{n-}$, n =12 to 7); Region (C) is the protein-protein complexes anions with 2 ubiquitins in the complexes ($[aMb+2Ub-mH]^{m-}$, m= 6 or 5).

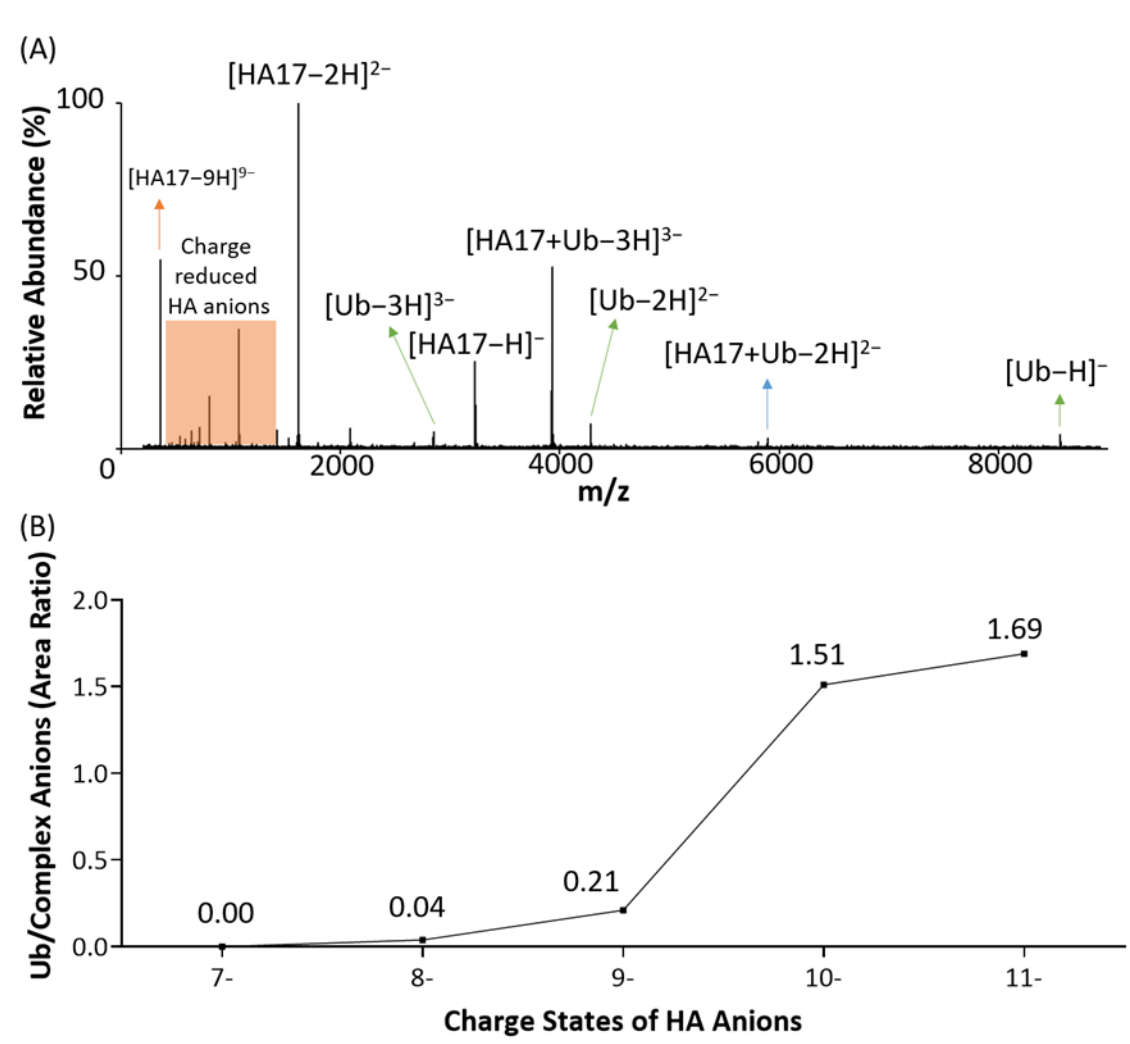

Figure 3.7. (A) The mass spectrum of post-ion/ion reaction of HA17 anion ($[HA17-9H]^{9-}$ and protonated ubiquitin $[Ub+6H]^{6+}$). (B) The integrated area-under-the-peak ratio of the ubiquitin anions to protein-HA complex anions while using different HA anions as the charge inversion reagent reacting with $[Ub+6H]^{6+}$.

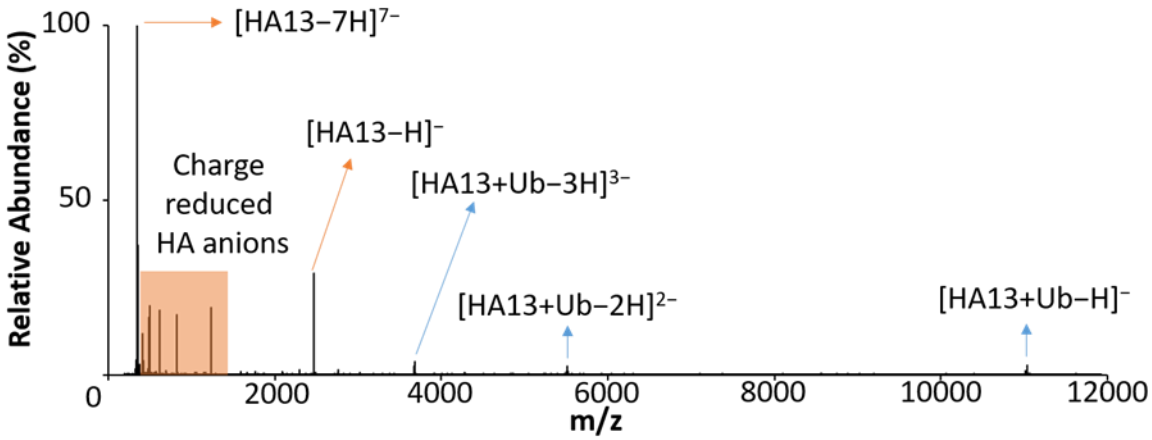

Figure 3.8. The post-ion/ion reaction mass spectrum of $[Ub+6H]^{6+}$ reacted with $[HA13-7H]^{7-}$ (MW=2469) in negative mode.

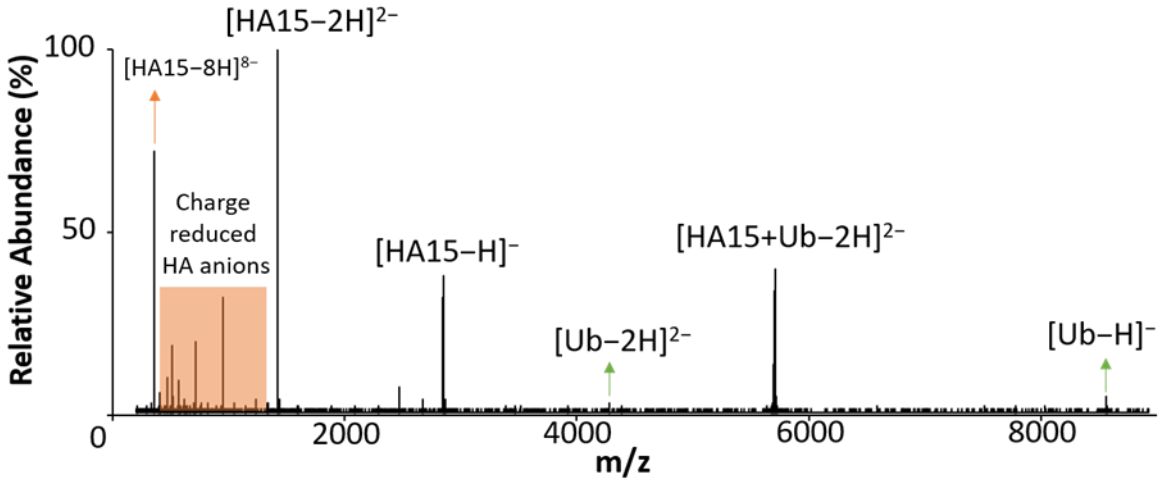

Figure 3.9. The post-ion/ion reaction mass spectrum of $[Ub+6H]^{6+}$ reacted with $[HA15-8H]^{8-}$ (MW=2848) in negative mode.

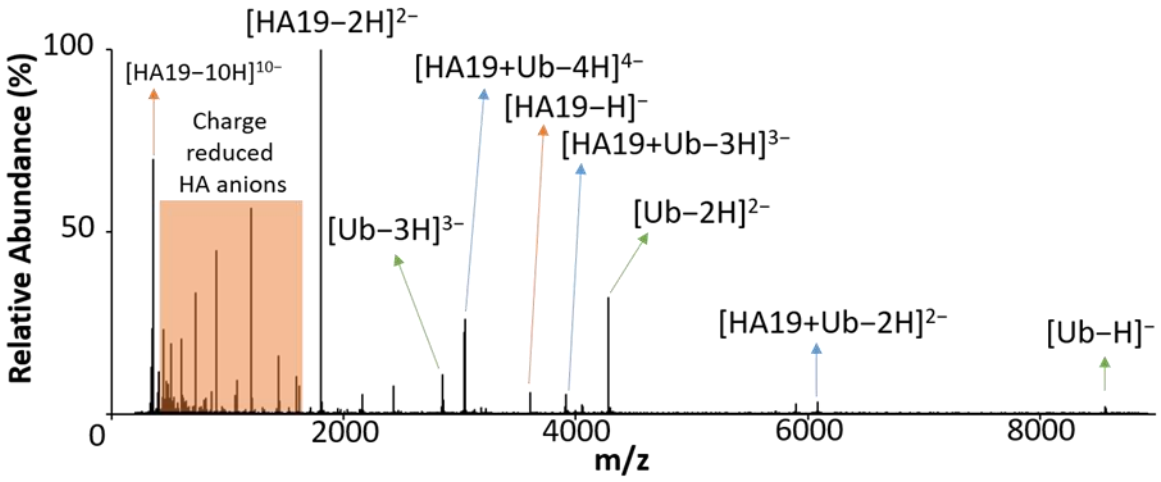

Figure 3.10. The post-ion/ion reaction mass spectrum of $[Ub+6H]^{6+}$ reacted with $[HA19-10H]^{10-}$ (MW=3606) in negative mode.

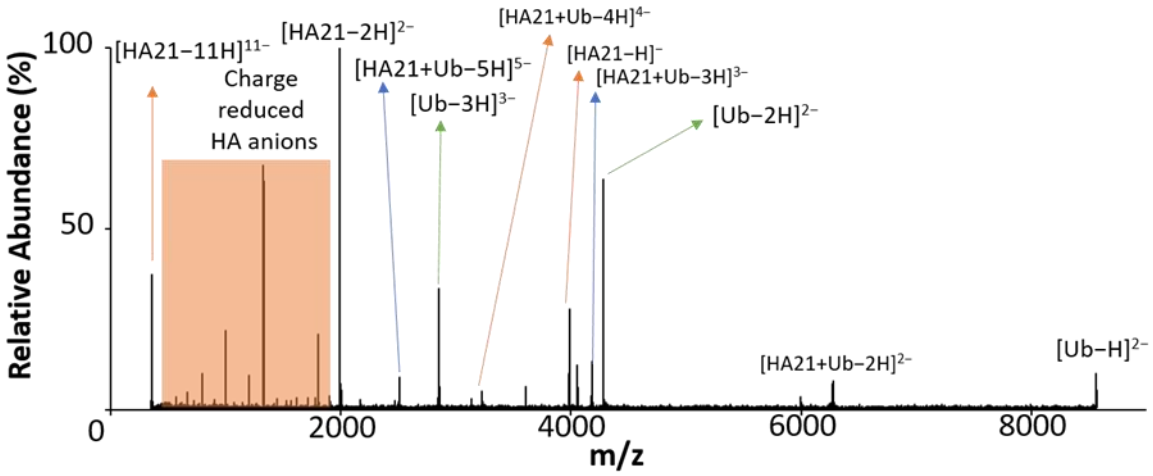

Figure 3.11. The post-ion/ion reaction mass spectrum of $[Ub+6H]^{6+}$ reacted with $[HA21-11H]^{11-}$ (MW=3985) in negative mode.

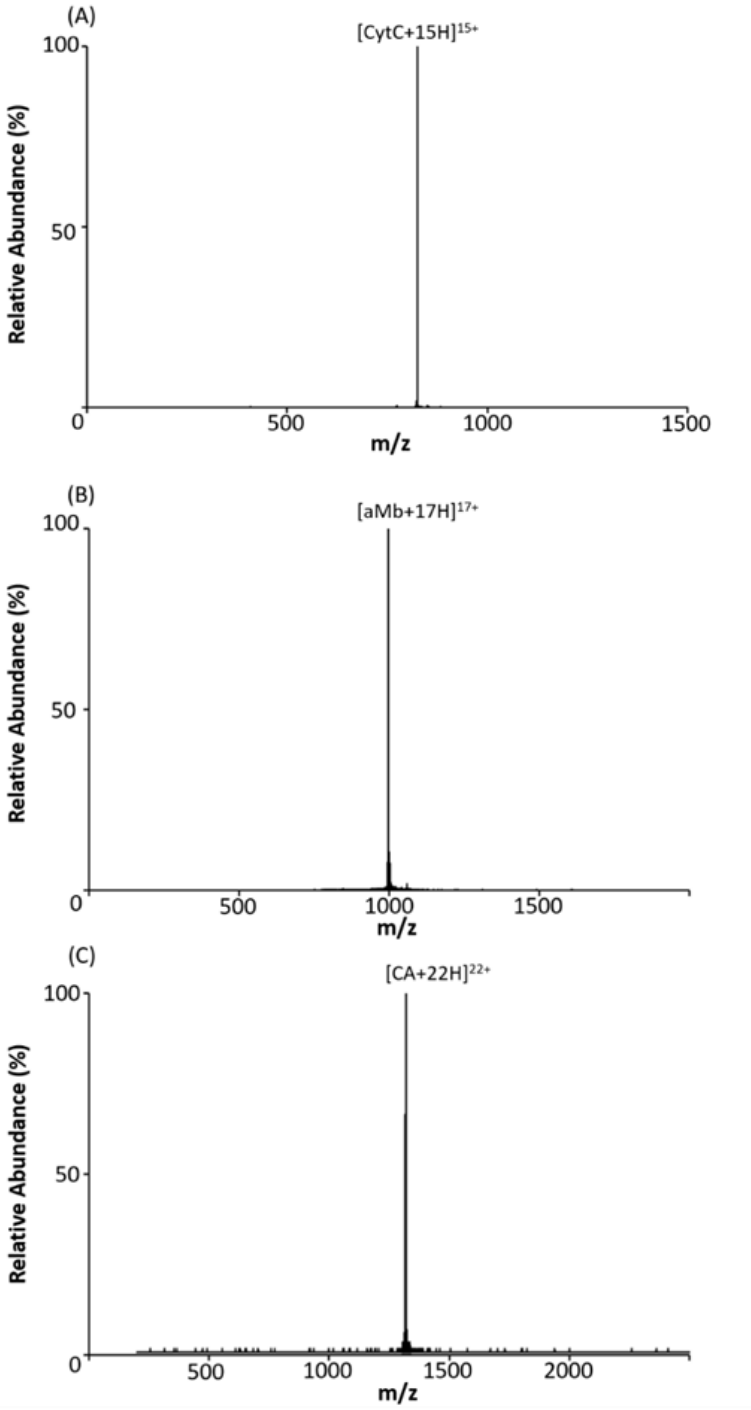

Figure 3.12. The mass spectra of the isolated protein precursor cations for the charge inversion reaction with HA 50k mixture. (A) $[CytC+15H]^{15+}$, (B) $[aMb+17H]^{17+}$, and (C) $[CA+22H]^{22+}$

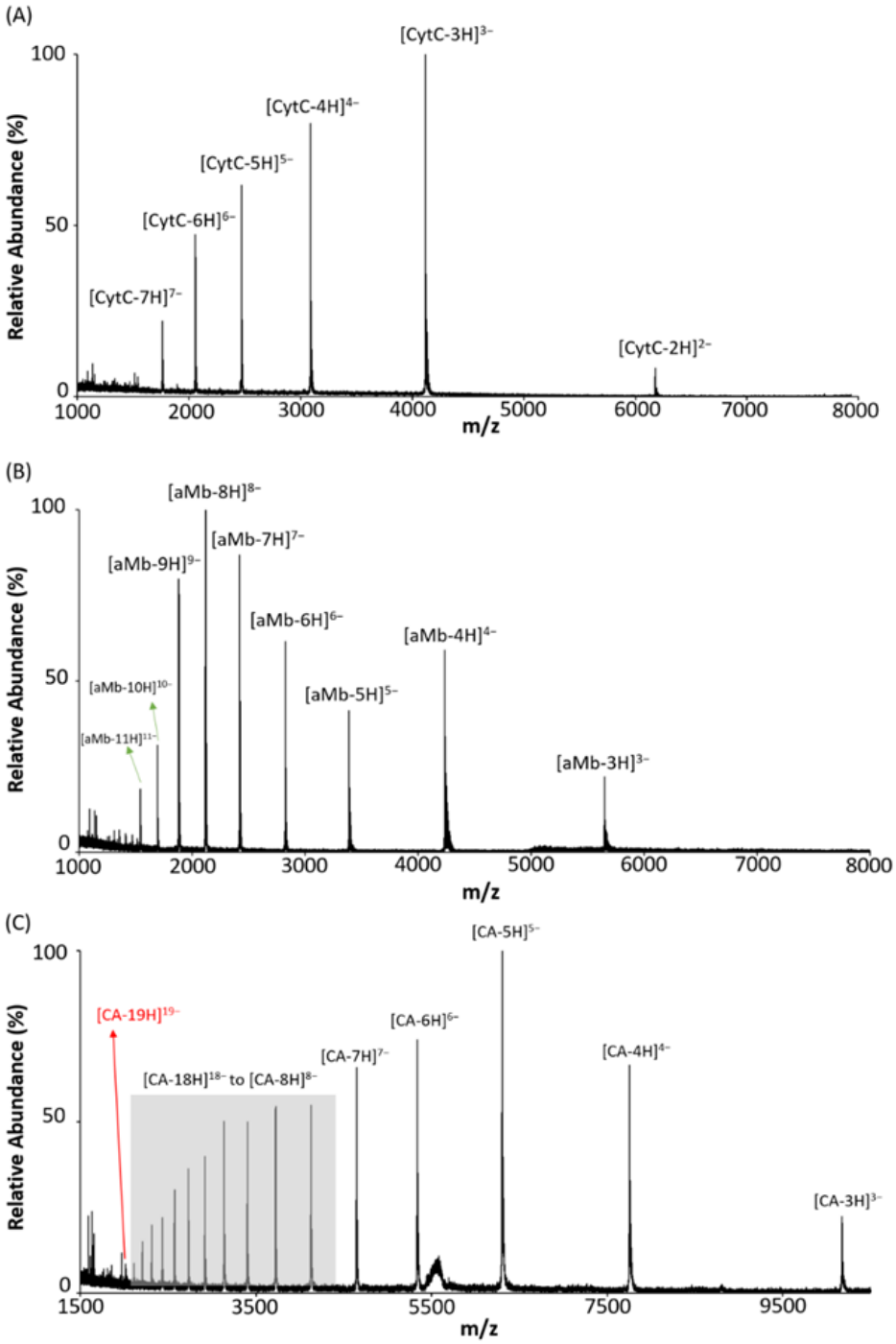

Figure 3.13. The mass spectra of post-ion/ion reaction from different protein cations and HA 50k mixture anions. (A) Charge inverted CytC, (B) charge inverted aMb, and (C) charge inverted CA. The protein solutions were prepared as described in experimental section with final concentrations at 20 μM with 0.5% acetic acid (v/v) for CytC, 10 μM with 2.0% acetic acid for aMb, and 10 μM with 1.0% acetic acid for CA.

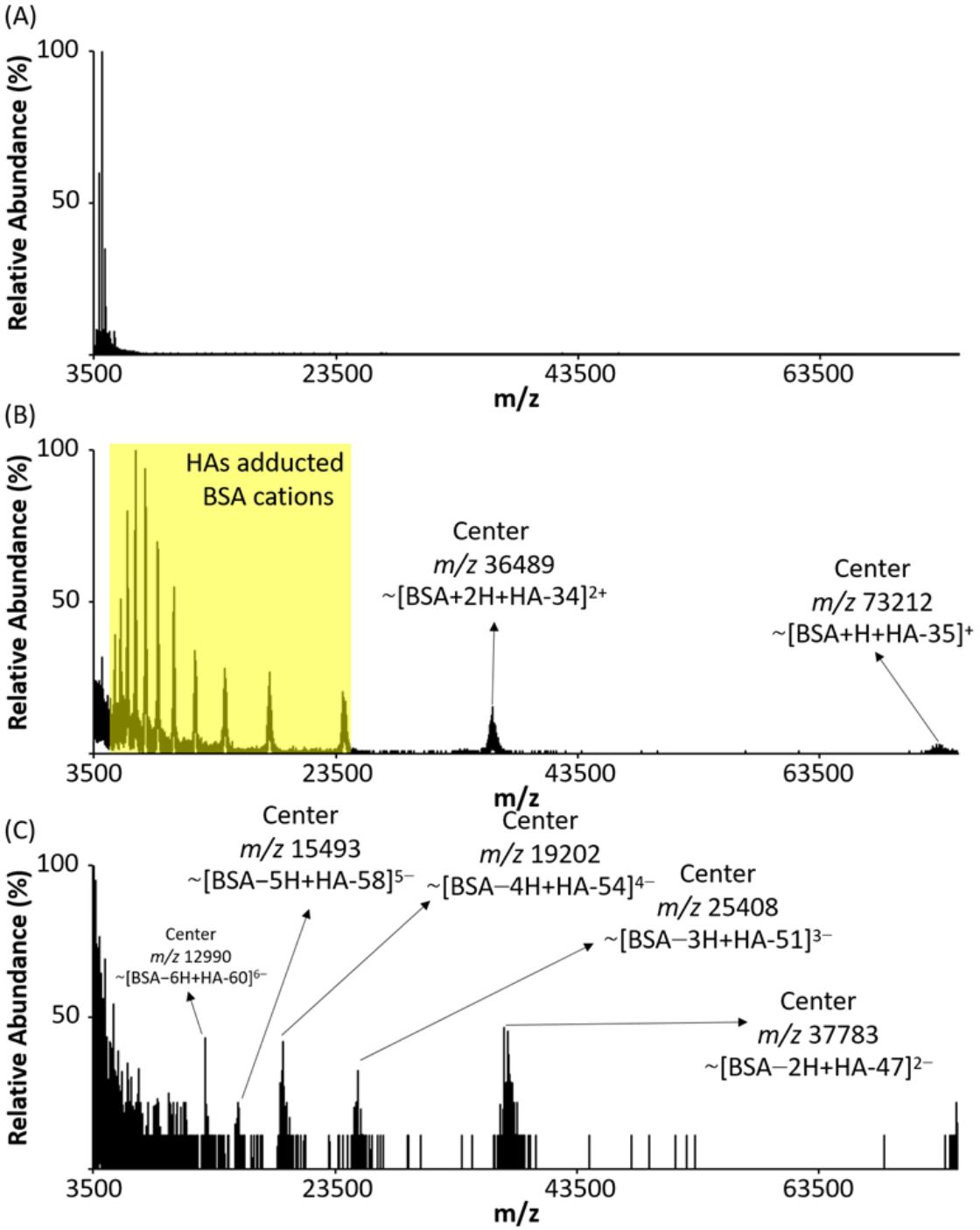

Figure 3.14. The mass spectra of BSA precursor ions and post ion/ion reaction in both positive and negative ion modes. (A) protonated BSA cations, post-ion/ion reaction mass spectrum in (B) positive, and (C) negative ion mode. The isotope distributions of the post-ion/ion spectra are hard to define, so we use the center of the bulk peak to estimate the mass of the complex product ions, and estimate the HA species adducted on BSA.

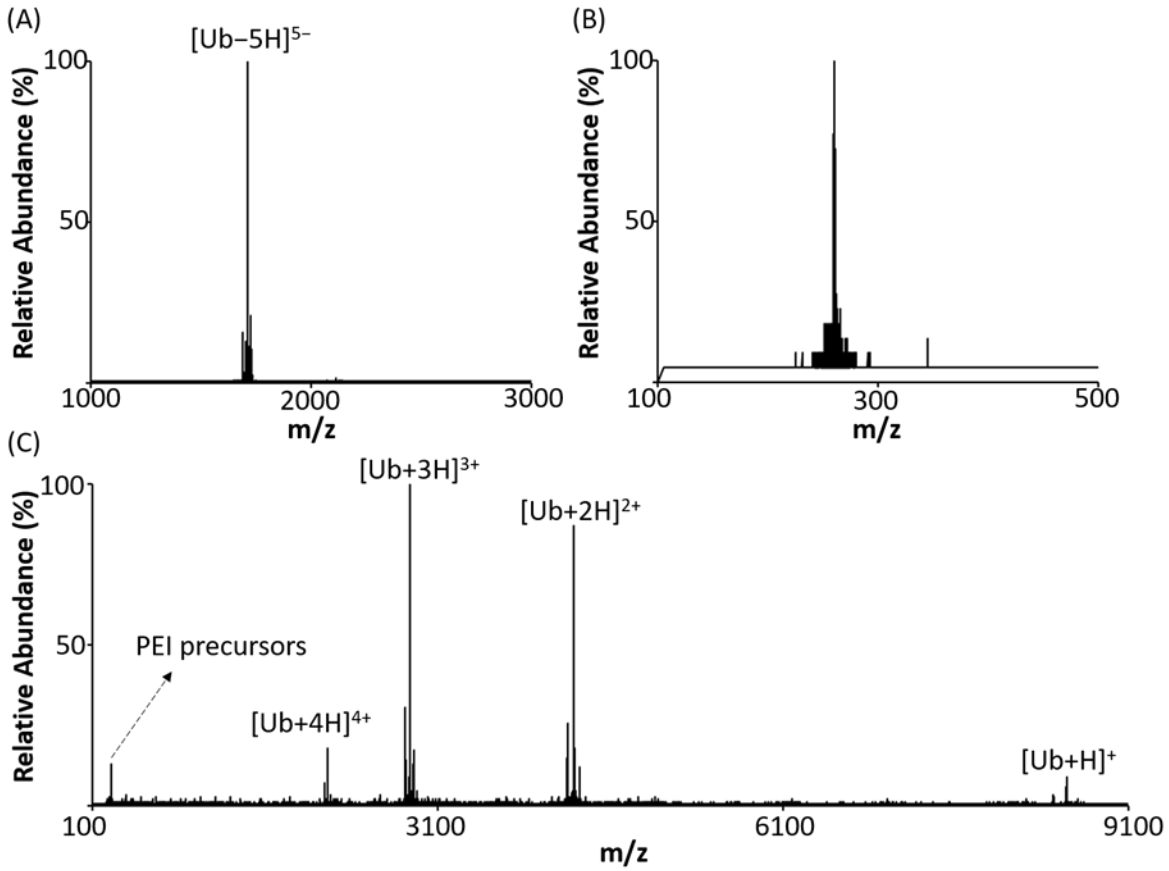

Figure 3.15. (A) The −nESI spectrum of isolation of deprotonated ubiquitin, $[Ub-5H]^{5-}$. (B) The +nESI spectrum of wide isolation of the PEI 10k mixture. (C) The mass spectrum after gas phase ion/ion reaction. The charge-inverted ubiquitin anions were observed with different charge states.

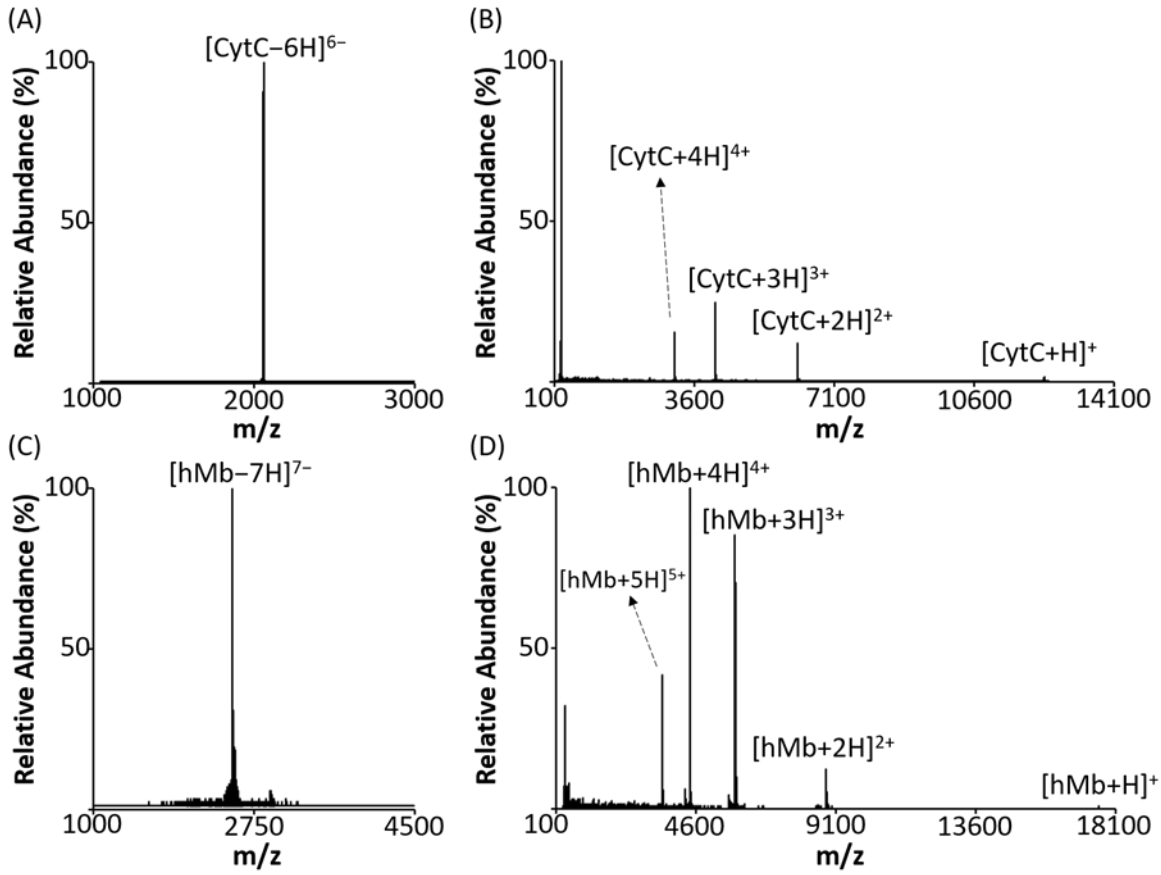

Figure 3.16. The mass spectra of the isolated protein precursor ions for the charge inversion reaction with PEI 10k mixture and their respective post-ion/ion reaction spectra. (A) $[CytC-6H]^{6-}$, (B) charge inverted CytC, (C) $[hMb-7H]^{7-}$, and (D) charge inverted hMb.

CHAPTER 4. DIFFERENTIATION AND QUANTIFICATION OF DIASTEREOMERIC PAIRS OF GLYCOSPHINGOLIPIDS USING GAS-PHASE ION CHEMISTRY

Adapted with permission from Chao, H.-C., and McLuckey, S. A. Anal. Chem. 2020, 92, 19, 13387–13395.

Abstract

Glycosphingolipids (GSLs), including glycosphingosine (lyso-GSLs) and cerebrosides (HexCer), constitute a sphingolipid subclass. The diastereomerism between their monosaccharide head groups, glucose and galactose in mammalian cells, gives rise to an analytical challenge in the differentiation of their biological roles in healthy and disease states. Shotgun tandem mass spectrometry has been demonstrated to be a powerful tool in lipidomics analysis, in which the differentiation of diastereomeric pairs of GSLs could be achieved with offline chemical modifications. However, the limited number of standards, as well as the lack in comprehensive coverage of the GSLs, complicates the qualitative and quantitative analysis of GSLs. In this work, we describe a novel strategy that couples shotgun tandem mass spectrometry with gas-phase ion chemistry to achieve both differentiation and quantification of the diastereomeric pairs of GSLs. In brief, deprotonated GSL anions, $[GSL-H]^-$, and terpyridine-magnesium complex dications, $[Mg(Terpy)_2]^{2+}$, are sequentially injected and mutually stored in a linear ion trap to form charge-inverted complex cations, $[GSL–H+MgTerpy]^+$. Collision-induced dissociation of the charge-inverted complex cations leads to significant spectral differences between the diastereomeric pairs of GSLs, which permits their distinction. Moreover, we describe a relative quantification strategy with the normalized %Area extracted from selected diagnostic ions in binary mixtures. Analytical performance with the selected pure-component pairs, HexSph(d18:1) and HexCer(d18:1/18:0), were also evaluated in terms of accuracy, repeatability, and inter-day precision. The pure-components could be extended to different fatty acyl chains on cerebrosides with limited error, which allows for the relative quantitation of the diastereomeric pairs without all standards. We successfully applied the presented method to identify and quantify, on a relative basis, the GSLs in commercially available total cerebroside extracts from the porcine brain.

4.1 Introduction

Glycosphingolipids (GSLs), including lyso-glycosphingolipids (lyso-GSLs) and cerebrosides (HexCer), constitute a sphingolipid subclass. In general, lyso-GSL structures consist of a sphingosine moiety linked to a glycan head group while cerebrosides have a single sugar residue and an esterified fatty acyl side chain linked to the sphingoid base, as depicted in **Figure 4.1**.[1] In mammalian cells, glucose or galactose is the monosaccharide head group linked to the sphingosine backbone via a beta-glycosidic bond.[2] The only difference between the diastereomeric pairs of GSLs is the orientation of the hydroxyl group (OH) at the C4'-position on the monosaccharide. The GSL subclass glucosylsphingolipid (GlcSL) has an equatorial OH at the C4' position whereas galactosylsphingolipid (GalSL) has an axial OH at the C4' position (**Figure 4.1**). As many analytical approaches do not achieve isomeric resolution, this isomeric pair is usually reported as a single species.[3-4] However, failing to unambiguously identify these isomers results not only in an underestimation of lipid diversity, but also precludes understanding of their individual roles in biological functions and disease progression.

Gaucher disease is a disorder arising from a mutation in the human GBA gene that causes a deficiency of the glucocerebrosidase (or glucosylceramidase, GCase) enzyme leading to abnormal glucosylceramide (GlcCer) accumulation in the brain.[5] In another example, Parkinson's disease (PD) is also associated with the metabolic pathway of GlcCers in which higher levels of GlcCers in the substantia nigra have been found in PD patients.[6] These examples correlate GlcCer levels with neuron dysfunction. However, cerebrosides are also reported to have neuroprotective activity such that increasing cerebroside levels by altering the *de novo* synthesis pathway of sphingolipids leads to deactivation of downstream apoptosis signaling pathways.[7-8] These results of different cerebroside levels reflect an incomplete understanding of the physiological roles of cerebrosides. A more complete understanding of this sphingolipid subclass will likely require both differentiation and quantification of the diastereomers in biological milieu.

Currently, the primary strategy to analyze GSLs utilizes liquid chromatography coupled with mass spectrometry (LC-MS). Normal phase chromatography (NPLC)[9] or hydrophilic interaction chromatography (HILIC)[10] can separate GlcSL and GalSL diastereomeric pairs. Li *et al.* developed a 2D NP/RP-LC-MS to analyze GlcSLs and GalSLs that is able to separate both the sugar headgroups and the length of fatty acyl chains.[11] However, the 2D separation strategy takes longer analysis times (up to hours), suggesting the need for more rapid analytical tools for GSL analysis.

Shotgun analysis via direct electrospray ionization tandem mass spectrometry (ESI-MS/MS) has become a popular tool for lipid analysis due to ease of use, lower sample volume, and decreased analysis time requirements.[3] Despite many successes, shotgun approaches often struggle to provide detailed structural information, including the differentiation of GlcSLs and GalSLs. Recently, offline chemical derivatization strategies have helped overcome these difficulties. Leary et al., for example, used metal-ligand complexes to coordinate with the monosaccharides to differentiate the diastereomers.[12] Coupled with ion trap tandem mass spectrometry, N-acetylglucosamine and N-acetylgalactosamine could be quantitated by virtue of the distinct product ion relative abundances formed from the isomeric complexes upon activation.[13-14] Julian and co-workers reported a strategy using photodissociation (PD) to initiate radical chemistry to differentiate diastereomeric pairs of lyso-GSLs. They used 4-iodobenzoyl 18-crown-6 (IB18C6) to form complexes with the lyso-GSLs followed by PD to generate a radical cation. With further collisional activation, differences in the ratios of relative abundances from the diagnostic product ions derived from the diastereomers were reported.[15] Moreover, they also reported a derivatization method using 4-iodophenyl boronic acid (IPBA), which selectively binds to GalCer because of the C4' axial OH, to separate the diastereomers in solution. Both methods were effective in distinguishing the diastereomers within the context of shotgun analysis. However, offline derivatization steps, as well as post-derivatization sample treatment steps, are time consuming and can lead to low abundances of derivatized products.

Chloride or lithium adduction are alternative approaches to achieve lipid structural elucidation by doping salts into lipid ESI solutions. For example, Han and co-workers developed a strategy in which chloride adducted cerebrosides anions were exploited to differentiate the diastereomeric pairs of cerebrosides (HexCer).[16] Briefly, collision-induced dissociation (CID) of the $[HexCer+Cl]^-$ adduct ion generated different ratios of product ions from GlcCer and GalCer, in which the inner-sugar fragmentation was slightly greater from CID of the $[GlcCer+Cl]^-$ ion. The same group also proposed a multidimensional strategy to quantify GalCer in the sample using internal standard addition.[16-17] However, chloride adduction can only differentiate between GlcCer and GalCer, but not lyso-GSLs. Furthermore, the method relies on multidimensional operation, which involves multiple salt additions, and can quantify only GalCer, but not GlcCer.

Gas-phase ion/ion chemistry has been shown to be effective in modifying lipid analytes directly within the mass spectrometer. Due to the attractive Coulombic potential associated with

the reactions of oppositely charged ions, reaction rates of 10-100 s^{-1} are typical under readily accessible conditions in quadrupole ion traps.[18-19] Recently, our group has described charge inversion ion/ion strategies to facilitate lipid identification and relative quantitation.[20-23] For example, fatty acid (FA) anions derived from non-esterified FAs or released from complex lipid precursors, are reacted in the gas-phase with tris-phenanthroline magnesium complex dications to generate $[FA–H+MgPhen]^+$ product ions. Ensuing dissociation of the charge inverted FA complex cation gives rise to spectral patterns that facilitate unambiguous isomeric discrimination and FA identification.[20] Additionally, this charge inversion strategy, in combination with a multiple linear regression approach, enables relative quantitation of FA isomers.[21] In this study, we describe a shotgun mass spectrometry strategy using ion chemistry to chemically modify GSLs in the gas phase to differentiate and quantify the diastereomeric pairs of GSLs in the samples.

4.2 Experimental Section

4.2.1 Materials.

All lipid standards and total cerebrosides extract (porcine brain) were purchased from Avanti Polar Lipids, Inc (Alabaster, AL). Magnesium chloride ($MgCl_2$), 2,2';6',2"-terpyridine (Terpy), and 4'-chloro-2,2';6',2"-terpyridine (Terpy-Cl) were purchased from Sigma-Aldrich (St. Louis, MO). MS-grade water and methanol (MeOH) were purchased from Fisher Scientific (Pittsburgh, PA).

4.2.2 Sample Preparation

Solutions of GSL standards were prepared in methanol to a final concentration of 0.01 mg mL^{-1}. Magnesium chloride and 2,2';6',2"-terpyridine (Terpy) were mixed in methanolic solution with 1:1 (molar ratio) to a final concentration of ~50 μM for the metal-ligand complex.[20] For relative quantification, different ratios of GlcSL/GalSL were prepared, holding the final GSL concentration at 0.01 mg mL^{-1}. For total cerebrosides extract analysis, 1 mg of purified extract powder was dissolved in 1 mL of methanol as the stock solution and stored at −20°C before use. Prior to analysis, the lipid extract was diluted to a final concentration of 0.01 mg mL^{-1}.

4.2.3 Mass Spectrometry

All experiments were performed on a TripleTOF 5600 quadrupole time-of-flight mass spectrometer (SCIEX, Concord, ON, Canada) that has been modified for ion/ion reactions.[24] Alternately pulsed dual nano-electrospray ionization (nESI) allows for the sequential injection of anions and cations.[25] GSL anions, denoted $[GSL-H]^-$, were ionized and isolated in Q1, and then accumulated in the high-pressure collision cell q2. Next, metal-ligand reagent dications, referred to as $[Mg(Terpy)_2]^{2+}$ were generated via direct positive nESI, mass-selected in Q1, and transferred to q2 to for storage. Once in q2, the lipid anions and reagent dications were mutually stored for 10-30 ms, undergoing a charge inversion ion/ion reaction. Charge-inverted complex cations were subjected to MS^n experiments. Mass analysis was performed via orthogonal acceleration time-of-flight (TOF).

4.2.4 Analytical Performance Evaluation

The analytical performance was evaluated for accuracy, repeatability, and inter-day precision. Three samples each differing in the ratios of concentrations from both the GlcSph/GalSph and GlcCer(d18:1/18:0)/GalCer(d18:1/18:0) pairs, (i.e., 90/10, 50/50, and 10/90) with a total GSL concentration of 0.01 mg mL^{-1} were prepared. Note that for each ratio, three individual sample replicates were prepared in order to evaluate repeatability and accuracy. The accuracy was calculated based on the following **equation 4.1**:

$$\text{Accuracy (\%)} = \frac{\text{Calculated percentage of the GSL}}{\text{Theroetical percentage of the GSL}} \times 100\%$$

(**eq. 4.1**)

The repeatability was expressed by the standard deviation of the calculated accuracy (n = 3). For inter-day precision, the individually prepared samples at different concentration ratios (n = 3) were analyzed on three non-consecutive days. Interday precision was calculated using **equation 4.2**:

$$\text{Interday Precision (\%RSD)} = \frac{\text{Standard deviation of the calculated percentage of the GSL}}{\text{Mean of the calculated percentage of the GSL}}$$

(**eq.4.2**)

4.2.5 Absolute Quantification

To achieve absolute quantification, the two different amounts of GlcCer (d18:1/18:0) were spiked into separate aliquots of the total cerebrosides solution. For the high concentration spike, 1μL of 0.01 mg mL^{-1} of GlcCer(d18:1/18:0) was added to a 99 μL aliquot of the cerebrosides solution. For the low concentration spike, a total of 1μL of 0.001 mg mL^{-1} of GlcCer(d18:1/18:0) was added to a 49 μL aliquot of the cerebrosides solution. Three replicates were used to calculate the percentage of the GSL pairs in the samples, and further back-calculated the absolute concentration in the total cerebrosides extracts using the known spiked amount of GlcCer(d18:1/18:0) by the following **equation 4.3 and 4.4:**

$$\mathrm{GalCer_{sample}} = \frac{\%\mathrm{GalCer_{high-spiked}} \times (\mathrm{GlcCer_{sample}} + \mathrm{GlcCer_{high-spiked}})}{\%\mathrm{GlcCer_{high-spiked}}}$$

(eq. 4.3)

$$\mathrm{GalCer_{sample}} = \frac{\%\mathrm{GalCer_{low-spiked}} \times (\mathrm{GlcCer_{sample}} + \mathrm{GlcCer_{low-spiked}})}{\%\mathrm{GlcCer_{low-spiked}}}$$

(eq. 4.4)

Where the GalCer and GlcCer were expressed in μg mL^{-1}, and %GalCer and %GlcCer were the calculated percentages from the relative quantification.

4.3 Results and Discussion

4.3.1 Differentiation of Diasteromeric Glycosphingosines Pair via Gas-Phase Ion Chemistry

As described above, diastereomeric GSL pairs differ only in the orientation of the hydroxyl (OH) group at the C4'-position of the monosaccharide. Specifically, glycosphingolipids (GlcSLs) exhibit equatorial OH orientation while galactosylsphingolipids (GalSLs) display axial orientation of the OH moiety (**Figure 4.1**). We first examined a diastereomeric pair of lyso-GSLs, or are called glycosphingosine (hexosylsphingosine, HexSph) and illustrate with glucosylsphinogsine (GlcSph) and galactosylsphingosine (GalSph). As is commonly observed, the diastereomeric pair of glycosphingosine show only limited differences in their fragmentation patterns from either protonated or deprotonated ions upon conventionally used ion-trap collision-induced dissociation (ion-trap CID) (**Figure 4.2**). The results again demonstrate the challenge while applying shotgun lipidomics approach for differentiation of these diastereomeric isomers.

Therefore, we applied gas-phase ion/ion reaction to modify the targeted deprotonated HexSph anions, trying to enhance the structural characterization between the isomeric pair. **Figure 4.3a** shows the positive ion spectrum obtained following the reaction between $[GlcSph-H]^-$ anions and $[Mg(Terpy)_2]^{2+}$ reagent dications, which yielded the charge-inverted complex cations, $[GlcSph–H+MgTerpy]^+$ (*m/z* 717.4). The reaction between $[GalSph–H]^-$ anion and $[Mg(Terpy)_2]^{2+}$ also yielded the charge-inverted complex cation, $[GalSph–H+MgTerpy]^+$. The reactions showed no differences between the two diastereomers (data not shown), so we labeled the charge-inverted complex cations as the generic label, $[HexSph – H + MgTerpy]^+$ in **Figure 4.3a**. Next, the charge-inverted glycosphingosine complex cation was mass-selected and subjected to ion-trap collisional activation. **Figures 4.3b** and **4.3c** show the CID spectra from the charge-inverted GlcSph and GalSph complex cations, respectively. Importantly, significant spectral differences were observed following interrogation of the two charge-inverted HexSph complex cations. Specifically, interrogation of the $[GlcSph–H+MgTerpy]^+$ ion resulted in a dominant neutral loss (NL) of the sugar moiety (*m/z* 555.3, NL = 162 Da), generating a Y-type ion using the widely used carbohydrate fragment nomenclature.[26] A Z-type ion is also observed at much lower abundance corresponding to a NL = 180 Da. In contrast, the CID spectrum of $[GalSph–H+MgTerpy]^+$ shows a dominant product ion corresponding to a neutral loss of a Terpy ligand, NL = 233 Da (*m/z* 484.3), along with an ion at an apparent NL = 215 Da (*m/z* 502.3) that arises from the attachment of a water molecule in the collision cell to the NL = 233 Da loss product. Previous work with divalent alkaline earth metal complexes has shown water attachment to occur in the gas phase subsequent to ligand loss. Ultimately, these spectral differences permit distinction between the GalSph and GlcSph components of the diastereomeric pair.

We have not performed a detailed mechanistic study to determine the origin(s) of the different dissociation behaviors of the $[HexSph–H+MgTerpy]^+$ ions. However, the differences in fragmentation patterns observed following CID of the charge-inverted lyso-GSL complex cations presumably reflect the nature of the interactions of the $[Mg(Terpy)_2]^{2+}$ cation with the lipids. In both cases, upon attachment of the $[Mg(Terpy)_2]^{2+}$ reagent a single Terpy ligand is lost, presumably due to displacement of one of the Terpy ligands by the lipid. On the other hand, the loss of the second Terpy ligand is highly dependent on the stereochemistry of the sugar. The $[GalSph–H+MgTerpy]^+$ ion, for example, predominantly loses the second Terpy ligand upon CID, which likely reflects a greater degree of stabilization of the Mg^{2+} ion than is afforded by the GalSph lipid.

We speculate that the additional stabilization of the Mg^{2+} ion is afforded by deprotonation of one of the sugar hydroxyl groups at the C4' or C3' positions with additional coordination by the hydroxyl group at the C4' or C3' site that is not deprotonated (see **Scheme 4.1**).[27-28] This additional interaction with the Mg^{2+} ion can facilitate the loss of the second Terpy ligand. In contrast, the glucose head group in GlcSph apparently does not interact with $MgTerpy^{2+}$ in the same way as the galactose head group in GalSph such that an alternate pathway (i.e., sugar loss) dominates. The facile loss of the neutral sugar indicates that the deprotonation site either originates or can migrate to the sphingosine chain as part of the sugar loss channel.

4.3.2 Differentiation of Diasteromeric Cerebrosides Pair via Gas-Phase Ion Chemistry

To test the ability of the gas-phase ion/ion reaction in differentiation of cerebrosides (HexCer), we performed the same reaction described above with deprotonated HexCer, $[HexCer-H]^-$. Again, the CID spectra of protonated and deprotonated diastereomeric ions show little or no differences in product ion masses and relative abundances (**Figure 4.4**). After the reactions between $[GlcCer(d18:1/18:0) - H]^-$ or $[GalCer(d18:1/18:0)-H]^-$ with $[Mg(Terpy)_2]^{2+}$, charge-inverted complex cations $[GlcCer(d18:1/18:0)–H+MgTerpy]^+$ or $[GalCer(d18:1/18:0) – H+MgTerpy]^+$ were observed (*m/z* 983.6). The fragmentation patterns of charge-inverted HexCer complex cations generated by CID are similar but not identical, to those of the analogous charge-inverted lyso-GSLs complex cations (**Figure 4.5**). The CID spectrum of $[GalCer(d18:1/18:0)–H+MgTerpy]^+$ (*m/z* 983.6) is dominated by the neutral loss of Terpy (*m/z* 750.6, NL = 233 Da) (**Figure 4.5b**), which is similar to the behavior of the $[GalSph-H+MgTerpy]^+$, with the exception that the addition of a water molecule to the Terpy loss product is far more prominent in the latter case (**Figure 4.3b**). The $[GalCer(d18:1/18:0)–H+Mg]^+$ product ion clearly solvates the magnesium dication more effectively than the corresponding $[GalSph-H+MgTerpy]^+$ product ion. The CID spectrum of $[GlcCer(d18:1/18:0)–H+MgTerpy]^+$, on the other hand, not only shows a neutral loss of the sugar moiety (*m/z* 821.6, NL =162 Da), but also shows major neutral losses of water (*m/z* 965.6, NL = 18 Da) and 443 Da (*m/z* 540.3).

To clarify the origin of the 443 Da loss from the charge-inverted complex after CID, we further applied the same reaction to GlcCer(d18:1/16:0) and a soy-based cerebroside, GlcCer(d18:2/h16:0) (**Figure 4.6a**), and compared the results. **Figures 4.6b** and **4.6c** show the

CID spectra when we subjected the charge-inverted GSL complex cations to CID. A 443 Da loss is observed in the CID spectrum from the [GlcCer(d18:1/16:0) – H + Mg(Terpy)]$^{2+}$ complex (*m/z* 955.6), whereas a 441 Da loss is observed from the [GlcCer(d18:2/h16:0) – H + Mg(Terpy)]$^{2+}$ complex (*m/z* 969.5). This result suggests that the 443 Da loss from the charge-inverted GSL complex cations described above includes the sphingosine backbone.

We further used MgTerpy-4'-Cl as the ligand for the charge inversion reagent ([Mg(Terpy-Cl)$_2$]$^{2+}$ (**Figure 4.6a**) in reaction with all three glycosylceramides, GlcCer(d18:1/18:0), GlcCer(d18:1/16:0) and GlcCer(d18:2/h16:0) followed by CID of the charge-inverted complex cations. The results show that 443 Da losses from both [GlcCer(d18:1/18:0)–H+Mg(Terpy-Cl)]$^{2+}$ and [GlcCer(d18:1/16:0)–H+Mg(Terpy-Cl)]$^{2+}$ are still observed as well as a 441 Da loss from [GlcCer(d18:2/h16:0)–H+Mg(Terpy-Cl)]$^{2+}$ (**Figure 4.6**). This result strongly suggests that the loss of 443 Da does not include the loss of the ligand and that MgTerpy is retained in the product ion. Additionally, we performed MS^3 of the 233 Da loss product (the product ion at *m/z* 750.6 in **Figure 4.4a**), and it did not show evidence for the loss of 210 Da (**Figure 4.7**), which further supports the conclusion that the 443 Da loss described above does not arise from losses of the Terpy ligand and another fragment of mass 210 Da. A previous report suggested a mechanism for losing a hydrocarbon chain from a deprotonated ceramide by various bond cleavages, including cleavage of the N-C bond.[29-30] Therefore, we performed an MS^3 experiment by subjecting the sugar loss ion (*m/z* 821.6 in **Figure 4.4a** to CID, and the *m/z* 540.3 ion is observed (**Figure 4.8**). Hence, the 443 Da loss is comprised of sugar loss (162 Da) and a loss of 281 Da. Furthermore, a 443 Da loss was observed in the CID spectra from both deprotonated cerebrosides (**Figure 4.4b and 4.4d**). Therefore, the 443 Da loss is most likely to be the sequential cleavages of the glycosidic bond and the N-C bond, with the MgTerpy coordinated with the amide. However, further studies into the detailed mechanism for the net loss of 443 Da from [HexCer(d18:1/18:0)–H+MgTerpy]$^+$ are needed to confirm the product ion structure.

4.3.3 The Relative Quantification of the Diastereomeric Pairs of GSLs

Due to extensive lipid structural diversity, quantification has remained a significant challenge in shotgun lipidomics. The most common strategy to quantify lipids involves preparation of a calibration curve. However, this approach requires the preparation of external calibration

standards, which are not always commercially available. Furthermore, calibration curve construction is sample-, time-, and labor-intensive. We developed a quantification strategy exploiting pure component analysis, in which only limited standards are required to achieve relative quantification.

To do so, we first generated the charge-inverted glycosphingosine complex cations in an identical fashion as described above (**Figure 4.3a**). Next, the charged-inverted complex cations were subjected to ion-trap CID, noting that the entire precursor cation population was fully dissociated. We chose categories of diagnostic product ions mentioned in the previous section, viz. the two major fragments associated with Terpy loss (NL = 233 Da and NL = 215 Da, NL 233 + NL 215) and the ion associated with the loss of the sugar (NL = 162 Da, NL 162). Various molar ratios of the diastereomeric pair of lyso-GSLs were prepared and analyzed using the outlined approach. Specifically, we used GlcSph/GalSph binary mixtures with the ratios 90/10, 80/20, 60/40, 50/50, 40/60, 20/80, and 10/90. The CID spectra of the fully dissociated precursor cation mixtures are provided in **Figure 4.9** and show monotonic changes in relative abundances of the diagnostic product ions as the fractions of GlcSph and GalSph decrease and
increase, respectively.

We further extracted areas of the monoisotopic peak from the diagnostic product ions from the pure-component CID results (100% GlcSph and 100% GalSph) for relative quantification. The areas were normalized to the total area from the extracted peaks and expressed as %Area (%A). **Table 4.1** shows the normalized %A of the two groups of product ions from nine replicates (three replicates per day for three days). The %A are placed in the following equations to calculate the percentage of lyso-GSLs (%GlcSph and %GalSph) in unknown samples:

$$\%\mathrm{GlcSph}_{\mathrm{unkown}} \times \%\mathrm{A}_{\mathrm{NL\,Terpy}} + \%\mathrm{GalSph}_{\mathrm{unknown}} \times \%\mathrm{A}_{\mathrm{NL\,Terpy}} = \mathrm{detected}\ \%\mathrm{A}_{\mathrm{NL\,Terpy}} \quad \textbf{(eq. 4.5)}$$

$$\%\mathrm{GlcSph}_{\mathrm{unkown}} \times \%\mathrm{A}_{\mathrm{NL\,sugar}} + \%\mathrm{GalSph}_{\mathrm{unknown}} \times \%\mathrm{A}_{\mathrm{NL\,sugar}} = \mathrm{detected}\ \%\mathrm{A}_{\mathrm{NL\,sugar}} \quad \textbf{(eq. 4.6)}$$

Three different molar ratios of GlcSph/GalSph at 90/10, 50/50, and 10/90, were chosen to demonstrate the approach as well as to evaluate the analytical performance in terms of accuracy, repeatability, and inter-day precision. The normalized %A of the product ions from different NL groups were obtained as detected %A and was input into eq. 5 and eq. 6. The bottom panel from **Table 4.1** summarizes the relative quantification results with the analytical performance. The

accuracies for relative quantification of the GlcSph and GalSph diastereomeric pair ranged from 96.8 to 104.1% from different molar ratios, with the highest SD around 11.7%. The results suggest that relative quantification is achieved applying the strategy. Moreover, the inter-day precisions of the lyso-GSLs results are all below 12.5%RSD, which suggests that the relative quantification results obtained from different days were still comparable. Correlation curves between the calculated % and the spiked % are also shown in **Figure 4.10**. We note that the inter-day precision suggests that the use of the sum of the abundances of the NL = 233 Da and NL = 215 Da signals minimizes sensitivity of this approach to quantification to changes in water levels in the collision cell.

A similar strategy was applied to the cerebroside diastereomeric pair GlcCer(d18:1/18:0) and GalCer(d18:1/18:0). The diagnostic product ions were chosen based on the previous section, and also divided into two groups, NL of Terpy (NL 233 + NL 215) versus NL of water (NL =18 Da, NL 18), NL of sugar (NL 162), and NL of 443 Da (NL 443). The different molar ratios of GlcCer(d18:1/18:0)/GalCer(d18:1/18:0) were analyzed, and the changes in relative abundances of the diagnostic product ions from samples with different molar ratios were also observed (**Figure 4.11**). Again, the extracted areas of the monoisotopic peak from the diagnostic product ions were normalized to the total area from the extracted peaks and expressed as %A in the top panel from **Table 4.2**. Another set of equations to quantify the percentage of the cerebroside diastereomers are shown as follows:

$$\%\mathrm{GlcCer}_{\mathrm{unkown}} \times \%\mathrm{A}_{\mathrm{NL\,Terpy}} + \%\mathrm{GalCer}_{\mathrm{unknown}} \times \%\mathrm{A}_{\mathrm{NL\,Terpy}} = \text{detected } \%\mathrm{A}_{\mathrm{NL\,Terpy}}$$

(eq. 4.7)

$$\%\mathrm{GlcCer}_{\mathrm{unkown}} \times \%\mathrm{A}_{\mathrm{NL\,other}} + \%\mathrm{GalCer}_{\mathrm{unknown}} \times \%\mathrm{A}_{\mathrm{NL\,other}} = \text{detected } \%\mathrm{A}_{\mathrm{NL\,other}}$$

(eq. 4.8)

Three different molar ratios of GlcCer/GalCer were chosen to demonstrate the approach as well as to evaluate the analytical performance. The bottom panel from **Table 4.2** summarizes the relative quantification results with the analytical performances. The accuracies for relatively quantifying the cerebroside diastereomeric pair were ranged from 92.6 to 101.4% with the highest SD around 6.7%, and the inter-day precisions are all below 6.8%RSD. Also, correlation curves between the calculated % and the spiked % are shown in **Figure 4.12**. All of the above results show the applicability of the strategy to achieve relative quantification of both lyso-GSLs and the

cerebroside diastereomeric pairs, which only require the analysis of the two pure components prior to the quantification.

Lack of commercially available calibration standards is often a challenge in lipidomics analysis, especially for quantification. Therefore, we evaluated the use of the same pure components from a single pair of cerebroside diastereomers to perform the relative quantification for other cerebrosides, which vary only in the fatty acyl chain. This assumes that all charge-inverted cerebroside complex cations have similar fragmentation patterns after activation since none of the selected diagnostic product ions arise from the fatty acyl chain (R1 group in **Figure 4.1**). Two different pairs of cerebroside diastereomers, HexCer(d18:1/16:0) and HexCer(d18:1/18:1), at five different molar ratios between the diastereomers (GlcCer/GalCer), including 100/0, 80/20, 50/50, 20/80, and 0/100, were analyzed. The CID spectra of the fully dissociated precursor cations are shown in **Figure 4.13,** showing the same monotonic changes in the relative abundances of the diagnostic product ions as a function of molar ratio. The relative quantification is achieved by using the same %A obtained from pure components of HexCer(d18:1/18:0), and eq.7 and eq. 8 The relative quantification results are summarized in **Table 4.3**. The accuracies ranged from 96.5 to 113.0%, with the highest SD around 3.2% for the HexCer(d18:1/16:0) pair, and the accuracies ranged from 89.4 to 106.6%, with the highest SD around 8.4%, for HexCer(d18:1/18:1). To validate the results, we also performed the same approach using the pure-component %A obtaining from their own calibration standards. The relative quantification results are also reported (**Table 4.4 and Table 4.5**), and less than 6% error were observed when comparing the two data sets. However, it is noticeable that there is a greater difference in the normalized %A from the pure GlcCer(d18:1/18:1) relative to GlcCer(d18:1/18:0) (i.e., 35.9% (**Table 4.5**) vs. 39.4% (**Table 4.1**)) than GlcCer(d18:1/16:0) relative to GlcCer(d18:1/18:0) (i.e., 39.9% (**Table 4.4**) vs. 39.4% (**Table 4.1**)). This suggests that unsaturation in the fatty acyl chain could give rise to slight differences in product ion abundances relative to a saturated fatty acyl chain.[31] More studies would be required to establish a firm correlation, however. Overall, the relative quantitation for different fatty acyl chain GSLs using the %area from HexCer(d18:1/18:0) pair is demonstrated.

4.3.4 Analysis of Total Cerebrosides Extracts

We examined commercially available total cerebroside extracts from porcine brain using the approaches described above. We identified a total of 11 *m/z* values that correspond to different sizes of cerebrosides common in mammalian systems.[32-33] To differentiate the diastereomeric pairs that might be present in the putative cerebrosides, we exploited the strategy described above. Due to the lack of commercially available standards mentioned above, we were able to perform relative quantification on the diastereomeric pairs of cerebrosides using only our evaluated quantification %Area from HexCer(d18:1/18:0) pair. The CID spectra of the fully dissociated precursor ions after all reactions are shown in **Figure 4.14.** After the relative quantification, a total of 14 cerebrosides were identified and relatively quantified from the 11 *m/z* values expected to arise from cerebrosides. The results are reported in **Table 4.6**. Most of the cerebrosides that we detected in the porcine brain are GalCers with only three minor components within the diastereomeric pairs, including GlcCer(d18:1/16:0), GlcCer(d18:1/20:0), and GlcCer(d18:1/22:0). The results agree with previous reports showing that the majority of the cerebrosides in mammalian brain are galactosylsphingolipid.[5, 16, 34-35]

In the event that a standard is available, such as the case for GlcCer(d18:1/18:0), a measurement of absolute concentration is possible. We spiked two aliquots of the sample with different known amounts of GlcCer(d18:1/18:0). **Figure 4.15** shows the CID spectra of the pre- and post-spiked samples. The changes in the relative abundances of the diagnostic product ions after spiking the standard were observed. The different percentages of GlcCer(d18:1/18:0) and GalCer(d18:1/18:0) from the different spiked samples were obtained using the relative quantitation described above. Due to the fact that we did not detect any GlcCer(d18:1/18:0) in the total cerebrosides extract, we can modify **eq. 4.3** and **eq. 4.4** to yield the absolute amount of GalCer(d18:1/18:0) in the sample by **eq. 4.9** and **eq. 4.10**:

$$\mathrm{GalCer}_{\mathrm{sample}} = \frac{\%\mathrm{GalCer}_{\mathrm{high-spiked}} \times \mathrm{GlcCer}_{\mathrm{high-spiked}}}{\%\mathrm{GlcCer}_{\mathrm{high-spiked}}}$$

(eq. 4.9)

$$\mathrm{GalCer}_{\mathrm{sample}} = \frac{\%\mathrm{GalCer}_{\mathrm{low-spiked}} \times \mathrm{GlcCer}_{\mathrm{low-spiked}}}{\%\mathrm{GlcCer}_{\mathrm{low-spiked}}}$$

(eq. 4.10)

The absolute quantitation results from both high concentration and low concentration spiked samples are shown in **Table 4.7**. Normally, spiking two different concentrations in the same sample is needed for applying eq. 4.3 and eq. 4.4 if both the cerebroside diastereomers exist in the sample. The mean calculated concentration of GalCer(d18:1/18:0) is 1.90±0.13 μg per mg extract powder. Here we also compared the two results from both high-spiked and low-spiked samples, which are each within one standard deviation of the mean. The primary benefit of this approach is that the absolute quantification of cerebroside diastereomers is achieved using addition of a single calibration standard comprised of only one of the diastereomers. Moreover, no external calibration curve is required, leading to reduced analysis time and cost. However, as with many lipidomics approaches, the lack of commercially available standards presents several challenges, including absolute quantification of GSLs in complex mixtures using the developed platform.

4.4 Conclusions

The differentiation of the diastereomeric glycosphingolipids is often a challenge, but essential for defining their biological roles in various diseases. We present a shotgun tandem mass spectrometry strategy using gas-phase ion chemistry to achieve the identification in both lyso-GSLs and cerebrosides without offline chemical derivatization. The gas-phase ion/ion reaction between the deprotonated GSLs ($[GSL-H]^-$) and $[Mg(Terpy)_2]^{2+}$ forming charge-inverted cations, $[GSL–H+Terpy]^+$, followed by collision-induced dissociation yield distinctive product ion spectra for the diastereomers. Moreover, relative quantification is achieved by analyzing the normalized %Area from the diagnostic product ions. The analytical performance of the relative quantification of both lyso-GSL and cerebroside diastereomeric pairs are also evaluated in terms of accuracy, repeatability, and inter-day precision. We also extended the strategy using the %Area from the validated cerebroside diastereomers, GlcCer(d18:1/18:0) and GalCer(d18:1/18:0), to provide relative quantification of other cerebrosides with different fatty acyl chains.

We extended the strategy to the analysis of total cerebroside extracts. A total of 14 cerebrosides were identified and quantified based on of their percentages within the diastereomeric pairs. This work also demonstrated an absolute quantification strategy for a cerebroside component in the total cerebroside extract from the porcine brain. By spiking two different sample solutions with known amounts of GlcCer(d18:1/18:0), the quantity of GalCer(d18:1/18:0) was obtained. The

proposed absolute quantification method requires a calibration standard for only one of the diastereomers within the diastereomeric pair, and also with only two spiked concentrations, which reduces the required of numbers of calibration standards and obviates the generation of a calibration curve. However, the lack of a calibration standard from each diastereomeric pair prevents the absolute quantification of all cerebrosides.

4.5 Acknowledgements

This work was supported by the National Institutes of Health (NIH) under Grants GM R37-45372 and GM R01-118484. Dr. Elissia T. Franklin, Dr.. Caitlin E. Randolph, and Dr. John T. Lawler are acknowledged for helpful discussions.

4.6 References

1. Merrill, A. H., Sphingolipid and Glycosphingolipid Metabolic Pathways in the Era of Sphingolipidomics. Chem Rev 2011, 111 (10), 6387-6422.
2. Schnaar RL, K. T., Glycosphingolipids. In Essentials of Glycobiology [Internet], 3rd edition ed.; Varki A, C. R., Esko JD et al, Ed. Cold Spring Harbor (NY): Cold Spring Harbor Laboratory Press, 2017.
3. Han, X.; Gross, R. W., Shotgun lipidomics: Electrospray ionization mass spectrometric analysis and quantitation of cellular lipidomes directly from crude extracts of biological samples. Mass Spectrom Rev 2005, 24 (3), 367-412.
4. Hakomori, S.-i., Structure and function of glycosphingolipids and sphingolipids: Recollections and future trends. Biochim Biophys Acta Gen Subj 2008, 1780 (3), 325-346.
5. Stirnemann, J.; Belmatoug, N.; Camou, F.; Serratrice, C.; Froissart, R.; Caillaud, C.; Levade, T.; Astudillo, L.; Serratrice, J.; Brassier, A.; Rose, C.; Billette de Villemeur, T.; Berger, M. G., A Review of Gaucher Disease Pathophysiology, Clinical Presentation and Treatments. Int J Mol Sci 2017, 18 (2), 441.
6. Huebecker, M.; Moloney, E. B.; van der Spoel, A. C.; Priestman, D. A.; Isacson, O.; Hallett, P. J.; Platt, F. M., Reduced sphingolipid hydrolase activities, substrate accumulation and ganglioside decline in Parkinson's disease. Mol Neurodegener 2019, 14 (1), 40.
7. Bleicher, R. J.; Cabot, M. C., Glucosylceramide synthase and apoptosis. Biochim Biophys Acta Mol Cell Biol Lipids 2002, 1585 (2), 172-178.
8. Jin, Y.; Fan, J.-T.; Gu, X.-L.; Zhang, L.-Y.; Han, J.; Du, S.-H.; Zhang, A.-X., Neuroprotective Activity of Cerebrosides from Typhonium giganteum by Regulating Caspase-3 and Bax/Bcl-2 Signaling Pathways in PC12 Cells. J Nat Prod 2017, 80 (6), 1734-1741.
9. Shaner, R. L.; Allegood, J. C.; Park, H.; Wang, E.; Kelly, S.; Haynes, C. A.; Sullards, M. C.; Merrill, A. H., Quantitative analysis of sphingolipids for lipidomics using triple quadrupole and quadrupole linear ion trap mass spectrometers. J Lipid Res 2009, 50 (8), 1692-1707.

10. Scherer, M.; Leuthäuser-Jaschinski, K.; Ecker, J.; Schmitz, G.; Liebisch, G., A rapid and quantitative LC-MS/MS method to profile sphingolipids. J Lipid Res 2010, 51 (7), 2001-2011.

11. Li, M.; Tong, X.; Lv, P.; Feng, B.; Yang, L.; Wu, Z.; Cui, X.; Bai, Y.; Huang, Y.; Liu, H., A not-stop-flow online normal-/reversed-phase two-dimensional liquid chromatography–quadrupole time-of-flight mass spectrometry method for comprehensive lipid profiling of human plasma from atherosclerosis patients. J Chromatogr A 2014, 1372, 110-119.

12. Gaucher, S. P.; Leary, J. A., Stereochemical Differentiation of Mannose, Glucose, Galactose, and Talose Using Zinc(II) Diethylenetriamine and ESI-Ion Trap Mass Spectrometry. Anal Chem 1998, 70 (14), 3009-3014.

13. Desaire, H.; Leary, J. A., Differentiation of Diastereomeric N-Acetylhexosamine Monosaccharides Using Ion Trap Tandem Mass Spectrometry. Anal Chem 1999, 71 (10), 1997-2002.

14. Desaire, H.; Leary, J. A., Multicomponent Quantification of Diastereomeric Hexosamine Monosaccharides Using Ion Trap Tandem Mass Spectrometry. Anal Chem 1999, 71 (19), 4142-4147.

15. Pham, H. T.; Julian, R. R., Characterization of glycosphingolipid epimers by radical-directed dissociation mass spectrometry. Analyst 2016, 141 (4), 1273-1278.

16. Han, X.; Cheng, H., Characterization and direct quantitation of cerebroside molecular species from lipid extracts by shotgun lipidomics. J Lipid Res 2005, 46 (1), 163-175.

17. Han, X.; Yang, K.; Gross, R. W., Multi-dimensional mass spectrometry-based shotgun lipidomics and novel strategies for lipidomic analyses. Mass Spectrom Rev 2012, 31 (1), 134-178.

18. He, M.; McLuckey, S. A., Two Ion/Ion Charge Inversion Steps to Form a Doubly Protonated Peptide from a Singly Protonated Peptide in the Gas Phase. J Am Chem Soc 2003, 125 (26), 7756-7757.

19. McLuckey, S. A.; Huang, T.-Y., Ion/Ion Reactions: New Chemistry for Analytical MS. Analy Chem 2009, 81 (21), 8669-8676.

20. Randolph, C. E.; Foreman, D. J.; Betancourt, S. K.; Blanksby, S. J.; McLuckey, S. A., Gas-Phase Ion/Ion Reactions Involving Tris-Phenanthroline Alkaline Earth Metal Complexes as Charge Inversion Reagents for the Identification of Fatty Acids. Anal Chem 2018, 90 (21), 12861-12869.

21. Randolph, C. E.; Foreman, D. J.; Blanksby, S. J.; McLuckey, S. A., Generating Fatty Acid Profiles in the Gas Phase: Fatty Acid Identification and Relative Quantitation Using Ion/Ion Charge Inversion Chemistry. Anal Chem 2019, 91 (14), 9032-9040.

22. Randolph, C. E.; Blanksby, S. J.; McLuckey, S. A., Toward Complete Structure Elucidation of Glycerophospholipids in the Gas Phase through Charge Inversion Ion/Ion Chemistry. Anal Chem 2020, 92 (1), 1219-1227.

23. Franklin, E. T.; Betancourt, S. K.; Randolph, C. E.; McLuckey, S. A.; Xia, Y., In-depth structural characterization of phospholipids by pairing solution photochemical reaction with charge inversion ion/ion chemistry. Anal Bioanal Chem 2019, 411 (19), 4739-4749.

24. Xia, Y.; Chrisman, P. A.; Erickson, D. E.; Liu, J.; Liang, X.; Londry, F. A.; Yang, M. J.; McLuckey, S. A., Implementation of Ion/Ion Reactions in a Quadrupole/Time-of-Flight Tandem Mass Spectrometer. Anal Chem 2006, 78 (12), 4146-4154.

25. Xia, Y.; Liang, X.; McLuckey, S. A., Pulsed Dual Electrospray Ionization for Ion/Ion Reactions. J Am Soc Mass Spectrom 2005, 16 (11), 1750-1756.

26. Domon, B.; Costello, C. E., A systematic nomenclature for carbohydrate fragmentations in FAB-MS/MS spectra of glycoconjugates. Glycoconjugate J 1988, 5 (4), 397-409.

27. Salpin, J.-Y.; Tortajada, J., Gas-phase acidity of D-glucose. A density functional theory study. J Mass Spectrom 2004, 39 (8), 930-941.

28. Bythell, B. J.; Abutokaikah, M. T.; Wagoner, A. R.; Guan, S.; Rabus, J. M., Cationized Carbohydrate Gas-Phase Fragmentation Chemistry. J Am Soc Mass Spectrom 2017, 28 (4), 688-703.

29. Hsu, F. F.; Turk, J., Structural determination of glycosphingolipids as lithiated adducts by electrospray ionization mass spectrometry using low-energy collisional-activated dissociation on a triple stage quadrupole instrument. J Am Soc Mass Spectrom 2001, 12 (1), 61-79.

30. Hsu, F. F., Complete structural characterization of ceramides as $[M-H]^{(-)}$ ions by multiple-stage linear ion trap mass spectrometry. Biochimie 2016, 130, 63-75.

31. Yang, K.; Zhao, Z.; Gross, R. W.; Han, X., Identification and Quantitation of Unsaturated Fatty Acid Isomers by Electrospray Ionization Tandem Mass Spectrometry: A Shotgun Lipidomics Approach. Anal Chem 2011, 83 (11), 4243-4250.

32. Fahy, E.; Sud, M.; Cotter, D.; Subramaniam, S., LIPID MAPS online tools for lipid research. Nucleic Acids Res 2007, 35 (Web Server issue), W606-W612.

33. Fahy, E.; Subramaniam, S.; Murphy, R. C.; Nishijima, M.; Raetz, C. R. H.; Shimizu, T.; Spener, F.; van Meer, G.; Wakelam, M. J. O.; Dennis, E. A., Update of the LIPID MAPS comprehensive classification system for lipids. J Lipid Res 2009, 50 (Suppl), S9-S14.

34. Dandana, A.; Ben Khelifa, S.; Chahed, H.; Miled, A.; Ferchichi, S., Gaucher Disease: Clinical, Biological and Therapeutic Aspects. Pathobiology 2016, 83 (1), 13-23.

35. von Gerichten, J.; Schlosser, K.; Lamprecht, D.; Morace, I.; Eckhardt, M.; Wachten, D.; Jennemann, R.; Gröne, H.-J.; Mack, M.; Sandhoff, R., Diastereomer-specific quantification of bioactive hexosylceramides from bacteria and mammals. J Lipid Res 2017, 58 (6), 1247-1258.

4.7 Tables

Table 4.1. The normalized %area for quantifying glycosphingosines and the analytical performance of glycosphingosines quantification.

Normalized %Area for Glycosphingosines (HexSph) (N=9)						
100% of lyso-GSLs	**NL of Terpy (%, NL 215 + NL 233)**			**NL of sugar (%, NL 162)**		**SD**
GlcSph	15.7			84.3		1.4
GalSph	90.5			9.5		0.6
Analytical Performance						
%GlcSph /%GlcSph	**Avg_Cal %GlcSph**	**Accuracy (%)***	**Inter-day Precision (RSD%)****	**Avg_Cal %GalSph**	**Accuracy (%)***	**Inter-day Precision (RSD%)****
90/10	90.1	100.0±0.0	0.7	9.9	98.9±4.7	6.3
50/50	52.1	104.1±1.2	2.7	48.4	96.8±1.1	2.9
10/90	9.8	97.7±11.7	12.5	90.2	100.3±1.3	1.4

*Mean±SD, N=3

**Relative standard deviation, calculated from three different days with 9 different samples.

Table 4.2. The normalized %area for quantifying cerebrosides and the analytical performance of GSLs quantification

Normalized %Area for cerebrosides (N=9)						
100% of GSLs		**NL of Terpy (%, NL215 + NL233)**		**NL of others* (%, NL18 +N L162 + NL443)**		**SD**
GlcCer(d18:1/18:0)		39.4		60.6		1.2
GalCer(d18:1/18:0)		92.5		7.5		0.2
Analytical Performance						
%GlcCer /%GalCer	**Avg_Cal %GlcCer**	**Accuracy (%)****	**Inter-day Precision (RSD%)*****	**Avg_Cal %GalCer**	**Accuracy (%)***	**Inter-day Precision (RSD%)****
90/10	89.9	99.8±0.4	1.0	10.1	101.4±3.9	6.8
50/50	49.3	98.6±2.1	2.2	50.7	101.4±0.9	1.4
10/90	9.3	92.6±4.3	6.7	90.7	100.8±0.5	0.6

*NL of water, sugar, and Terpy with sphingosine backbone

**Mean±SD, N=3

***Relative standard deviation, calculated from three different days with 9 different samples

Table 4.3. The relative quantification results of different acyl chains on GSLs with the constants from HexCer(d18:1/18:0).

HexCer(d18:1/16:0)				
%GlcCer/%GalCer	**Avg_Cal %GlcCer**	**Accuracy (%)***	**Avg_Cal %GalCer**	**Accuracy (%)***
100/0	98.9	98.9±0.2	1.1	Not applicable
80/20	80.1	100.2±0.6	19.7	98.7±0.8
50/50	49.6	99.1±0.4	50.4	100.9±0.4
20/80	22.6	113.0±3.2	77.2	96.5±2.1
0/100	1.8	Not applicable	98.2	98.1±0.5
HexCer(d18:1/18:1)				
100/0	106.4	106.4±0.1	< 0	Not applicable
80/20	82.1	102.7±2.1	17.9	89.4±1.4
50/50	53.3	106.6±1.9	46.5	93.0±1.9
20/80	20.5	102.3±5.8	79.5	99.4±8.4
0/100	2.5	Not applicable	97.5	97.5±0.2

*Mean±SD

Table 4.4. The normalized %area for quantifying HexCer(d18:1/16:0) and the quantification results.

Normalized %A from HexCer(d18:1/16:0)				
100% of GSLs	**NL of Terpy loss (%, NL215 + NL233)**		**NL of others (%, NL18+NL162+NL443)**	**SD**
GlcCer(d18:1/16:0)	39.9		60.1	0.12
GalCer(d18:1/16:0)	91.5		8.5	0.29
Analytical Performance (N=3)				
16:0 ratio %GlcCer/ %GalCer	**Avg_Cal %GlcCer**	**Accuracy (%)***	**Avg_Cal %GalCer**	**Accuracy (%)***
100/0	100	100.0±0.2	0	Not applicable
80/20	82.3	102.9±0.6	19.2	96.1±0.8
50/50	50.2	100.4±0.4	49.8	99.6±0.4
20/80	21.4	107.0±3.4	78.4	98.0±2.6
0/100	0	Not applicable	100	100.0±0.5

*Mean±SD

Table 4.5. The normalized %area for quantifying HexCer(d18:1/18:1) and the quantification results.

Normalized %A from HexCer(d18:1/18:1)				
100% of GSLs	**NL of Terpy loss (%, NL215 + NL233)**		**NL of others (%, NL18+NL162+NL443)**	**SD**
GlcCer(d18:1/18:1)	35.9		64.1	0.05
GalCer(d18:1/18:1)	91.2		8.8	0.12
Analytical Performance (N=3)				
18:1 ratio %GlcCer/ %GalCer	**Avg_Cal %GlcCer**	**Accuracy (%)***	**Avg_Cal %GalCer**	**Accuracy (%)***
100/0	100	100.0±0.1	0	Not applicable
80/20	78.2	97.7±2.1	22.9	114.5±1.4
50/50	49.9	99.9±1.8	50.1	100.1±1.8
20/80	17.2	86.2±5.6	82.8	103.4±7.9
0/100	2.5	Not applicable	100	10.0±0.2

*Mean±SD

Table 4.6. The relative quantitation results of the profiled cerebrosides from porcine brain extract. (N=3)

HexCer	Avg Cal_Glc (%)	Avg Cal_Gal (%)	SD
d18:1/14:0	ND	99.7	0.9
d18:1/16:0	10.9	89.1	0.8
d18:1/18:1	ND	106.7	2.0
d18:1/18:0	ND	99.5	1.9
d18:1/20:0	1.3	98.7	0.5
d18:1/22:0	0.9	99.1	0.2
d18:1/23:0	ND	100.3	0.0
d18:1/24:1	ND	102.0	0.5
d18:1/24:0	ND	100.8	1.5
d18:1/26:1	ND	100.7	0.5
d18:1/26:0	ND	101.9	0.5

ND: non-detectable, indicated the calculated percentages ≤ 0, or ≤ SD.

Table 4.7. The summary table of the absolute quantification results from both low concentration and high concentration spiking test (N=3).

	Avg_Cal GalCer(d18:1/18:0) (μg mg^{-1})	**SD**
High spiked	1.98	0.10
Low spiked	1.82	0.08
Avg (N=6)	1.90	0.13

4.8 Scheme and Figures

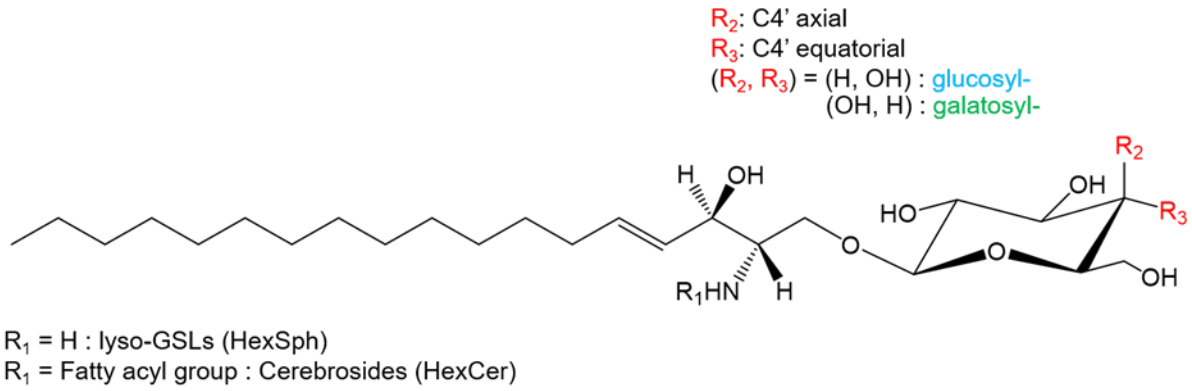

Figure 4.1. The common structure of glycosphingolipids (GSLs) in the mammalian system.

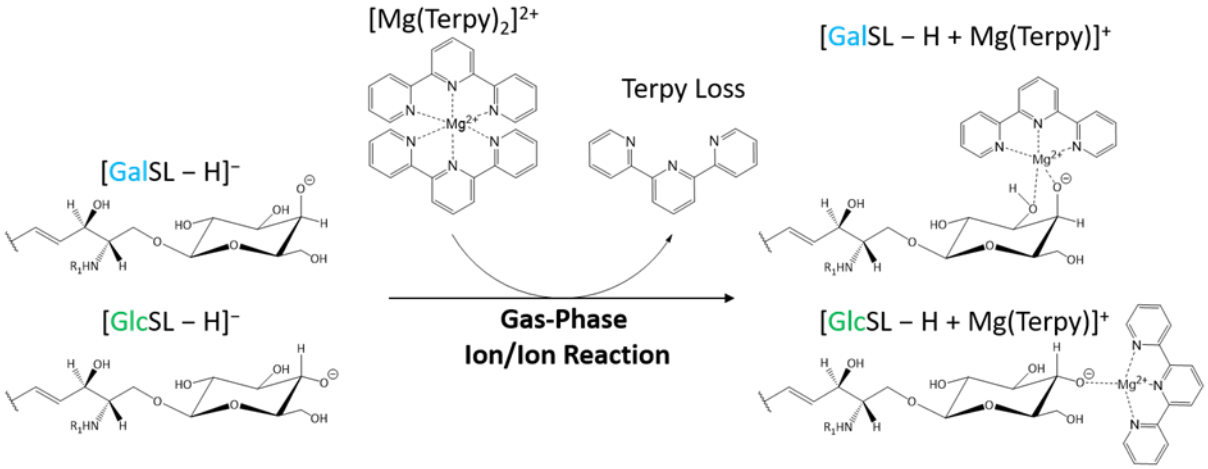

Scheme 4.1. The gas-phase ion/ion reaction between deprotonated GSLs and $[Mg(Terpy)_2]^{2+}$. Note that the multiple structures that solvate the Mg^{2+} ion can contribute. However, the mixture of structures differs for the two diastereomers.

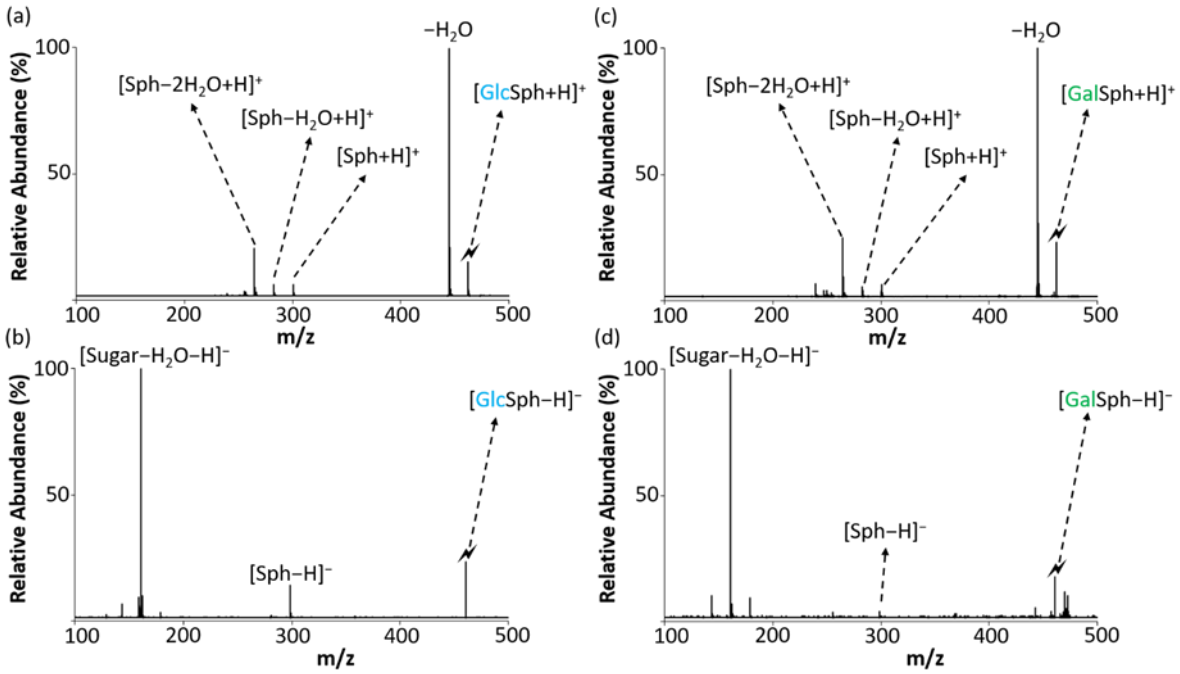

Figure 4.2. The CID spectra of protonated and deprotonated HexSphs. (a) The CID spectrum of $[GlcSph+H]^+$. (b) The CID spectrum of $[GlcSph-H]^-$. (c) The CID spectrum of $[GalSph+H]^+$. (b) The CID spectrum of $[GalSph-H]^-$.

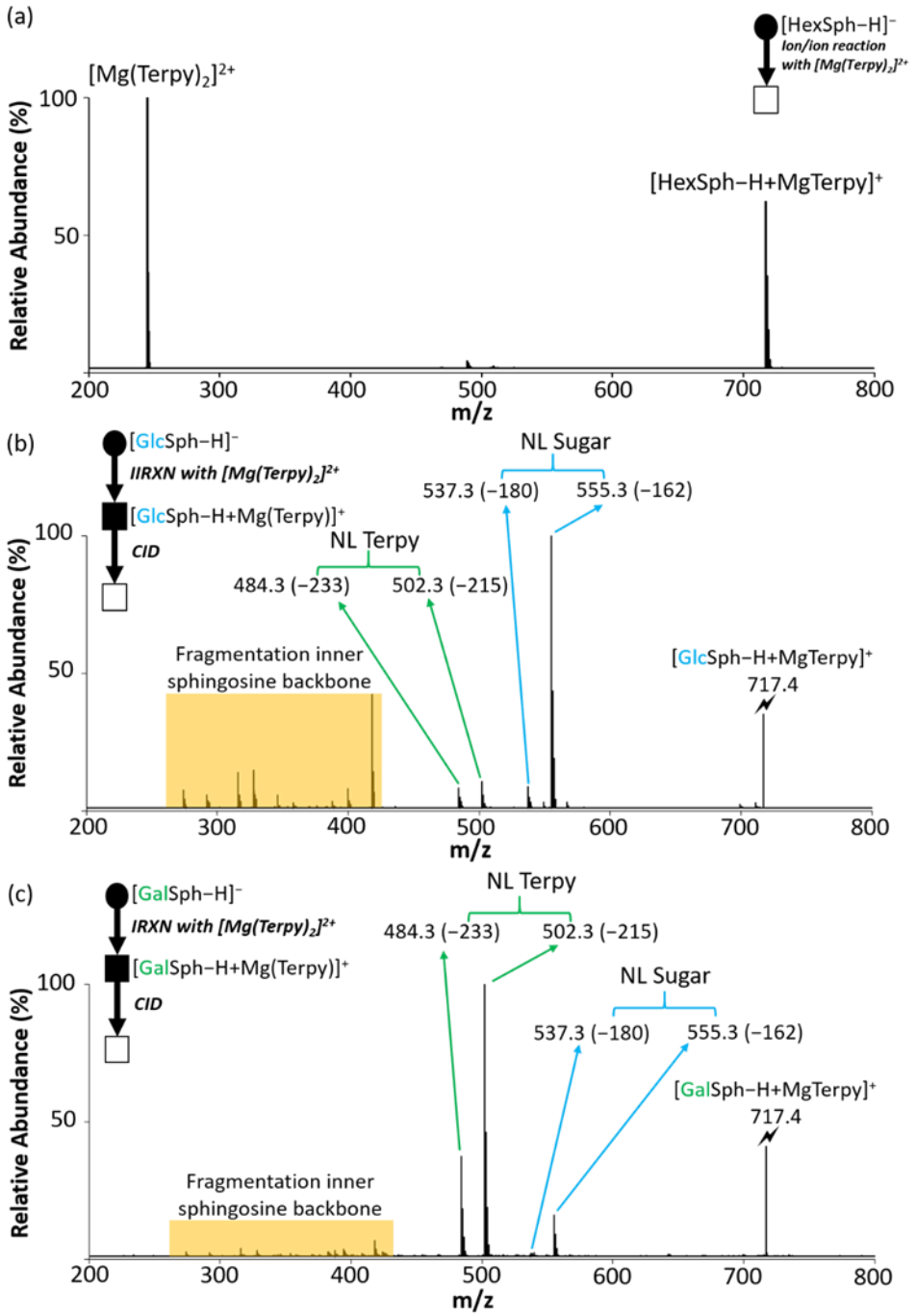

Figure 4.3. The comparison of the CID spectra between glycosphingosine after gas-phase ion/ion reaction. (a) The post-ion/ion reaction spectrum of HexSph anion with $Mg(Terpy)_2$ cation. (b) The CID spectrum of the $[GlcSph–H+ MgTerpy]^+$ (m/z 717.4) . (c) The CID spectrum of the $[GalSph–H+MgTerpy]^+$ (m/z 717.4). The values inside the parenthesis indicate the neutral loss. The lightning bolt ( ) signifies collisionally activated precursor ion. The solid circle (●) indicates the mass selection in the negative ion mode analysis and the black and white squares (■/□) indicate the positive ion mode analysis with and without mass selection, respectively.

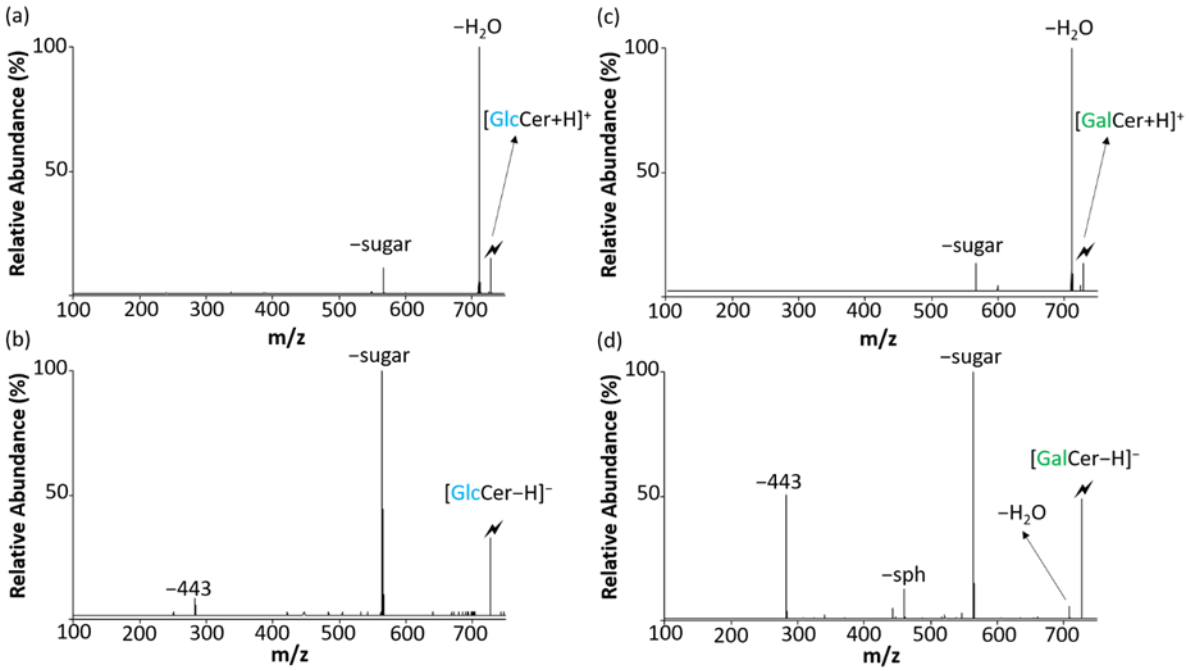

Figure 4.4. The CID spectra of protonated and deprotonated cerebrosides. (a) The CID spectrum of $[GlcCer(d18:1/18:0)+H]^+$. (b) The CID spectrum of $[GlcCer(d18:1/18:0)-H]^-$. (c) The CID spectrum of $[GalCer(d18:1/18:0)+H]^+$. (d) The CID spectrum of $[GalCer(d18:1/18:0)-H]^-$.

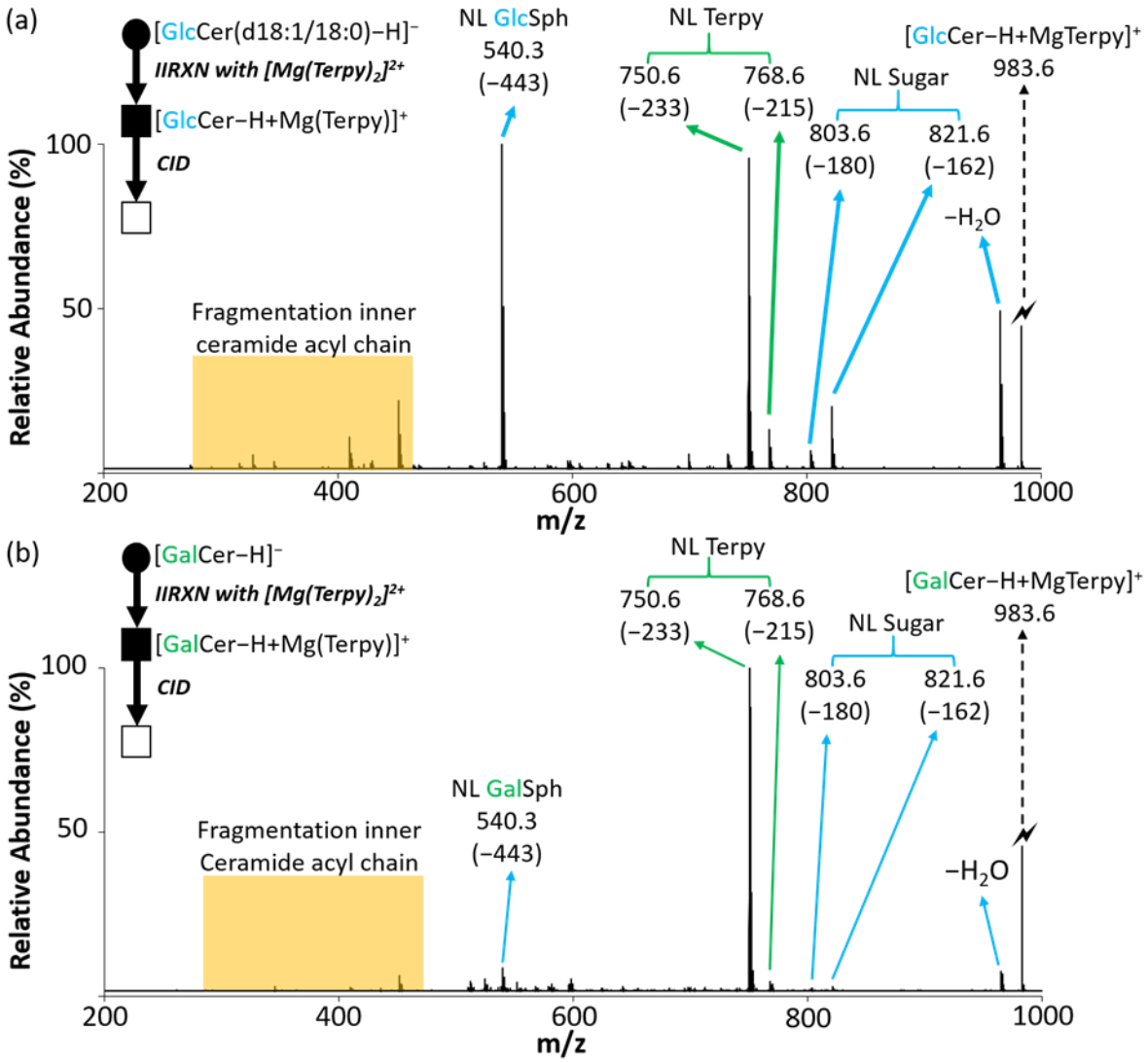

Figure 4.5. The comparison of the CID spectra between cerebrosides after gas-phase ion/ion reaction. (a) The CID spectrum of the [GlcCer(d18:1/18:0)–H+MgTerpy]$^+$ complex (*m/z* 983.6) generated via gas-phase ion/ion reaction between singly deprotonated GlcCer anion and [Mg(Terpy)$_2$]$^{2+}$. (b) The CID spectrum of the [GalCer(d18:1/18:0)–H+MgTerpy]$^+$ complex (*m/z* 983.6) generated via gas-phase ion/ion reaction between singly deprotonated GalCer anion and [Mg(Terpy)$_2$]$^{2+}$. The values inside the parenthesis indicate the neutral loss. The lightning bolt ( ) signifies collisionally activated precursor ion. The solid circle (●) indicates the mass selection in the negative ion mode analysis and the black and white squares (■/□) indicate the positive ion mode analysis with and without mass selection, respectively.

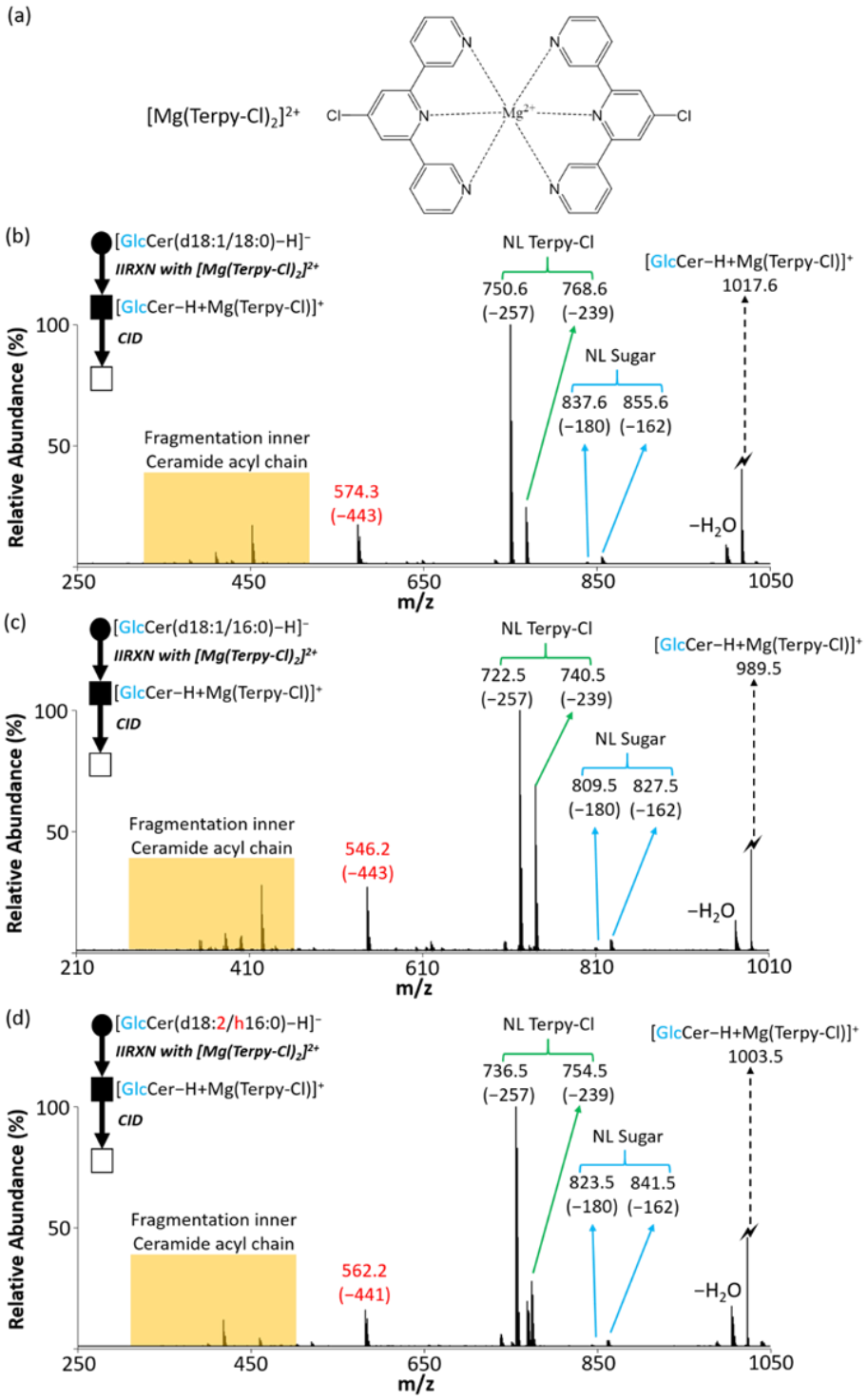

Figure 4.6. (a) The structure of $Mg(Terpy\text{-}Cl)_2$. (b) The CID spectrum of the $[GlcCer(d18:1/18:0)–H+Mg(Terpy\text{-}Cl)]^+$ complex (*m/z* 1017.6). (c) The CID spectrum of the $[GlcCer(d18:1/16:0)–H+Mg(Terpy\text{-}Cl)]^+$ complex (*m/z* 989.5). (d) The CID spectrum of the $[GlcCer(d18:1/16:0)–H+Mg(Terpy\text{-}Cl)]^+$ complex (*m/z* 1003.5).

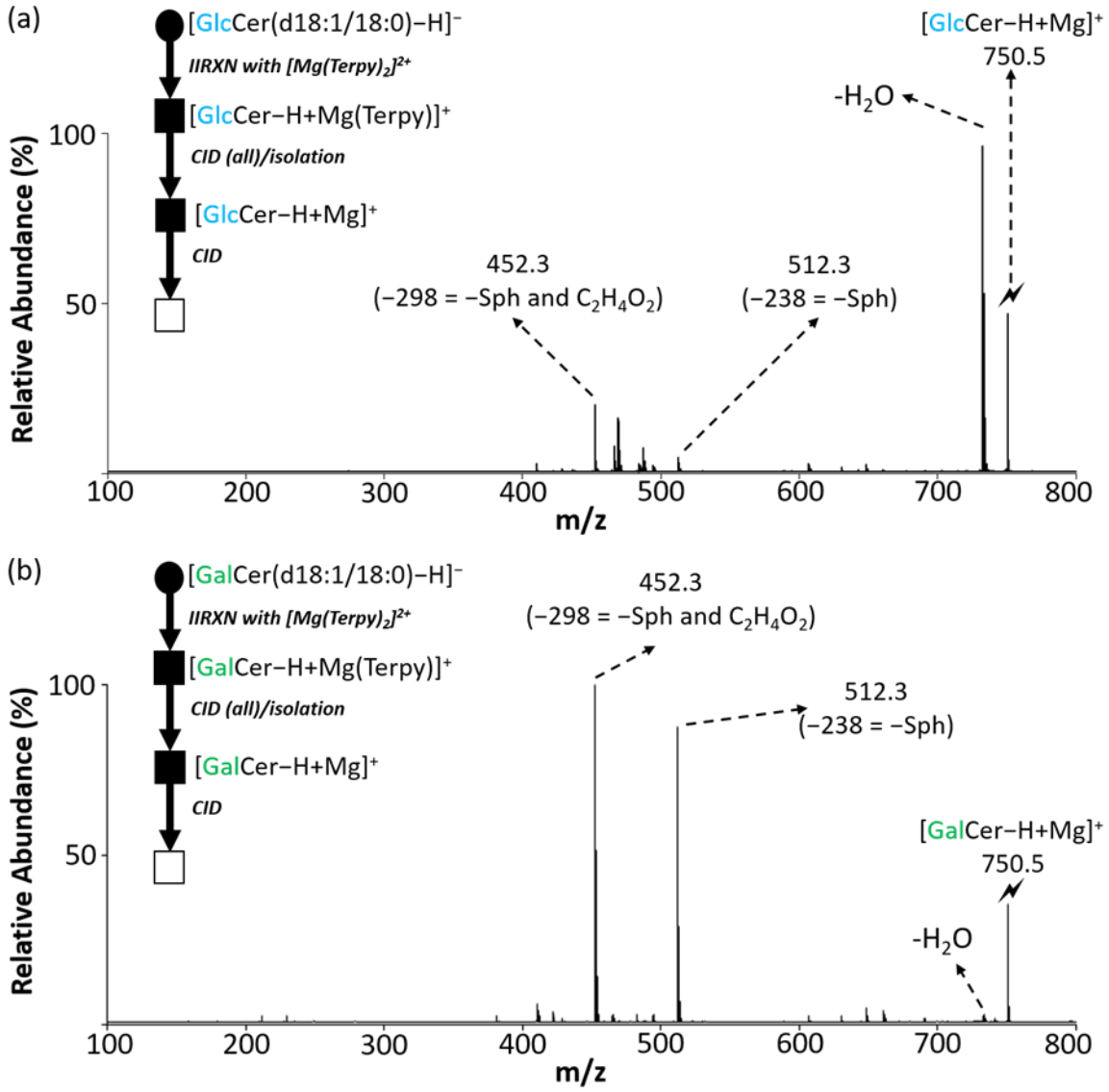

Figure 4.7. (a) MS^3 product ion spectrum of $[GlcCer(d18:1/18:0)–H+Mg]^+$ (*m/z* 750.5) derived from Terpy loss from $[GlcCer(d18:1/18:0)–H+MgTerpy]^+$. (b) MS^3 product ion spectrum of $[GalCer(d18:1/18:0)–H+Mg]^+$ (*m/z* 750.5) derived from Terpy loss from $[GalCer(d18:1/18:0)–H+MgTerpy]^+$.

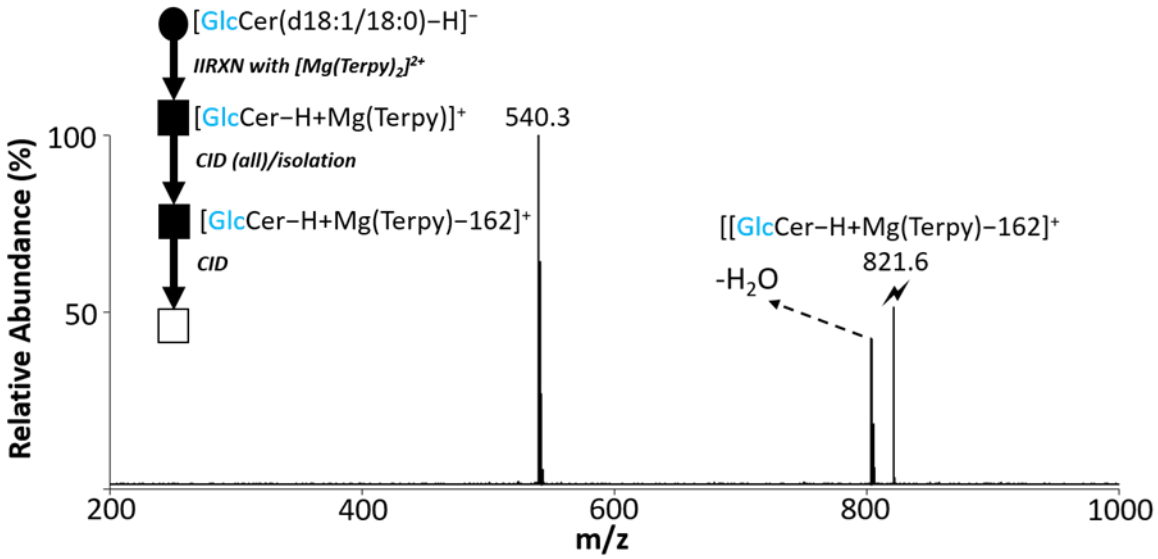

Figure 4.8. MS^3 product ion spectrum of $[GlcCer(d18:1/18:0)–H+Mg(Terpy)−162]^+$ (*m/z* 821.6) derived from sugar loss from $[GlcCer(d18:1/18:0)–H+MgTerpy]^+$.

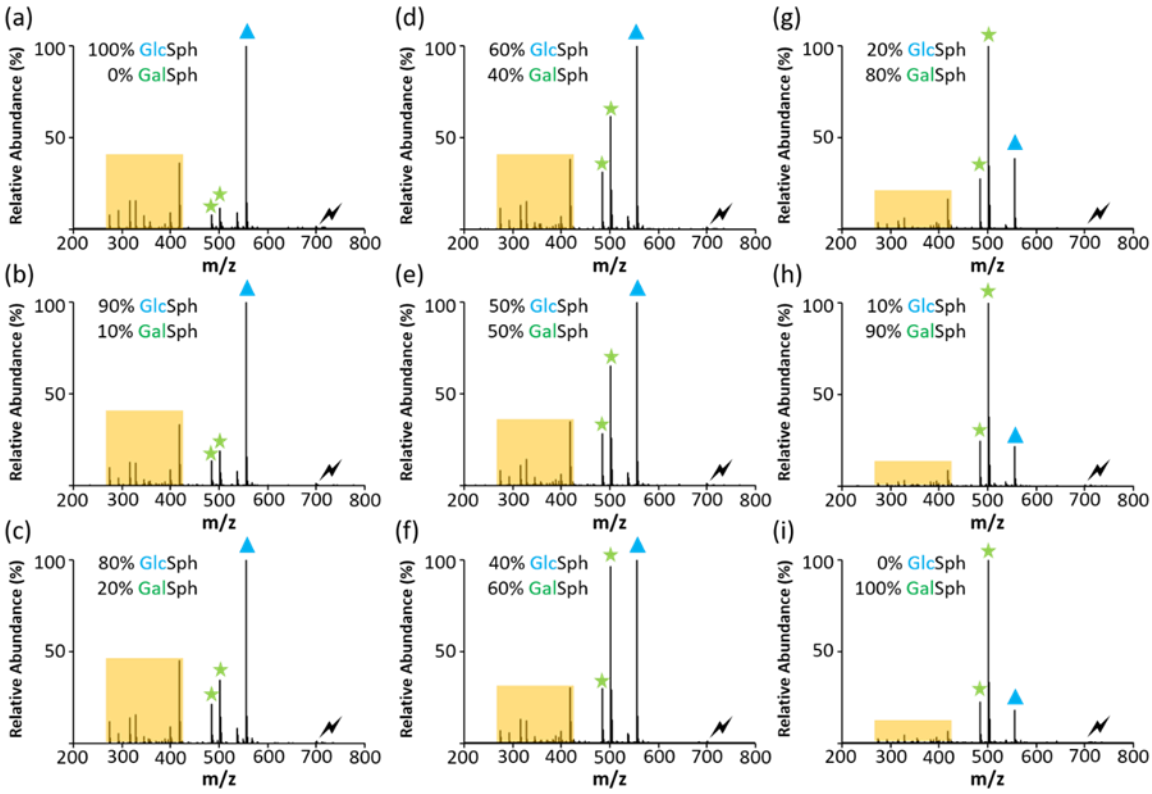

Figure 4.9. The CID spectra of the $[HexSph - H + MgTerpy]^+$ complex with different molar ratios of lyso-GSLs in the sample. The lightning bolt (↯) signifies collisionally activated precursor ion. The blue triangle (▲) indicates the fragment ion from NL of sugar and the green stars (★) indicate the fragment ion from NL of Terpy ligand. Yellow box are the fragment ions mostly from the sphingosine chain/sugar head group.

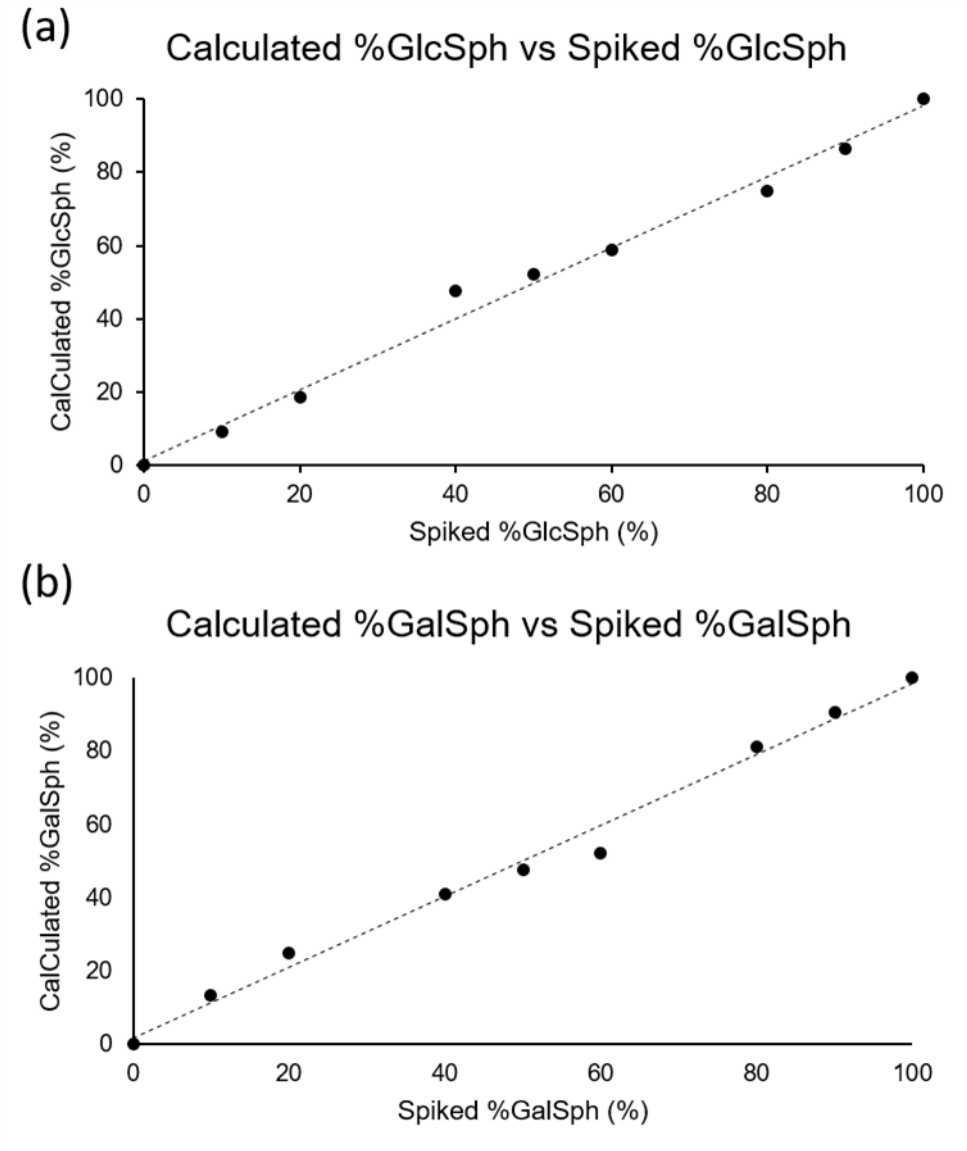

Figure 4.10. The correlations between calculated %HexSph and spiked %HexSph. (a) GlcSph-d18:1 and (b) GalSph-d18:1.

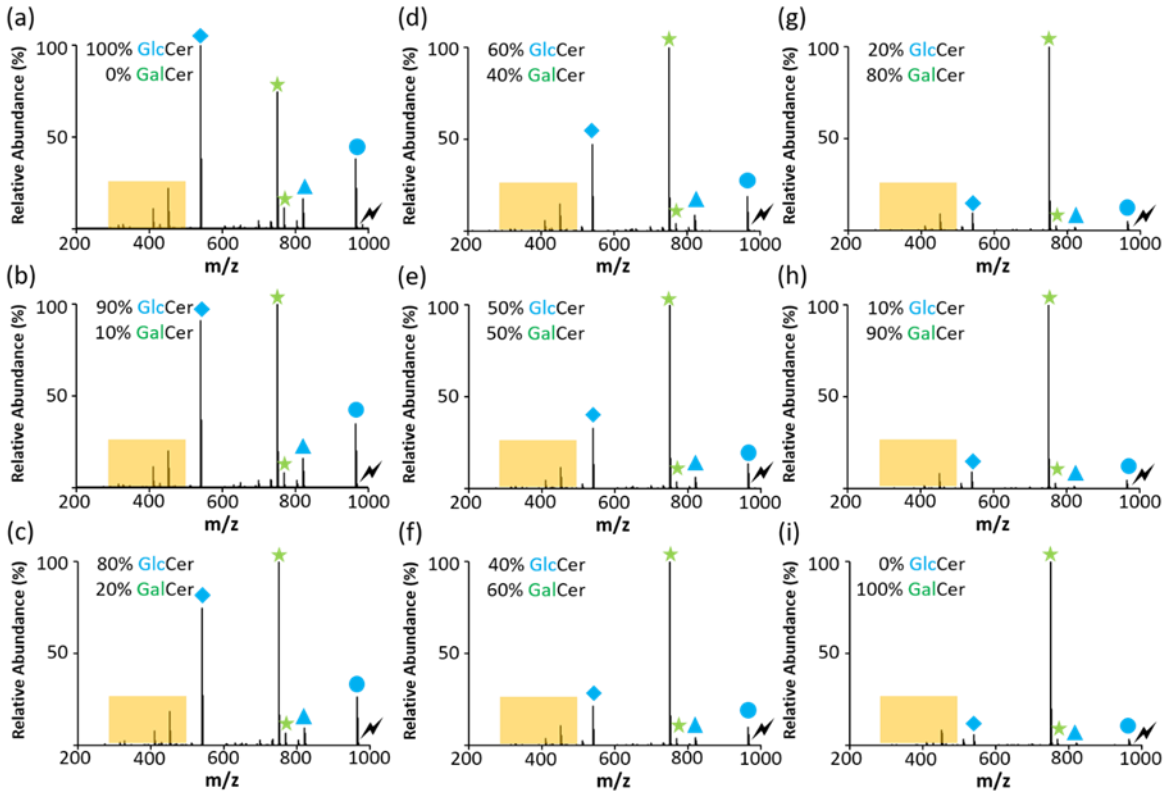

Figure 4.11. The CID spectra of the [HexCer –H + MgTerpy]$^+$ complex with different molar ratios of cerebrosides in the sample. The lightning bolt (↯) signifies collisionally activated precursor ion. The blue symbols indicates the group of fragment ions from NL of other ions, including triangle (▲, NL of sugar; ●, NL of water; and ◆, NL of 443), and the green stars (★) indicate the fragment ion from NL of Terpy ligand. Yellow box are the fragmented ions mostly from ceramides chains.

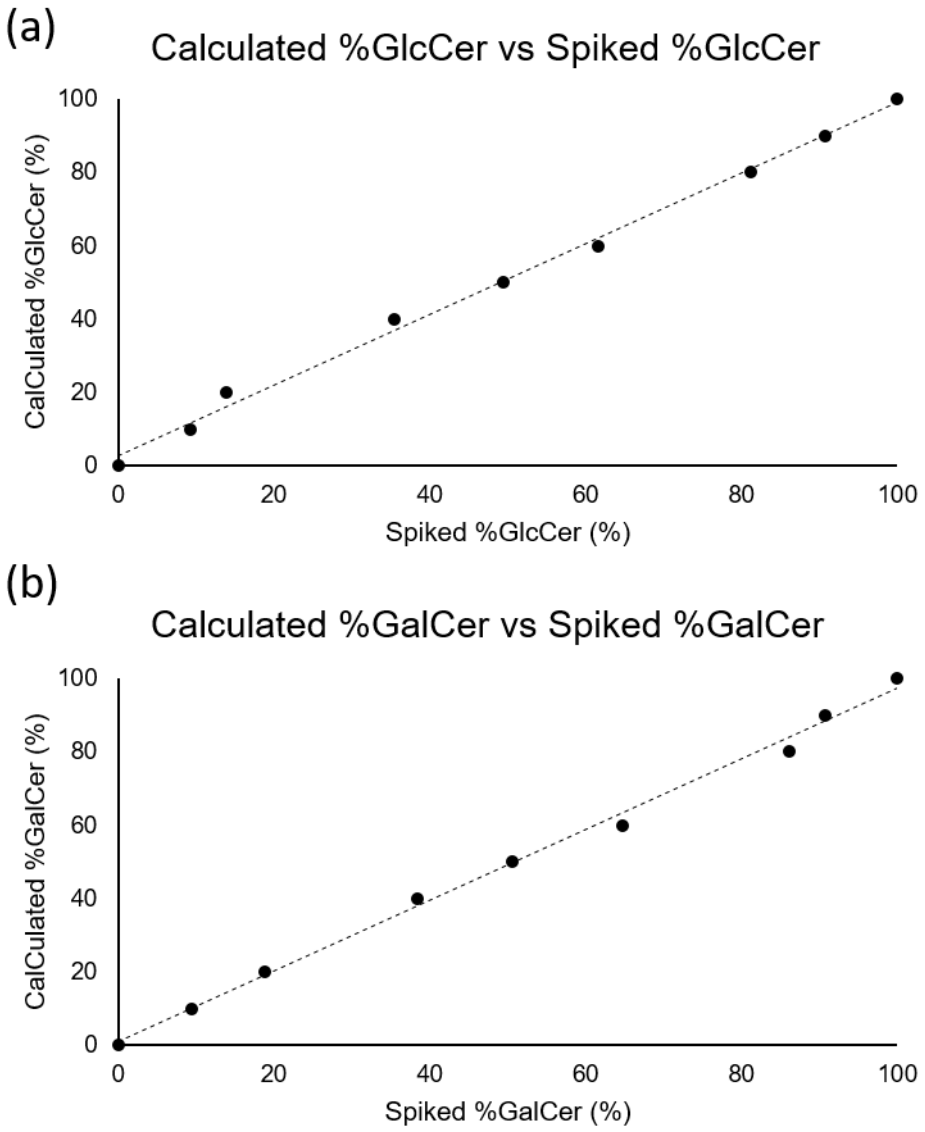

Figure 4.12. The correlations between calculated %HexCer and spiked %HexCer. (a) GlcCer(d18:1/18:0) and (b) GalCer(d18:1/18:0).

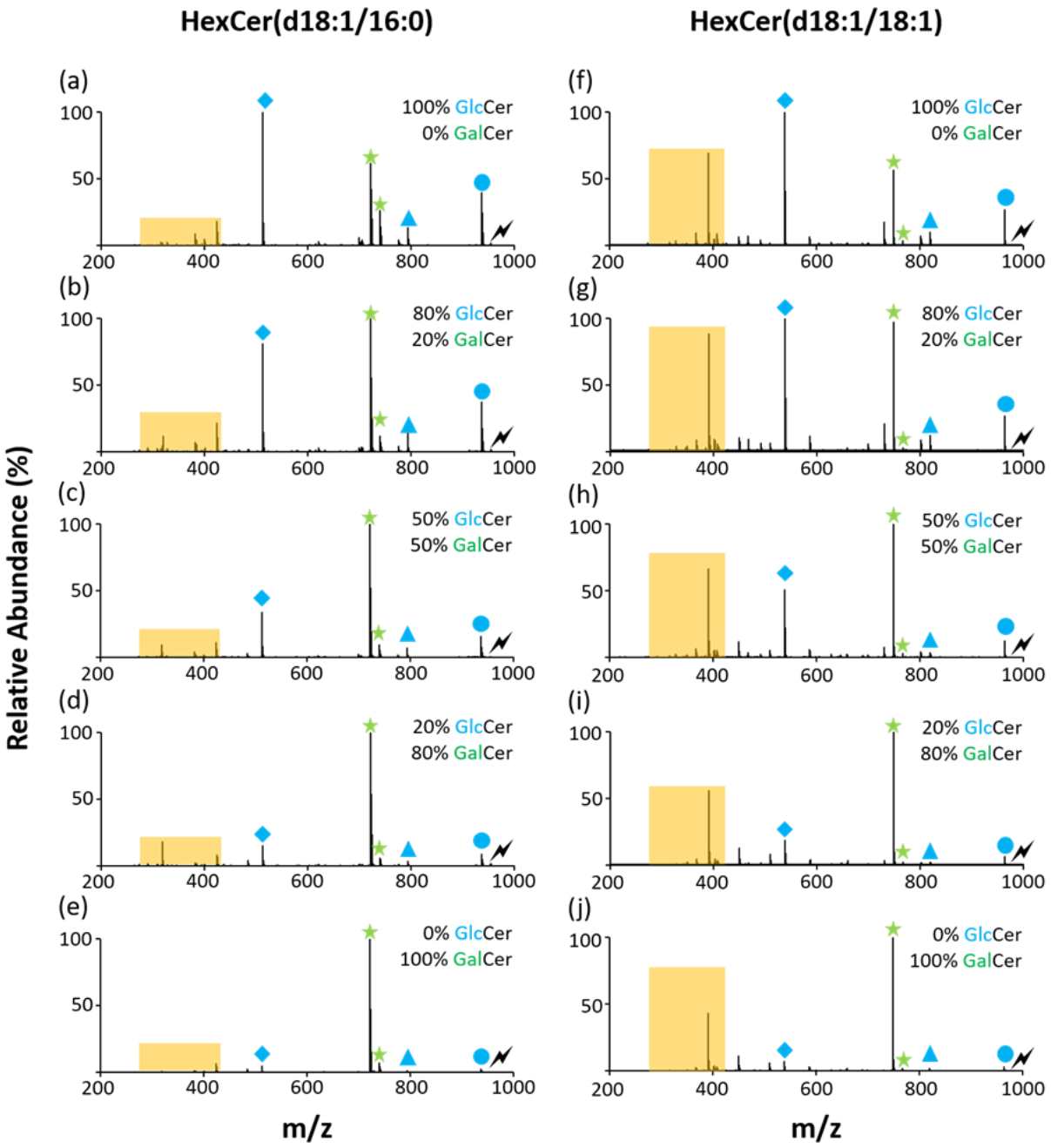

Figure 4.13. The CID spectra of the [HexCer(d18:1/16:0) –H + MgTerpy]$^+$ and [HexCer(d18:1/18:1) – H + MgTerpy]$^+$ complex with different molar ratios in the sample. The lightning bolt (🗲) signifies collisionally activated precursor ion. The blue symbols indicates the group of fragment ions from NL of other ions, including triangle (▲, NL of sugar; ●, NL of water; and ◆, NL of 443), and the green stars (★) indicate the fragment ion from NL of Terpy ligand. Yellow box are the fragment ions mostly from ceramides chains.

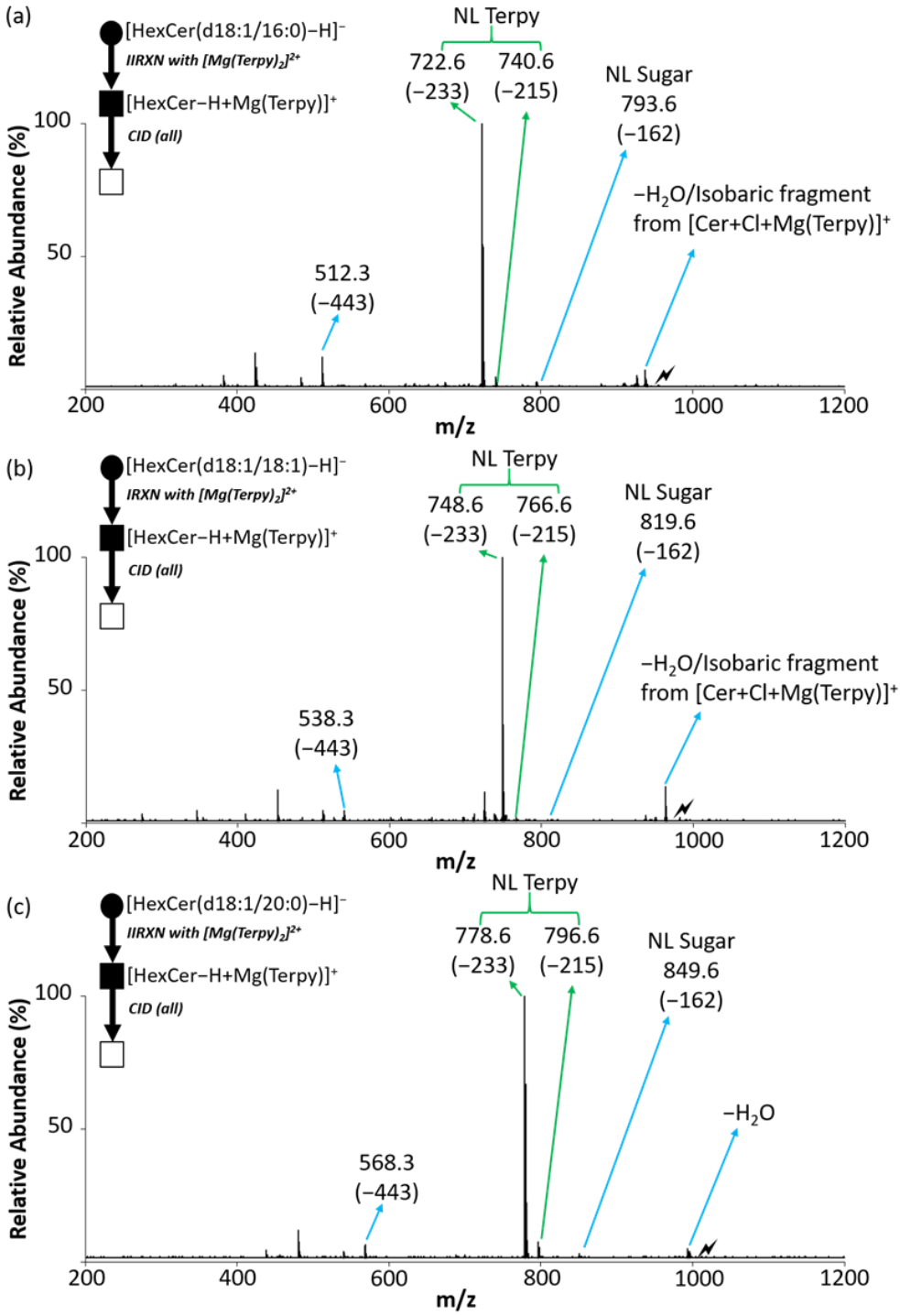

Figure 4.14. The CID spectra of [HexCer – H + MgTerpy]+ from the profiled cerebrosides in the total cerebroside extracts from porcine brain. (a) HexCer(d18:1/16:0). (b) HexCer(d18:1/18:1). (c) HexCer(d18:1/20:0). (d) HexCer(d18:1/22:0). (e) HexCer(d18:1/23:0). (f) HexCer(d18:1/24:1). (g) HexCer(d18:1/24:0). (h) HexCer(d18:1/26:1). (i) HexCer(d18:1/26:0).

Figure 4.14 continued

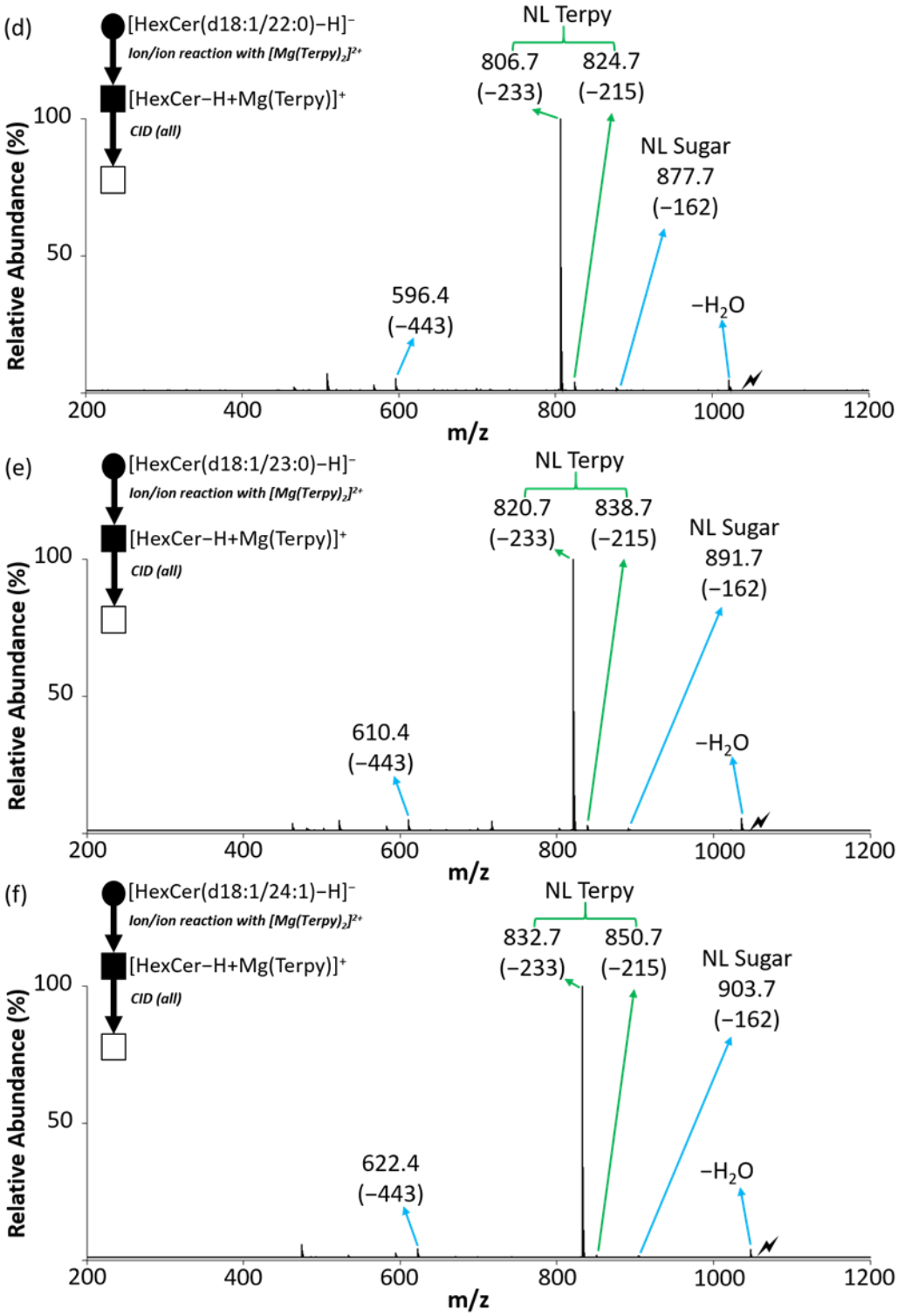

Figure 4.14 continued

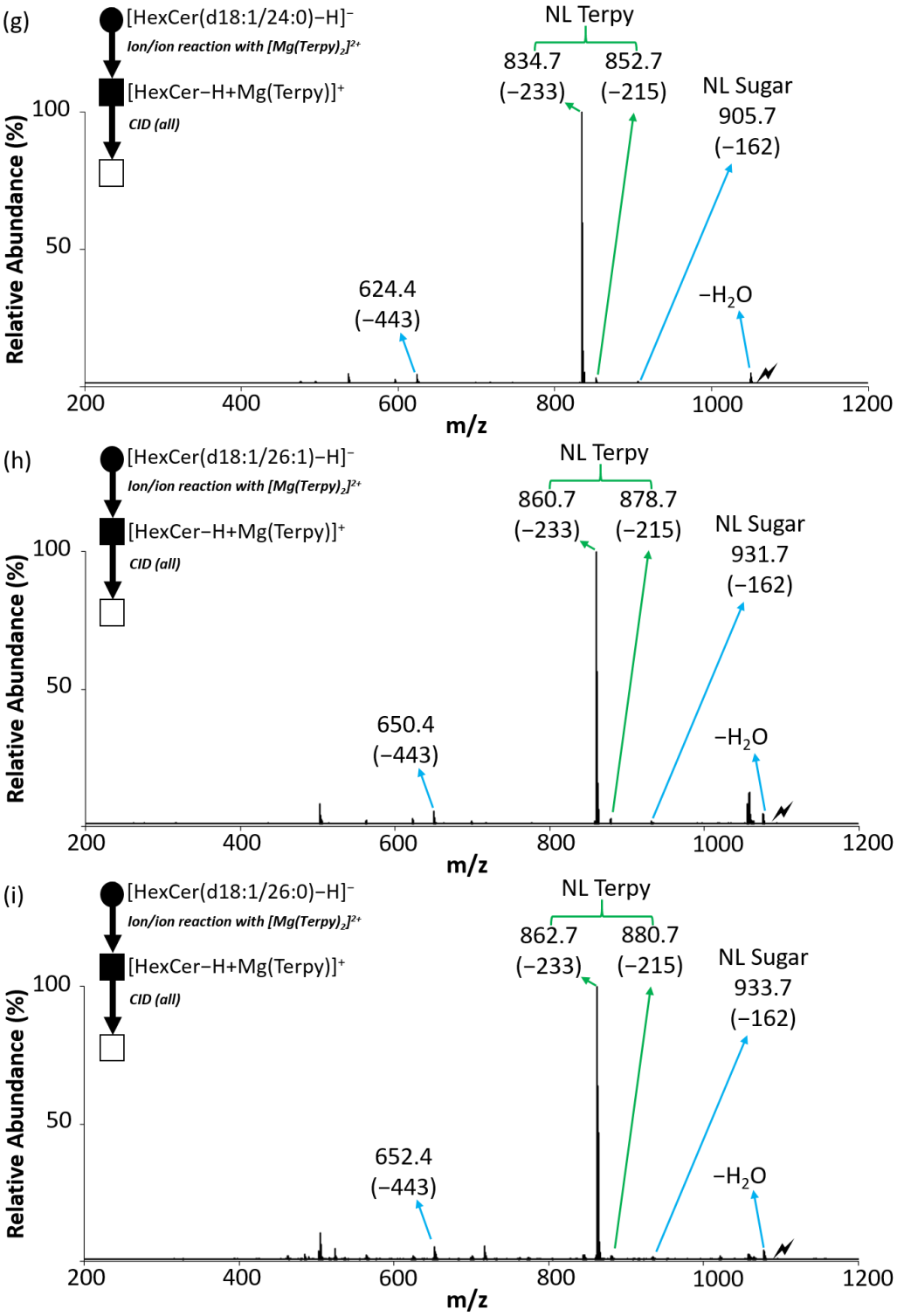

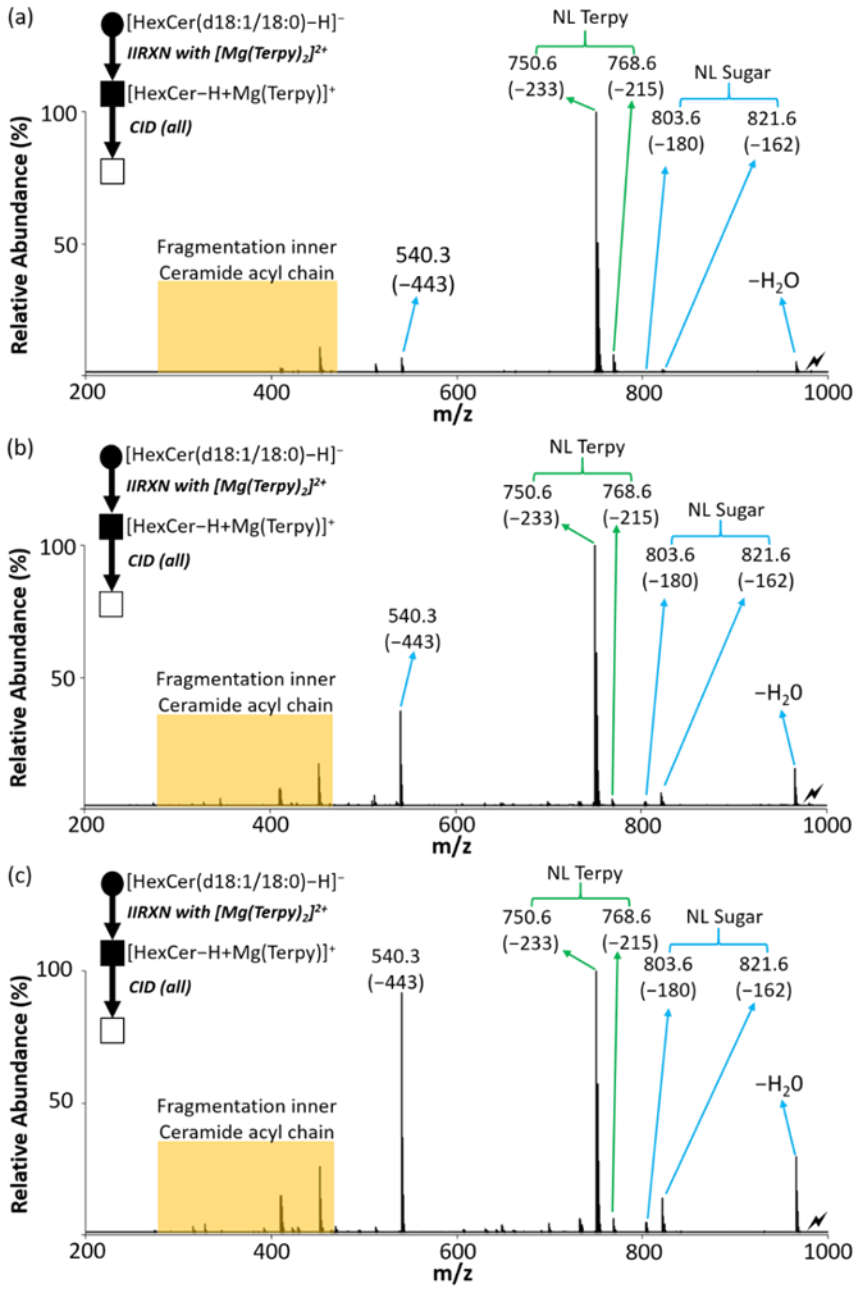

Figure 4.15. The single standard spiking strategy for absolute quantitation of GSLs in total brain extract. (a) The CID spectrum of the [HexCer(d18:1/18:0)–H+MgTerpy]$^+$ complex (*m/z* 983.6) without spiking any standard. (b) The CID spectrum of the [HexCer(d18:1/18:0)–H+MgTerpy]$^+$ complex with spiking low concentration of GlcCer(d18:1/18:0). (c) The CID spectrum of the [HexCer(d18:1/18:0)–H+MgTerpy]$^+$ complex with spiking high concentration of GlcCer(d18:1/18:0). The values insides the parenthesis indicate the neutral loss. The lightning bolt ( ) signifies the location of the fully depleted precursor ion. The solid circle (●) indicates the mass selection in the negative ion mode analysis and the black and white squares (■/□) indicate the positive ion mode analysis with and without mass selection, respectively.

CHAPTER 5. IN-DEPTH STRUCTURAL CHARACTERIZATION AND QUANTIFICATION OF CEREBROSIDES AND GLYCOSPHINGOSINES WITH GAS-PHASE ION CHEMISTRY

Abstract

Cerebrosides (n-HexCer) and glycosphingosines (n-HexSph) constitute two sphingolipid subclasses. Both are comprised of a monosaccharide head group (glucose or galactose in mammalian cells) linked via either an alpha- or beta- glycosidic linkage to the sphingoid backbone (n = α or β, depending upon the nature of the linkage to the anomeric carbon of the sugar). Cerebrosides have an additional amide-bonded fatty acyl chain linked to the sphingoid backbone. While differentiating the multiple isomers (i.e., glucose vs. galactose, α- vs. β-linkage) is difficult, it is crucial for understanding their specific biological roles in health and disease states. Shotgun mass spectrometry has been a powerful tool in both lipidomics and glycomics analysis but is often limited in its ability to distinguish isomeric species. In this this chapter, we exteneded the previous strategy using shotgun mass spectrometry with gas-phase ion chemistry to achieve both differentiation and quantification of isomeric cerebrosides and glycosphingosines. Briefly, $[\text{n-HexCer}-\text{H}]^-$ or $[\text{n-HexSph}-\text{H}]^-$, are reacted with $[\text{Mg(Terpy)}_2]^{2+}$ in the gas phase to produce $[\text{n-HexCer}-\text{H}+\text{MgTerpy}]^+$ or $[\text{n-HexSph}-\text{H}+\text{MgTerpy}]^+$. CID of the product cations leads to significant spectral differences between the two groups of isomers, α-GalCer, β-GlcCer, and β-GalCer for cerebrosides, and α-GlcSph, α-GalSph, β-GlcSph, and β-GalSph for glycosphingosines, which allows for isomer distinction. Moreover, we describe a quantification strategy using normalized %Area extracted from selected diagnostic ions to quantify three isomeric cerebroside or four isomeric glycosphingosine mixtures. Furthermore, CID of the product ions resulting from 443 Da loss from the ($[\text{n-HexCer}-\text{H}+\text{MgTerpy}]^+$) is performed and demonstrated for localizing the double bond position on the amide-bonded monounsaturated fatty acyl chain in the cerebroside structure. The proposed strategy was successfully applied to the analysis of total cerebroside extracts from the porcine brain providing in-depth structural information of cerebrosides from a biological mixture. (**Scheme 5.1**)

5.1 Introduction

Cerebrosides (HexCer) and glycosphingosines (HexSph) constitute two subclasses of glycosphingolipids. Both are comprised of a monosaccharide head group and a sphingoid base backbone, while HexCers also have a fatty acyl chain that links to the base with an amide bond.[1] In mammalian systems, the *de novo* synthesis pathway generates most of the glycosphingolipids (GSLs) with either glucose or galactose as the head group. The sugars are linked to the sphingoid backbone via a beta-glycosidic linkage (β-linkage) or an alpha-glycosidic linkage (α-linkage), with the former dominating in mammalian cells.[2-3] Due to the difficulty of differentiating isomers, they are usually reported as a single cerebroside, thereby preventing the recognition of possible differences in function of the isomers in a biological system.[4-6]

Advances in analytical techniques have led to some strategies for the differentiation of the diastereomerism between glucose and galactose head group on lipids, including liquid chromatography coupled with mass spectrometry (LC-MS)[7-11] and shotgun mass spectrometry.[12-13] The former methods usually require long separation times while the latter requires offline sample pretreatment steps. Recently, our group reported a shotgun mass spectrometry approach employing gas-phase ion/ion chemistry to differentiate and quantify diastereomeric pairs of glycosphingosines and cerebrosides in binary mixtures without recourse to condensed-phase derivatization. The reaction of deprotonated glycosphingolipids, $[GSL-H]^-$, with magnesium-terpyridine complex dications, $[Mg(Terpy)_2]^{2+}$, leads to complex cations, $[GSL-H + MgTerpy]^+$, that generate different fragmentation patterns upon ion-trap collisional-induced dissociation (CID), providing the ability to unambiguously identify diastereomeric pairs and their relative compositions in the mixtures.[14]

In recent decades, attention has been drawn to α-linked cerebrosides for their roles in mediating the immune system in various models.[15] Alpha-galactosylceramides (α-GalCer), for example, have been demonstrated to be a substrate for type I natural killer T cells that could be used for regulating innate immunity by activating the costimulatory signals with both NKT cells and dendritic cells.[16-17] This makes α-GalCer a potential drug motif for the immunotherapy of different autoimmune diseases and cancers.[18] Therefore, while the natural *de novo* synthetic pathway of GSLs in mammals strongly disfavors α-glycosidic linked GSLs,[19] differentiation of the anomeric α- and β- glycosidic linkages may be needed for various biomedical studies. We show below how an α-glycosidic linked GSL can be used as an internal standard for the absolute

quantitation of isomeric β-glycosidic linked GSLs. Most of the studies that have involved α-GalCer identification relate to synthesis, wherein nuclear magnetic resonance (NMR) was used for the characterization of the products.[20-22] However, it is often a challenge for NMR to analyze complex matrices often associated with biological samples (e.g., cell extracts). Recently, cryogenic gas-phase infrared (IR) action spectroscopy has been demonstrated to be able to distinguish anomeric glycosidic linkages in glycolipids. However, this requires both incorporation of specialized IR techniques with mass spectrometry and post-acquisition spectra fitting.[23] Therefore, a simple mass spectrometry based strategy that can directly probe the anomeric glycosidic bond is needed.

Several strategies to differentiate the anomericity of the glycosidic bonds via mass spectrometry have been described. Most of the methods include cationization by different metal ions, such as alkali metal ions,[24-25] alkaline earth metal ions,[26] and transition metal ions,[27-28] in which the fragmentation patterns yield different results after the activation of the metal ion-saccharide complexes. Salpin et al., for example, reported a lead ion adduction method in which the CID spectrum of $[Pb(disaccharide)-H]^+$ gave different base peaks and fragmentation fingerprints from different glycosidic linkages.[29] The specific ion type, $[Pb(disaccharide)-H]^+$, is analogous to the charge-inverted complex cations from the gas-phase ion/ion reaction described herein. However, addition of metal salts to the sample solution often leads to variations in yields and increased complexity of the mass spectrum, which may cause additional analytical problems. Moreover, none of the above methods demonstrated the ability to identify different glycosidic linked isomers in a mixture.

Quantifying isomeric mixture components presents a further challenge. To our knowledge, there are no reported methods for differentiating and quantifying both α- and β-glycosidic linkages and their different head groups simultaneously for cerebrosides and glycosphingosines with shotgun mass spectrometry. Therefore, in this work we describe a shotgun mass spectrometry strategy using ion chemistry to chemically modify both cerebroside and glycosphingosine ions in the gas phase to differentiate stereoisomers and achieve both relative and absolute quantification with a single spiking test that requires less use of analytical standards.

In addition to the structural complexities associated with the saccharide head groups in glycosphingolipids, the amide-bonded fatty acyl chain can add to the overall challenge of fully characterizing the lipid species. For example, reports have suggested that signaling functions of sphingolipids are related to fatty acyl chain length.[30-31] In the case of unsaturated fatty acyl chains,

locating the double bond can be particularly challenging. The different fatty acyl side chains (i.e., chain length and degree and location of unsaturation) have also been shown to influence the effect of α-GalCer on immune response.[32] Previous reports have demonstrated the use of reversed-phase LC-MS to differentiate the fatty acyl chain, but the poor ability for differentiating hydrophilic groups hinders the distinction of the monosaccharide head group.[33-35] Besides orthogonal separation techniques, various dissociation methods including ultraviolet photodissociation (UVPD)[36] and ozone induced dissociation (OzID)[37-38] have been demonstrated to identify the double bond position of the unsaturated fatty acyl chain in glycosphingolipids. Using gas-phase ion chemistry coupled with ion-trap CID, our group has also presented the ability to identify the double positions in various lipid classes, including fatty acids,[39-40] glycerolphospholipids,[41-42] and fatty acid esters of hydroxy fatty acids.[43] Therefore, in this work we also demonstrate that gas-phase ion chemistry coupled with tandem mass spectrometry (MS^3) can differentiate the double bond position on the amide-bonded monounsaturated fatty acyl chain in cerebrosides. Overall, we present a shotgun strategy that couples gas-phase ion/ion chemistry with ion-trap CID to provide in-depth structural information (**Figure 5.1**) and the relative composition of cerebrosides and glycosphingosines in mixtures.

5.2 Experimental

5.2.1 Materials

All lipid standards and total cerebrosides extract (porcine brain) were purchased from Avanti Polar Lipids, Inc (Alabaster, AL). Magnesium chloride ($MgCl_2$) and 2,2';6',2"-terpyridine (Terpy) were purchased from Sigma-Aldrich (St. Louis, MO). MS-grade water and methanol (MeOH) were purchased from Fisher Scientific (Pittsburgh, PA).

5.2.2 Sample Preparation

Solutions of cerebrosides and glycosphingosine standards were prepared in MeOH to a final concentration of 0.01 mg/mL. $MgCl_2$ and Terpy were mixed in methanolic solution with 1:1 (molar ratio) to a final concentration of ~50 μM for the metal-ligand complex.[20] For relative quantification, different ratios of isomeric cerebrosides or glycosphingosine solutions were prepared, holding the final lipid concentration at 0.01 mg/mL. For total cerebrosides extract

analysis, 1 mg of purified extract powder was dissolved in 1 mL of methanol as the stock solution and stored at −20°C before use. Prior to analysis, the lipid extract was diluted with MS grade MeOH to a final concentration of 0.01 mg/mL.

5.2.3 Mass Spectrometry

All experiments were performed on a TripleTOF 5600 quadrupole time-of-flight mass spectrometer (SCIEX, Concord, ON, Canada) that has been modified for ion/ion reactions.[44] Alternately pulsed dual nano-electrospray ionization (nESI) allows for the sequential injection of anions and cations.[45] The experimental procedures were similar to reported previously.[14] In short, lipid anions ($[GSL-H]^-$) and metal-ligand reagent dications ($[Mg(Terpy)_2]^{2+}$) were alternately generated via nESI, mass-selected in Q1, and transferred to q2 for mutual storage (10-30 ms). Sequential resonance ejection ramps in q2 were used to mass-select targeted ion/ion reaction product ions for MS^n experiments.[46] Ion-trap CID was performed under the following conditions: q=0.2, AC amplitudes = 0.115V (n-HexCer complex); 0.078V (n-HexSph complex), activation time = 150 ms, and the CAD gas pressure set at 8 (estimated to be 8 mtorr). Mass analysis was performed via orthogonal acceleration time-of-flight (TOF).

5.2.4 Dissociation Kinetic Study

The dissociation rate experiments were conducted with dipolar direct current (dipolar DC, DDC) activation of the ions. Dipolar DC was implemented as previously reported.[47] After the charge-inverted cerebroside complex cation was produced and isolated in the q2 cell, a fixed amplitude of DDC, at 20V, was applied to opposing rods with various times, including 50, 100, 150, 200, and 250 ms. The RF voltage for the q2 cell was fixed at the value for which m/z 100 was at q = 0.908 (low-mass cutoff = m/z 100) for the DDC broadband activation. The integrated areas under the curves of the precursor complex cation ([n-GalCer(d18:1/16:0−H + Mg(Terpy)]+) were extracted and normalized to the total ion count (TIC) through the whole collected m/z range. A total of three replicates were tested at each time point. The kinetic plot was plotted with the logarithm of the mean of the normalized areas versus times (ms). Linear regression analyses were performed, and the reported p-value of the difference between the slope was tested with a modified student t-test via Microsoft Excel.

5.2.5 Analytical Performance Evaluation.

The analytical performance was evaluated for accuracy, repeatability, and inter-day precision. Various cerebroside mixtures (α-GalCer(d18:1/16:0)/β-GlcCer(d18:1/16:0)/β-GalCer(d18:1/16:0)) with different molar ratios, including 1/0/0, 0/1/0, 0/0/1, 1/1/0, 1/0/1, 0/1/1, and 4/3/3 with a total cerebroside concentration of 0.01 mg mL-1 were prepared. Five replicates were used for the evaluation of the analytical performance. Glycosphingosine mixtures (α-GlcSph/α-GalSph/β-GlcSph/β-GalSph) with different molar ratios, including 1/0/0/0, 0/1/0/0, 0/0/1/0, 0/0/0/1, 1/1/0/0, 1/0/1/0, 1/0/0/1, 0/1/1/0, 0/1/0/1, 0/0/1/1, 0/1/2/2, 1/0/2/2, 2/2/1/0, 2/2/0/1, and 1/1/1/1 were also prepared and three replicates were used for evaluation. The accuracy was calculated based on the following **equation 5.1**:

$$\text{Accuracy (\%)} = \frac{\text{Calculated percentage of the GSL}}{\text{Theroetical percentage of the GSL}} \times 100\% \quad (\textbf{eq. 5.1})$$

The repeatability was expressed by the standard deviation of the calculated accuracy (n = 3 or 5). For inter-day precision, the individually prepared samples at different concentration ratios (n = 3 or 5) were analyzed on three non-consecutive days. Inter-day precision was calculated using **equation 5.2**:

$$\text{Inter} - \text{day Precision (\%RSD)} = \frac{\text{Standard deviation of the calculated percentage of the GSL}}{\text{Mean of the calculated percentage of the GSL}} \quad (\textbf{eq. 5.2})$$

5.2.6 Absolute Quantification

To achieve absolute quantification, a single amount of α-GalCer(d18:1/16:0) was spiked into an aliquot of the total cerebrosides solution. In brief, a total of 1μL of 0.001 mg mL^{-1} of α-GalCer(d18:1/16:0) was added to a 99 μL aliquot of the cerebrosides solution. Three replicates were used to calculate the percentage of the all cerebroside isomers in the samples, and further back-calculated the absolute concentration in the total cerebrosides extracts solution using the known spiked amount of α-GalCer(d18:1/16:0) via **equations 5.3 and 5.4:**

$$\beta - \text{GlcCer}_{\text{sample}} = \frac{\%\beta - \text{GlcCer}_{\text{spiked}} \times \alpha - \text{GalCer}_{\text{spiked}}}{\%\,\alpha - \text{GalCer}_{\text{spiked}}} \quad (\textbf{eq. 5.3})$$

$$\beta - \text{GalCer}_{\text{sample}} = \frac{\%\beta - \text{GalCer}_{\text{spiked}} \times \alpha - \text{GalCer}_{\text{spiked}}}{\%\alpha - \text{GalCer}_{\text{spiked}}} \quad (\textbf{eq. 5.4})$$

where all the concentrations were expressed in μg mL-1, and can further back-calculate the amount of the cerebrosides in the total extract in the unit of ng mg-1. %α-GalCer, %β-GlcCer, and %β-GlcCer were the calculated percentages from the relative quantification.

5.3 Results and Discussion

5.3.1 Differentiation of Glycosidic Linkages and Monosaccharide Head Group of Cerebrosides via Gas-Phase Ion Chemistry

In the previous chapter (chapter 4) and report, an ion/ion reaction shotgun tandem mass spectrometry strategy to identify the diastereomeric pairs of cerebrosides in binary mixtures has been reported.[14] In summary, after producing the cerebroside complex cation, [HexCer−H + MgTerpy]$^+$, via ion/ion reaction and subjecting it to ion-trap CID, specific diagnostic product ion spectra from both [GlcCer−H+MgTerpy]$^+$ and [GalCer−H+MgTerpy]$^+$ were generated allowing us to differentiate and quantify the diastereomeric pair in the sample (**Figure 4.5**). In this chapter, we further extend this strategy to investigate the ability of gas-phase chemistry (i.e., ion/ion reaction followed by CID) to differentiate the anomericity of the glycosidic linkages in cerebrosides. **Figure 5.2** shows the gas-phase ion/ion reaction results and the mass spectra after ion-trap CID of the charge-inverted cerebroside complex cations, [α-GalCer(d18:1/16:0)–H+MgTerpy]$^+$ (*m/z* 955.6), [β-GlcCer(d18:1/16:0)−H+MgTerpy]$^+$ (*m/z* 955.6), and [β-GalCer(d18:1/16:0)–H+MgTerpy]$^+$ (*m/z* 955.6). We note that an α-glucosylceramide analytical standard was not commercially available at the time of this report, and therefore, our data only examines α-galactosylceramide. Paralleling previous observations, we observed that product ions with neutral loss (NL) of a single Terpy ligand (*m/z* 740.6, NL = 233 Da) and its subsequent water-adducted product (*m/z* 722.6, NL = 215 Da) show the highest abundances in the CID spectrum of [β-GalCer(d18:1/16:0)–H+MgTerpy]$^+$ (**Figure 5.2d**), and neutral loss of water (*m/z* 937.6) and neutral loss of 443 Da (**Figure 5.3**, *m/z* 512.3) are more prominent upon CID of [β-GlcCer(d18:1/16:0)–H+MgTerpy]$^+$ (**Figure 5.2c**). It was also noticeable that neutral losses associated with the sugar (NL = 162 Da and NL = 180 Da) are more significant in the CID spectrum of [β-GlcCer(d18:1/16:0)–H+MgTerpy]$^+$ than that of [β-GalCer(d18:1/16:0)–H+MgTerpy]$^+$. **Figure 5.2b** shows an even more significant loss of sugar in the CID spectrum of [α-GalCer(d18:1/16:0)–H+MgTerpy]$^+$, and there is almost no neutral loss of Terpy observed in the α-linked cerebroside CID spectrum.

The ease with which the Terpy ligand is lost from a given complex ion is related to how well the cerebroside can stabilize the Mg^{2+} ion and therefore reflects the interactions of the cerebroside with the $MgTerpy^{2+}$ adduct. In the previous chapter, we noted that the different orientations of the hydroxyl groups on the C3' and C4' positions on the sugar head group leads to differences in the stabilization of Mg^{2+}, and therefore propensities for the loss of the Terpy ligand for the two β-isomers (compare **Figures 5.2c** and **5.2d**).[14] The α-galactosylceramide has a similar C3'-C4' orientation to that of the β-galactosylceramide but no Terpy loss was observed from the α-galactosylceramide complex (compare **Figure 5.2b** to **Figure 5.2d**). Therefore, it is apparent that the two anomeric anions (viz., $[\alpha\text{-GalCer}-H]^-$ and $[\beta\text{-GalCer}-H]^-$) interact with the $MgTerpy^{2+}$ adduct in distinct ways.

Therefore, we measured the dissociation kinetics of the two charge-inverted galactosylceramide complex cations under a common set of activation conditions to determine their relative kinetic stabilities (see **section 5.2.4** for the description of the dissociation rate measurement). **Figure 5.4** shows that the $[\beta\text{-GalCer(d18:1/16:0)}–H+MgTerpy]^+$ complex is significantly less stable (i.e. it fragments at a 4-5x greater rate) than the $[\alpha\text{-GalCer(d18:1/16:0)}–H + MgTerpy]^+$ complex. Furthermore, the comparison of **Figures 5.2b** and **5.2d** shows that the two complexes differ dramatically in the Terpy loss fragmentation pathway (i.e., Terpy loss dominates for CID of $[\beta\text{-GalCer(d18:1/16:0)}–H+MgTerpy]^+$ whereas it is absent in the case of $[\alpha\text{-GalCer(d18:1/16:0)}–H + MgTerpy]^+$). The β-GalCer(d18:1/16:0) anion clearly stabilizes the Mg^{2+} ion more than does the α-GalCer(d18:1/16:0) anion thereby facilitating Terpy loss. This observation reflects the fact that cation interaction effects can play a major role in the dissociation of carbohydrate ions.[48] The distinct product ion spectra from the ion-trap CID of the charge-inverted cerebroside complex cations allow us to empirically differentiate the anomeric configuration of the glycosidic linkages between α- and β-, as well as the diastereomerism from the monosaccharide head group, glucose and galactose.

5.3.2 Differentiation of Glycosidic Linkages and Monosaccharide Head Group of Glycosphingosines via Gas-Phase Ion Chemistry

The same complexity of anomericity and diasteromericity can be found in glycosphingosines, making the analysis more challenged. Again, from the previous chapter (chapter 4, section 4.3.1), we have discussed how we differentiate the different monosacchride

head groups on glycosphingosine by coupling shotgun tandem mass spectrometry and gas-phase ion/ion reactions. In this section, we will focus on the differentiation of the anomericities among the glycosphingosine isomers. All four analytical standards, α-glucosylsphingosine (d18:1) (α-GlcSph), α-galactosylsphingosine (d18:1) (α-GalSph), β-glucosylsphingosine (d18:1) (β-GlcSph), and β-galactosylsphingosine (d18:1) (β-GalSph), were commercially available. Therefore, we performed the gas-phase ion/ion reaction with the deprotonated standards ($[\text{n-HexSph}-\text{H}]^-$) and $[\text{Mg(Terpy)}_2]^{2+}$, followed by ion-trap CID (**Figure 5.5**). Analogous to the cerebrosides, the charge-inverted α-linked glycosphingosine complex cations show almost no Terpy loss upon ion-trap CID (**Figures 5.5a** and **5.5b**). For $[\alpha\text{-GalSph}-\text{H} + \text{MgTerpy}]^+$ (**Figure 5.5b**), the prominent product ion at *m/z* 418 is consistent with sphingoid backbone loss (NL = 299 Da). In the case of $[\alpha\text{-GlcSph}-\text{H} + \text{MgTerpy}]^+$ (**Figure 5.5a**), the *m/z* 418 product ion is less abundant and an ion at *m/z* 400, likely a water loss following loss of the sphingoid backbone, is observed to be slightly more abundant than the *m/z* 418 product. Overall, using the sugar loss, Terpy loss, sphingoid base loss, and water loss following sphingoid base loss, it is possible to differentiate the four isomers experimentally via the gas-phase ion/ion reaction coupled with ion-trap CID.

5.3.3 Relative Quantification of the Cerebroside and Glycosphingosine Isomers in mixtures

It is typically challenging to do quantitative analysis with shotgun lipidomics, and it becomes more complicated with multiple isomers (e.g., more than two isomers). In our previous work, we demonstrated the use of a gas-phase ion/ion reaction combined with tandem mass spectrometry to quantify the relative composition of the diastereomeric pairs of both cerebrosides and glycosphingosines in binary mixtures.[14] Here, we extend the strategy to quantify three and four commercially available isomers from cerebrosides and glycosphingosines, respectively, in a mixture.

First, the charge-inverted cerebroside complex cations are produced as described above, followed by ion-trap CID (**Figure 5.2**). In order to differentiate three isomers in the mixture, diagnostic product ions mentioned from the previous section were pooled into three classes; Terpy loss (NL = 233 Da and NL = 215 Da, NL 233 + NL 215), the ions associated with water and 443 Da loss (NL = 18 and NL = 443 Da, NL 18+NL 443), and the ions related to glycosidic bond cleavage (neutral loss of sugar, NL = 162 Da and NL = 180 Da, NL 162+NL 180). Commercially

available isomers, α-GalCer(d18:1/16:0), β-GlcCer(d18:1/16:0), and β-GalCer(d18:1/16:0), were mixed to prepare various molar ratios among the isomers in the mixtures (**section 5.2.2**). The CID spectra of the fully dissociated precursor cation mixtures are provided in **Figure 5.6.**

To quantify the relative compositions of the isomers in the mixtures, the areas of the monoisotopic peaks from the diagnostic product ions were extracted and normalized to the total extracted peaks from the pure-component CID results. **Table 5.1** shows the normalized %area (%A) of the three groups of product ions from fifteen replicates (five replicates per day for three days). The %A are placed in the following equations to calculate the percentage of three isomers in unknown samples:

$$(\%\alpha - \mathrm{GalCer}_{\mathrm{unknown}} \times \%\mathrm{A}_{\mathrm{NL\ Terpy}}) + (\%\beta - \mathrm{GlcCer}_{\mathrm{unknown}} \times \%\mathrm{A}_{\mathrm{NL\ Terpy}}) + (\%\beta - \mathrm{GalCer}_{\mathrm{unknown}} \times \%\mathrm{A}_{\mathrm{NL\ Terpy}}) = \mathrm{Detected}\ \%\mathrm{A}_{\mathrm{NL\ Terpy}}$$

(**eq.5.5**)

$$(\%\alpha - \mathrm{GalCer}_{\mathrm{unkown}} \times \%\mathrm{A}_{\mathrm{NL\ 18+NL\ 443}}) + (\%\beta - \mathrm{GlcCer}_{\mathrm{unknown}} \times \%\mathrm{A}_{\mathrm{NL\ 18+NL\ 443}}) + (\%\beta - \mathrm{GalCer}_{\mathrm{unknown}} \times \%\mathrm{A}_{\mathrm{NL\ 18+NL\ 443}}) = \mathrm{Detected}\ \%\mathrm{A}_{\mathrm{NL\ 18+NL\ 443}}$$

(**eq.5.6**)

$$(\%\alpha - \mathrm{GalCer}_{\mathrm{unkown}} \times \%\mathrm{A}_{\mathrm{NL\ Sugar}}) + (\%\beta - \mathrm{GlcCer}_{\mathrm{unknown}} \times \%\mathrm{A}_{\mathrm{NL\ Sugar}}) + (\%\beta - \mathrm{GalCer}_{\mathrm{unknown}} \times \%\mathrm{A}_{\mathrm{NL\ Sugar}}) = \mathrm{Detected}\ \%\mathrm{A}_{\mathrm{NL\ Sugar}}$$

(**eq.5.7**)

The analytical performance in terms of accuracy, repeatability, and inter-day precision were also evaluated at various molar ratio of the isomeric mixtures (procedures can be found in the **section 5.2.5**). **Table 5.2** summarizes the relative quantification results with the analytical performance. The accuracies for relative quantification of the cerebrosides ranged from 94.9 to 105.2% from different molar ratios, with the highest SD around 3.2%. The results suggest the relative quantitation is achieved with the applied strategy. In addition, the inter-day precisions of the platform from various molar ratios are all below 5.4% RSD, indicating the relative quantification results obtained from different days were comparable.

As mentioned at the beginning of this section, increasing the number of isomers in a mixture complicates quantification with shotgun mass spectrometry. To our knowledge, no examples of quantifying more than three isomers simultaneously with shotgun lipidomics have been reported.[40, 49-51] Therefore, we explored the ability of this strategy to quantify four glycosphingosine isomers,

α-GlcSph(d18:1), α-GalSph(d18:1), β-GlcSph(d18:1), and β-GalSph(d18:1), in the mixture. A similar strategy from the cerebrosides section was applied. The diagnostic product ions were chosen based on the previous section and divided into four groups, NL of Terpy (NL 233 + NL 215), NL of sugar (NL = 162 Da), NL of sphingosine backbone (NL of Sph, NL = 299 Da), and its sequential loss of water (NL = 317 Da). Various molar ratios of the four isomers in the mixtures were analyzed, and changes in relative abundances of the diagnostic product ions from different mixtures were also observed (**Figure 5.7**). The extracted the areas of the monoisotopic peak from the diagnostic product ions were normalized to the total extracted area (**Table 5.3**). Another set of equations to quantify the percentage of the four glycosphingosines are shown as follows:

$$(\%\alpha - \mathrm{GlcSph}_{\mathrm{unknown}} \times \%\mathrm{A}_{NL\ Terpy}) + (\%\alpha - \mathrm{GalSph}_{\mathrm{unknown}} \times \%\mathrm{A}_{NL\ Terpy}) + (\%\beta - \mathrm{GlcSph}_{\mathrm{unknown}} \times \%\mathrm{A}_{NL\ Terpy}) + (\%\beta - \mathrm{GalSph}_{\mathrm{unknown}} \times \%\mathrm{A}_{NL\ Terpy}) = \text{Detected } \%\mathrm{A}_{NL\ Terpy} \quad \textbf{(eq. 5.8)}$$

$$(\%\alpha - \mathrm{GlcSph}_{\mathrm{unknown}} \times \%\mathrm{A}_{NL\ Sugar}) + (\%\alpha - \mathrm{GalSph}_{\mathrm{unknown}} \times \%\mathrm{A}_{NL\ Sugar}) + (\%\beta - \mathrm{GlcSph}_{\mathrm{unknown}} \times \%\mathrm{A}_{NL\ Sugar}) + (\%\beta - \mathrm{GalSph}_{\mathrm{unknown}} \times \%\mathrm{A}_{NL\ Sugar}) = \text{Detected } \%\mathrm{A}_{NL\ Sugar} \quad \textbf{(eq. 5.9)}$$

$$(\%\alpha - \mathrm{GlcSph}_{\mathrm{unknown}} \times \%\mathrm{A}_{NL\ Sph}) + (\%\alpha - \mathrm{GalSph}_{\mathrm{unknown}} \times \%\mathrm{A}_{NL\ Sph}) + (\%\beta - \mathrm{GlcSph}_{\mathrm{unknown}} \times \%\mathrm{A}_{NL\ Sph}) + (\%\beta - \mathrm{GalSph}_{\mathrm{unknown}} \times \%\mathrm{A}_{NL\ Sph}) = \text{Detected } \%\mathrm{A}_{NL\ Sph} \quad \textbf{(eq. 5.10)}$$

$$(\%\alpha - \mathrm{GlcSph}_{\mathrm{unknown}} \times \%\mathrm{A}_{NL\ 317}) + (\%\alpha - \mathrm{GalSph}_{\mathrm{unknown}} \times \%\mathrm{A}_{NL\ 317}) + (\%\beta - \mathrm{GlcSph}_{\mathrm{unknown}} \times \%\mathrm{A}_{NL\ 317}) + (\%\beta - \mathrm{GalSph}_{\mathrm{unknown}} \times \%\mathrm{A}_{NL\ 317}) = \text{Detected } \%\mathrm{A}_{NL\ 317} \quad \textbf{(eq. 5.11)}$$

Table 5.4 summarizes the relative quantification results along with the analytical performances from the analysis of various mixtures. The accuracies for relatively quantifying the four isomeric glycosphingosines ranged from 84.2 to 114.0%, with the highest SD around 8.0%, and the inter-day precisions are all below 13.5% RSD. We note that it is crucial to have an accurate measurement of the relative abundances of the diagnostic ions to obtain accurate quantitative results. There is a higher variation for the quantification of the four isomers, which is most likely due to the low percentage from several ion groups in the pure component table (e.g., NL = 317 Da for both α-GalSph and β-GalSph), leading to an approximately 5% error when there is no other

isomer in the sample. Overall, the above results show the applicability of the strategy to achieve relative quantification of three cerebroside isomers and four glycosphingosine isomers.

5.3.4 Identification of the Double Bond Position on the Fatty Acyl Side Chain of Cerebrosides via Gas-Phase Ion Chemistry

In addition to the isomerism arising from the monosaccharide head group, the amide-bonded fatty acyl chain on the cerebrosides (**Figure 5.1**) adds to the structural diversity of this lipid class. A single platform that could provide structural information from both the monosaccharide head group and the fatty acyl chain would comprehensively cover the isomerism in cerebrosides. We previously reported a charge switching gas-phase ion/ion reaction strategy to identify the double bond position(s) on unsaturated fatty acids by reacting a deprotonated fatty acid with tris-phenanthroline magnesium dications followed by ion-trap CID.[39] In brief, the charge-inverted fatty acid complex cations generate a spectral gap with 12 Da spacing at the corresponding double bond position upon ion-trap CID.[39] This approach, in some cases with some variation in the overall workflow, has been extended to various classes of lipids containing fatty acyl chains including glycerolphospholipids,[41] ether glycerolphospholipids,[42] and fatty acid esters of hydroxy fatty acids.[43]

Instead of the tris-phenanthroline magnesium dication, we used the terpyridine magnesium dication as the charge switching reagent in the current work because, in the former case, ligand loss (180 Da) could be confused with one of the sugar neutral loss channels. After CID of the charge-inverted cerebroside complex cations (**Figure 5.2**), no abundant product ions directly reveal fatty acyl chain structural information. We previously proposed the structure of the ion generated by 443 Da loss (**Figure 5.3**)[14] to be similar in structure to a charge-inverted fatty acid complex cation.[40] Therefore, another round of ion isolation and CID was performed on the first generation product ions formed from 443 Da loss. **Figure 5.8** shows the MS^3 result derived from both β-GlcCer(d18:1/18:0) and β-GlcCer(d18:1/18:1). The product ion spectra of 443 Da loss ions reveal the informative spectral pattern previously noted for monounsaturated fatty acyl chains. An informative spectral gap and a 12 Da spacing at the double bond position can be observed in **Figure 5.8b** whereas saturated a fatty acyl chain only shows 14 Da spacings among the fragmented ions **(Figure 5.8a).** The standard obtained from the vendor suggests a double bond at the n-9 position on the fatty acyl chain, which agrees with our result. As expected, there is no significant difference

between the MS^3 spectra from analytical standards of β-GlcCer(d18:1/18:1(*n*-9)) and β-GalCer(d18:1/18:1(*n*-9)) (data not shown). The above results demonstrate the ability to identify double bond position from the amide-bonded monounsaturated fatty acyl side chain on cerebrosides using the gas-phase charge inversion ion/ion reaction with deprotonated cerebroside anions and terpyridine-magnesium dication.

5.3.5 Analysis of Total Cerebroside Extract from Porcine Brain

The strategy described here was applied to total cerebroside extracts from porcine brain. In the previous chapter, we profiled 14 different cerebrosides in the extracts (**Table 4.6**).[14] As indicated above, α-linked cerebrosides are present in bacteria or can be synthetic products but they are not prominent in mammalian systems.[19] We therefore focused on the only available commercial α-linkage cerebroside standard, α-GalCer(d18:1/16:0), and its corresponding isomers in the brain extracts. **Figure 5.9** shows the CID spectra of the *m/z* 955.6 precursor ion before and after spiking α-GalCer(d18:1/16:0) into the sample, and the top panel from **Table 5.5** summarizes the relative quantities of the isomers in the sample. The pre-spiked results of the relative compositions of β-GlcCer(d18:1/16:0) and β-GalCer(d18:1/16:0), which were 11.9% and 89.3%, respectively, agreed with the results reported in chapter 4 (10.9% and 89.1%, **Table 4.6**). After spiking α-GalCer(d18:1/16:0) into the sample, the percentages among the three isomers change but the molar ratio for the two non-spiked isomers, β-GlcCer(d18:1/16:0) and β-GalCer(d18:1/16:0), remained the same, which is 0.133 (β-GlcCer(d18:1/16:0) to β-GalCer(d18:1/16:0)), suggesting that the spiking test would still be able to reflect their original relative composition, and to accurately quantify as low as 2% of the isomer. The result demonstrates the applicability of using the gas-phase ion chemistry to differentiate and quantify the three cerebroside isomers in the biological extract.

In addition to relative quantification, we also attempted to perform absolute quantification with this isomer species. By applying **equations 5.3** and **5.4**, we can back-calculate the absolute quantity of β-GlcCer(d18:1/16:0) and β-GalCer(d18:1/16:0) after spiking the known amount of α-GalCer(d18:1/16:0). **Table 5.5** also shows the results of absolute quantification. This approach uses α-GalCer(d18:1/16:0) as an internal standard that is absent in the non-spiked sample. If all three isomers were to be present in the original sample, modification of the strategy would be

needed (e.g., two-point spiking test with a revised equation set.) The proposed strategy has the advantage that it requires only a single analytical standard (i.e., α-GalCer(d18:1/16:0)) for the isomeric cerebroside group to achieve absolute quantification, thereby avoiding the need for a calibration curve for each isomer.

We also probed double bond position of selected cerebrosides from the porcine brain extract. Three cerebrosides that we profiled with a monounsaturated fatty acyl chain, including β-GalCer(d18:1/18:1), β-GalCer(d18:1/24:1), and β-GalCer(d18:1/26:1), were further subjected to MS^3 experiments for the identification of the double bond position. **Figures 5.10** and **5.11** show the CID spectra, and the bottom panel from **Table 5.5** summarizes the results. Two of the cerebrosides, β-GalCer(d18:1/18:1) and β-GalCer(d18:1/26:1), proved to be dominated by a single component with unsaturation at the *n*-9 and *n*-6 positions, respectively. In the case of β-GalCer(d18:1/24:1), *de novo* spectral interpretation suggests the presence of two major components with unsaturation at either the *n*-8 or *n*-9 positions. The difference between the CID spectra from the standard of β-GalCer(d18:1/24:1(*n*-9)) (**Figure 5.11a**) and the corresponding isomer(s) from the brain extract sample (**Figure 5.11b**) suggest that, while the the n-9 isomer is present, another isomer with unsaturation at *n*-8 is also there. However, there is no analytical standard for β-GalCer(d18:1/24:1(*n*-8)) to allow for a clear validation of this result. We also did not profile any cerebrosides from the brain extracts or find standards with more than one double bond on the amide-bonded fatty acyl chain.

5.4 Conclusions

In this chapter, we demonstrated a shotgun tandem mass spectrometry approach involving gas-phase ion/ion chemistry and ion trap CID to provide in-depth structural information from both cerebrosides and glycosphingosines. The gas-phase ion/ion reaction between deprotonated cerebrosides ($[\text{n-HexCer}-\text{H}]^-$) and $[\text{Mg(Terpy)}_2]^{2+}$ leads to charge-inverted complex cations, $[\text{n-HexCer}-\text{H} + \text{Mg(Terpy)}]^+$. Ion trap CID of these ions yields distinctive product ion spectra for the three isomers, α-GalCer, β-GlcCer, and β-GalCer. The same $[\text{Mg(Terpy)}_2]^{2+}$ reaction with deprotonated glycosphingosines derived from four isomers, α-GlcSph, α-GalSph, β-GlcSph, and β-GalSph, also forms charge-inverted complex cations. Subsequent CID of these cations allows for each isomer to be identified and profiled. This strategy enables the distinction of

monosaccharide head group diastereomers and anomeric glycosidic linkage to the sphingoid backbone. Moreover, relative quantification of three isomeric cerebrosides and four isomeric glycosphingosines mixtures is achieved by analyzing the normalized %area from the diagnostic product ions. The analytical performance for the quantification in terms of accuracy, repeatability, and inter-day precision is also reported.

The ion/ion reaction followed byion trap CID strategy has been extended to locate the double bond position on the cerebroside amide-bonded fatty acyl chain. The site of unsaturation in a cerebroside's fatty acyl chain can be identified via an informative spectral gap and a characteristic 12 Da spacing at the double bond in an MS^3 experiment on the 443 Da loss ion generated from the MS^2 experiment of the cerebroside. A total cerebroside extract from porcine brain was subjected to these approaches. By spiking a known amount of α-GalCer(d18:1/16:0) into the extract as an internal standard, it is possible to generate both relative and absolute quantities of the β-GlcCer(d18:1/16:0) and β-GalCer(d18:1/16:0) isomers in the extract. Finally, we identified the sites of double bond location in four cerebrosides in the porcine brain extract with monounsaturated fatty acyl chains, including β-GalCer(d18:1/18:1(n-9)), β-GalCer(d18:1/24:1(n-8)), β-GalCer(d18:1/24:1(n-9)), and β-GalCer(d18:1/26:1(n-6)). However, a lack of calibration standards is a complication for quantifying cerebrosides with isomeric monounsaturated amide-bonded fatty acyl chains, and for identifying sites of unsaturation when multiple double bonds are present.

5.5 Acknowledgements

This work was supported by the National Institutes of Health (NIH) under Grants GM R37-45372 and GM R01-118484.

5.6 References

1. Merrill, A. H., Sphingolipid and Glycosphingolipid Metabolic Pathways in the Era of Sphingolipidomics. Chem Rev 2011, 111 (10), 6387-6422.
2. Breton, C.; Šnajdrová, L.; Jeanneau, C.; Koča, J.; Imberty, A., Structures and mechanisms of glycosyltransferases. Glycobiology 2005, 16 (2), 29R-37R.

3. Schnaar RL, K. T., Glycosphingolipids. In Essentials of Glycobiology [Internet], 3rd edition ed.; Varki A, C. R., Esko JD et al, Ed. Cold Spring Harbor (NY): Cold Spring Harbor Laboratory Press, 2017.

4. Han, X.; Gross, R. W., Shotgun lipidomics: Electrospray ionization mass spectrometric analysis and quantitation of cellular lipidomes directly from crude extracts of biological samples. Mass Spectrom Rev 2005, 24 (3), 367-412.

5. Hakomori, S.-i., Structure and function of glycosphingolipids and sphingolipids: Recollections and future trends. Biochim Biophys Acta Gen Subj 2008, 1780 (3), 325-346.

6. Dufresne, M.; Patterson, N. H.; Norris, J. L.; Caprioli, R. M., Combining Salt Doping and Matrix Sublimation for High Spatial Resolution MALDI Imaging Mass Spectrometry of Neutral Lipids. Anal Chem 2019, 91 (20), 12928-12934.

7. Shaner, R. L.; Allegood, J. C.; Park, H.; Wang, E.; Kelly, S.; Haynes, C. A.; Sullards, M. C.; Merrill, A. H., Quantitative analysis of sphingolipids for lipidomics using triple quadrupole and quadrupole linear ion trap mass spectrometers. J Lipid Res 2009, 50 (8), 1692-1707.

8. Scherer, M.; Leuthäuser-Jaschinski, K.; Ecker, J.; Schmitz, G.; Liebisch, G., A rapid and quantitative LC-MS/MS method to profile sphingolipids. J Lipid Res 2010, 51 (7), 2001-2011.

9. Li, M.; Tong, X.; Lv, P.; Feng, B.; Yang, L.; Wu, Z.; Cui, X.; Bai, Y.; Huang, Y.; Liu, H., A not-stop-flow online normal-/reversed-phase two-dimensional liquid chromatography–quadrupole time-of-flight mass spectrometry method for comprehensive lipid profiling of human plasma from atherosclerosis patients. J Chromatogr A 2014, 1372, 110-119.

10. Boutin, M.; Sun, Y.; Shacka, J. J.; Auray-Blais, C., Tandem Mass Spectrometry Multiplex Analysis of Glucosylceramide and Galactosylceramide Isoforms in Brain Tissues at Different Stages of Parkinson Disease. Anal Chem 2016, 88 (3), 1856-1863.

11. von Gerichten, J.; Schlosser, K.; Lamprecht, D.; Morace, I.; Eckhardt, M.; Wachten, D.; Jennemann, R.; Gröne, H.-J.; Mack, M.; Sandhoff, R., Diastereomer-specific quantification of bioactive hexosylceramides from bacteria and mammals. J Lipid Res 2017, 58 (6), 1247-1258.

12. Han, X.; Cheng, H., Characterization and direct quantitation of cerebroside molecular species from lipid extracts by shotgun lipidomics. J Lipid Res 2005, 46 (1), 163-175.

13. Pham, H. T.; Julian, R. R., Characterization of glycosphingolipid epimers by radical-directed dissociation mass spectrometry. Analyst 2016, 141 (4), 1273-1278.

14. Chao, H.-C.; McLuckey, S. A., Differentiation and Quantification of Diastereomeric Pairs of Glycosphingolipids Using Gas-Phase Ion Chemistry. Anal Chem 2020, 92 (19), 13387-13395.

15. Nakayama, H.; Nagafuku, M.; Suzuki, A.; Iwabuchi, K.; Inokuchi, J.-I., The regulatory roles of glycosphingolipid-enriched lipid rafts in immune systems. FEBS Lett 2018, 592 (23), 3921-3942.

16. Kawano, T.; Cui, J.; Koezuka, Y.; Toura, I.; Kaneko, Y.; Sato, H.; Kondo, E.; Harada, M.; Koseki, H.; Nakayama, T.; Tanaka, Y.; Taniguchi, M., Natural killer-like nonspecific tumor cell lysis mediated by specific ligand-activated Vα14 NKT cells. Proc Natl Acad Sci 1998, 95 (10), 5690-5693.

17. Rossjohn, J.; Pellicci, D. G.; Patel, O.; Gapin, L.; Godfrey, D. I., Recognition of CD1d-restricted antigens by natural killer T cells. Nat Rev Immunol 2012, 12 (12), 845-857.

18. Kumar, A.; Suryadevara, N.; Hill, T. M.; Bezbradica, J. S.; Van Kaer, L.; Joyce, S., Natural Killer T Cells: An Ecological Evolutionary Developmental Biology Perspective. Front Immunol 2017, 8, 1858.

19. Li, W.; Guillaume, J.; Baqi, Y.; Wachsmann, I.; Gieselmann, V.; Van Calenbergh, S.; Müller, C. E., Synthesis and structure-activity relationships of cerebroside analogues as substrates of cerebroside sulphotransferase and discovery of a competitive inhibitor. J Enzyme Inhib Med Chem 2020, 35 (1), 1503-1512.

20. Plettenburg, O.; Bodmer-Narkevitch, V.; Wong, C.-H., Synthesis of α-Galactosyl Ceramide, a Potent Immunostimulatory Agent. J Org Chem 2002, 67 (13), 4559-4564.

21. Du, W.; Gervay-Hague, J., Efficient Synthesis of α-Galactosyl Ceramide Analogues Using Glycosyl Iodide Donors. Org Lett 2005, 7 (10), 2063-2065.

22. Fan, G.-T.; Pan, Y.-s.; Lu, K.-C.; Cheng, Y.-P.; Lin, W.-C.; Lin, S.; Lin, C.-H.; Wong, C.-H.; Fang, J.-M.; Lin, C.-C., Synthesis of α-galactosyl ceramide and the related glycolipids for evaluation of their activities on mouse splenocytes. Tetrahedron 2005, 61 (7), 1855-1862.

23. Kirschbaum, C.; Greis, K.; Mucha, E.; Kain, L.; Deng, S.; Zappe, A.; Gewinner, S.; Schöllkopf, W.; von Helden, G.; Meijer, G.; Savage, P. B.; Marianski, M.; Teyton, L.; Pagel, K., Unravelling the structural complexity of glycolipids with cryogenic infrared spectroscopy. Nat Comm 2021, 12 (1), 1201.

24. Zhou, Z.; Ogden, S.; Leary, J. A., Linkage position determination in oligosaccharides: mass spectrometry (MS/MS) study of lithium-cationized carbohydrates. J Org Chem 1990, 55 (20), 5444-5446.

25. Cerda, B. A.; Wesdemiotis, C., Thermochemistry and structures of Na+ coordinated mono- and disaccharide stereoisomers. Int J Mass spectrom 1999, 189 (2), 189-204.

26. Fura, A.; Leary, J. A., Differentiation of calcium(2+)- and magnesium(2+)-coordinated branched trisaccharide isomers: An electrospray ionization and tandem mass spectrometry study. Anal Chem 1993, 65 (20), 2805-2811.

27. Smith, G.; Leary, J. A., Differentiation of stereochemistry of glycosidic bond configuration: Tandem mass spectrometry of diastereomeric cobalt-glucosyl-glucose disaccharide complexes. J Am Soc Mass Spectrom 1996, 7 (9), 953-957.

28. Smith, G.; Leary, J. A., Mechanistic Studies of Diastereomeric Nickel(II) N-Glycoside Complexes Using Tandem Mass Spectrometry. J Am Chem Soc 1998, 120 (50), 13046-13056.

29. Firdoussi, A. E.; Lafitte, M.; Tortajada, J.; Kone, O.; Salpin, J. Y., Characterization of the glycosidic linkage of underivatized disaccharides by interaction with Pb(2+) ions. J Mass Spectrom 2007, 42 (8), 999-1011.

30. Grösch, S.; Schiffmann, S.; Geisslinger, G., Chain length-specific properties of ceramides. Prog Lipid Res 2012, 51 (1), 50-62.

31. Chao, H.-C.; Lee, T.-H.; Chiang, C.-S.; Yang, S.-Y.; Kuo, C.-H.; Tang, S.-C., Sphingolipidomics Investigation of the Temporal Dynamics after Ischemic Brain Injury. J Proteome Res 2019, 18 (9), 3470-3478.

32. Iwabuchi, K.; Nakayama, H.; Oizumi, A.; Suga, Y.; Ogawa, H.; Takamori, K., Role of Ceramide from Glycosphingolipids and Its Metabolites in Immunological and Inflammatory Responses in Humans. Mediators Inflamm 2015, 2015, 120748-120748.

33. Whitaker, B. D., Analysis of Plant Cerebrosides by C18 and C6 HPLC. In Physiology, Biochemistry and Molecular Biology of Plant Lipids, Williams, J. P.; Khan, M. U.; Lem, N. W., Eds. Springer Netherlands: Dordrecht, 1997; pp 143-145.

34. Merrill, A. H.; Sullards, M. C.; Allegood, J. C.; Kelly, S.; Wang, E., Sphingolipidomics: High-throughput, structure-specific, and quantitative analysis of sphingolipids by liquid chromatography tandem mass spectrometry. Methods 2005, 36 (2), 207-224.

35. Sullards, M. C.; Liu, Y.; Chen, Y.; Merrill, A. H., Jr., Analysis of mammalian sphingolipids by liquid chromatography tandem mass spectrometry (LC-MS/MS) and tissue imaging mass spectrometry (TIMS). Biochim Biophys Acta 2011, 1811 (11), 838-853.

36. Ryan, E.; Nguyen, C. Q. N.; Shiea, C.; Reid, G. E., Detailed Structural Characterization of Sphingolipids via 193 nm Ultraviolet Photodissociation and Ultra High Resolution Tandem Mass Spectrometry. J Am Soc Mass Spectrom 2017, 28 (7), 1406-1419.

37. Thomas, M. C.; Mitchell, T. W.; Harman, D. G.; Deeley, J. M.; Nealon, J. R.; Blanksby, S. J., Ozone-Induced Dissociation: Elucidation of Double Bond Position within Mass-Selected Lipid Ions. Anal Chem 2008, 80 (1), 303-311.

38. Barrientos, R. C.; Vu, N.; Zhang, Q., Structural Analysis of Unsaturated Glycosphingolipids Using Shotgun Ozone-Induced Dissociation Mass Spectrometry. J Am Soc Mass Spectrom 2017, 28 (11), 2330-2343.

39. Randolph, C. E.; Foreman, D. J.; Betancourt, S. K.; Blanksby, S. J.; McLuckey, S. A., Gas-Phase Ion/Ion Reactions Involving Tris-Phenanthroline Alkaline Earth Metal Complexes as Charge Inversion Reagents for the Identification of Fatty Acids. Anal Chem 2018, 90 (21), 12861-12869.

40. Randolph, C. E.; Foreman, D. J.; Blanksby, S. J.; McLuckey, S. A., Generating Fatty Acid Profiles in the Gas Phase: Fatty Acid Identification and Relative Quantitation Using Ion/Ion Charge Inversion Chemistry. Anal Chem 2019, 91 (14), 9032-9040.

41. Randolph, C. E.; Blanksby, S. J.; McLuckey, S. A., Toward Complete Structure Elucidation of Glycerophospholipids in the Gas Phase through Charge Inversion Ion/Ion Chemistry. Anal Chem 2020, 92 (1), 1219-1227.

42. Randolph, C. E.; Shenault, D. S. M.; Blanksby, S. J.; McLuckey, S. A., Structural Elucidation of Ether Glycerophospholipids Using Gas-Phase Ion/Ion Charge Inversion Chemistry. J Am Soc Mass Spectrom 2020, 31 (5), 1093-1103.

43. Randolph, C. E.; Marshall, D. L.; Blanksby, S. J.; McLuckey, S. A., Charge-switch derivatization of fatty acid esters of hydroxy fatty acids via gas-phase ion/ion reactions. Anal Chim Acta 2020, 1129, 31-39.

44. Xia, Y.; Chrisman, P. A.; Erickson, D. E.; Liu, J.; Liang, X.; Londry, F. A.; Yang, M. J.; McLuckey, S. A., Implementation of Ion/Ion Reactions in a Quadrupole/Time-of-Flight Tandem Mass Spectrometer. Anal Chem 2006, 78 (12), 4146-4154.

45. Xia, Y.; Liang, X.; McLuckey, S. A., Pulsed Dual Electrospray Ionization for Ion/Ion Reactions. J Am Soc Mass Spectrom 2005, 16 (11), 1750-1756.

46. McLuckey, S. A.; Goeringer, D. E.; Glish, G. L., Selective ion isolation/rejection over a broad mass range in the quadrupole ion trap. J Am Soc Mass Spectrom 1991, 2 (1), 11-21.

47. Webb, I. K.; Londry, F. A.; McLuckey, S. A., Implementation of dipolar direct current (DDC) collision-induced dissociation in storage and transmission modes on a quadrupole/time-of-flight tandem mass spectrometer. Rapid Commun Mass Spectrom 2011, 25 (17), 2500-10.

48. Bythell, B. J.; Abutokaikah, M. T.; Wagoner, A. R.; Guan, S.; Rabus, J. M., Cationized Carbohydrate Gas-Phase Fragmentation Chemistry. J Am Soc Mass Spectrom 2017, 28 (4), 688-703.

49. Hsu, F.-F., Mass spectrometry-based shotgun lipidomics - a critical review from the technical point of view. Anal Bioanal Chem 2018, 410 (25), 6387-6409.

50. Han, X.; Yang, K.; Gross, R. W., Multi-dimensional mass spectrometry-based shotgun lipidomics and novel strategies for lipidomic analyses. Mass Spectrom Rev 2012, 31 (1), 134-178.

51. Nielsen, I. Ø.; Vidas Olsen, A.; Dicroce-Giacobini, J.; Papaleo, E.; Andersen, K. K.; Jäättelä, M.; Maeda, K.; Bilgin, M., Comprehensive Evaluation of a Quantitative Shotgun Lipidomics Platform for Mammalian Sample Analysis on a High-Resolution Mass Spectrometer. J Am Soc Mass Spectrom 2020, 31 (4), 894-907.

5.7 Tables

Table 5.1. The normalized %area from the pure components of cerebroside isomers.

100% CB	NL of Terpy (%, NL 215 + NL 233)	NL of water+443 (%, NL 18 + NL 443)	NL of sugar (%, NL 162 + NL 180)	SD*
α-GalCer(d18:1/16:0)	0.2	56.3	43.5	0.03
β-GlcCer(d18:1/16:0)	41.6	49.1	9.3	0.2
β-GalCer(d18:1/16:0)	90.7	7.3	2.0	0.1

*Standard deviation (SD) is obtained from the %A group with the lowest percentage.

Table 5.2. The results of quantification of the three cerebroside isomers and the analytical performance of the mixture analysis.

Molar ratio AA/BC/BA[#]	Cal_%AA	Accuracy (%)**	Inter-day Precision (%RSD)***	Cal_%BC	Accuracy (%)**	Inter-day Precision (%RSD)***	Cal_BA	Accuracy (%)**	Inter-day Precision (%RSD)***
1/0/0	100.2	100.2 ± 0.7	2.0	ND*	Not applicable	Not applicable	0.2	Not applicable	Not applicable
0/1/0	0.12	Not applicable	Not applicable	101.0	101.0 ± 0.7	4.4	ND*	Not applicable	Not applicable
0/0/1	ND*	Not applicable	Not applicable	1.4	Not applicable	Not applicable	99.1	99.1 ± 0.6	0.9
1/1/0	47.5	94.9 ± 2.0	3.6	52.6	105.2 ± 3.2	3.9	ND*	Not applicable	Not applicable
1/0/1	49.7	99.47 ± 1.9	5.4	0.7	Not applicable	Not applicable	49.6	99.1 ± 1.1	2.5
0/1/1	ND*	Not applicable	Not applicable	50.9	101.7 ± 2.1	5.3	49.3	98.7 ± 1.9	4.7
4/3/3	40.0	100.0 ± 1.5	2.4	32.2	103.0 ± 2.4	2.4	27.9	96.7 ± 0.8	3.1

[#]AA stands for α-GalCer, BC stands for β-GlcCer, and BA stands for β-GalCer in the table. *Not-detectable

**Mean±SD, N=5; ***Relative standard deviation, calculated from three different days with 9 different samples.

Table 5.3. The normalized %area from the pure components of glycosphingosine isomers

100% HexSph	NL of Terpy (%, NL 215 + NL 233, m/z 502 + m/z 484)	NL of sugar (%, NL 162, m/z 555)	NL of Sph (%, NL 299, m/z 418)	NL of Sph+water (%, NL 317, m/z 400)	SD*
α-GlcSph d18:1	0.2	79.6	5.9	14.2	0.01
α-GalSph d18:1	0.7	59.6	39.5	0.2	0.01
β-GlcSph d18:1	14.8	62.4	18.4	4.3	0.8
β-GalSph d18:1	88.3	8.6	2.9	0.2	0.01

*Standard deviation (SD) is obtained from the %A group with the lowest percentage (N=12).

Table 5.4. The results of quantification of the four glycosphingosine isomers and the analytical performance of the mixture analysis.

Molar ratio AC/AA/BC/BA#	**Cal_%AC**	**ACU ****	**PRE *****	**Cal_%AA**	**ACU ****	**PRE *****	**Cal_%BC**	**ACU ****	**PRE *****	**Cal_BA**	**ACU ****	**PRE *****
1/0/0/0	100.0	100.0 ± 2.0	1.8	ND*	NA$	NA	ND*	NA	NA	ND*	NA	NA
0/1/0/0	ND*	NA	NA	100.0	100.0 ± 2.7	2.8	ND*	NA	NA	ND*	NA	NA
0/0/1/0	ND*	NA	NA	ND*	NA	NA	100.0	100.0 ± 5.8	6.1	ND*	NA	NA
0/0/0/1	ND*	NA	NA	ND*	NA	NA	ND*	NA	NA	100.0	100.0 ± 0.4	0.3
1/1/0/0	55.9	111.9 ± 2.5	4.1	47.6	95.6 ± 3.5	6.9	ND*	NA	NA	0.7	NA	NA
1/0/1/0	48.3	96.7 ± 2.3	5.6	0.7	NA	NA	50.3	100.6 ± 6.2	9.4	ND*	NA	NA
1/0/0/1	57.0	114.0 ± 2.05	4.6	4.5	NA	NA	ND	NA	NA	49.7	99.2 ± 1.0	2.4
0/1/1/0	ND	NA	NA	47.2	94.7 ± 0.4	7.4	52.4	104.8 ± 0.4	13.5	0.6	NA	NA

Table 5.4 continued

0/1/0/1	2.1	NA	NA	48.7	97.5 ± 2.8	4.5	ND	NA	NA	56.1	111.8 ± 1.0	1.9
0/0/1/1	1.0	NA	NA	ND	NA	NA	52.8	105.5 ± 2.6	3.4	46.6	93.0 ± 0.6	2.3
1/0/2/2	21.8	109.0 ± 4.3	5.3	ND	NA	NA	39.3	98.7 ± 4.4	10.2	42.1	104.5 ± 0.6	7.0
0/1/2/2	1.9	NA	NA	19.5	97.5 ± 2.8	8.4	42.5	104.9 ± 2.9	6.1	39.5	98.6 ± 0.5	5.2
2/2/1/0	42.8	106.9 ± 1.4	4.1	36.0	90.8 ± 2.1	3.8	21.7	104.7 ± 8.0	10.8	ND	NA	NA
2/2/0/1	43.7	109.2 ± 1.0	5.8	34.1	84.2 ± 3.1	4.9	ND	NA	NA	20.0	100.7 ± 3.8	9.6
1/1/1/1	25.9	103.6 ± 2.4	2.8	24.0	95.3 ± 4.3	3.9	27.0	109.6 ± 4.9	5.9	23.0	91.5 ± 1.1	4.1

[#]AC stands for α-GlcSph, AA stands for α-GalSph, BC stands for β-GlcSph, and BA stands for β-GalSph in the table. *Not-detectable **ACU stands for accuracy which is reported as mean±SD, (%,N=3); ***PRE stands for interday precision which is reported as relative standard deviation (%RSD), calculated from three different days with 9 different samples. $ Not applicable, the percentage supposed to be 0)

Table 5.5. The analytical results of the cerebroside isomers in total brain extract.

Quantification of Cerebroside Isomers				
n-HexCer (d18:1/16:0)	**Relative Quantification**			
	Test (N=5)	**Calculated α-GalCer (%)***	**Calculated β-GlcCer (%)**	**Calculated β-GalCer (%)**
	Non-spiked test	ND**	11.9 ± 2.8	89.3 ± 2.1
	Spiked test	80.1 ± 1.6	2.2 ± 0.6	16.60 ± 1.6
	Absolute Quantification (N=5)			
	Calculated β-GlcCer ng mg^{-1}***		**Calculated β-GalCer ng mg^{-1}**	
	27.9 ± 6.6		209.8 ± 24.2	

Profiled Cerebrosides with Monounsaturated Fatty Acyl Chain		
Profiled β-GalCer (total carbon number)	**Fatty acyl chains (sphingoid backbone/side chain)**	**Double bond position (amide bonded side chain)**
36:2	d18:1/18:1	*n*-9
42:2	d18:1/24:1	*n*-8 and *n*-9
44:2	d18:1/26:1	*n*-6

*Mean ± SD. ** Not-detectable. ***The concentrations of cerebrosides are expressed as per mg brain extract.

5.8 Scheme and Figures

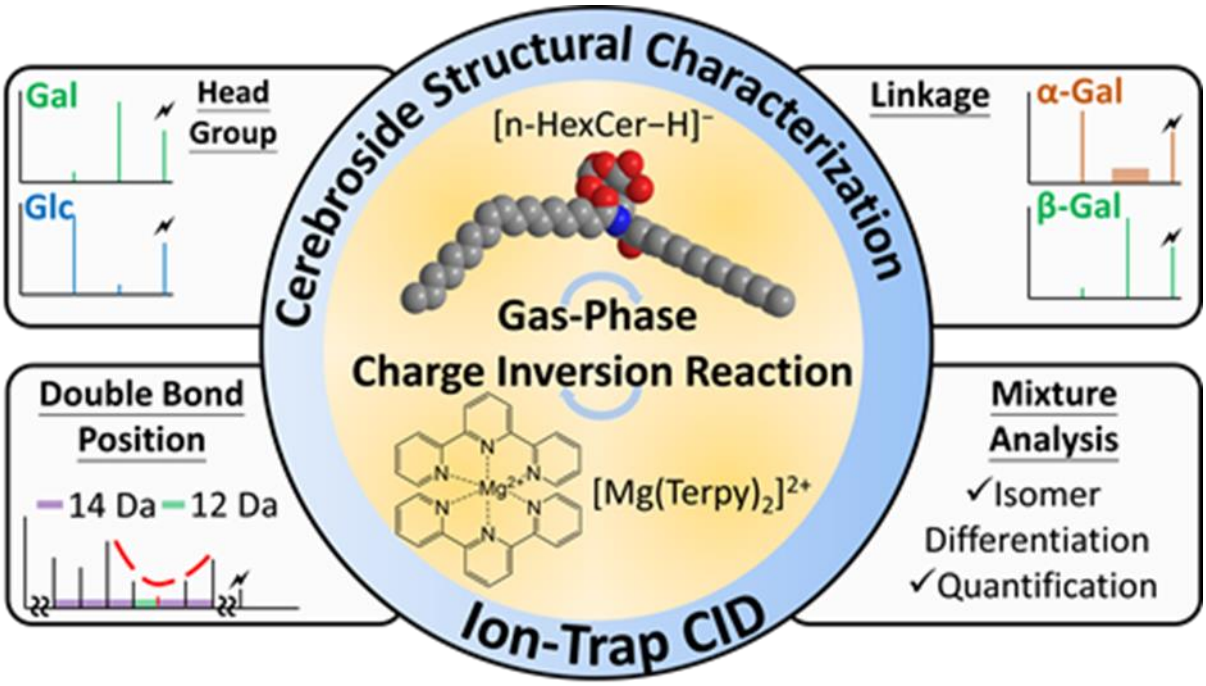

Scheme 5.1. Graphical abstract of chapter 5.

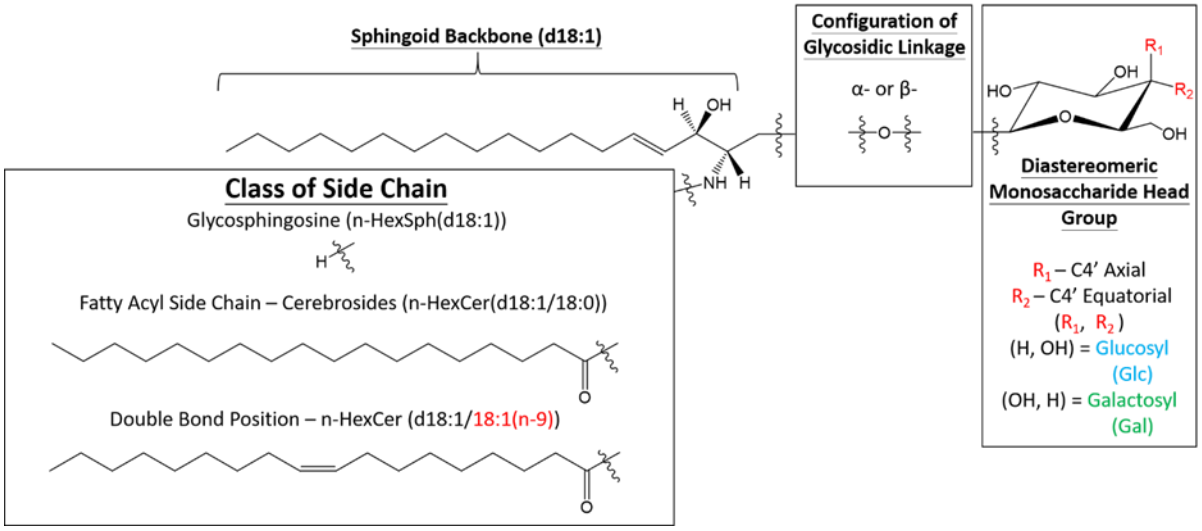

Figure 5.1. The general structures of glycosphingosines and cerebrosides with the possible isomeric positions within the structure.

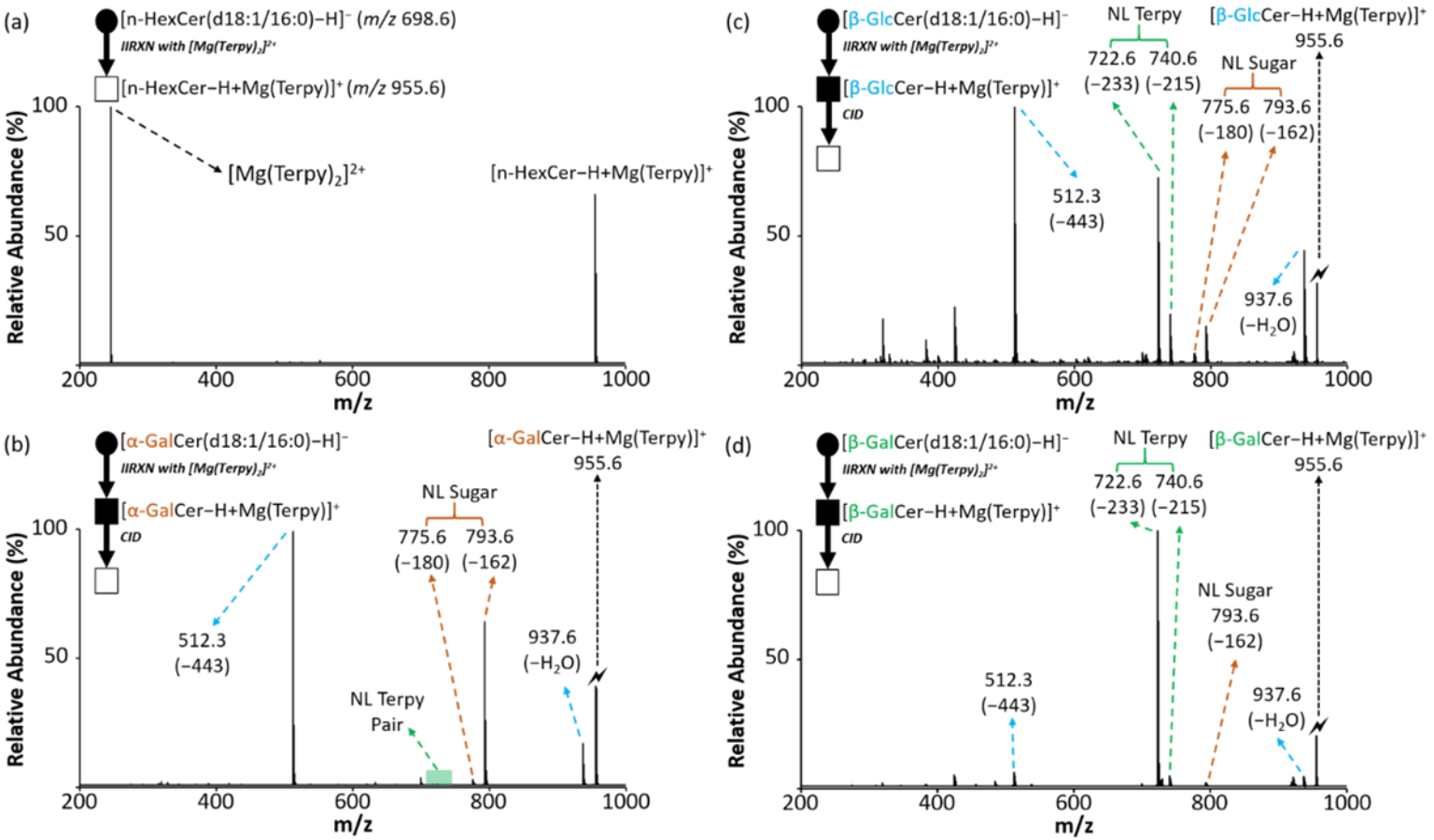

Figure 5.2. The comparison of the CID spectra among cerebrosides after gas-phase ion/ion reaction. (a) The post-ion/ion reaction spectrum of cerebroside anion with $[Mg(Terpy)_2]^{2+}$ cation. (b) The CID spectrum of the $[\alpha\text{-GalCer–H+MgTerpy}]^+$ (*m/z* 955.6). (c) The CID spectrum of the $[\beta\text{-GlcCer–H+MgTerpy}]^+$ (*m/z* 955.6). (d) The CID spectrum of the $[\beta\text{-GalCer–H+MgTerpy}]^+$ (*m/z* 955.6). The values inside the parenthesis indicate the neutral loss. The lightning bolt (↯) signifies the collisionally activated precursor ion. The solid circle (●) indicates the mass selection in the negative ion mode analysis and the black and white squares (■/□) indicate the positive ion mode analysis with and without mass selection, respectively.

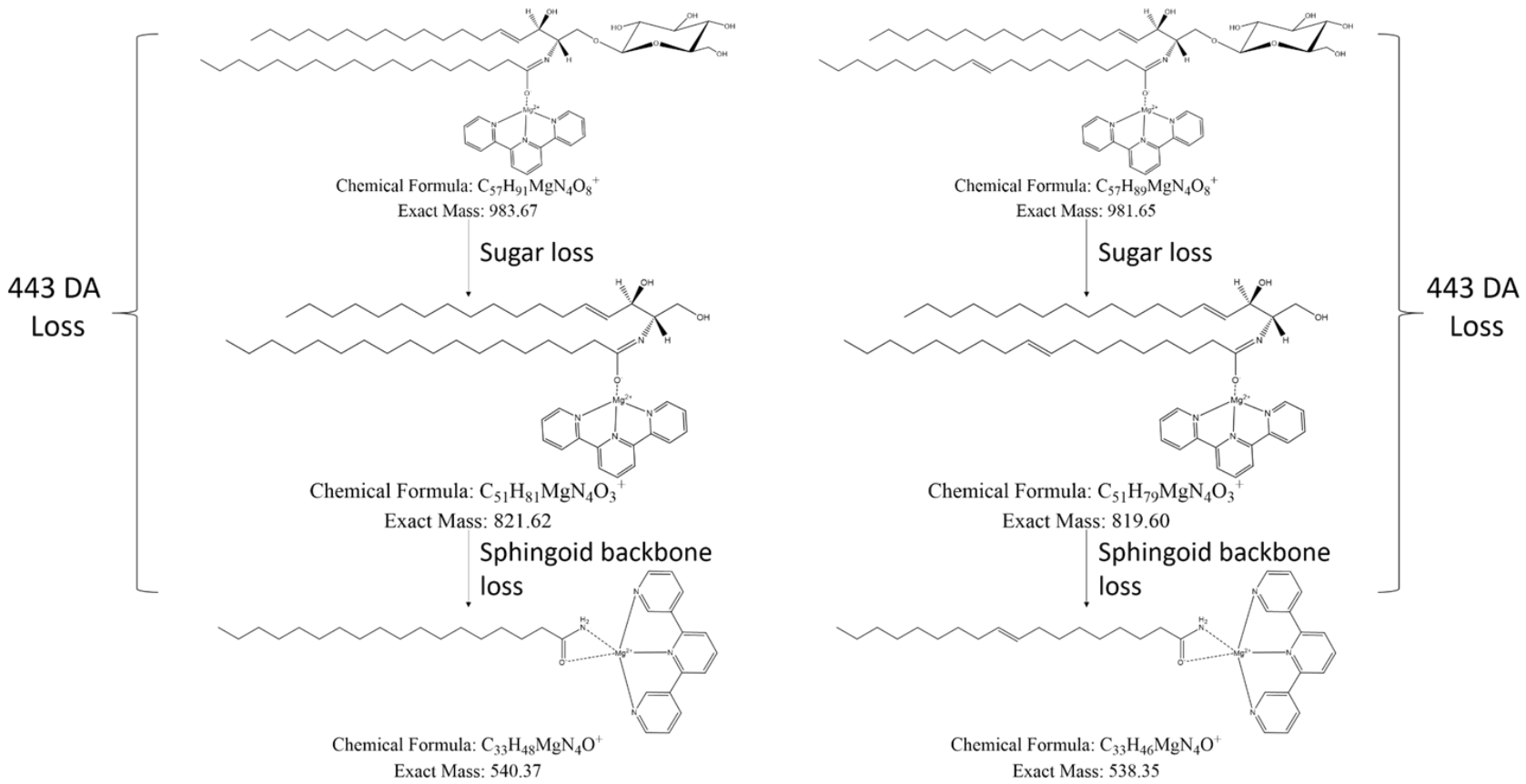

Figure 5.3. The proposed structures of neutral loss of 443Da ion from both [n-GlcCer(d18:1/18:0)−H+Mg(Terpy)]$^+$ (left) and [n-GlcCer(d18:1/18:1)−H+Mg(Terpy)]$^+$ (right.)

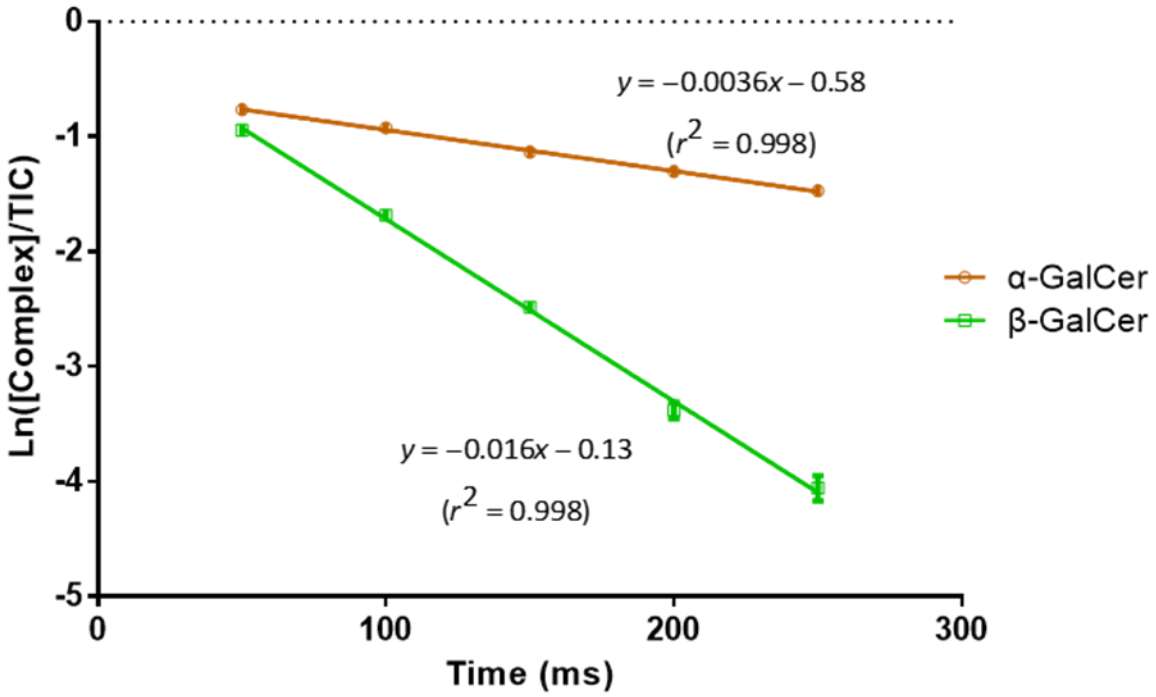

Figure 5.4. The dissociation kinetic plot of isomeric charge-inverted galactosylceramide complex cations. Error bars are express with standard deviation (n=3). The p-value between the two slope is < 0.01 indicating the significantly different rate constant between the two complex cations. (The procedure for the dissociation rate measurement is provided in **section 5.2.4**)

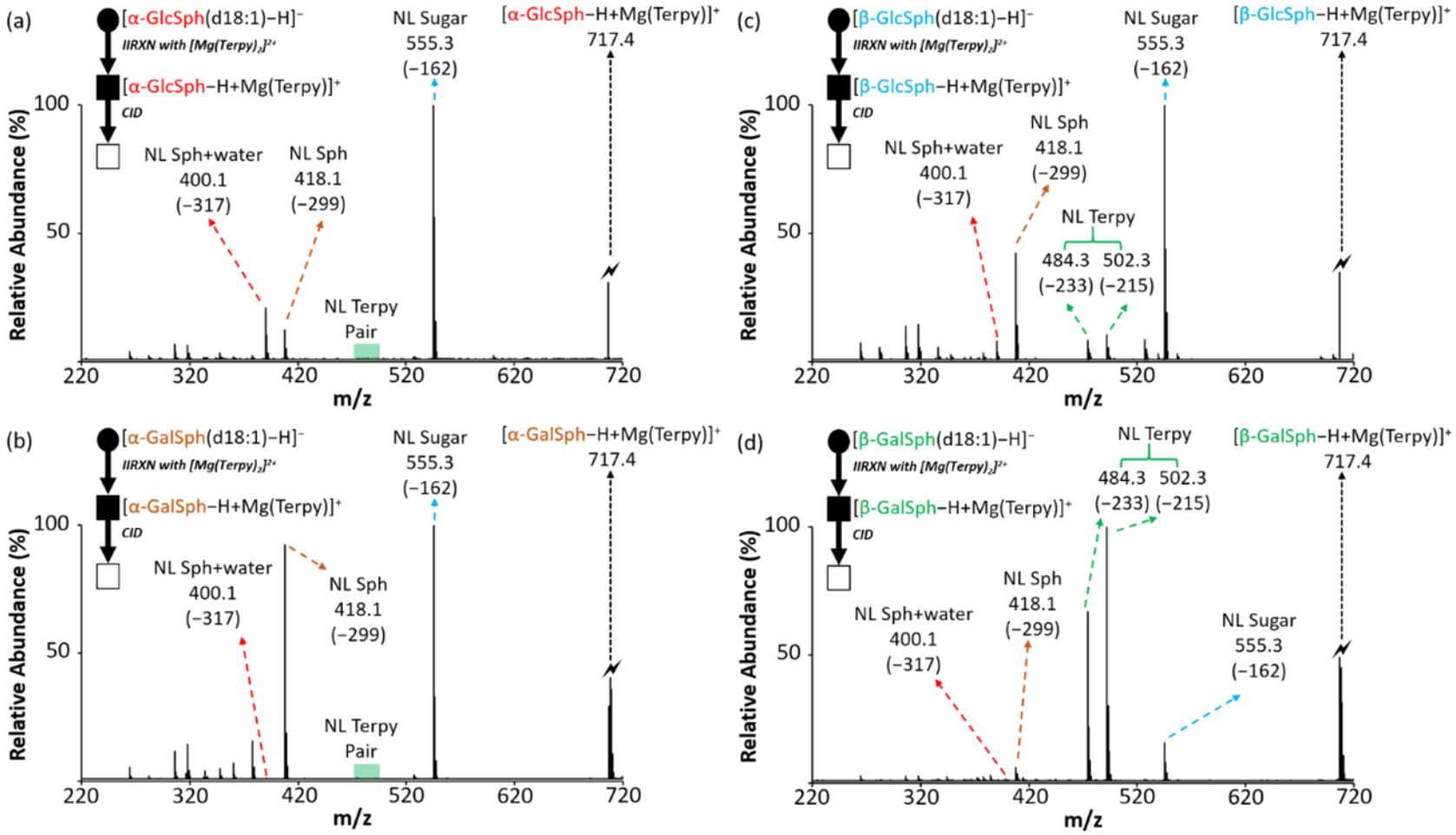

Figure 5.5. The comparison of the CID spectra among glycosphingosines after gas-phase ion/ion reaction. (a) The CID spectrum of the [α-GlcSph–H + MgTerpy]$^+$ (*m/z* 717.4). (b) The CID spectrum of the [α-GalSph–H + MgTerpy]$^+$ (*m/z* 717.4). (c) The CID spectrum of the [β-GlcSph–H + MgTerpy]$^+$ (*m/z* 717.4). (d) The CID spectrum of the [β-GaSph–H + MgTerpy]$^+$ (*m/z* 717.4). The values inside the parenthesis indicate the neutral loss. The symbols represent as same as those in **Figure 5.2**.

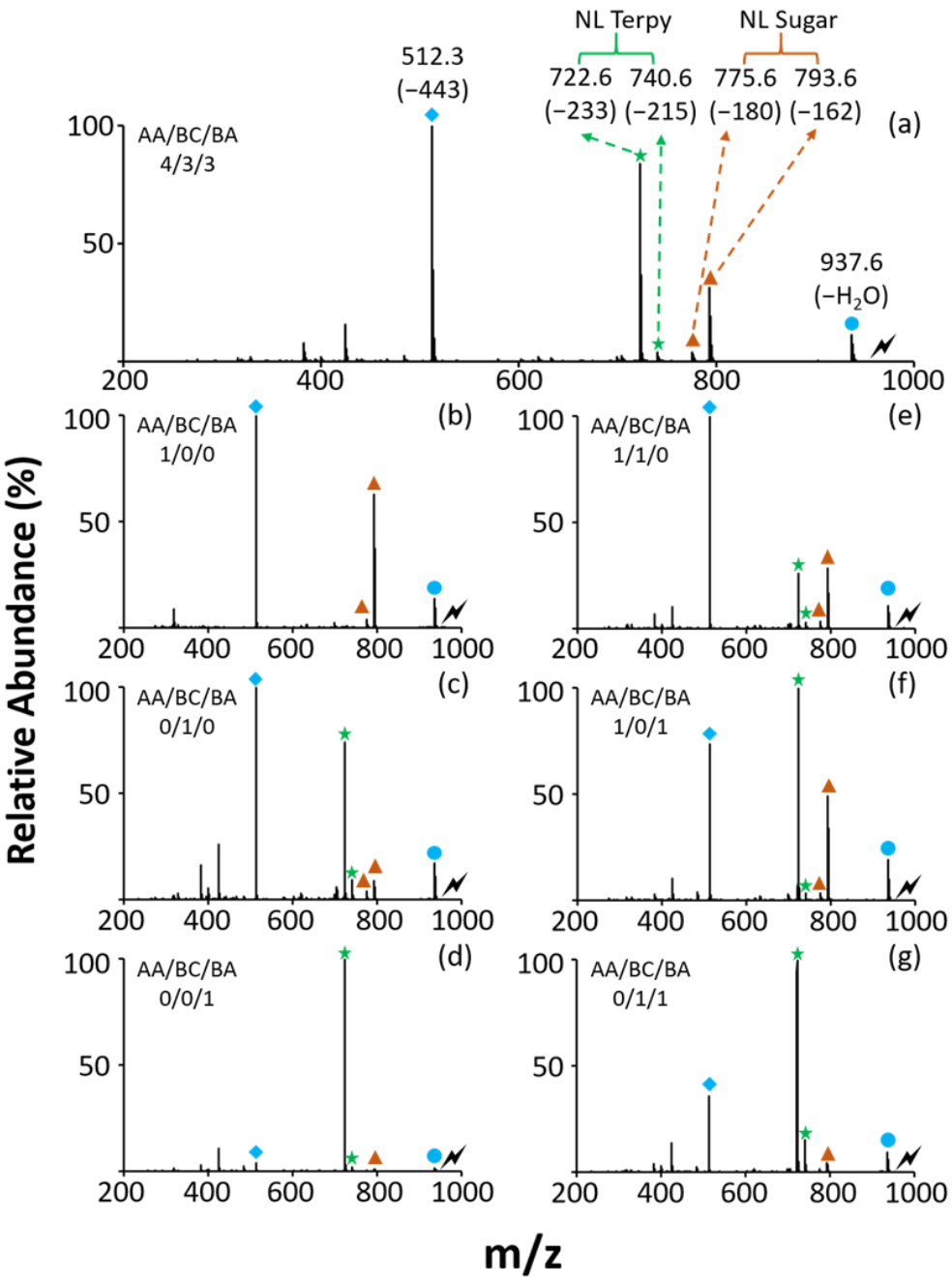

Figure 5.6. The CID spectra of the [n-HexCer(d18:1/16:0–H + MgTerpy]$^+$ complex with different molar ratios (top-left inserts) in the sample. The lightning bolt (🗲) signifies collisionally activated precursor ion. The blue circle (●) and diamond (◆) indicate fragment ion from NL of water, and NL of 443 Da, respectively. The brown triangle (▲) indicates the fragment ion from NL of sugar and the green stars (★) indicate the fragment ion from NL of Terpy ligand. AA stands for α-GalCer, BC stands for β-GlcCer, and BA stands for β-GalCer.

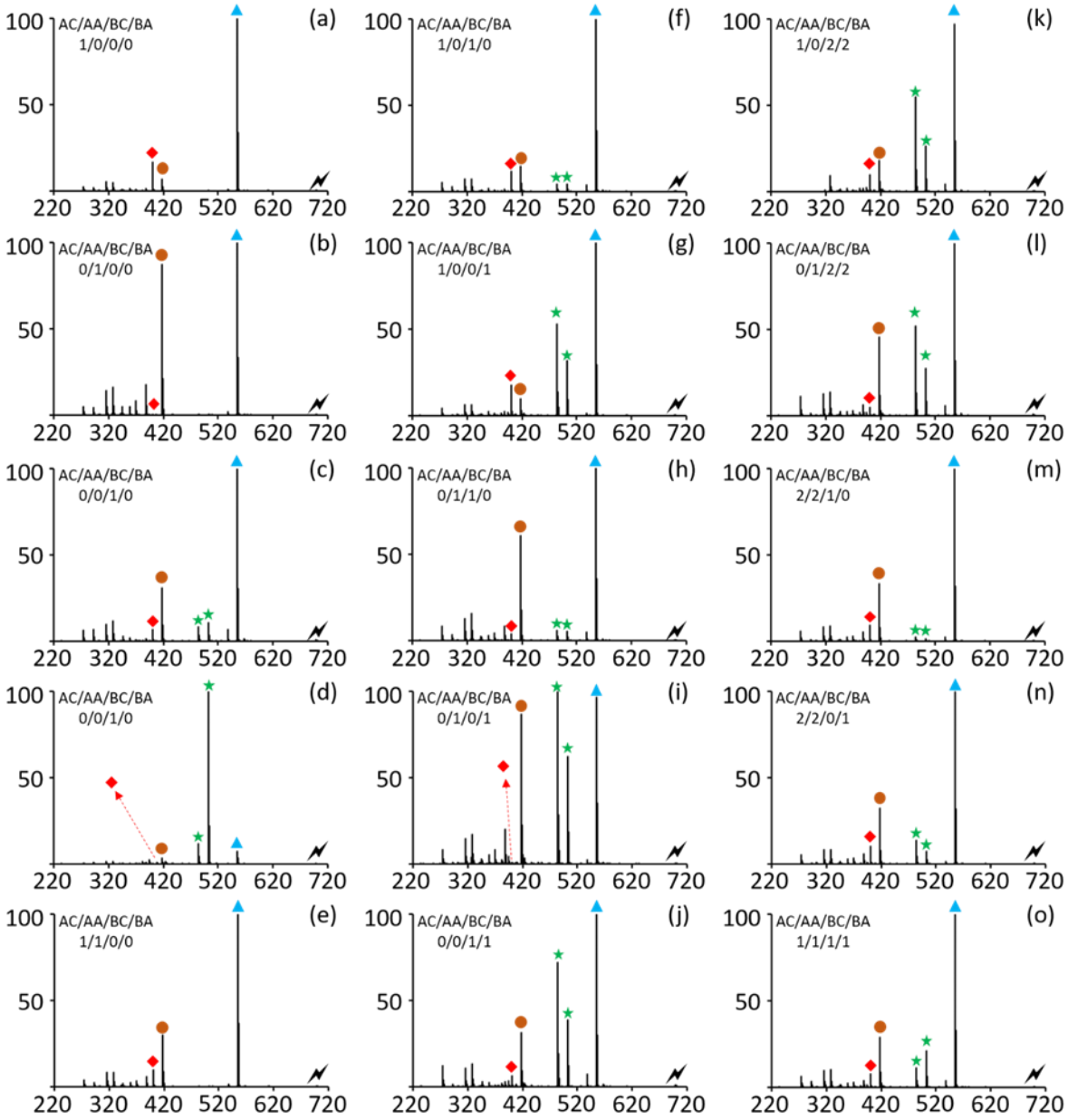

Figure 5.7. The CID spectra of the [n-HexSph(d18:1)–H + MgTerpy]$^+$ complex with different molar ratios (top-left inserts) in the sample. The lightning bolt (🗲) signifies collisionally activated precursor ion. The brown triangle (▲) indicates the fragment ion from NL of sugar and the green stars (★) indicate the fragment ion from NL of Terpy ligand. The brown circle (●) indicates the ion from NL of 299 Da (*m/z* 418), and red diamond (◆) indicate fragment ion from NL of 317 Da (*m/z* 400), respectively. AC stands for α-GlcSph, AA stands for α-GalSph, BC stands for β-GlcSph, and BA stands for β-GalSph

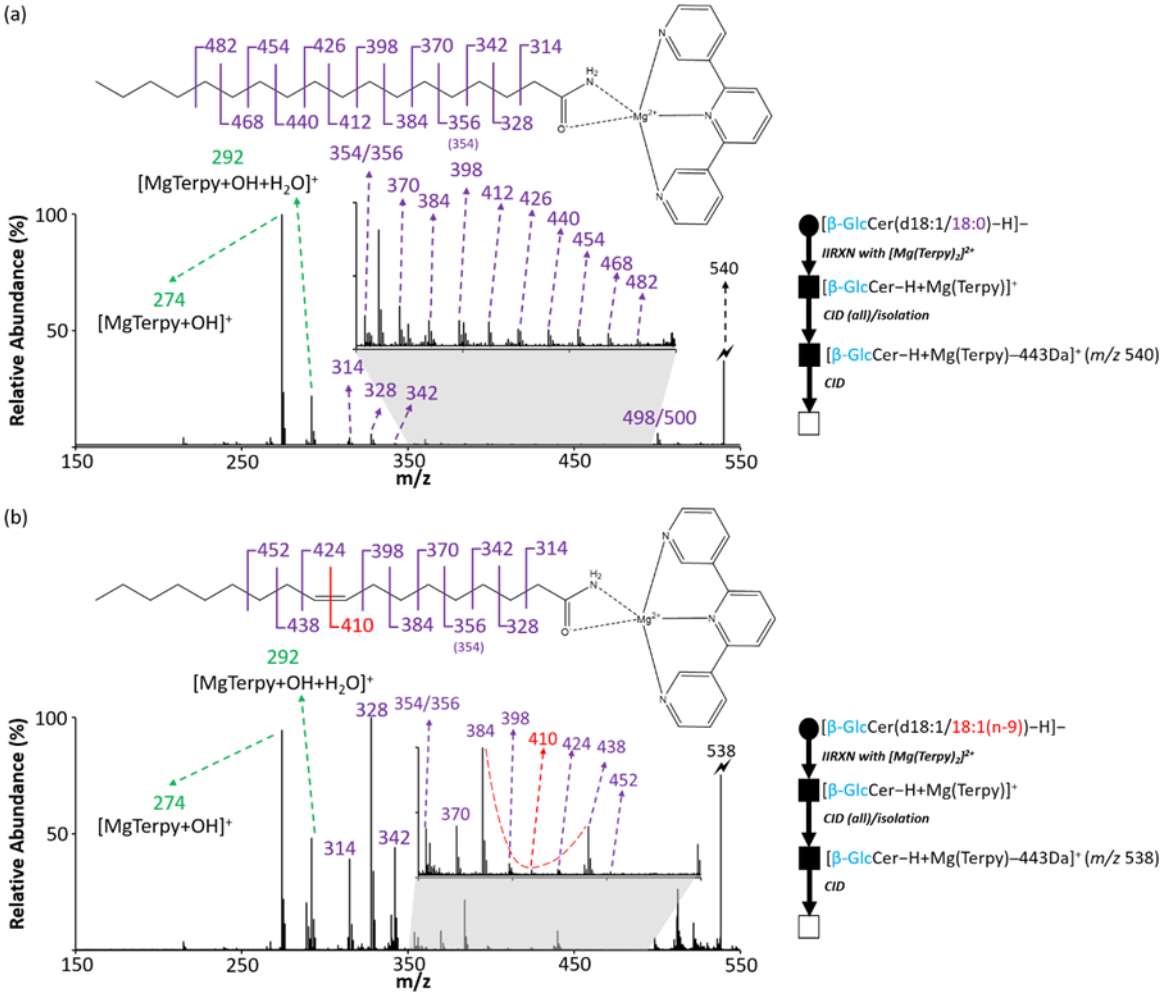

Figure 5.8. The identification of double bond position from the monounsaturated fatty acyl side chain on cerebrosides. (a) The CID spectrum of 443 Da loss ion from [β-GlcCer(d18:1/18:0)−H+MgTerpy]$^+$. (b) The CID spectrum of 443 Da loss ion from [β-GlcCer(d18:1/18:1 (n-9))−H+MgTerpy]$^+$. The inserts are the zoom-in spectra of m/z region ranged from 350 to 500. The red dashed line signifies the special spectral gap pointing the double bond position. The symbols represent as same as those in **Figure 5.2.**

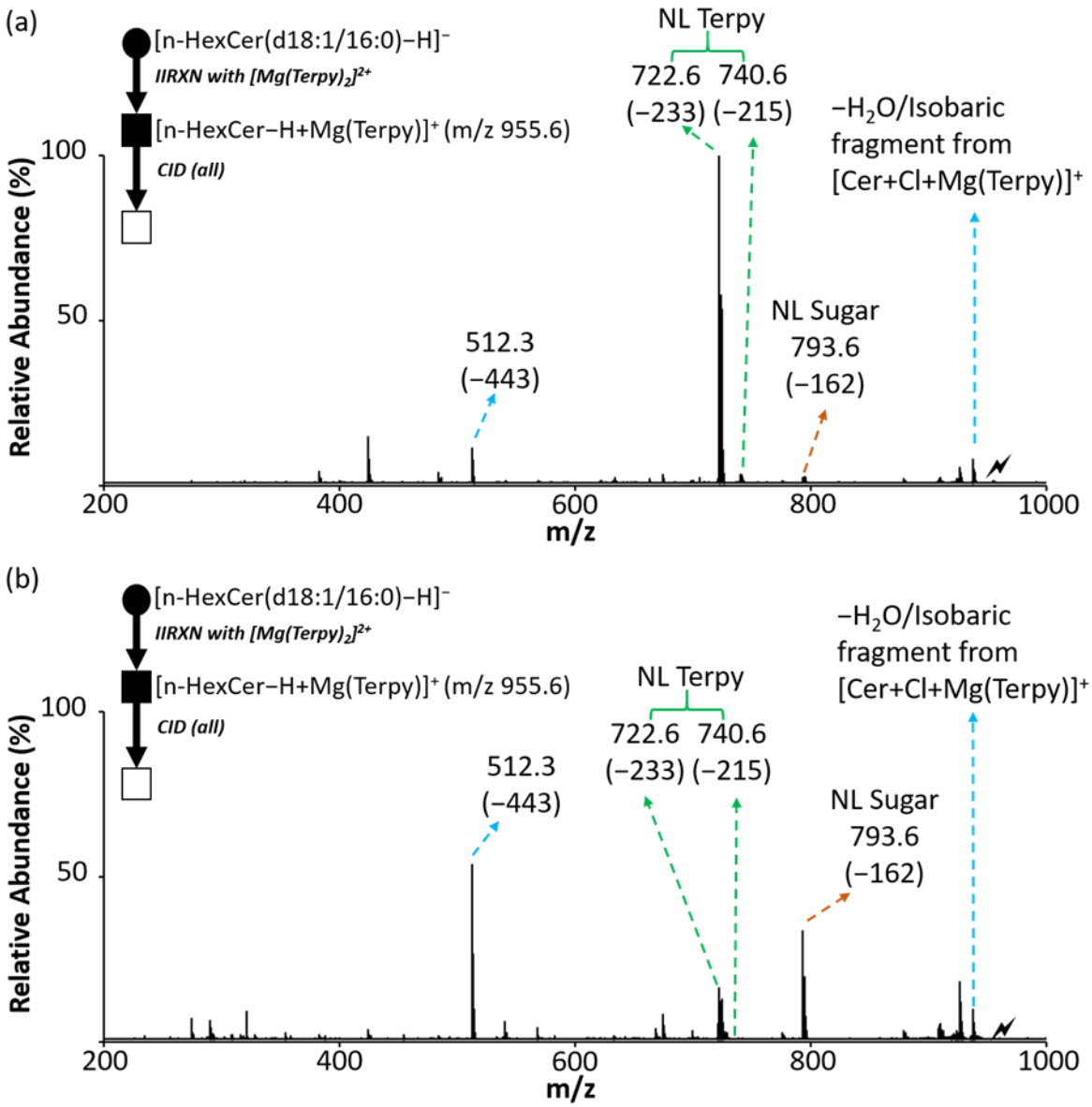

Figure 5.9. The standard spike test for quantitation of cerebroside isomers in total brain extract. (a) The CID spectrum of the [n-HexCer(d18:1/16:0)–H + MgTerpy]$^+$ complex (*m/z* 955.6) without spiking any standard. (b) The CID spectrum of the [HexCer(d18:1/18:0) – H + MgTerpy]$^+$ complex with spiked α-GalCer(d18:1/16:0). The values insides the parenthesis indicate the neutral loss. The symbols represent as same as those in **Figure 5.2.**

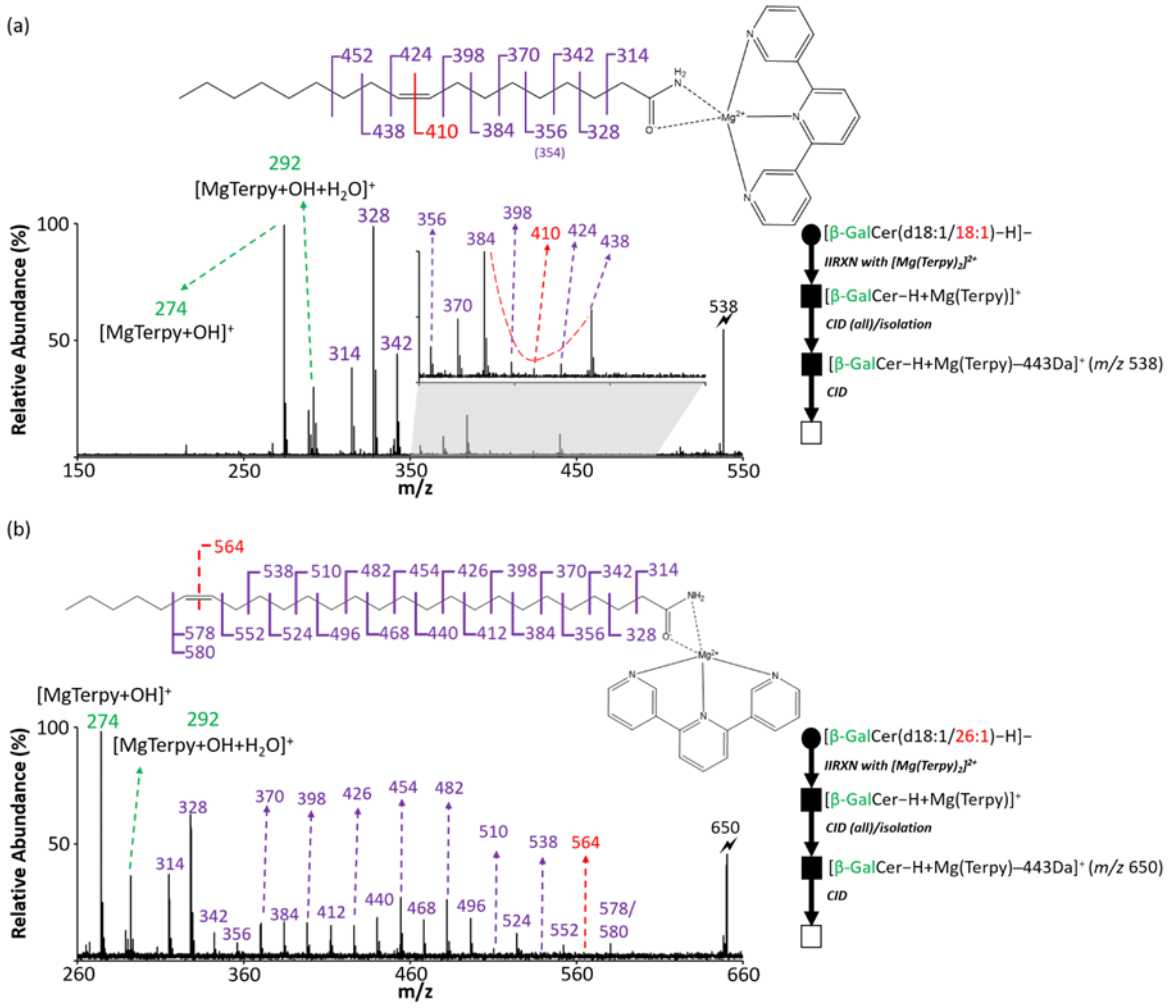

Figure 5.10. The identification of double bond position from the monounsaturated fatty acyl side chain on cerebrosides in porcine brain sample. (a) The CID spectrum of 443 Da loss ion from [β-GalCer(d18:1/18:1(n-9))–H+MgTerpy]$^+$. (b) The CID spectrum of 443 Da loss ion from [β-GalCer(d18:1/26:1 (n-6))–H+MgTerpy]$^+$. The insert in **Figure 5.10a** is the zoom-in spectrum of *m/z* region ranged from 350 to 500. The red dashed line signifies the special spectral gap pointing the double bond position. Other symbols represent as same as those in **Figure 5.2.**

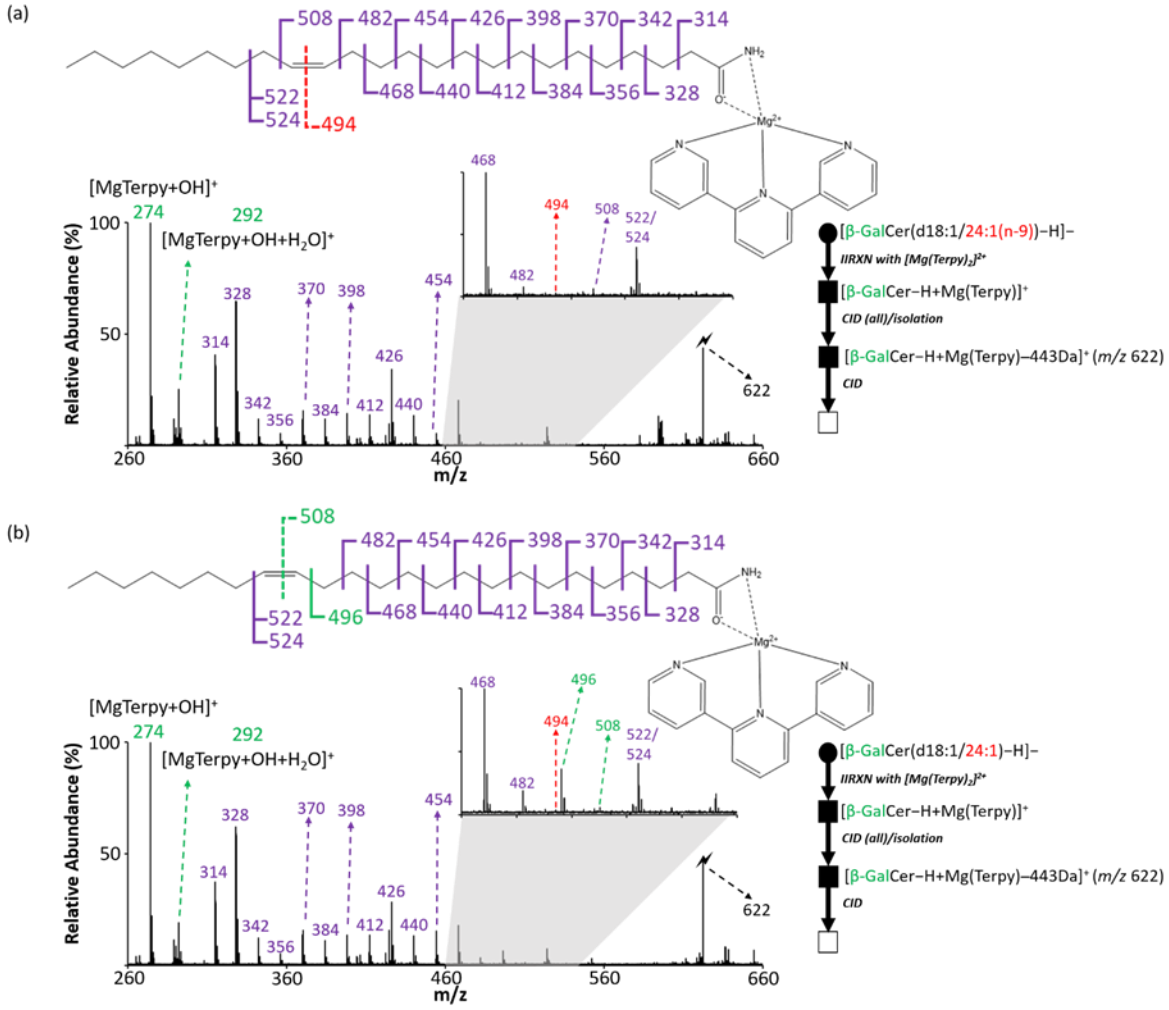

Figure 5.11. The identification of double bond position from the monounsaturated fatty acyl side chain on β-GalCer(d18:1/24:1) from the analytical standard and porcine brain extract. (a) The CID spectrum of 443 Da loss ion from [β-GalCer(d18:1/18:1(n-9))–H+MgTerpy]$^+$ from analytical standard. (b) The CID spectrum of 443 Da loss ion from [β-GalCer(d18:1/18:1)–H+MgTerpy]$^+$ from porcine brain extract. The inserts are the zoom-in spectra of *m/z* region ranged from 460 to 550. The red dashed line signifies the special spectral gap pointing the double bond position and the green dashed line indicates another 12 Da spacing from porcine brain sample. Other symbols represent as same as those in **Figure 5.2.**

CHAPTER 6. MANIPULATION OF ION TYPES VIA GAS-PHASE ION/ION CHEMISTRY FOR THE STRUCTURAL CHARACTERIZATION OF THE GLYCAN MOIETY ON GANGLIOSIDES

Adapted with permission from Chao, H.-C., and McLuckey, S. A. Anal. Chem. 2021, 93, 47, 15752–15760.

Abstract

Gangliosides are the most abundant glycolipid among eukaryotic cell membranes and consist of a glycan head moiety containing one or more sialic acids and a ceramide chain. The analysis of the glycan moieties among different subclass gangliosides, including GM, GD, and GT gangliosides, remains a challenge for shotgun lipidomics. In this chapter, we investigated the derivatization strategy using gas-phase ion/ion reactions, which provide rapid ways to manipulate the ion-types of precursor ions, and, in conjunction with CID, allows for the elucidation of the structures of the glycan moieties from gangliosides. In addition to the enhancement of structural characterization, gas-phase ion chemistry leads to a form of purification of the precursor ions prior to CID by neutralizing isobaric or isomeric ions with different charge states but with similar or identical *m/z* values. To demonstrate the proposed strategy, both deprotonated GM3 and GM1 gangliosides ($[GM-H]^-$) were isolated and subjected to reaction with $[Mg(Terpy)_2]^{2+}$. The post-reaction product spectra showed the elimination of possible contamination, illustrating the ability of charge-switching derivatization to purify the precursor ions. Isomeric differentiation between GD1a and GD1b was achieved by sequential ion/ion reactions, that CID of $[GD1-H+Mg]^+$ shows diagnostic fragment ions from the isomers. Moreover, isomeric identification among GT1a, GT1b, and GT1c was accomplished while performing a gas-phase magnesium transfer reaction and CID. Lastly, the presented workflow was applied to ganglioside profiling in a porcine brain extract. In total, 34 gangliosides were profiled among only 20 precursor ion *m/z* values by resolving isomers. Furthermore, the fucosylation site on GM1 and N-glycolylneuraminic acid conjugated GT1 isomers was identified. Relative quantification of isomeric two GD1a/b pairs was also achieved using pure component product ion spectra coupled with a total least squares method. The results demonstrate the applicability and strength of using shotgun MS coupled with gas-phase ion/ion chemistry to characterize the glycan moiety structures on different subclasses of gangliosides.

6.1 Introduction

Gangliosides are a type of glycolipid composed of a hydrophilic glycan head moiety that contains one or more sialic acids and a hydrophobic ceramide chain (**Figure 6.1**), are the most abundant glycolipids on eukaryotic cell membranes[1]. Gangliosides in cell membranes are strongly associated with lipid rafts, which are thought to serve as anchors to stabilize the lipid-protein interactions on the membrane, and can be used as indicators of the cell membrane dynamics.[2-3] Gangliosides are also rich in the central nervous systems (CNS) and provide more than 75% of the sialic acid in the mammalian brain, serving as the dominant glycan source, in contrast with other organs and tissues where glycans are mostly from glycoproteins.[4] Therefore, gangliosides play essential roles in the CNS for both cell signaling and intercellular interactions.[5] Many reports have suggested that imbalances in ganglioside levels are correlated with both neurodegenerative and neurodevelopmental diseases, such as Alzheimer's disease,[6-7] Parkinson's disease,[8-9] and Huntington's disease[10-11].

Gangliosides can be further classified into GM, GD, and GT series, which correspond to the numbers of sialic acids on the glycan. The isomeric linkage arising from the sialic acids, N-acetylneuraminic acid (NeuAc), and how they are linked to the glycan chain lead to further sub-classifications (e.g., GD1a/b, and GT1a/b/c, **Figure 6.1**).[12] The biosynthetic pathways of gangliosides diversify the structures of the glycan moiety on gangliosides.[13] Unambiguously differentiating the isomers of gangliosides is a daunting analytical challenge that leads many reports to forego differentiation and simply group the isomers from biological samples.[14-16] Therefore, a method to differentiate isomeric gangliosides in biological samples is of interest.

Mass spectrometry (MS) has been used to analyze gangliosides for decades. Particularly, soft-ionization methods like matrix-assisted laser desorption/ionization (MALDI) have aided in ganglioside analysis. Specifically, isobars and isomers of gangliosides have been separated by thin-layer chromatography preceding MALDI-MS analysis.[17-18] However, other strategies to differentiate isomeric pairs using only MS analysis have also been developed, particularly for GD1a and GD1b, using MALDI. For example, Ivleva et al. applied a partial cooling strategy during the desorption/ionization process, resulting in sodiated GD1a and GD1b having different relative fragment intensities.[19] In another report, Ito et al. used negative ion atmospheric pressure-MALDI coupled with a MS^n switching strategy to differentiate the isomeric gangliosides, showing that GD1a and GD1b have characteristic product ions.[20] This method required the generation of

specific ion-types, which could be challenging and would likely require careful matrix selection to produce the correct ion-type (e.g., $[M-H]^-$ or $[M+Na]^+$).[19, 21] Further, the preparation steps are complicated by requiring different wash procedures prior to analysis.[22] Therefore, most of the MALDI-MS reports still utilize the positive ion mode neglecting to resolve isomeric species.

Electrospray ionization (ESI) is also used in ganglioside analysis. ESI is usually coupled with liquid chromatography (LC) prior to mass spectrometry.[23] Both reversed-phase (RP) and hydrophilic interaction liquid chromatography (HILIC) have been applied to ganglioside analysis, with the former usually separating the different gangliosides based on their carbon number[24] and the latter providing the ability to separate isomeric glycan head moieties.[25] Hájek et al. optimized a HILIC platform that can partially separate isomeric GD1a/b and their respective carbon numbers simultaneously, which is powerful for profiling gangliosides from biological matrixes.[26] Recently, two-dimensional (2D) chromatography methods, combining RP with either HILIC or normal phase LC, have been developed for lipidomics analysis to improve coverage.[27-29] Si et al. developed a 2D chromatography method that coupled supercritical fluid chromatography and RPLC that expanded the number of profiled gangliosides in the sample.[30] These LC-MS methods enable isomeric separation, but are time consuming.

On the other hand, shotgun ESI-MS lipidomics approaches have the advantage of short analysis time, but often struggle to differentiate isomers. Recently, Sabru et al. coupled a shotgun approach with ion mobility mass spectrometry (IMS) to separate various classes of gangliosides in the gas phase.[31] Moreover, high-resolution IMS, using the structures for lossless ion manipulations (SLIM) approach, has demonstrated the capability of separating sodiated GD1a/b isomers in positive ion mode,[32] and the same GD series and GT1a/b/c isomers in negative ion mode. Tandem mass spectrometry was used to validate the isomeric structures.[33]

In addition to the IMS method mentioned above, other pure gas phase approaches including dissociation methods, such as ultraviolet photo-dissociation[34] and electron-induced dissociation,[35] have been shown to generate backbone cleavages within the glycan head moieties, allowing for the differentiation of isomers. Recently, our group has developed shotgun MS strategies involving gas-phase ion/ion chemistry and MS^n to differentiate isomeric lipids[36-39] and glycosphingolipids.[40-41] Gas-phase ion/ion chemistry allows for the transformation of targeted ions into different charge states or derivatized product ions.[42] Therefore, ion-types can be readily manipulated for various purposes.[43] The MALDI-MS work indicated that sodium cationization can be helpful for the

structural determination of gangliosides. However, the most sensitive ESI conditions generate deprotonated gangliosides ($[M-nH]^{n-}$, where n is related to the number of sialic acids on the glycan moiety),[44] which do not fragment under conventional CID conditions in ways that allow for isomer differentiation. Sodiated ions could be generated by adding sodium salts, but salt addition could adversely affect the ionization efficiency, which may further impact the sensitivity and complicate the spectrum.[45-47] Gas-phase ion/ion chemistry provides a way to modify the ion type without affecting the solution or ionization conditions. Moreover, by using a pulsed dual spray system, reagents can be quickly interchanged, providing rapid and ready access to the different ion-types required to interrogate gangliosides.[48] In this work, we focused on using gas-phase ion/ion reactions to generate the targeted ion types for the structural elucidation of a wide range of gangliosides, including GM3, GM1, GD1, and GT1. We demonstrated the capability of applying various gas-phase ion chemistries to reduce interferences and differentiate isomeric species. The described workflow was also successfully applied to biological extracts

6.2 Experimental

6.2.1 Materials

All ganglioside extracts were purchased from Avanti Polar Lipids, Inc. (Alabaster, AL). Sodium chloride (NaCl), magnesium chloride ($MgCl_2$), 2,2';6',2"-terpyridine (Terpy), 4'-Chloro-2,2';6',2"-terpyridine (Terpy-Cl), 4,4',4''-tri-tert-butyl-2,2';6',2"-terpyridine (ttb-Terpy), and proton sponge (N, N, N′, N′-tetramethyl-1,8-naphthalenediamine, PrS) were purchased from Sigma-Aldrich (St. Louis, MO). MS-grade methanol (MeOH) and LC-grade chloroform (CH_3Cl) were purchased from Fisher Scientific (Pittsburgh, PA).

6.2.2 Sample Preparation

Stock solutions of different classes of ganglioside extracts and total gangliosides extract (porcine brain) were prepared in MeOH/$CHCl_3$ (v/v, 50/50) to a concentration of 0.5 or 1 mg-mL^{-1}, and stored at −80 °C. Before the analysis, the stock solutions were diluted using the same MeOH/$CHCl_3$ solvent to 0.01mg mL^{-1}. For total ganglioside extract analysis, 1 mg of extract powder was dissolved in 1 mL of MeOH/$CHCl_3$ (v/v, 50/50) as the stock solution and stored at −80℃ before use. Prior to analysis, the lipid extract was diluted with MS grade MeOH to a final

concentration of 0.05 mg mL^{-1}. $MgCl_2$ or NaCl and differebt Terpy reagents were mixed in methanolic solution with 1:1 (molar ratio) to a final concentration of ~50 μM for the metal-ligand complex. Proton sponge powder was dissolved in MeOH with the stock concentration at 1 mM, and then spiked into the metal-terpy complex solution with a final concentration of 20 μM.

6.2.3 Mass Spectrometry

All experiments were performed on a TripleTOF 5600 quadrupole time-of-flight mass spectrometer (SCIEX, Concord, ON, Canada) that has been modified for ion/ion reactions.[49] Alternately pulsed dual nano-electrospray ionization (nESI) allows for the sequential injection of anions and cations.[48] Ganglioside anions (e.g., $[GM-H]^-$ or $[GT-3H]^{3-}$) and metal-ligand reagent cations (e.g., $[Mg(Terpy)_2]^{2+}$) were alternately generated via nESI, mass-selected in Q1, and transferred to q2 for mutual storage (10-30 ms). Sequential resonance ejection ramps in q2 were used to mass-select targeted ion/ion reaction product ions for MS^n experiments.[50] For GD anions ($[GD-2H]^{2-}$), sequential ion/ion reactions were performed. First, $[GD-2H]^{2-}$ was generated via nESI, and stored in q2. Next, both $[PrS+H]^+$ and metal-ligand complex ($[Mg(Terpy)_2]^{2+}$) ions were generated via alternately pulsed nESI, but only $[PrS+H]^+$ was mass-selected in Q1 and transferred to q2 for mutual storage (10-30 ms). A supplemental AC amplitude of 0.02V p-p at the secular frequency of the targeted proton transfer product ($[GD-H]^-$) was applied during the entire mutual storage period to park the ion to prevent further neutralization of the anion.[51] Sequential resonance ejection ramps in q2[50] were then used to mass-select targeted $[GD-H]^-$ ions and store them in q2. Another pulse from the cation emitter was applied and generated both cations via nESI, and only the mass-selected metal-ligand complex cation was transferred to q2 for mutual storage (10-30 ms). Further sequential resonance ejection ramps in q2 were used to mass-select targeted ion/ion reaction product ions for MS^n experiments. The total time to complete a full cycle of steps (i.e., ion fills, ion isolations, ion/ion reactions, ion activation, and mass analysis) ranged from 0.5 to 0.8 s.

6.3 Results and Discussion

6.3.1 Analysis of GM Series

The GM series are gangliosides that consist of only one sialic acid (N-Acetylneuraminic acid, NeuAc) on the glycan moiety. We obtained two different purified GM extracts, GM3 and GM1, which differ in the total numbers of saccharides on the glycan (**Figure 6.1**). Data for these ions is presented here to illustrate the behaviors of the ion types relevant to this work. Singly deprotonated GM anions ($[GM-H]^-$) could be generated via direct negative nESI. We first mass-selected the ion population for the singly deprotonated GM3, [GM3 C40:1−H]$^-$ (*m/z* 1235.8) and performed ion-trap CID of the selected ion population. **Figure 6.2a** shows the product ion spectrum of [GM3 C40:1−H]$^-$, and the insert shows the isolated ion population from the mass selection. The abnormal isotopic distribution indicates the presence of multiply-charged ions (most likely doubly charged anions) in the isolated population in addition to the singly deprotonated GM3. The appearance of product ions higher in *m/z* than that of the precursor ion is also consistent with the presence of multiply-charged ions in the activated ion population. To eliminate mixtures of charge states, we performed a gas-phase ion/ion reaction between the isolated anion population shown in the **Figure 6.2a** insert with $[Mg(Terpy)_2]^{2+}$. Importantly, singly deprotonated ions undergo charge inversion, yielding singly charged complex cations, while the doubly-charged ions are effectively neutralized and are not observed in the resulting product ion spectrum. Two charge-inversion product cations were observed from this reaction, including [GM3 C40:1−H+Mg]$^+$ (*m/z* 1259.8) and [GM3 C40:1−H+MgTerpy]$^+$ (*m/z* 1492.8) (**Figure 6.3**). CID of [GM3 C40:1−H+MgTerpy]$^+$ (*m/z* 1492.8) ion resulted in Terpy loss to yield the [GM3 C40:1−H+Mg]$^+$ cation (**Figure 6.2b**). After another round of CID of the [GM3 C40:1−H+Mg]$^+$ (*m/z* 1259.8) ion, a cleaner product ion spectrum (compared with that of **Figure 6.2a**) was generated (**Figure 6.2c)**, showing a dominant $Y_2^{\blacklozenge}$ ion (−NeuAc, neutral loss (NL) of 291 Da). Much smaller signals corresponding to losses of 162 (*m/z* 1097) and 144 Da (*m/z* 1115) were also observed. We postulate that these product ions are associated with in-ring fragmentation from the sialic acid ($^{0,4}X_2$, and $^{4,5}X_2$, respectively) combined with a CO_2 or C_2H_4O (44 Da) loss. X ions and CO_2/C_2H_4O losses from gangliosides and other glycans are common in product ion spectra generated via various dissociation techniques.[34-35] MS^4 experiments were performed on both the 162 Da and 144 Da loss ions (**Figures 5.4a and 5.4b**, respectively), and the results show that the dissociation of the 144

Da loss ion produces an ion of *m/z* 1097, which is identical to the overall 162 Da loss mentioned earlier. In addition, MS^4 results also showed that the 144 Da loss ion and 162 Da loss ion share some same fragments, indicating they are related.

The same strategy as GM3 analysis is applied for GM1 analysis. **Figure 6.5a** shows the CID spectrum of the isolated ion population ([GM1 C36:1−H]$^-$, *m/z* 1544.9) with the insert showing the presence of a doubly-charged interferent. The CID spectrum shows some product ions (transparent blue boxes in **Figure 6.5a**) from the isolated ion population that could not be rationalized on the basis of the GM1 structure and presumably arise from the doubly-charged interfering species. **Figure 6.5b** shows the CID spectrum of the charge-inverted complex cation, [GM1 C36:1−H+MgTerpy]$^+$ (*m/z* 1801.9), and **Figure 6.5c** shows CID spectrum of [GM1 C36:1−H+Mg]$^+$ (*m/z* 1568.9). As with the GM1 system described above, loss of the remaining Terpy ligand dominates **Figure 6.5c**. **Figure 6.5c** shows three dominant fragment ions, including water loss, $Y_{2\alpha}^{\blacklozenge}$ (−[Gal-GalNAc], NL of 365), and $Y_{2\beta}^{\blacklozenge}$ (−[NeuAc], NL of 291) without the low level unidentified products apparent in **Figure 6.5c.**

6.3.2 Charge Inversion and Magnesium Cation Transfer Reactions of GM series with Different Metal-Ligand Complexes

From the previous section, we recognized that the main fragment ion from the charge-inverted complex cation, [GM−H+MgTerpy]$^+$, is another Terpy ligand loss ([GM−H+Mg]$^+$) (**Figure 6.2b and Figure 6.5b**), which is the ion-type giving us the structural information after CID. From the post-ion/ion spectrum (**Figure 6.3**), we also can observe [GM3 C40:1−H+Mg]$^+$ was formed right after the charge-inversion ion/ion reaction. Therefore, it shows the potential of the formation of magnesium transfer cation might be facilitated by the facile loss of the Terpy ligand after the ion/ion reaction. A single ligand loss is usually observed after the charge inversion ion/ion reaction in the gas phase, in which the anion accommodates the interaction sites and replaces the ligand after the reaction.[36, 40] Therefore, altering the ligand could enhance, or hinder, magnesium transfer, encouraging the study of different ligands. **Figure 6.6b** s shows the reaction between [GM3 C40:1−H]$^-$ and [Mg(Terpy-Cl)$_2$]$^{2+}$, with more Terpy ligand loss after the reaction which Terpy is with electron-withdrawing modification (Terpy-Cl). In contrast, when Terpy with an electron-donating modification is used (ttb-Terpy, **Figure 6.6c**), no ligand loss is observed. The results suggest that the ligand loss is related to the binding affinity between magnesium and ligands.

Figure 6.7 also demonstrates the phenomenon via applying different activation AC amplitudes to resonance activate all the charge inverted GM3 C40:1 complex cation empirically. The required amplitudes follow the order of the predicted ionic interaction between the ligand and magnesium (Mg(Terpy-Cl) < MgTerpy < Mg(ttb-Terpy)).[52] Using the same substituted ligands as in GM3 for GM1 reaction, the same trend of the required AC amplitude for activating the charge inverted GM1 C36:1 complex cations as GM1 C40:1 was also observed, validating the hypothesis (**Figure 6.8**).

6.3.3 Analysis of GD Series.

Unlike the GM series, the GD series contains two sialic acids that can differ in branching arrangement on the glycan chain, forming two major isomeric gangliosides, GD1a and GD1b (**Figure 6.1**). CID was performed on both doubly deprotonated GD ions, $[GD1a\ C36{:}1{-}2H]^{2-}$ and $[GD1b\ C36{:}1{-}2H]^{2-}$. The results show that two unique diagnostic ions are observed in the GD1b product ion spectrum, namely the $Y_{2\beta}$ and $B_{2\beta}$ ($[2NeuAc{-}H]^{-}$) ions (**Figure 6.9b**), which are complementary ions from the same cleavage. However, no unique diagnostic ions from GD1a are observed, leading to ambiguities in ganglioside identification and thus hindering isomeric discrimination (**Figure 6.9a**).

To provide isomeric resolution, we first used a proton transfer reaction to reduce the charge-state of GD anions. Charge reduced GD1 anions ($[GD1{-}H]^{-}$) were obtained after the reaction between $[GD1{-}2H]^{2-}$ and $[PrS{+}H]^{+}$ (**Section 6.2.3**) and the results are shown in **Figure 6.11a**. The product ion spectra of the singly-deprotonated species yielded the same product ions observed with the dianions (compare **Figure 6.11b** and **6.11c**). The $[GD{-}2H]^{2-}$ ions obviously cannot undergo charge inversion using $[Mg(Terpy)_2]^{2+}$. We therefore pursued a sequential ion/ion reaction strategy (**Section 6.2.3**) involving single proton transfer using protonated proton sponge to generate the $[GD{-}H]^{-}$ ion followed by reaction with $[Mg(Terpy)_2]^{2+}$ to produce the charge-inverted complex cation, $[GD{-}H{+}Mg(Terpy)]^{+}$. Sequential ion/ion reactions involving different reagents have been reported previously with a triple spray ionization system.[53] However, we simplified the three emitter system by mixing Mg(Terpy) and proton sponge and using just two emitters. By taking advantage of Q1 mass selection, we were able to select a single reagent (i.e., protonated proton sponge) for the first reaction, and then with a subsequent pulse on the same emitter, select a different reagent (i.e. $[Mg(Terpy)_2]^{2+}$) for the charge inversion step.

As depicted in **Figure 6.9**, ion-trap CID of the charge inverted complex cation was performed to produce the magnesium transfer product, denoted [GD C36:1−H+Mg]$^+$. Both GD1a and GD1b isomers share similar product ions, such as neutral loss of water (NL of 18 Da), one sialic acid (NeuAc, NL of 291 Da), and the $B_5^\bullet$ or $B_4^\bullet$ ion (the whole glycan moiety, *m/z* 1294.3) for GD1a or GDlb, respectively. However, GD1a has a unique diagnostic fragment ion, $Y_{2\alpha}^\bullet$ ion (*m/z* 1203.5, blue box in **Figure 6.9c**), which corresponds to the loss of the alpha chain from the glycan moiety (−[NeuAc-Gal-GalNAc], NL of 656). GD1b also has a unique diagnostic fragment, $Y_{2\alpha}^\bullet$ ion (*m/z* 1495.6, green box in **Figure 6.9d**) formed from the loss of [Gal-GalNAc] (NL of 365 Da) on the alpha chain. The two distinct diagnostic fragment ions permit unambiguous isomeric differentiation of GD1a and GD1b. We also produced sodiated GD anions, [GD C36:1−2H+Na]$^-$, via sodium transfer from [Na(Terpy)$_2$]$^+$ in a gas-phase ion/ion reaction and the CID results are shown in **Figure 6.12**. It is noted that sodiated GD1a and GD1b give different product ions patterns, in which the former gives intense water and sialic acid losses, and the latter again has a pair of complementary ions corresponding with the cleavage of two sialic acids. However, unique diagnostic ions, such as those generated via charge inversion with [Mg(Terpy)$_2$]$^{2+}$, are more beneficial for isomeric differentiation in mixture analysis.

6.3.4 Analysis of GT Series

GT gangliosides have three sialic acids on the glycan moiety, and the isomerism in GT is more diverse (**Figure 6.1**). However, we were able to obtain only a purified GT1b extract from a commercial vendor. Therefore, we performed the gas-phase ion/ion reaction only between the GT1b anions with the reagent cations. The CID spectrum of [GT1b C36:1−3H]$^{3-}$ is shown in **Figure 6.13a**. This ion was subjected to the reaction with [Mg(Terpy)$_2$]$^{2+}$, forming the magnesium transfer product ion, [GT1b C36:1−3H+Mg]$^-$ (**Figure 6.13b**). **Figure 6.13c** shows the product ion spectrum after ion-trap CID of the magnesium adducted anion. Comparing it with the CID spectrum of [GT1b C36:1−3H]$^{3-}$ (**Figure 6.13a**), the magnesium adduct anion gives a diagnostic ion, $Y_{2\alpha}^\bullet$ (loss of alpha chain, −[NeuAc-Gal-GalNAc], NL of 656 Da, blue box in **Figure 6.13c**) and a potential diagnostic ion, $Y_{2\alpha}$−NeuAc$^\bullet$ (NL of 947), while none of the fragment ions from the [GT1b C36:1−3H]$^{3-}$ provide structurally specific information for GT1b. Additionally, we also performed CID on [GT1b C36:1−2H]$^{2-}$ and its sodium transferred product ion, [GT1b

C36:1−2H+Na]$^-$ (**Figure 6.15a and 6.15b**), neither of which provided specific structural information for GT1b. We conclude that, of the ion types examined, only the magnesium transfer product has the potential to differentiate isomeric GT gangliosides. Consequently, we propose a workflow, summarized in **Scheme 6.2**, using a range of ion chemistries to comprehensively cover GM, GD, and GT gangliosides. These chemistries include charge inversion reactions, proton transfer reactions, cation transfer reactions, and gas-phase dissociation.

6.3.5 Analysis of Total Ganglioside Extracts from Porcine Brain

We adopted the findings discussed above to profile the gangliosides in biological extracts from porcine brain. A total of 20 *m/z* values corresponding to 4 GM1, 3 GD, and 13 GT gangliosides were identified based on their respective masses from LIPIDMAPS. We further applied the workflow to profile the isomeric compositions of the putative gangliosides. **Table 6.1** shows that a total of 34 unique gangliosides were identified among the profiled 20 *m/z* values. Among the 4 GM1, we identified two GM1 with fucose (Fuc) conjugations. After CID of the magnesium transferred products, we were also able to identify that the fucose is linked terminally to the alpha chain on the glycan moiety via neutral loss of one fucose ($Y_{4\alpha}$, NL of 146 Da) and the further alpha chain loss $Y_{2a}^{\blacklozenge}$ ion (−[Fuc-Gal-GalNAc], NL of 511), the latter of which shares the same *m/z* as the analogous fragment from non-fucosylated GM1. Moreover, the neutral loss of one sialic acid ($Y_{2\beta}^{\blacklozenge}$, −NeuAc, NL of 291) could also be found in the spectrum with the mass shift according to the fucose mass (**Figure 6.16**). Therefore, using the charge inversion reaction with magnesium transfer for profiling the [GM−H]$^-$ series provides the potential to eliminate other interferences and provides structural information for fucose conjugated GM gangliosides.

Next, we also profiled 5 different GD gangliosides, including 2 isomeric GD1a/b pairs and 1 fucosyl GD1b C38:1. The diagnostic fragment ions, NL of 656 and NL of 365, from both isomeric pairs matched what we observed in the GD analysis section, corresponding to GD1a and GD1b, respectively (**Figure 6.17a**). We observed that the ion with NL of 656 Da has a higher abundance than the ion with NL of 365, suggesting that GD1a might be present in a higher concentration in the porcine brain, assuming equivalent ionization efficiencies. To further investigate the isomeric composition within the porcine brain extracts, we proposed a relative quantification method using

the Total Least Square (TLS) strategy to match the abundant fragment ions from the isomeric mixture with the two "pure component" CID spectra.[54]

To perform the relative quantification of porcine brain extracts, we first analyzed the pure GD1a or GD1b from the standard mixture. We are able to obtain pure GD1a or GD1b from Q1 mass selection via the instrument. The selected ions were then subjected into q2 for further reaction and dissociation to produce magnesium transfer product cations, $[GD1-H+Mg]^+$. Next, ion-trap CID were performed to fully deplete the precursor cation, $[GD1-H+Mg]^+$, obtaining the CID spectra. We further extracted the peak areas from the monoisotopic peaks of the major fragment ions and normalized with the total extracted peak area. The normalized results are showed in the following **Table 6.2**. Next, the same procedures were performed on the profiled GD gangliosides, GD1 C36:1 and GD1 C38:1, from the porcine brain sample, and the normalized %area of the diagnositc fragments are also obtained**.** The TLS algorithm is then utilized to match the normalized peak area from the profiled gangliosides from the porcine brain to those corresponding pure component analyses.[54] We then could obtain the percentages from the both isomers in the isomeric pair to know their relative quantity in the sample. The results suggested that both GD1 C36:1 and GD1 C38:1 isomeric pairs show a higher GD1a percentage than GD1b, in which the calculated percentages were 71.7±2.3 % to 24.9±2.1 % for GD1a C36:1 to GD1b C36:1, and 86.2±2.1 % to 13.0±2.3 % for GD1a C38:1 to GD1b C38:1 (**Table 6.3**), which validates our speculation. However, we could not perform absolute quantification because we could not obtain pure GD1a and GD1b standards with only a single carbon number. Commercially available purified GD1a and GD1b extracts contained a mixture of different GD gangliosides with a range of total carbon numbers on their lipid moieties. Fucosylated GD1b C38:1 was also profiled. The diagnostic $Y_{2\alpha}^{\blacklozenge}$ fragment ion (−[Fuc-Gal-GalNAc], NL of 511) after CID reveals the loss of the whole alpha chain, including the conjugated fucose, indicating the fucosylation site on the ganglioside (**Figure 6.17b**).

We profiled ions of a total of 13 *m/z* values corresponding to 25 GT gangliosides, including 15 GT1 and 10 N-glycolylneuraminic acid (NeuGc) conjugated GT1 (Gc-GT1). When we performed ion-trap CID of the magnesium transfer product ion from the GT1 anions, we observed different fragment ions than from the CID spectrum of the pure GT1b sample described above. Ions with *m/z* 968 and *m/z* 894 were both observed in the product ion spectrum, corresponding to the $B_{4\alpha}^{\blacklozenge}$ ion ($[2NeuAc-Gal-GalNAc-3H+Mg]^-$) and $B_{3\beta}^{\blacklozenge}$ ($[3NeuAc-3H+Mg]^-$) from GT1a and GT1c, respectively (**Figure 6.18)**. These findings suggest that using magnesium cation transfer

reactions can be used to profile the three isomeric GT gangliosides. However, we cannot validate the finding with pure GT1a and GT1c standards. Additionally, the Gc-GT1 gangliosides were also profiled and also showed a similar trend to the regular GT1 gangliosides. **Figure 6.19** shows that the NeuGc is most likely linked to the alpha chain on the glycan, which might also be the first sialic acid on that alpha chain because no mass shift is observed from the first sialic acid loss ions and $B_{4\alpha}^{\blacklozenge}$ ions ([2NeuAc-Gal-GalNAc−3H+Mg]$^-$) from Gc-GT1a, but $Y_{2\alpha}^{\blacklozenge}$ ions (−[NeuAc-Gal-GalNAc], NL of 656) from Gc-GT1b and $B_{3\beta}^{\blacklozenge}$ ions ([NeuGc-2NeuAc−3H+Mg]$^-$) from Gc-GT1c were observed, with the mass shift equaling the mass difference between NeuAc and NeuGc. Overall, the profiled results are comparable to other reports describing analysis of gangliosides in porcine brain, but we note that use of magnesium transfer ion/ion reactions can improve coverage among trace isomeric GT gangliosides.[26, 34]

6.4 Conclusions

We present a novel shotgun mass spectrometry strategy comprised of various ion/ion reactions and ion-trap CID to analyze the glycan moieties on different ganglioside subclasses, including GM3, GM1, GD1, and GT1. In this work, we observed that magnesium adduction facilitates structural elucidation of these ganglioside classes. Therefore, a workflow was proposed to utilize a series of various gas-phase ion/ion reactions for ganglioside analysis. For both GM3 and GM1, a single charge inversion reaction was used to eliminate the possible isobaric dianion interferences from a mixture, which is beneficial for identifying ganglioside species in a mixture. Furthermore, the proposed workflow can localize the fucose on the fucosylated GM1 from a biological extract. A sequential ion/ion reaction approach involving single proton transfer followed by a charge inversion was applied to the analysis of GD1 gangliosides. Both GD1a and GD1b show diagnostic fragment ions from the CID of the [GD1−H+Mg]$^+$ ion where the loss of the alpha chain on both GD1a (−[NeuAc-Gal-GalNAc], NL 656) and GD1b (−[Gal-GalNac], NL 365) can distinguish the isomeric pair. Moreover, like GM1, the fucose position on the GD1 could also be identified. We extended the strategy via the relative quantification of the isomeric pairs of GD1a/b C36:1 and C38:1 from porcine brain extracts. Lastly, a magnesium transfer reaction can differentiate the three isomeric GT1 gangliosides, GT1a, GT1b, and GT1c, wherein each isomer showed specific diagnostic fragment ions. The proposed workflow was applied to the analysis of

porcine brain extracts, and a total of 34 gangliosides were profiled across the 20 *m/z* values subjected to investigation. The results demonstrate the applicability of utilizing shotgun mass spectrometry and gas-phase ion/ion chemistry to generate magnesium adducted gangliosides for elucidating the structural information on the glycan moiety from gangliosides in both purified and biological extracts. We note that, while beyond the scope of this work, the ion/ion reaction work-flow described herein can also be compatible with LC and IMS separations. The separation must take place prior to the ion/ion reaction process in the former case whereas, given the gas-phase nature of the IMS separation, the use of ion/ion reactions before or after separation is possible in the latter case.

6.5 Acknowledgements

This work was supported by the National Institutes of Health (NIH) under Grants GM R37-45372 and GM R01-118484.

6.6 References.

1. Mauri, L.; Sonnino, S.; Prinetti, A., Chemical and Physicochemical Properties of Gangliosides. In Gangliosides: Methods and Protocols, Sonnino, S.; Prinetti, A., Eds. Springer New York: New York, NY, 2018; pp 1-17.
2. Sezgin, E.; Levental, I.; Mayor, S.; Eggeling, C., The mystery of membrane organization: composition, regulation and roles of lipid rafts. Nat Rev Mol Cell Biol 2017, 18 (6), 361-374.
3. Komura, N.; Suzuki, K. G.; Ando, H.; Konishi, M.; Koikeda, M.; Imamura, A.; Chadda, R.; Fujiwara, T. K.; Tsuboi, H.; Sheng, R.; Cho, W.; Furukawa, K.; Furukawa, K.; Yamauchi, Y.; Ishida, H.; Kusumi, A.; Kiso, M., Raft-based interactions of gangliosides with a GPI-anchored receptor. Nat Chem Biol 2016, 12 (6), 402-10.
4. Schnaar, R. L.; Gerardy-Schahn, R.; Hildebrandt, H., Sialic acids in the brain: gangliosides and polysialic acid in nervous system development, stability, disease, and regeneration. Physiol Rev 2014, 94 (2), 461-518.
5. Schengrund, C.-L., Gangliosides: glycosphingolipids essential for normal neural development and function. Trends Biochem Sci 2015, 40 (7), 397-406.
6. Kracun, I.; Kalanj, S.; Talan-Hranilovic, J.; Cosovic, C., Cortical distribution of gangliosides in Alzheimer's disease. Neurochem Int 1992, 20 (3), 433-438.

7. Caughlin, S.; Maheshwari, S.; Agca, Y.; Agca, C.; Harris, A. J.; Jurcic, K.; Yeung, K. K. C.; Cechetto, D. F.; Whitehead, S. N., Membrane-lipid homeostasis in a prodromal rat model of Alzheimer's disease: Characteristic profiles in ganglioside distributions during aging detected using MALDI imaging mass spectrometry. Biochim Biophys Acta Gen Subj 2018, 1862 (6), 1327-1338.

8. Seyfried, T. N.; Choi, H.; Chevalier, A.; Hogan, D.; Akgoc, Z.; Schneider, J. S., Sex-Related Abnormalities in Substantia Nigra Lipids in Parkinson's Disease. ASN Neuro 2018, 10, 1759091418781889.

9. Huebecker, M.; Moloney, E. B.; van der Spoel, A. C.; Priestman, D. A.; Isacson, O.; Hallett, P. J.; Platt, F. M., Reduced sphingolipid hydrolase activities, substrate accumulation and ganglioside decline in Parkinson's disease. Mol Neurodegener 2019, 14 (1), 40.

10. Desplats, P. A.; Denny, C. A.; Kass, K. E.; Gilmartin, T.; Head, S. R.; Sutcliffe, J. G.; Seyfried, T. N.; Thomas, E. A., Glycolipid and ganglioside metabolism imbalances in Huntington's disease. Neurobiol Dis 2007, 27 (3), 265-277.

11. Di Pardo, A.; Amico, E.; Maglione, V., Impaired Levels of Gangliosides in the Corpus Callosum of Huntington Disease Animal Models. Front Neurosci 2016, 10 (457).

12. Yu, R. K.; Tsai, Y.-T.; Ariga, T.; Yanagisawa, M., Structures, biosynthesis, and functions of gangliosides--an overview. J Oleo Sci 2011, 60 (10), 537-544.

13. Tettamanti, G., Ganglioside/glycosphingolipid turnover: New concepts. Glycoconjugate J 2003, 20 (5), 301-317.

14. Colsch, B.; Jackson, S. N.; Dutta, S.; Woods, A. S., Molecular Microscopy of Brain Gangliosides: Illustrating their Distribution in Hippocampal Cell Layers. ACS Chem Neurosci 2011, 2 (4), 213-222.

15. Zhang, Y.; Wang, J.; Liu, J. a.; Han, J.; Xiong, S.; Yong, W.; Zhao, Z., Combination of ESI and MALDI mass spectrometry for qualitative, semi-quantitative and in situ analysis of gangliosides in brain. Sci Rep 2016, 6 (1), 25289.

16. Harris, A.; Roseborough, A.; Mor, R.; Yeung, K. K. C.; Whitehead, S. N., Ganglioside Detection from Formalin-Fixed Human Brain Tissue Utilizing MALDI Imaging Mass Spectrometry. J Am Soc Mass Spectrom 2020, 31 (3), 479-487.

17. Dreisewerd, K.; Müthing, J.; Rohlfing, A.; Meisen, I.; Vukelić, Ž.; Peter-Katalinić, J.; Hillenkamp, F.; Berkenkamp, S., Analysis of Gangliosides Directly from Thin-Layer Chromatography Plates by Infrared Matrix-Assisted Laser Desorption/Ionization Orthogonal Time-of-Flight Mass Spectrometry with a Glycerol Matrix. Anal Chem 2005, 77 (13), 4098-4107.

18. Ivleva, V. B.; Sapp, L. M.; O'Connor, P. B.; Costello, C. E., Ganglioside Analysis by Thin-Layer Chromatography Matrix-Assisted Laser Desorption/Ionization Orthogonal Time-of-Flight Mass Spectrometry. J Am Soc Mass Spectrom 2005, 16 (9), 1552-1560.

19. Ivleva, V. B.; Elkin, Y. N.; Budnik, B. A.; Moyer, S. C.; O'Connor, P. B.; Costello, C. E., Coupling Thin-Layer Chromatography with Vibrational Cooling Matrix-Assisted Laser Desorption/Ionization Fourier Transform Mass Spectrometry for the Analysis of Ganglioside Mixtures. Anal Chem 2004, 76 (21), 6484-6491.

20. Ito, E.; Tominaga, A.; Waki, H.; Miseki, K.; Tomioka, A.; Nakajima, K.; Kakehi, K.; Suzuki, M.; Taniguchi, N.; Suzuki, A., Structural Characterization of Monosialo-, Disialo- and Trisialo-gangliosides by Negative Ion AP-MALDI-QIT-TOF Mass Spectrometry with MSn Switching. Neurochem Res 2012, 37 (6), 1315-1324.

21. Yang, E.; Dufresne, M.; Chaurand, P., Enhancing ganglioside species detection for MALDI-TOF imaging mass spectrometry in negative reflectron mode. Int J Mass spectrom 2019, 437, 3-9.

22. Angel, P. M.; Spraggins, J. M.; Baldwin, H. S.; Caprioli, R., Enhanced Sensitivity for High Spatial Resolution Lipid Analysis by Negative Ion Mode Matrix Assisted Laser Desorption Ionization Imaging Mass Spectrometry. Anal Chem 2012, 84 (3), 1557-1564.

23. Groux-Degroote, S.; Guérardel, Y.; Delannoy, P., Gangliosides: Structures, Biosynthesis, Analysis, and Roles in Cancer. ChemBioChem 2017, 18 (13), 1146-1154.

24. Ikeda, K.; Shimizu, T.; Taguchi, R., Targeted analysis of ganglioside and sulfatide molecular species by LC/ESI-MS/MS with theoretically expanded multiple reaction monitorings. J Lipid Res 2008, 49 (12), 2678-2689.

25. Zauner, G.; Deelder, A. M.; Wuhrer, M., Recent advances in hydrophilic interaction liquid chromatography (HILIC) for structural glycomics. Electrophoresis 2011, 32 (24), 3456-3466.

26. Hájek, R.; Jirásko, R.; Lísa, M.; Cífková, E.; Holčapek, M., Hydrophilic Interaction Liquid Chromatography–Mass Spectrometry Characterization of Gangliosides in Biological Samples. Anal Chem 2017, 89 (22), 12425-12432.

27. Li, M.; Feng, B.; Liang, Y.; Zhang, W.; Bai, Y.; Tang, W.; Wang, T.; Liu, H., Lipid profiling of human plasma from peritoneal dialysis patients using an improved 2D (NP/RP) LC-QToF MS method. Anal Bioanal Chem 2013, 405 (21), 6629-6638.

28. Li, M.; Tong, X.; Lv, P.; Feng, B.; Yang, L.; Wu, Z.; Cui, X.; Bai, Y.; Huang, Y.; Liu, H., A not-stop-flow online normal-/reversed-phase two-dimensional liquid chromatography–quadrupole time-of-flight mass spectrometry method for comprehensive lipid profiling of human plasma from atherosclerosis patients. J Chromatogr A 2014, 1372, 110-119.

29. Narváez-Rivas, M.; Vu, N.; Chen, G.-Y.; Zhang, Q., Off-line mixed-mode liquid chromatography coupled with reversed phase high performance liquid chromatography-high resolution mass spectrometry to improve coverage in lipidomics analysis. Anal Chim Acta 2017, 954, 140-150.

30. Si, W.; Liu, Y.; Xiao, Y.; Guo, Z.; Jin, G.; Yan, J.; Shen, A.; Zhou, H.; Yang, F.; Liang, X., An offline two-dimensional supercritical fluid chromatography × reversed phase liquid chromatography tandem quadrupole time-of-flight mass spectrometry system for comprehensive gangliosides profiling in swine brain extract. Talanta 2020, 208, 120366.

31. Sarbu, M.; Robu, A. C.; Ghiulai, R. M.; Vukelić, Ž.; Clemmer, D. E.; Zamfir, A. D., Electrospray Ionization Ion Mobility Mass Spectrometry of Human Brain Gangliosides. Anal Chem 2016, 88 (10), 5166-5178.

32. Wojcik, R.; Webb, I. K.; Deng, L.; Garimella, S. V. B.; Prost, S. A.; Ibrahim, Y. M.; Baker, E. S.; Smith, R. D., Lipid and Glycolipid Isomer Analyses Using Ultra-High Resolution Ion Mobility Spectrometry Separations. Int J Mol Sci 2017, 18 (1), 183.

33. Wormwood Moser, K. L.; Van Aken, G.; DeBord, D.; Hatcher, N. G.; Maxon, L.; Sherman, M.; Yao, L.; Ekroos, K., High-defined quantitative snapshots of the ganglioside lipidome using high resolution ion mobility SLIM assisted shotgun lipidomics. Anal Chim Acta 2021, 1146, 77-87.

34. O'Brien, J. P.; Brodbelt, J. S., Structural Characterization of Gangliosides and Glycolipids via Ultraviolet Photodissociation Mass Spectrometry. Anal Chem 2013, 85 (21), 10399-10407.

35. Wong, Y. L. E.; Chen, X.; Wu, R.; Hung, Y. L. W.; Chan, T. W. D., Structural Characterization of Intact Glycoconjugates by Tandem Mass Spectrometry Using Electron-Induced Dissociation. Anal Chem 2017, 89 (18), 10111-10117.

36. Randolph, C. E.; Foreman, D. J.; Betancourt, S. K.; Blanksby, S. J.; McLuckey, S. A., Gas-Phase Ion/Ion Reactions Involving Tris-Phenanthroline Alkaline Earth Metal Complexes as Charge Inversion Reagents for the Identification of Fatty Acids. Anal Chem 2018, 90 (21), 12861-12869.

37. Randolph, C. E.; Blanksby, S. J.; McLuckey, S. A., Toward Complete Structure Elucidation of Glycerophospholipids in the Gas Phase through Charge Inversion Ion/Ion Chemistry. Anal Chem 2020, 92 (1), 1219-1227.

38. Randolph, C. E.; Shenault, D. S. M.; Blanksby, S. J.; McLuckey, S. A., Structural Elucidation of Ether Glycerophospholipids Using Gas-Phase Ion/Ion Charge Inversion Chemistry. J Am Soc Mass Spectrom 2020, 31 (5), 1093-1103.

39. Randolph, C. E.; Marshall, D. L.; Blanksby, S. J.; McLuckey, S. A., Charge-switch derivatization of fatty acid esters of hydroxy fatty acids via gas-phase ion/ion reactions. Anal Chim Acta 2020, 1129, 31-39.

40. Chao, H.-C.; McLuckey, S. A., Differentiation and Quantification of Diastereomeric Pairs of Glycosphingolipids Using Gas-Phase Ion Chemistry. Anal Chem 2020, 92 (19), 13387-13395.

41. Chao, H.-C.; McLuckey, S. A., In-Depth Structural Characterization and Quantification of Cerebrosides and Glycosphingosines with Gas-Phase Ion Chemistry. Anal Chem 2021, 93 (19), 7332-7340.

42. McLuckey, S. A.; Huang, T.-Y., Ion/Ion Reactions: New Chemistry for Analytical MS. Anal Chem 2009, 81 (21), 8669-8676.

43. Foreman, D. J.; McLuckey, S. A., Recent Developments in Gas-Phase Ion/Ion Reactions for Analytical Mass Spectrometry. Anal Chem 2020, 92 (1), 252-266.

44. Suzuki, A.; Suzuki, M.; Ito, E.; Nitta, T.; Inokuchi, J.-i., Mass Spectrometry of Gangliosides. In Gangliosides: Methods and Protocols, Sonnino, S.; Prinetti, A., Eds. Springer New York: New York, NY, 2018; pp 207-221.

45. Kruve, A.; Kaupmees, K.; Liigand, J.; Oss, M.; Leito, I., Sodium adduct formation efficiency in ESI source. J Mass Spectrom 2013, 48 (6), 695-702.

46. DeMuth, J. C.; McLuckey, S. A., Electrospray Droplet Exposure to Organic Vapors: Metal Ion Removal from Proteins and Protein Complexes. Anal Chem 2015, 87 (2), 1210-1218.

47. Metwally, H.; McAllister, R. G.; Konermann, L., Exploring the Mechanism of Salt-Induced Signal Suppression in Protein Electrospray Mass Spectrometry Using Experiments and Molecular Dynamics Simulations. Anal Chem 2015, 87 (4), 2434-2442.

48. Xia, Y.; Liang, X.; McLuckey, S. A., Pulsed Dual Electrospray Ionization for Ion/Ion Reactions. J Am Soc Mass Spectrom 2005, 16 (11), 1750-1756.

49. Xia, Y.; Chrisman, P. A.; Erickson, D. E.; Liu, J.; Liang, X.; Londry, F. A.; Yang, M. J.; McLuckey, S. A., Implementation of Ion/Ion Reactions in a Quadrupole/Time-of-Flight Tandem Mass Spectrometer. Anal Chem 2006, 78 (12), 4146-4154.

50. McLuckey, S. A.; Goeringer, D. E.; Glish, G. L., Selective ion isolation/rejection over a broad mass range in the quadrupole ion trap. J Am Soc Mass Spectrom 1991, 2 (1), 11-21.

51. McLuckey, S. A.; Reid, G. E.; Wells, J. M., Ion Parking during Ion/Ion Reactions in Electrodynamic Ion Traps. Anal Chem 2002, 74 (2), 336-346.

52. Henderson, I. Tuning the Properties of Metal-Ligand Complexes to Modify the Properties of Supramolecular Materials. Dissertation, University of Massachusetts Amherst, 2012.

53. Liang, X.; Han, H.; Xia, Y.; McLuckey, S. A., A Pulsed Triple Ionization Source for Sequential Ion/Ion Reactions in an Electrodynamic Ion Trap. J Am Soc Mass Spectrom 2007, 18 (3), 369-376.

54. Randolph, C. E.; Foreman, D. J.; Blanksby, S. J.; McLuckey, S. A., Generating Fatty Acid Profiles in the Gas Phase: Fatty Acid Identification and Relative Quantitation Using Ion/Ion Charge Inversion Chemistry. Anal Chem 2019, 91 (14), 9032-9040.

6.7 Tables

Table 6.1. Profiled gangliosides from porcine brain using the proposed workflow.

GM1					
Carbon number	**Formula**	**$[M-H]^-$**	**$[M-H+Mg]^+$**	**$Y_{2\alpha}$ (−[Gal-GalNac], −365)**	**$Y_{2\beta}$ (−NeuAc, −291)**
36:1	$C_{73}H_{131}N_3O_{31}$	1544.9	1568.9	1203.9	1277.9
38:1	$C_{75}H_{135}N_3O_{31}$	1572.9	1596.9	1231.9	1305.9

Fuc-GM1						
Carbon number	**Formula**	**$[M-H]^-$**	**$[M-H+Mg]^+$**	**$Y_{3\alpha}$ (−Fuc, −146)**	**$Y_{2\alpha}$ (−[Fuc-Gal-GalNac], −511)**	**$Y_{2\beta}$ (−NeuAc, −291)**
36:1	$C_{79}H_{141}N_3O_{35}$	1690.9	1714.9	1568.9	1203.9	1423.9
38:1	$C_{81}H_{145}N_3O_{35}$	1719.0	1742.9	1596.9	1231.9	1451.9

GD1						
Carbon number	**Formula**	**$[M-2H]^{2-}$**	**$[M-H]^-$**	**$[M-H+Mg]^+$**	**GD1a-$Y_{2\alpha}$ (−[NeuAc-Gal-GalNAc], −656)**	**GD1b-$Y_{2\alpha}$ (−[Gal-GalNac], −365)**
36:1	$C_{84}H_{148}N_4O_{39}$	917.5	1836.0	1860.0	1204.0	1495.0
38:1	$C_{86}H_{152}N_4O_{39}$	931.5	1864.0	1888.0	1232.0	1523.0

Table 6.1 continued

Fuc-GD1						
Carbon number	**Formula**	**$[M-2H]^{2-}$**	**$[M-H]^{-}$**	**$[M-H+Mg]^{+}$**	**GD1a-$Y_{2\alpha}$ (−[Fuc-NeuAc-Gal-GalNAc], −656)**	**GD1b-$Y_{2\alpha}$ (−[Fuc-Gal-GalNac], −511)**
38:1	$C_{92}H_{162}N_4O_{43}$	1004.5	2010.1	2034.0	ND*	1523.0

GT1						
Carbon number	**Formula**	**$[M-3H]^{3-}$**	**$[M-3H+Mg]^{-}$**	**GT1a-$B_{4\alpha}$ ([2NeuAc-Gal-GalNAc−3H+Mg]$^{-}$)**	**GT1b-Y2α (−[NeuAc-Gal-GalNAc], −656)**	**GT1c-$B_{3\beta}$ ([3NeuAc−3H+Mg]$^{-}$)**
34:1	$C_{93}H_{161}N_5O_{47}$	699.0	2121.0	ND	1465.0	894.2
36:1	$C_{95}H_{165}N_5O_{47}$	708.4	2149.0	968.3	1493.0	894.2
36:2	$C_{95}H_{163}N_5O_{47}$	707.7	2147.0	ND	1491.0	894.2
38:1	$C_{97}H_{169}N_5O_{47}$	717.7	2177.0	968.3	1521.0	894.2
40:1	$C_{99}H_{173}N_5O_{47}$	727.0	2205.1	ND	1549.1	ND
42:1	$C_{101}H_{177}N_5O_{47}$	736.4	2233.1	ND	1577.1	ND
42:2	$C_{101}H_{175}N_5O_{47}$	735.7	2231.1	ND	1575.1	894.2
44:1	$C_{103}H_{181}N_5O_{47}$	745.7	2261.2	ND	1605.1	ND

Table 6.1 continued

		Gc-GT1				
Carbon number	**Formula**	**$[M-3H]^{3-}$**	**$[M-3H+Mg]^{-}$**	**Gc-GT1a-$B_{4\alpha}$ ([2NeuAc-Gal-GalNAc−3H+Mg]$^{-}$)**	**Gc-GT1b-$Y_{2\alpha}$ (−[NeuAc-Gal-GalNAc], −656)**	**Gc-GT1c-$B_{3\beta}$ ([NeuGc-2NeuAc−3H+Mg]$^{-}$)**
36:1	$C_{95}H_{165}N_5O_{48}$	713.7	2165.0	ND	1509.0	ND
36:2	$C_{95}H_{163}N_5O_{48}$	713.2	2163.0	968.3	1507.0	910.2
38:2	$C_{97}H_{167}N_5O_{48}$	722.4	2191.0	ND	1537.0	910.2
40:2	$C_{99}H_{171}N_5O_{48}$	731.7	2219.1	ND	1563.1	910.2
42:2	$C_{101}H_{175}N_5O_{48}$	741.0	2247.1	968.3	1591.0	ND

*ND: non-detected.

Table 6.2. The normalized %area from the extracted fragment ions from pure GD1 isomers.

Normalized %Area from Each Fragment Ion					
Carbon number	**Water Loss**	**NeuAc Loss**	**GD1b-$Y_{2\alpha}$**	**Glycan moiety**	**GD1a-$Y_{2\alpha}$**
C36:1					
GD1a	46.7 ± 0.4*	35.1 ± 0.5	0	11 ± 0.1	7.2 ± 0.1
GD1b	74.5 ± 0.4	15.8 ± 0.6	3.6 ± 0.2	6.1 ± 0.3	0
C38:1					
GD1a	51.7 ± 0.2	26.4 ± 0.5	0	13.6 ± 0.3	8.3 ± 0.4
GD1b	72.7 ± 0.7	16.2 ± 0.2	4.1 ± 0.1	7.0 ± 0.4	0

*Mean ± SD (n=3).

Table 6.3. The relative quantification (%) results of the profiled isomeric GD1 in porcine brain.

carbon number	GD1a	GD1b	Total
36:1	71.7 ± 2.3*	24.9 ± 2.1	96.6 ± 4.4
38:1	86.2 ± 2.1	13.0 ± 2.3	99.2 ± 4.4

*Mean ± SD (n=3).

6.8 Scheme and Figures

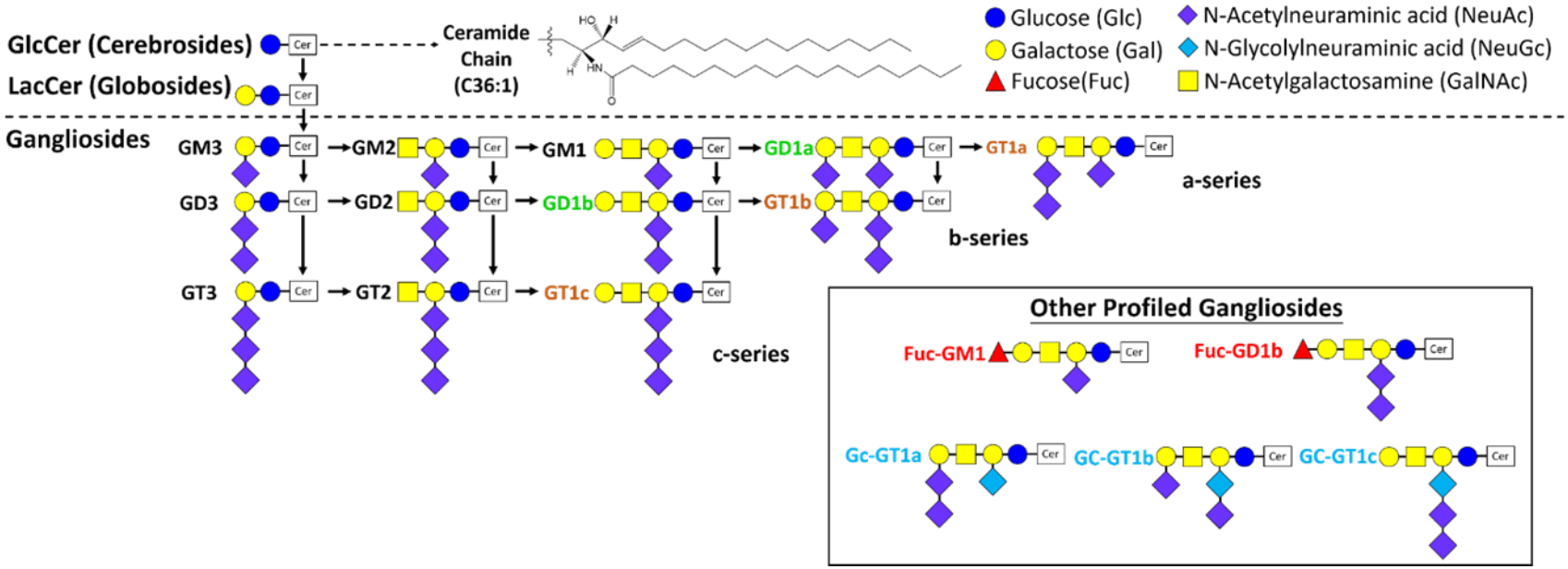

Figure 6.1. Structures of gangliosides. The map is drawn based on the *de novo* metabolic pathway of gangliosides and limited to the species that are discussed in the current work (GM3, GM1, GD1a/b, and GT1a/b/c). Other profiled gangliosides are the species that we profiled and identified in the biological samples.

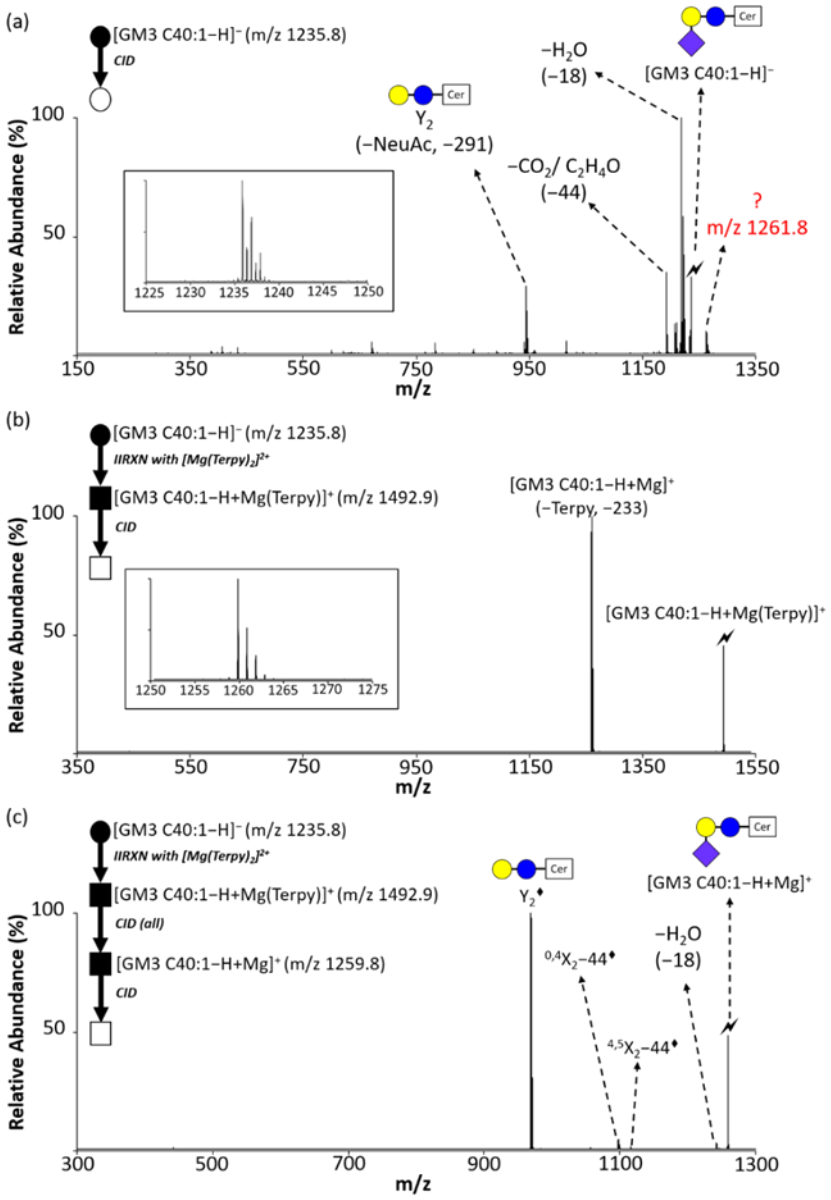

Figure 6.2. The CID spectra of various ion types of GM3-C40:1. (a) The CID spectrum of [GM3 C40:1−H]$^-$. (b) The CID spectrum of [GM3 C40:1−H+MgTerpy]$^+$. (c) The CID spectrum of [GM3-C40:1−H+Mg]$^+$. The insert in (a) is the zoom-in spectrum (*m/z* 1225 to 1250) for the isolated ion population for [GM3 C40:1−H]$^-$, and the insert in (b) is the zoom-in spectrum (*m/z* 1250 to 1275) for the isolated ion population the [GM3 C40:1−H+Mg]$^+$. The values inside the parenthesis indicate the neutral loss. The glycan moiety symbols are consistent with those of **Figure 6.1**. The lightning bolt signifies the collisionally activated precursor ion. The black and white circle (●/○) indicate the negative ion mode analysis with and without mass selection, respectively. The black and white squares (■/□) indicate the positive ion mode analysis with and without mass selection, respectively. The diamond (♦) indicates the ion with Mg^{2+}.

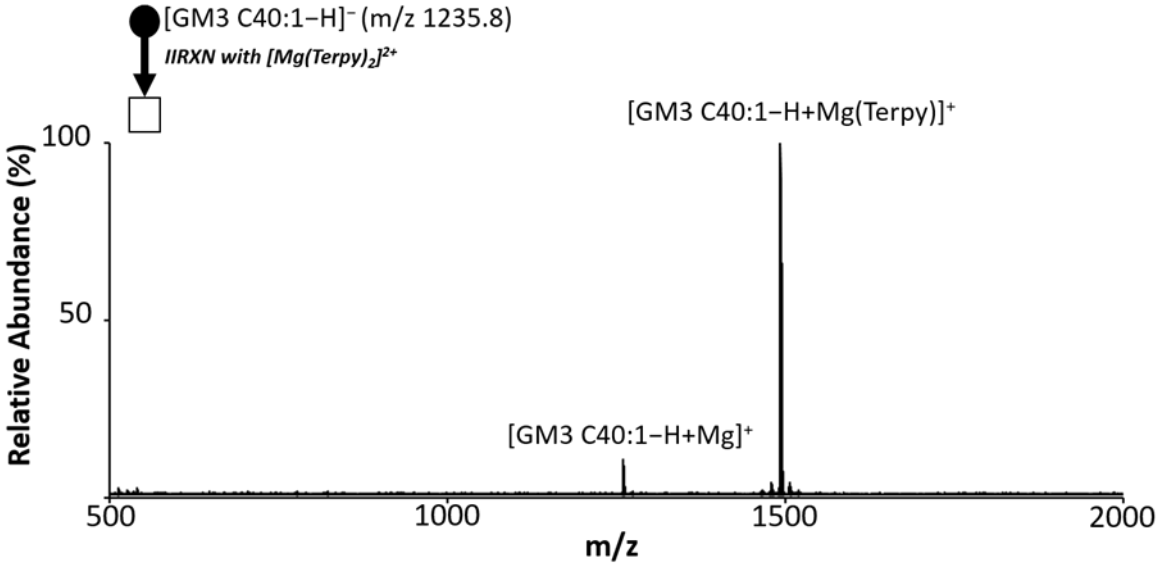

Figure 6.3. The post-ion/ion reaction spectrum of GM3 C40:1 reacting with $[Mg(Terpy)_2]^{2+}$.

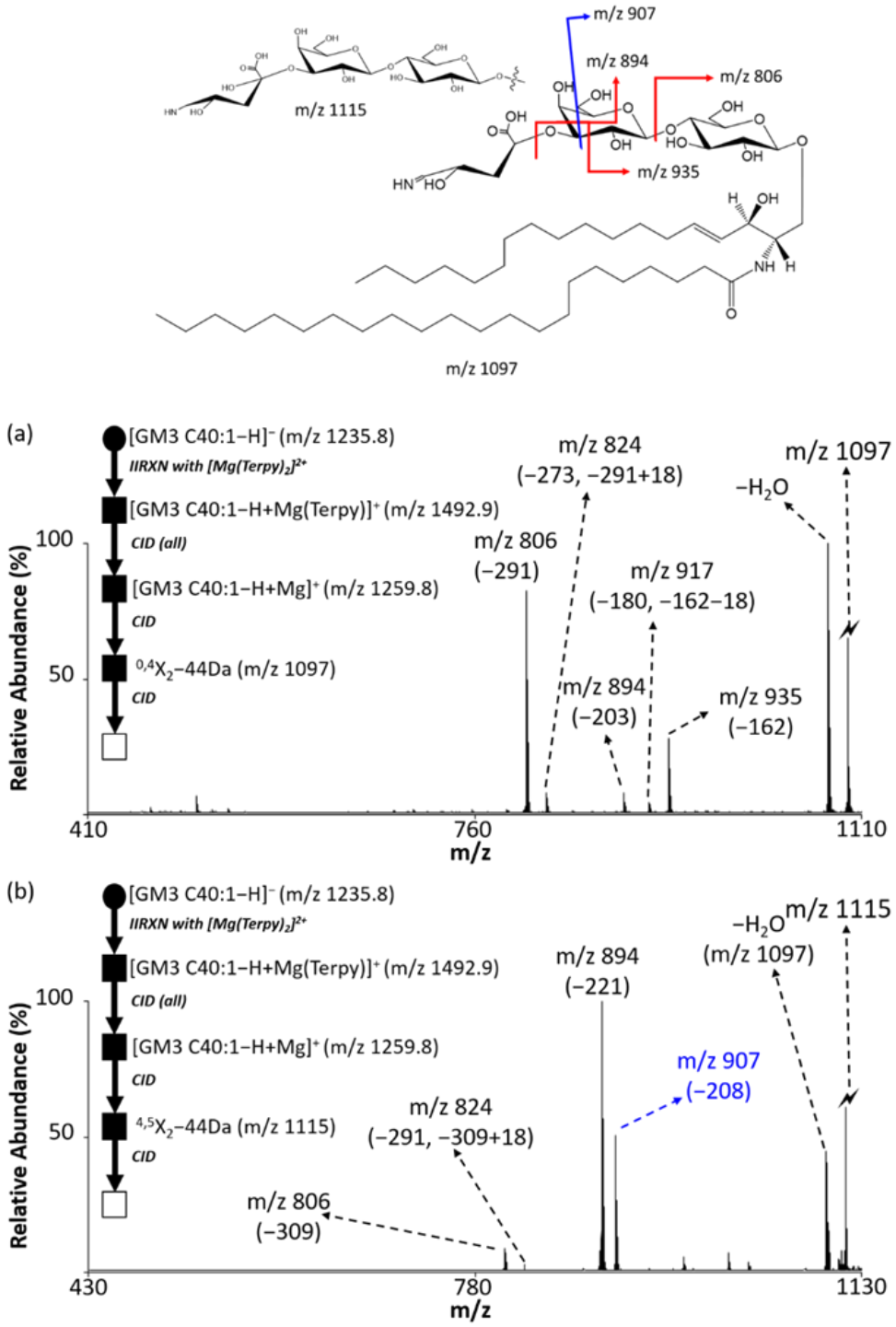

Figure 6.4. The MS^4 spectrum of fragment ions from $[GM3\ C40:1+Mg]^+$. (a) The CID spectrum from *m/z* 1097 ion. (b) The CID spectrum from *m/z* 1115 ion. The top structure shows the proposed $^{0,4}X_2$ ion and the product ions structures observed in both (a) and (b). The values inside the parenthesis indicate the neutral loss. The symbols represent as same as those in **Figure 6.2**. All ions are with Mg^{2+} adduction

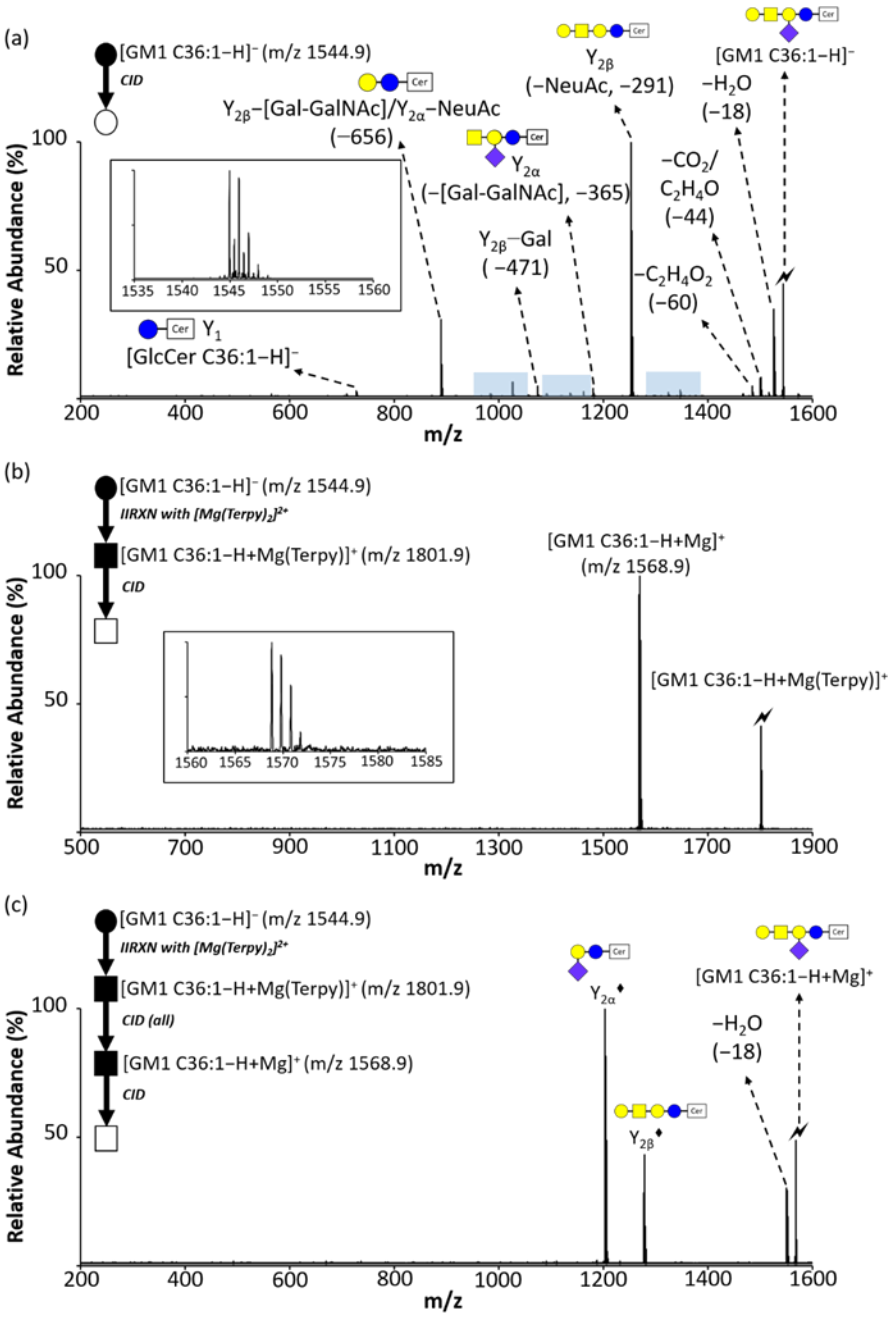

Figure 6.5. The CID spectra of various ion types of GM1 C36:1. (a) The CID spectrum of [GM1 C36:1−H]$^-$. (b) The CID spectrum of [GM1 C36:1−H+MgTerpy]$^+$. (c) The CID spectrum of [GM1 C36:1−H+Mg]$^+$. The insert in (a) is the zoom-in spectrum (*m/z* 1535 to 1560) for the isolated ion population for [GM1-C36:1−H]$^-$, and the insert in (b) is the zoom-in spectrum (*m/z* 1560 to 1585) for the isolated ion population the [GM1 C36:1−H+Mg]$^+$. The glycan moiety symbols are consistent with those of **Figure 6.1**. The transparent blue boxes highlight the unknown fragment ions. The values inside the parenthesis indicate the neutral loss. The symbols represent as same as those in **Figure 6.2**.

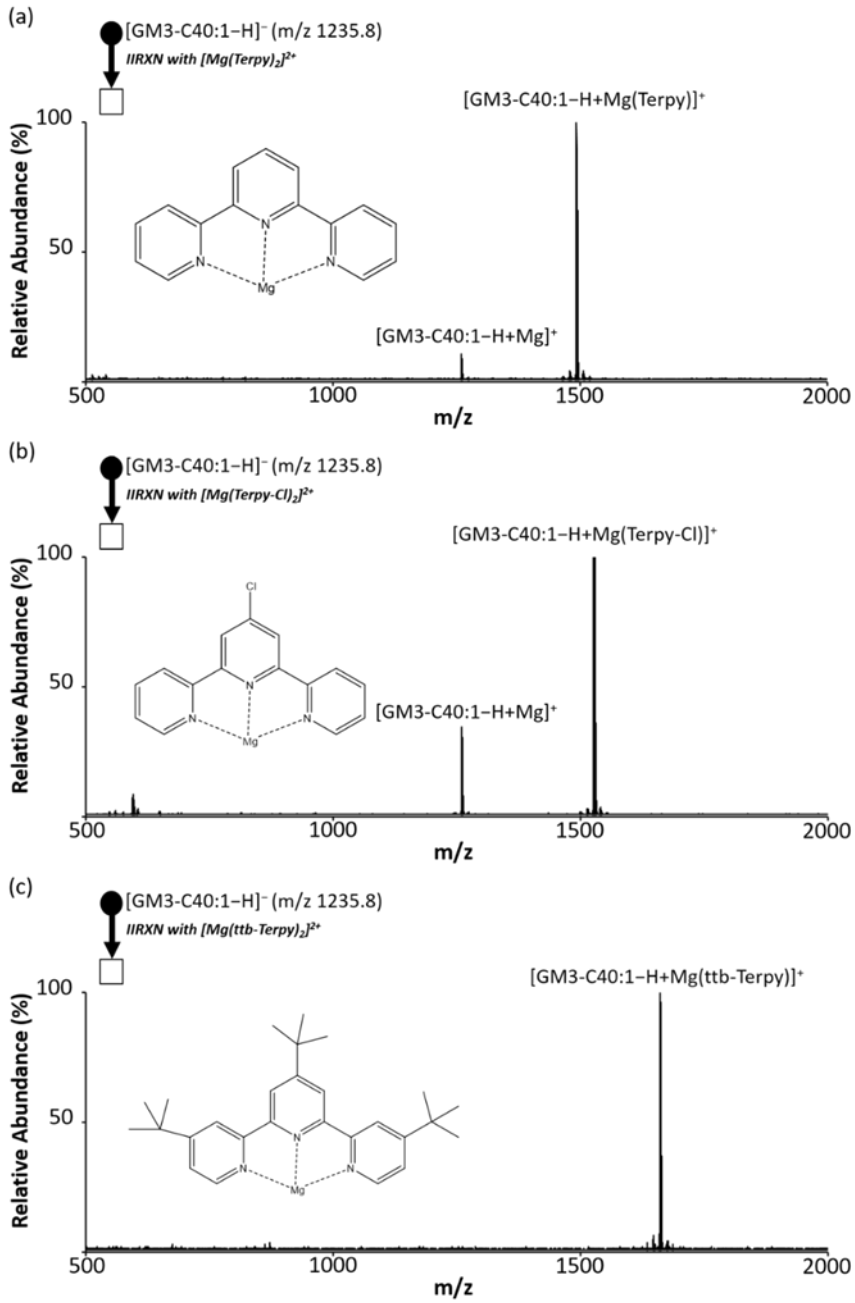

Figure 6.6. The post-ion/ion reaction spectra of GM3-C40:1 reacting with different metal-ligand dications. (a) Reaction with $[Mg(Terpy)_2]^{2+}$. (b) Reaction with $[Mg(Terpy\text{-}Cl)_2]^{2+}$. (c) Reaction with $[Mg(ttb\text{-}Terpy)_2]^{2+}$. The inserts in each spectrum are the structures of the adducted metal-ligand to the ganglioside. The symbols represent as same as those in **Figure 6.2**.

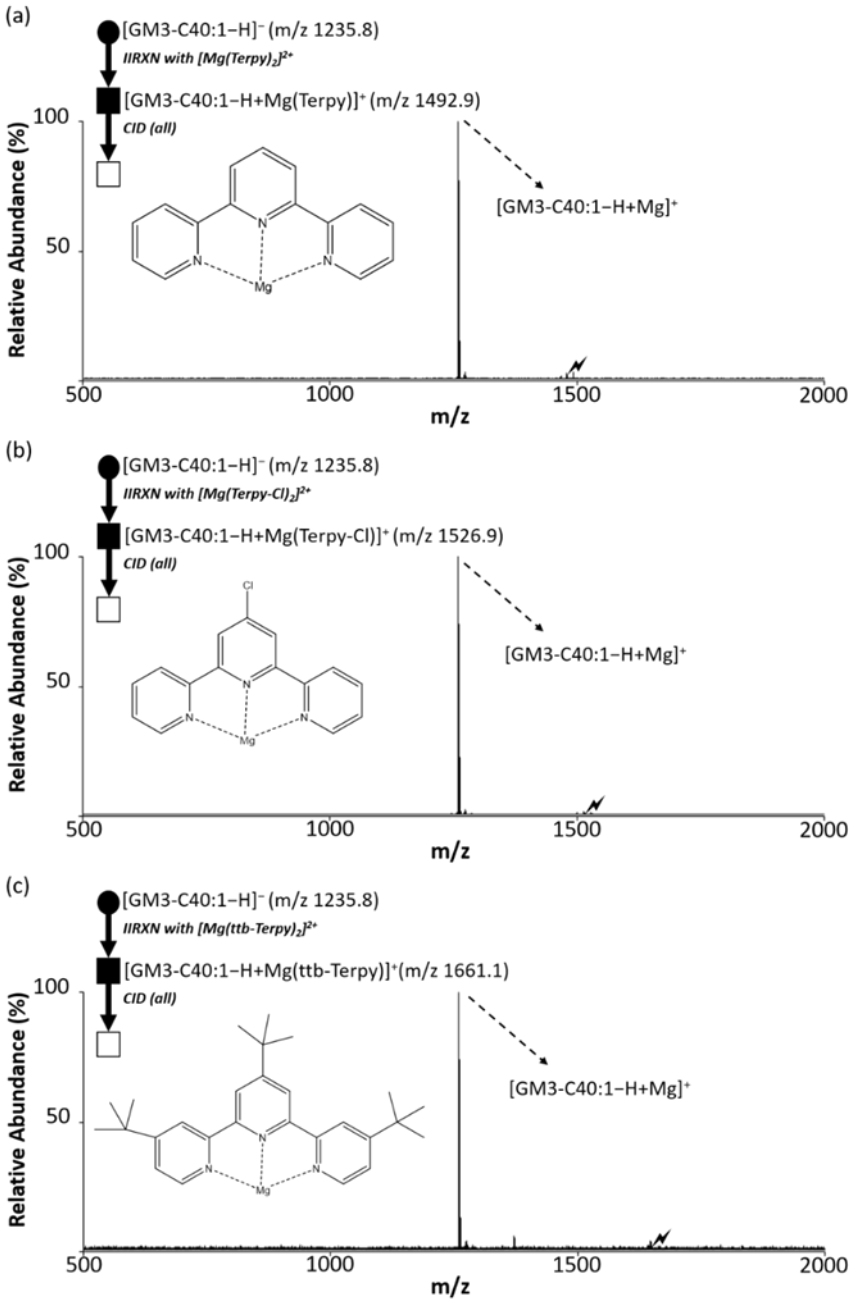

Figure 6.7. The CID spectra spectra from different GM3 C40:1-metal-ligand complex. (a) The CID spectrum of [GM3 C40:1−H+Mg(Terpy)]$^+$, AC = 0.09V. (b) The CID spectrum of [GM3 C40:1−H+Mg(Terpy-Cl)]$^+$, AC = 0.07V. (c) The CID spectrum of [GM3 C40:1−H+Mg(ttb-Terpy)]$^+$, AC = 0.13V. The inserts in each spectrum are the structures of the adducted metal-ligand to the ganglioside. The symbols represent as same as those in **Figure 6.2**.

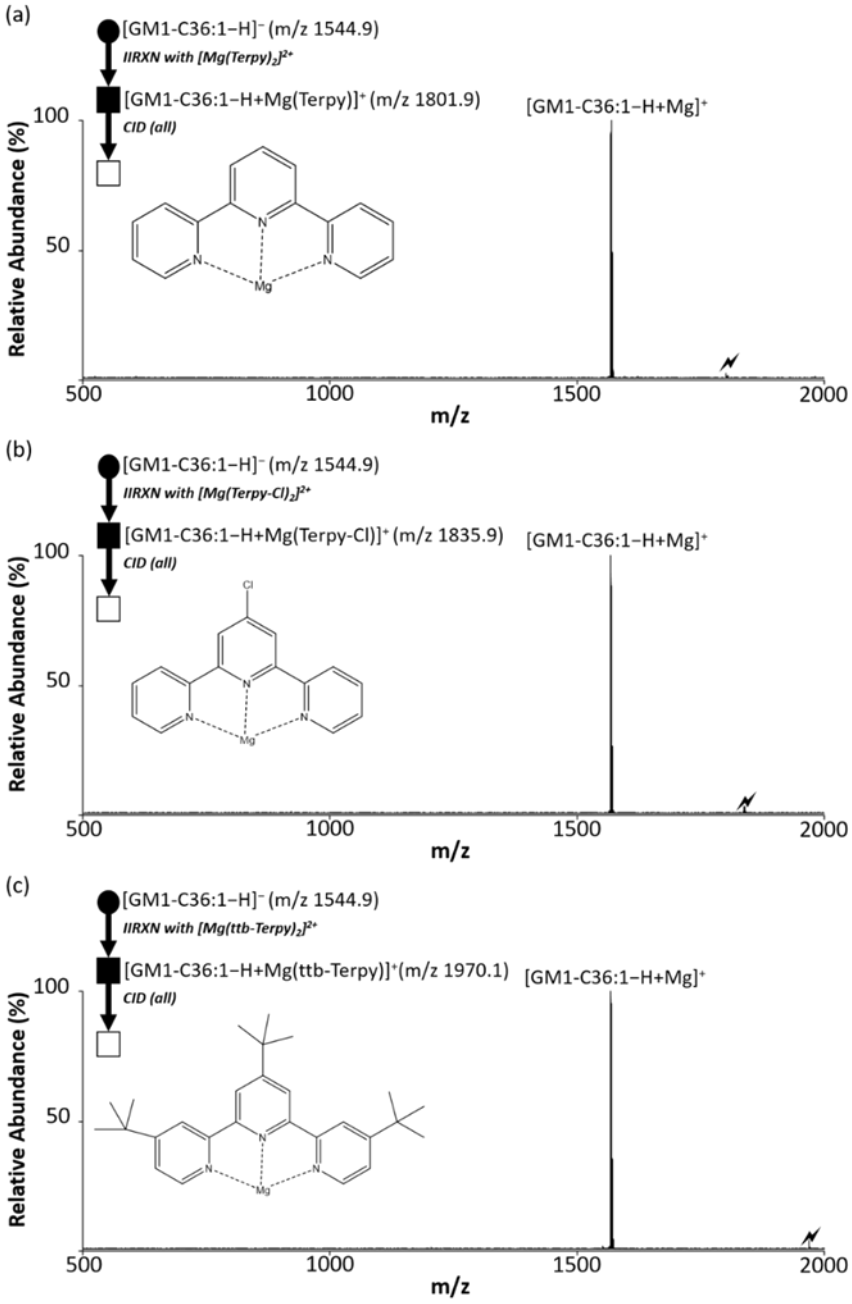

Figure 6.8. The CID spectra from different GM1 C36:1-metal-ligand complex. (a) The CID spectrum of [GM1 C36:1−H+Mg(Terpy)]$^+$, AC = 0.095V. (b) The CID spectrum of [GM1 C36:1−H+Mg(Terpy-Cl)]$^+$, AC = 0.084V. (c) The CID spectrum of [GM1 C36:1−H+Mg(ttb-Terpy)]$^+$, AC = 0.153V. The inserts in each spectrum are the structures of the adducted metal-ligand to the ganglioside. The symbols represent as same as those in **Figure 6.2**.

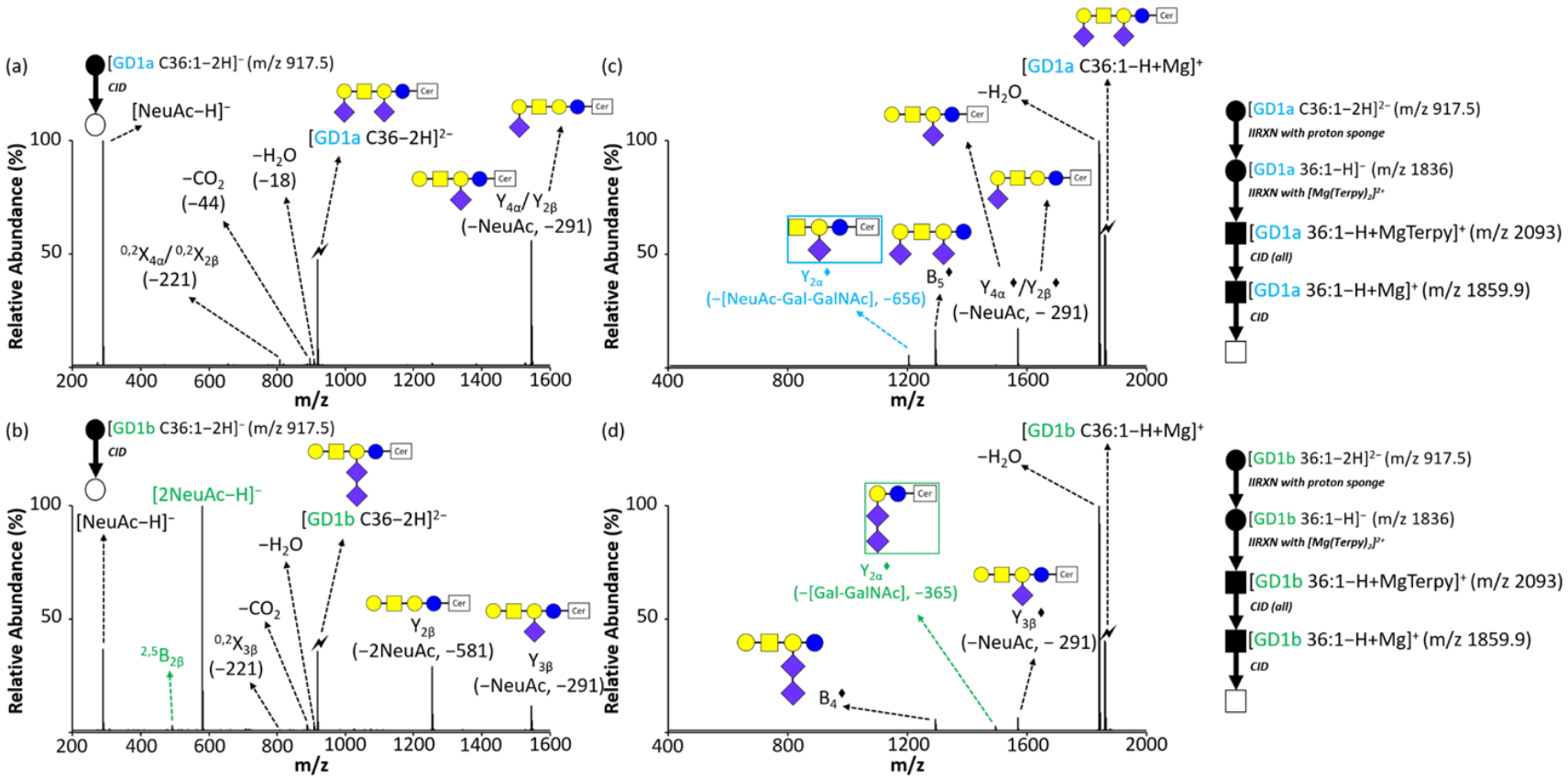

Figure 6.9. Comparison of CID spectra between isomeric GD1a and GD1b with different precursor ion types. (a) The CID spectrum of [GD1a C36:1−2H]$^{2-}$. (b) The CID spectrum of [GD1b C36:1−2H]$^{2-}$. (c) The CID spectrum of [GD1a C36:1−H+Mg]$^{+}$. (d) The CID spectrum of [GD1b C36:1−H+Mg]$^{+}$. The values inside the parenthesis indicate the neutral loss. The glycan moiety symbols are the same as in **Figure 6.1**, and the blue/green box in (c) and (d) are the diagnostic fragment ions for GD1a and GD1b isomer, respectively. The symbols represent as same as those in **Figure 6.2**. Detailed structure could be found in **Figure 6.10.**

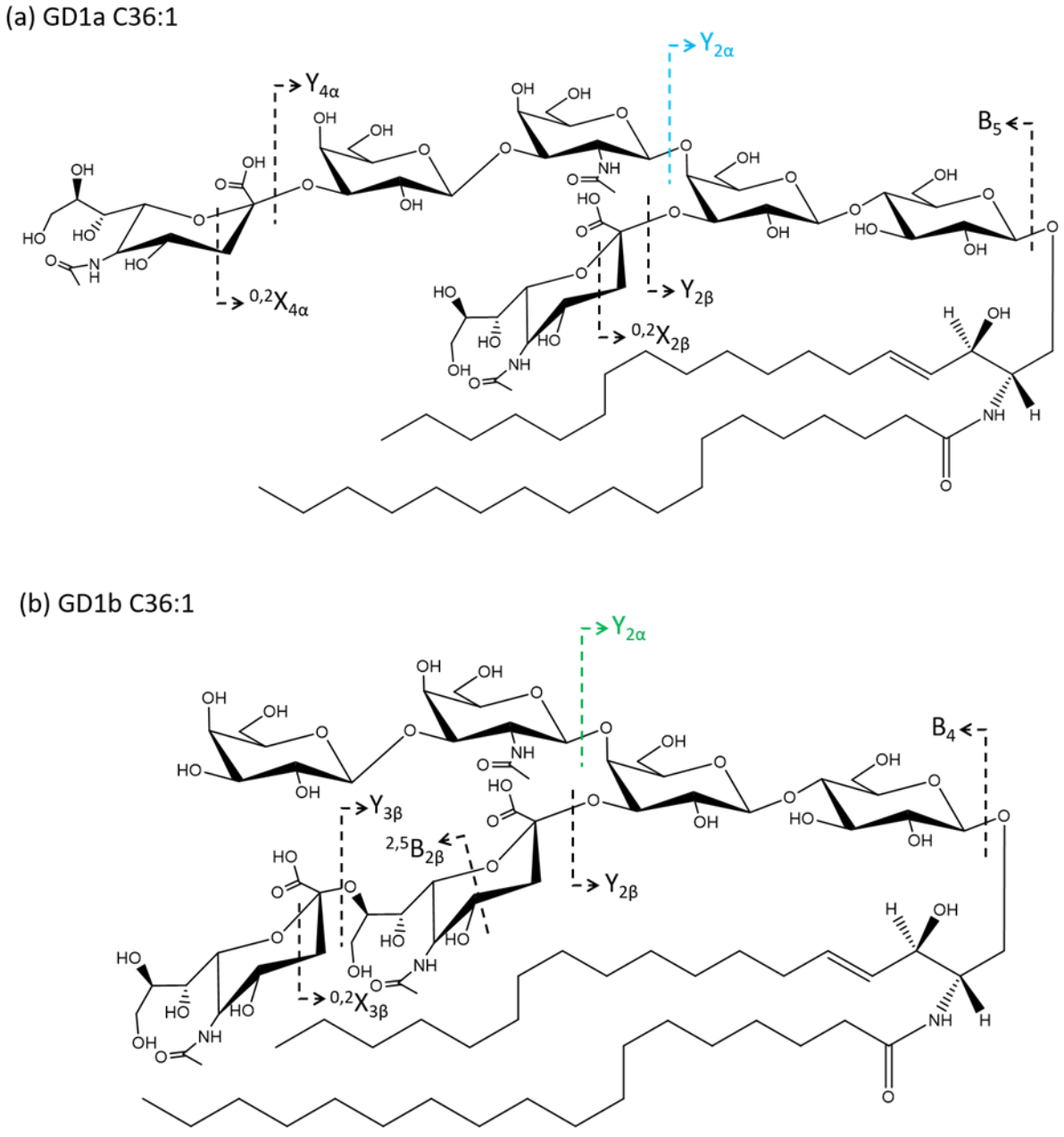

Figure 6.10. The structures of GD1-C36:1 and the proposed fragmentations. (a) GD1a C36:1. (b) GD1b C36:1.

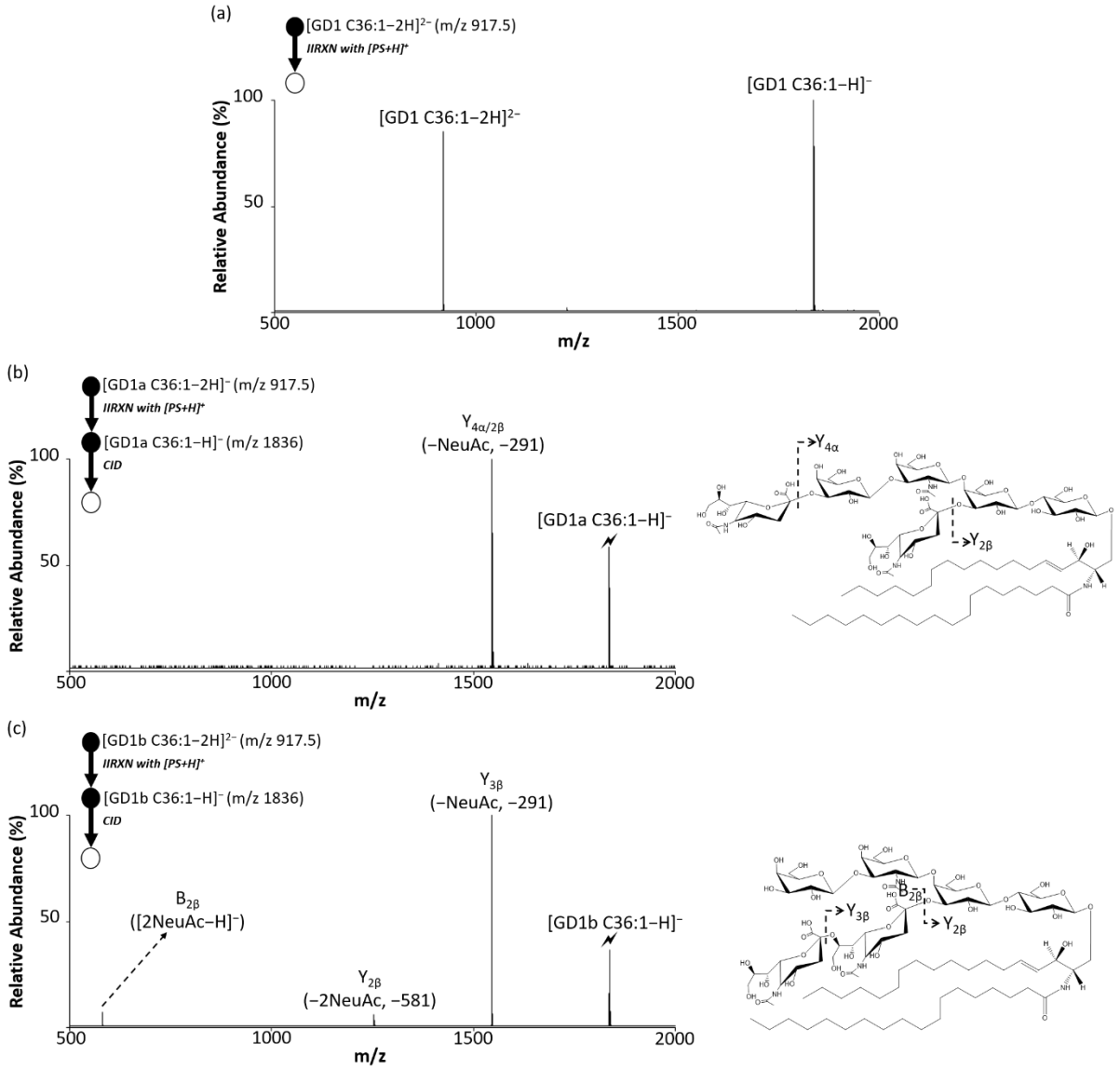

Figure 6.11. The MS spectra of GD1 C36:1. (a) The post-proton transfer reaction mass spectrum between $[GD1\ C36{:}1{-}2H]^{2-}$ and proton sponge ($[PrS{+}H]^{+}$). (b) The CID spectrum of $[GD1a\ C36{:}1{-}H]^{-}$ with the structure. (c) The CID spectrum of $[GD1b\ C36{:}1{-}H]^{-}$ with the structure. The lightning bolt signifies the collisionally activated precursor ion. The symbols represent as same as those in **Figure 6.2.**

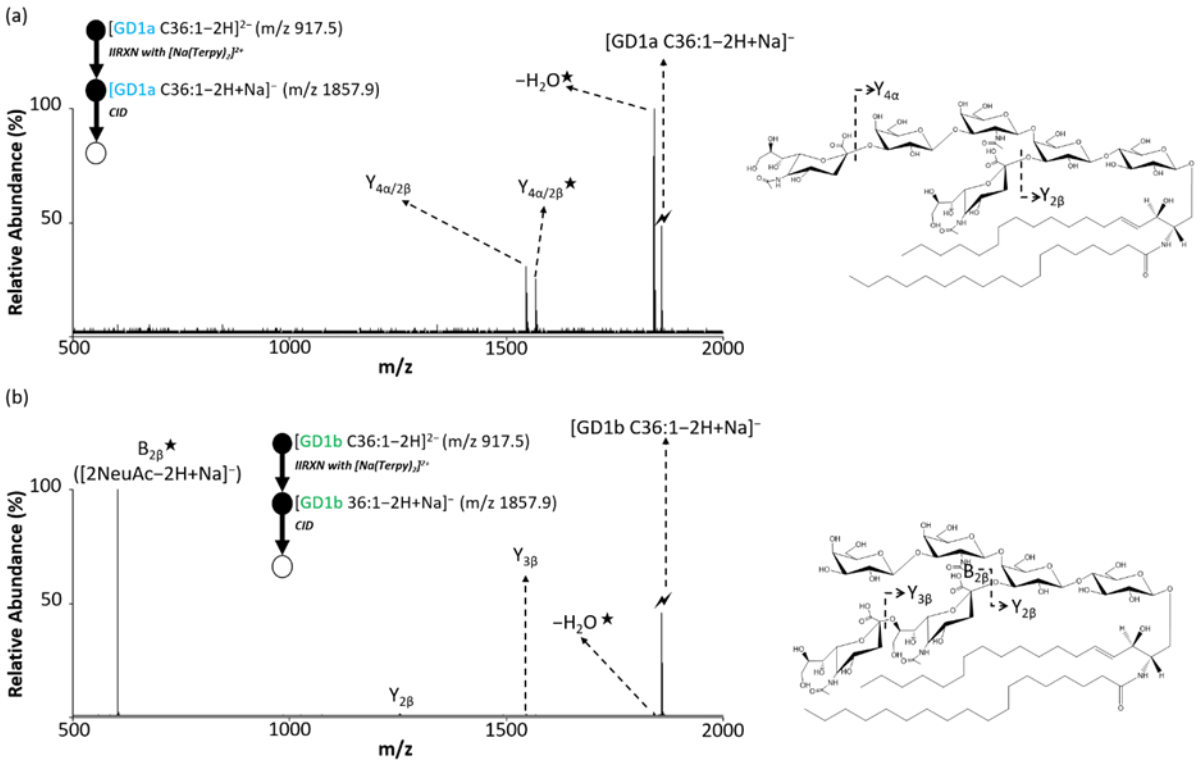

Figure 6.12. The CID spectra of sodium transfer GD1 C36:1 anions. (a) The CID spectrum of [GD1a C36:1−2H+Na]$^-$ with the structure. (b) The CID spectrum of [GD1b C36:1−2H+Na]$^-$ with the structure. The lightning bolt signifies the collisionally activated precursor ion. The black and white circle (●/○) indicate the negative ion mode analysis with or without mass selection. The ★ indicates the ion with sodium (Na^+).

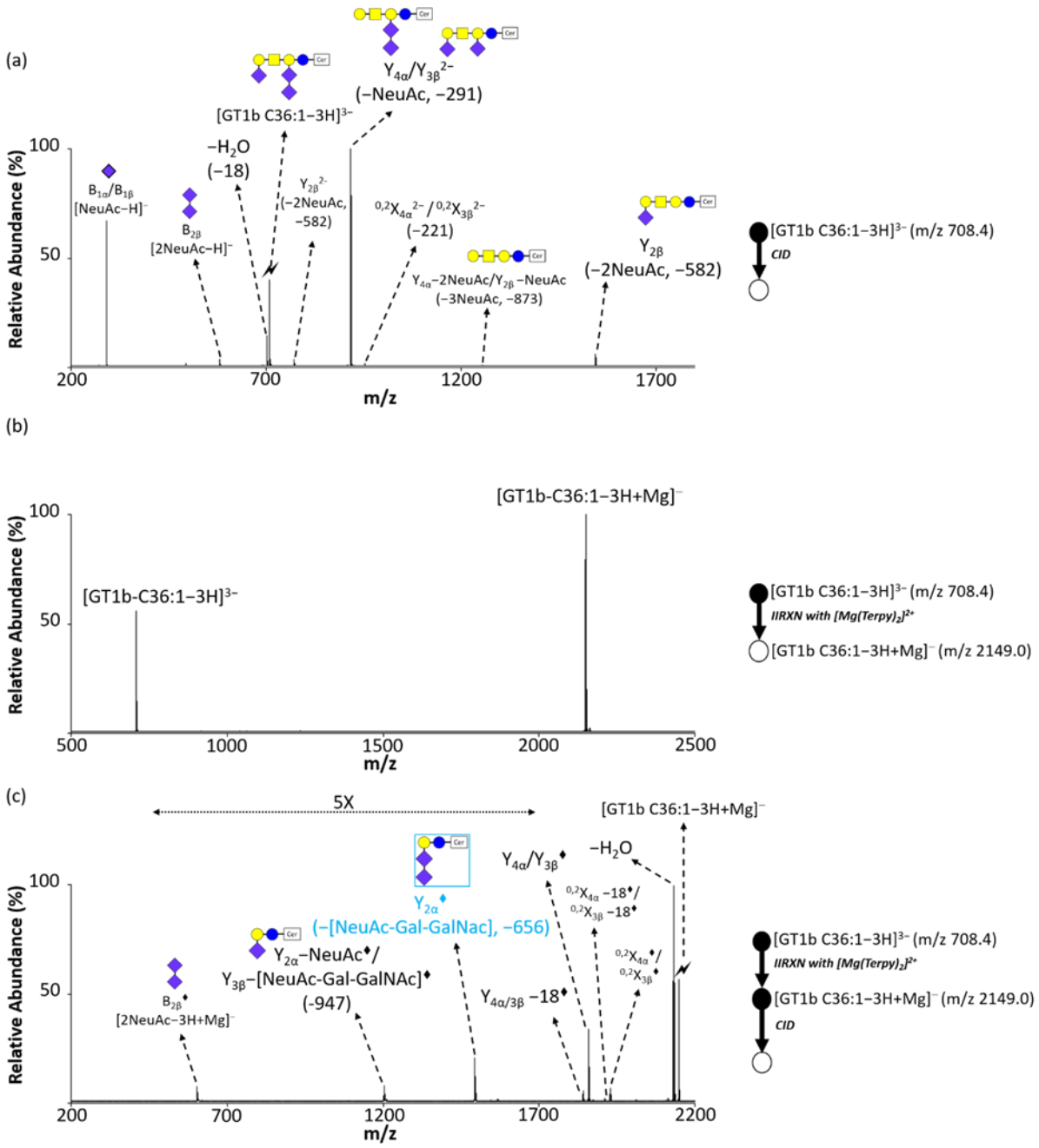

Figure 6.13. The mass spectra of GT1b C36:1. (a) The CID spectrum of $[GT1b\ C36:1{-}3H]^{3-}$. (b) The post-ion/ion reaction CID spectrum of $[GT1b\ C36:1{-}3H]^{3-}$ reacting with $[Mg(Terpy)_2]^{2+}$. (c) The CID spectrum of $[GT1b\ C36:1{-}H{+}Mg]^{-}$. The values inside the parenthesis indicate the neutral loss. The glycan moiety symbols represent as same in **Figure 6.1**, and the blue box in (c) is the diagnostic fragment ion specifically with GT1b isomer. The symbols represent as same as those in **Figure 6.2**. Detailed structure could be found in **Figure 6.14.**

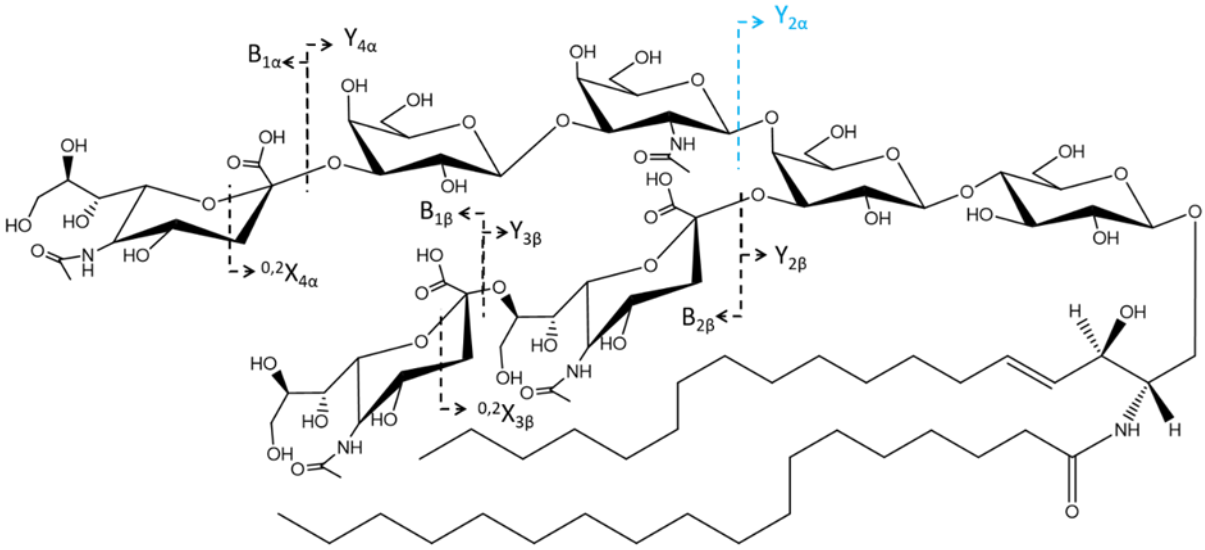

Figure 6.14. The structures of GT1b C36:1 and the proposed fragmentations.

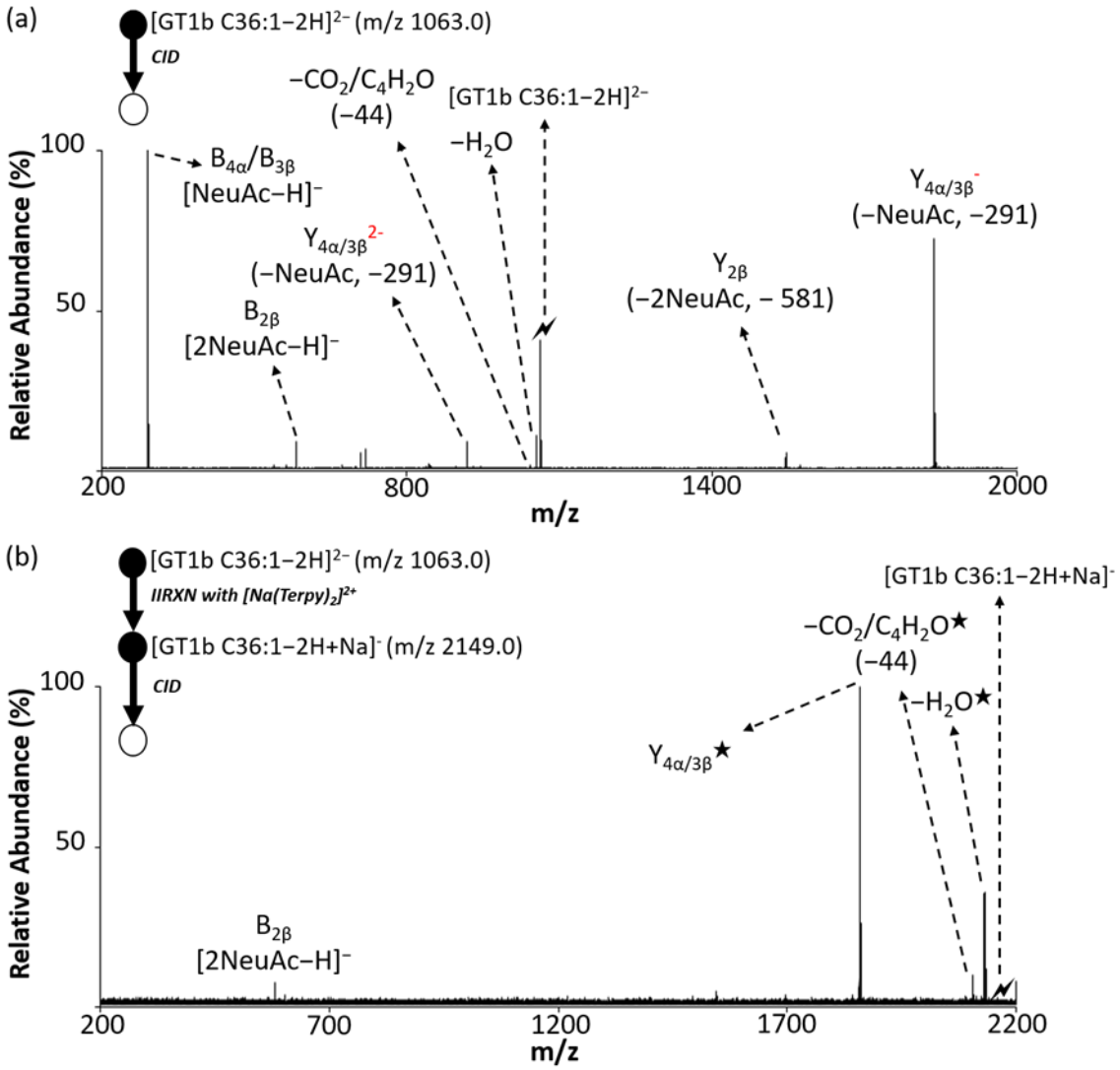

Figure 6.15. The CID spectra of different ion types of GT1b C36:1 anions. (a) The CID spectrum of $[GT1b\ C36:1{-}2H]^{2-}$. (b) The CID spectrum of $[GT1b\ C36:1{-}2H{+}Na]^{-}$. The lightning bolt signifies the collisionally activated precursor ion. The black and white circle (●/○) indicate the negative ion mode analysis with or without mass selection. The ★ indicates the ion with sodium (Na^{+}). The structures of the fragment ions are shown in **Figure 6.14**

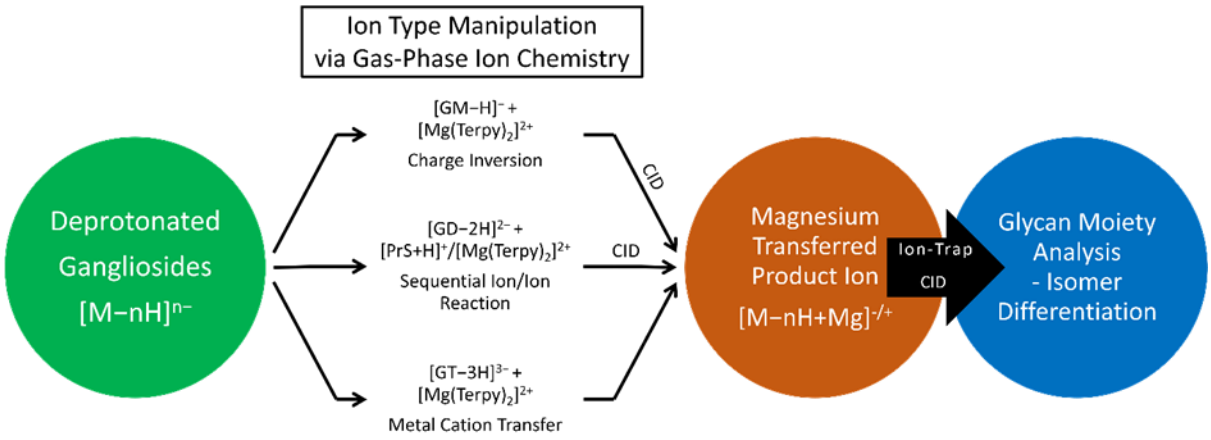

Figure 6.16. The workflow for structural elucidation of the glycan moiety on different classes of ganglioside ions via gas-phase ion chemistry. After generating deprotonated ganglioside anions, different series of gas-phase ion/ion reactions are applied to various classes of gangliosides anions with or without the combination of followed up ion-trap CID to produce targeted precursor ion-type $[M-nH+Mg]^{-/+}$, in which there is one Mg^{2+} adducting on the ganglioside. After another round of CID on the targeted precursor ion, the product ion spectra allow us to differentiate the glycan moieties.

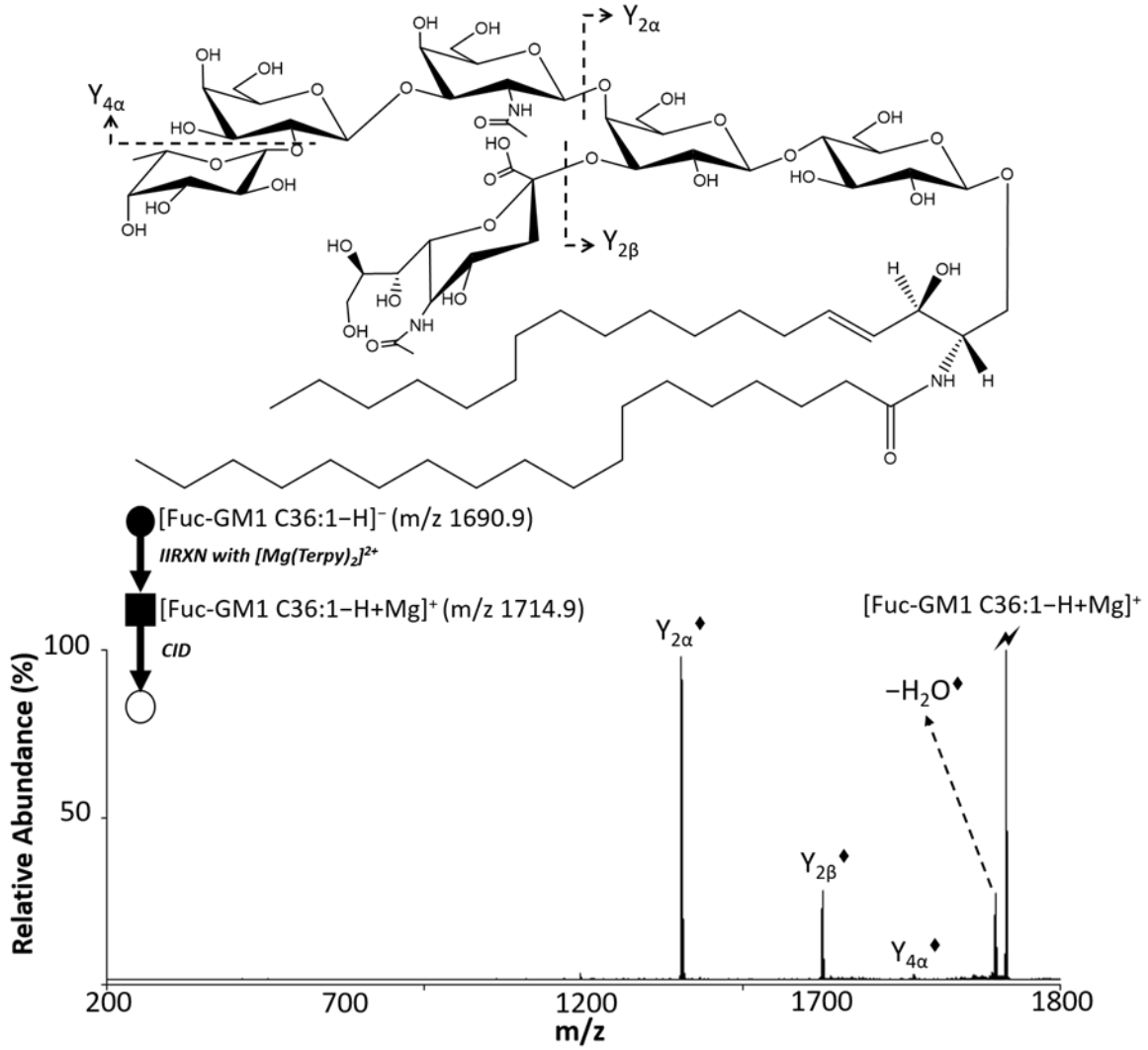

Figure 6.17. The structure of Fuc-GM1 C36:1 and CID spectrum of [Fuc-GM1 C36:1−H+Mg]$^{+}$. The lightning bolt signifies the collisionally activated precursor ion. The black and white circle (●/○) indicate the negative ion mode analysis with and without mass selection, respectively. The black and white squares (■/□) indicate the positive ion mode analysis with and without mass selection, respectively. The diamond (♦) indicates the ion with Mg^{2+}.

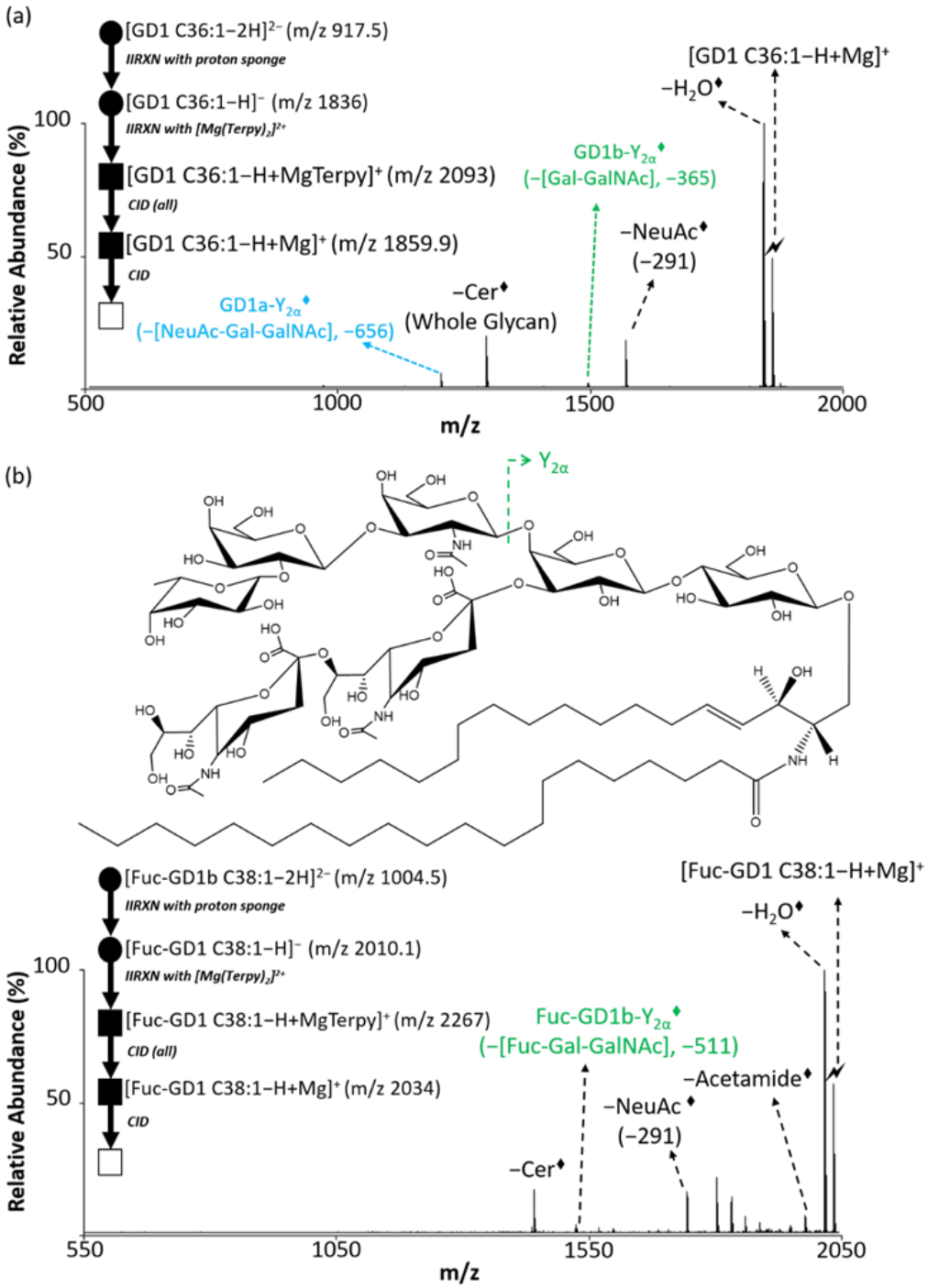

Figure 6.18. The CID spectra of the profiled GD1 C36:1 and Fuc-GD1 38:1 gangliosides from porcine brain. (a) The CID spectrum of $[GD1\ C36:1-H+Mg]^+$ (m/z 1859.9), and the structures of the fragment ions could be found in **Figure 6.10**. (b) The CID spectrum of $[Fuc\text{-}GD1\ C38:1-H+Mg]^+$ (m/z 2034) and the structure. he symbols represent as same as those in **Figure 6.2**.

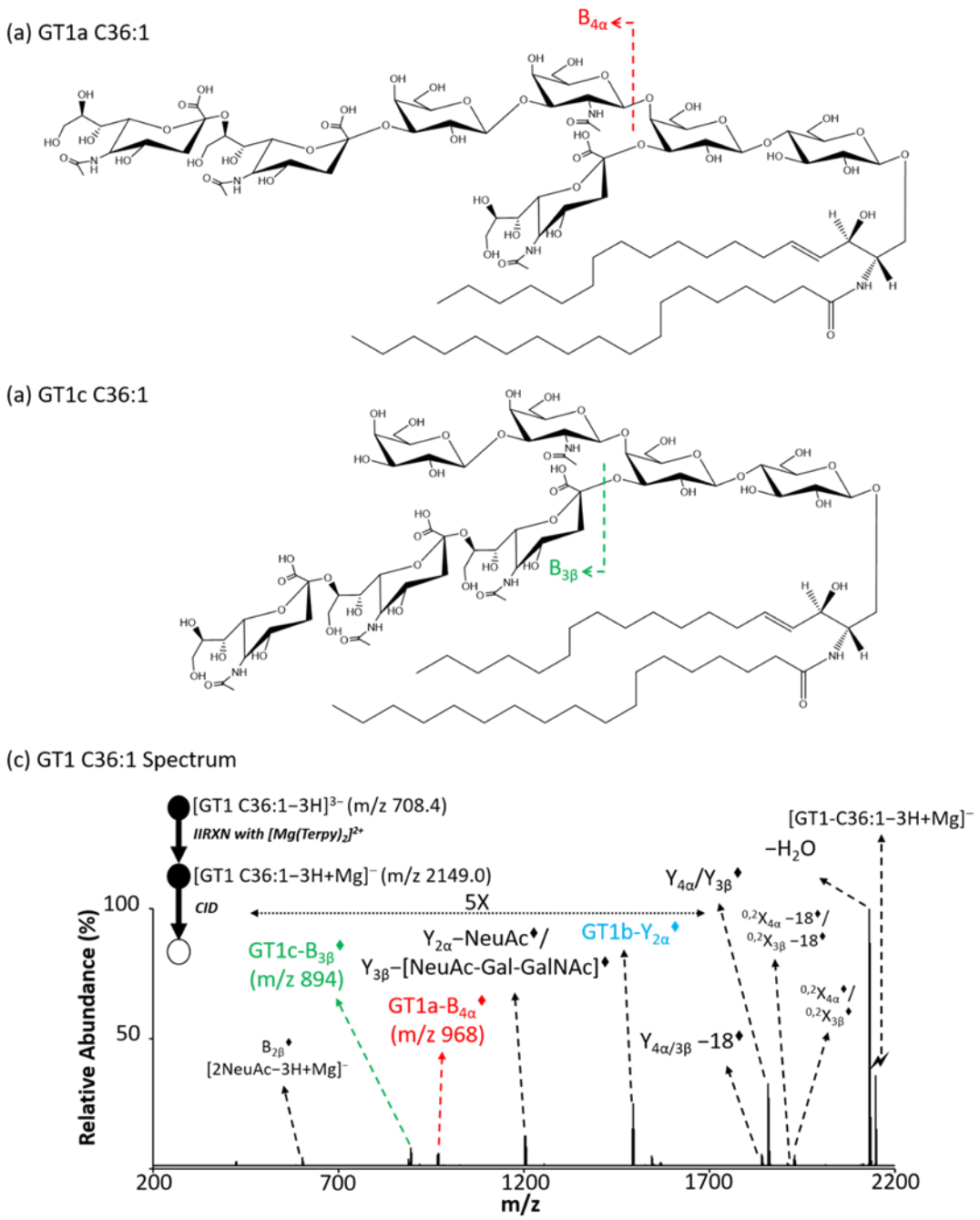

Figure 6.19. The profiled GT1 C36:1 gangliosides from porcine brain. (a) The structure of GT1a-C36:1 and the diagnostic ion. (b) The structure of GT1c C36:1 and the diagnostic ion. (c) The CID spectrum of the profiled [GT1 C36:1−3H+Mg]$^{-}$ from porcine brain. The labels in black are the labels from GT1b structure (**Figure 6.14**). The black and white circle (●/○) indicate the negative ion mode analysis with or without mass selection. The ◆ indicates the ion with Mg^{2+}.

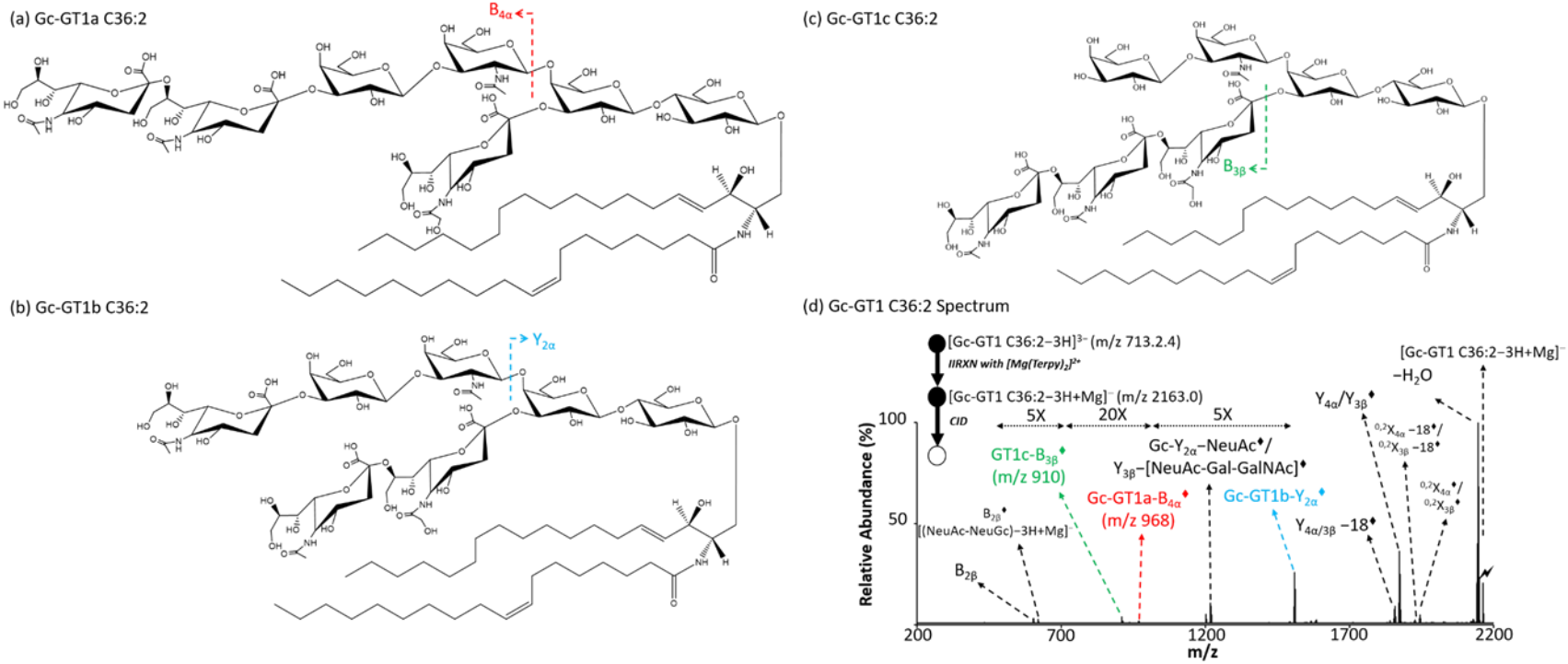

Figure 6.20. The profiled Gc-GT1 C36:2 gangliosides from porcine brain. (a) The structure of Gc-GT1a C36:2 and the diagnostic ion. (b) The structure of Gc-GT1b C36:2 and the diagnostic ion. (c) The structure of Gc-GT1b C36:2 and the diagnostic ion. (d) The CID spectrum of the profiled [Gc-GT1 C36:2−3H+Mg]$^-$ from porcine brain. The labels in black are the labels from GT1b structure (**Figure 6.14**). The black and white circle (●/○) indicate the negative ion mode analysis with or without mass selection. The ◆ indicates the ion with Mg^{2+}. Noted that the double bond on the amide-bonded fatty acyl chain only indicates the monounsaturated fatty acyl side chain is in the structure but not the real unsaturation site.

VITA

Hsi-Chun Chao was born on May 12th, 1991, in Taipei, Taiwan as the only child of Shou-Hung Chao and Ching-Chun Hsu. Hsi-Chun graduated from Taipei Municipal Jianguo High School with Honor in 2009 and then attended National Taiwan University (NTU), majoring in Pharmacy the same year. As an undergraduate student, Hsi-Chun explored a variety of interests among leadership, clinical practices, and academic research. He joined many departmental and national student associations and represented essential roles, such as director of international affairs for the pharmacy student association at NTU and executive committee member at the national pharmacy student association. He was also one of the board members who founded the NTU pharmacy student volunteer group in 2010. Hsi-Chun joined the summer shadowing program for pharmacy students in the hospital in 2010 and accomplished 640 legal hours' hospital pharmacy internship in 2013 for his development in clinical practice. He was further certified as a licensed Pharmacist by the Ministry of Examination in Taiwan in 2013 summer.

In parallel, Hsi-Chun began his undergraduate research program with Dr. Ching-Hua Kuo in Pharmaceutical Analysis Laboratory at NTU, focusing on identifying illegal phthalate plasticizer additives in pediatric pharmaceutics using capillary electrophoresis. Hsi-Chun was awarded College Student Research Scholarship from the Ministry of Science and Technology based on his undergraduate research. Hsi-Chun graduated from NTU with a Bachelor of Science in Pharmacy and was honored as the undergraduate pharmacy student representative for the commencement in 2013.

Hsi-Chun decided to pursue his academic career by entering the master's program at NTU studying pharmaceutical sciences. During the master study, Hsi-Chun focused on developing liquid chromatography coupled with tandem mass spectrometry approaches for biosample analysis. With greater concentrations on lipidomics analysis, Hsi-Chun's master thesis was about developing the concentration normalization method for cellular lipidomic studies and sphingolipidomic investigation of ischemia-induced neuron injury. Hsi-Chun earned his Master of Science in Pharmaceutical Sciences in 2015 and then began to work as a research associate at the Drug Discovery Center at NTU, focusing on both lipidomics and pharmacokinetic studies among different diseases and medications. Although he performed experiments and did research on a daily

basis, Hsi-Chun felt the gap between his theoretical background and experiments. Therefore, he entered Purdue University to pursue his doctoral degree in analytical chemistry in 2017.

During his time at Purdue, Hsi-Chun joined Dr. Scott McLuckey's research group to study the multiple charging phenomenon from the electrospray ionization process and various gas-phase ion/ion reactions for different bioanalytical purposes. Hsi-Chun was selected as W. Brooks Fortune Analytical Chemistry Fellow from 2018 to 2019 and joined academic honorary societies, Phi Lambda Upsilon (PLU) and Phi Kappa Phi (PKP) in 2018 and 2020, respectively. Hsi-Chun also served as a treasurer in the Taiwanese Graduate Student Association (ILTC) at Purdue in the 2018-2019 term and secretary in PLU Chapter Nu at Purdue in the 2020-2021 term. Besides the above academic achievement and leadership, Hsi-Chun never forgot his primary heart for helping people when he first founded the volunteer group. Therefore, Hsi-Chun joined multiple outreach groups in the chemistry department to promote chemistry and science education for K12 schoolers and general communities. Hsi-Chun successfully defended his dissertation in February 2022 and decided to integrate his background in both Pharmacy and analytical chemistry by pursuing a career in the pharmaceutical industry.

LIST OF PUBLICATIONS

1. Chao, H.-C.; Lee, K. W.; Shih, M.; McLuckey, S. A., Characterization of Homopolymer Distributions via Direct Infusion ESI-MS/MS using Wide Mass-to-Charge Windows and Gas-Phase Ion/Ion Reactions, J Am Soc Mass Spectrom, 2022, doi.org/10.1021/jasms.2c00001
2. Lee, T.-H.; Cheng, C.-N.; Chao, H.-C.; Lee, C.-H.; Kuo, C.-H.; Tang, S.-C. and Jeng, J.-S. Plasma ceramides are associated with outcomes in acute ischemic stroke patients, J Formos Med Assoc 2022, 121, 43-50.
3. Chao, H.-C.; McLuckey, S. A., Manipulation of Ion Types via Gas-Phase Ion/Ion Chemistry for the Structural Characterization of Glycan Moiety on Gangliosides, Anal Chem 2021, 93 (47), 15752–15760.
4. Chao, H.-C.; McLuckey, S. A, In-depth structural Characterization and Quantification of Cerebrosides and Glycosphingosines with Gas-phase Ion Chemistry, Anal Chem 2021, 93 (19), 7332-7340
5. Chao, H.-C.; McLuckey, S. A, Differentiation and Quantification of Diastereoisomer Pairs of Glycosphinolipids with Gas-phase Ion Chemistry, Anal Chem 2020, 92 (19), 13387-13395.
6. Chao, H.-C.; Shih, M.; McLuckey, S. A., Generation of Multiply-Charged Protein Anions from Multiply-Charged Protein Cations via Gas-Phase Ion/Ion Reactions, J Am Soc Mass Spectrom 2020, 31, 1509−1517.
7. Jhang, R.-S.; Lin, S.-Y.; Peng, Y.-F.; Chao, H.-C.; Tsai, I-L.; Lin, Y.-T.; Liao, H.-W.; Tang, S.-C.; Kuo, C.-H.; Jeng, J.-S., Using the PCI-IS Method to Simultaneously Estimate Blood Volume and Quantify Nonvitamin K Antagonist Oral Anticoagulant Concentrations in Dried Blood Spots, Anal Chem, 2020, 92 (3), 2511-2518.
8. Liao, H.-W.; Kuo, C.-H.; Chao, H.-C.; Chen, G.-Y., Post-column infused internal standard assisted lipidomics profiling strategy and its application on phosphatidylcholine research, Journal of Pharmaceutical and Biomedical Analysis, 178 (2020) 112956.
9. Chao, H.-C.; Lee, T.-H.; Chiang, C.-S.; Yang, S.-Y.; Kuo, C.-H.; Tnag, S.-C., Sphingolipidomics investigation of the temporal dynamics after ischemic brain injury, J Proteom Res, 2019, 9, 3470-3478
10. Chen, G.-Y.; Chao, H.-C.; Liao, H.-W.; Tsai, I.L.; Kuo, C.-H, Rapid quantification of glutaminase 2 (GLS2)-related metabolites by HILIC-MS/MS, Anal Biochem, 2017, 539, 39-44.
11. Jung, W.-H.; Liu, C.-C.; Yu, Y.-L.; Chang, Y.-C.; Lien, W.-Y.; Chao, H.-C.; S.-Y.; Kuo, C.-H.; Ho. H.-C.; Chan, C.-C. Chan. Lipophagy prevents activity-dependent neurodegeneration due to dihydroceramide accumulation in vivo, EMBO reports, 2017, 18, 1150-1165.
12. Chao, H.-C.; Chen, G.-Y.; Hsu, L.-C.; Liao, H.-W.; Yang, S.-Y.; Wang, S.-Y.; Li, Y.-L; Tang S.-C.; Tseng, Y.J. (this is going), Kuo C.-H., Using precursor ion scan of 184 with liquid chromatography-electrospray ionization-tandem mass spectrometry for concentration normalization in cellular lipidomic studies, Anal Chim Acta, 2017, 971, 68-7

13. Chepyala, D.; Tsai, I.-L.; Liao, H.-W.; Chen, G.-Y.; Chao, H.-C.; Kuo, C.-H. Kuo, Sensitive screening of abused drugs in dried blood samples using ultra-high-performance liquid chromatography-ion booster-quadrupole time-of-flight mass spectrometry, J Chromatog A, 2017, 1491, 57-66.
14. Chao, H.-C.; Liao, H.-W.; Kuo, C.-H., Using water plug-assisted analyte focusing by micelle collapse in combination with microemulsion electrokinetic chromatography for analyzing phthalate esters, J Chromatog A, 2016, 1445, 149-157.